Studying the self-assembly of networks of conjugated oligomers

Lim, Zheng Bang

2012

STUDYING THE SELF-ASSEMBLY OF NETWORKS OF CONJUGATED OLIGOMERS

LIM ZHENG BANG

SCHOOL OF MATERIALS SCIENCE AND ENGINEERING

2012

STUDYING THE SELF-ASSEMBLY OF NETWORKS OF CONJUGATED OLIGOMERS

LIM ZHENG BANG

School of Materials Science and Engineering

A thesis submitted to the Nanyang Technological University
in partial fulfillment of the requirement for the degree of
Doctor of Philosophy

2012

<u>Acknowledgements</u>

School of Materials Science and Engineering   I

Nanyang Technological University

<u>Abstract</u>

Two new tetrahedral symmetric core units (p-type **1** and n-type **2**) for forming organic supramolecules were successfully synthesized. They were then self-assembled by Zn(II)–coordination to form new 3D supramolecular networks **S1** and **S2** which could be disassembled by adding more Zn(II) ions and re-self-assembled to form extended 3D networks **S3–6** after inserting linear linking units (p-type **26** or n-type **27**) into. Energy transfer between core and linker units was observed in **S4** and **S6** who emit red fluorescence with the emission coming from the benzothiadiazole linker unit (n-type) within the networks due to its lower bandgap. **S1–6** are insoluble in any organic solvents at room temperature. They are found to be relatively amorphous and non-porous (highly interpenetrating) based on their XRD and BET results, respectively. CdSe nanoparticles were successfully incorporated in **S3** and **S4** to form new nancomposites **S3 (with CdSe)** and **S4 (with CdSe)** which were evaluated by TEM and XRD.

Same dialkoxybenzothiadiazole (acceptor) was combined with different types of thiophene-based monomers (donors, D) under Stille reaction to form new D–A π-conjugated organic copolymers **P1–4** with low bandgaps, proving the substituted benzothiadiazole was a good n-type unit. A PCE result of over 1% has been obtained from a photovoltaic device using **P4** combined with PCBM. As well as these covalently linked organic polymers, Zn(II)–coordinated self-assembled metallopolymers were produced including two metallo-homopolymers **P5** (p-type), **P6** (n-type) and a metallo-*alt*-copolymer (p-type-*alt*-n-type) (**P7**). They are soluble in highly polar aprotic solvents and hence can be used as models to compare with the insoluble networks **S1–6**. The electro-optical properties of the monomers as well as of the metallopolymers are strongly influenced by the nature of the attached π-conjugated

spacer unit. **P7** featured an energy transfer from the donor to the acceptor unit (substituted benzothiadiazole) and this acceptor unit acted as sole emissive unit to produce red fluorescence from the polymers due to its lower bandgap.

Table of Contents

Table of Figures

Table of Tables

Chapter 1 Introduction

1.1 Objective

The objectives of this project are to prepare and study several networks of organic conjugated molecules through metal-coordination self-assembly. These are done by formation of new 3D conjugated core units (p-type and n-type) which were self-assembled through metal-coordination to form a new generation of 3D metal-coordinated self-assembled supramolecular networks and extended 3D networks, after inserting different linkers (p-type and n-type) in between the original cores. They networks are then studied for their assembly and properties. The organic networks were then also combined with nanoparticles to form new nanocomposites. The n-type units mentioned above were proven to be good n-type units by combining them with different types of thiophene-based monomer to synthesize new moderate bandgap (E_g) π-conjugated polymers which were tested in OPV devices. To further evaluate the effect of metal complexation on the units, 1D linear metal-coordinated metallopolymers (n-type and p-type) using the same linkers (p-type and n-type) mentioned above were also synthesized to be used as models to study and compare with the self-assembled 3D supramolecular networks. The optoelectro-properties of all these types of organic molecules were examined to assess their utility as active components in electronic devices such as Organic Light Emitting Diodes (OLEDs), Organic Photovoltaics (OPVs), Organic Field Effect Transistors (OFETs) and/or as templates for formation of hybrid organic-inorganic nanomaterials.

1.2   Background

Electrically conducting polymers or π-conjugated polymers are composed of conjugated polymer chains with π-electrons delocalized along the chain backbone. By modifying their molecular structures, new polymers that exhibit electrical conductivities nearly comparable to metals while retaining the advantages of polymers (e.g. solution processability) have been developed. Instead of these traditional covalently linked π-conjugated polymers, non-covalent self-assembly rapidly and easily generates new types of large and complex supramolecular metallopolymers or even supramolecular networks—from easily available building blocks with maximum efficiency. Also, due to its thermodynamically driven self-correcting ability, self-assembly shows greater potential for the synthesis of defect free supramolecules. Among the approaches to supramolecules, one efficient interaction is metal–ligand coordination which is highly directional. Metal–ligand coordination allows the construction of defined supramolecular architectures and possesses an increased stability compared to hydrogen bonding (one metal–ligand bond is equivalent in energy to several hydrogen bonds). When functionalized with flexible or solubilizing functional groups, such materials can become soluble in organic solvents and can be solution processed at room temperature into large-area, optical-quality thin films which are readily fabricated into desired shapes that are potentially useful in inexpensive, flexible electronic devices to which a lot of research efforts, both in device design and materials' synthesis have been conducted during the past several decades.

1.3　Overview

The synthesis and characterization of two new 3D tetrahedral symmetric organic units for forming organic supramolecules, in which the structures begin from a central tetraphenylmethane unit, extending conjugation through the p-type or n-type linker units and end with 2,2':6',2''-terpyridines units in the four arms are mainly discussed in Chapter 2. Long alkoxy chains attached on the p-type and n-type linkers in these cores are to enhance the solubility of these two core molecules for 3D supramolecules. P-type organic molecules are defined as the organic molecules that are electron rich and thus strong in electron donating whereas n-type organic molecules are defined as the organic molecules that are electron poor and thus strong in electron accepting.

The previously mentioned n-type linker units, dialkoxybenzothiadiazole is likely to be a good electron acceptor. To prove it to be a good n-type unit, this acceptor unit (A) was combined with different types of thiophene-based monomers acting as donors (D) under Stille cross-coupling reaction to form new D–A π-conjugated organic copolymers. The bandgap and LUMO energies of these polymers were reduced which confirmed dialkoxybenzothiadiazole to be a good n-type unit. One of these copolymers was then mixed with PCBM to test its performance in OPV devices. The synthesis, characterization and the devices performance of these new OPV copolymers are discussed in Chapter 3.

Instead of traditional organic conjugated polymers as shown in Chapter 3, Chapter 4 describes the synthesis and characterization of several linear supramolecular metallopolymers which were formed by Zn(II)–coordination of π-conjugated bis(2,2':6',2''-terpyridines) molecules whose 4'-positions were linked to different p-type or n-type spacer

units. These linear metallopolymers include n-type and p-type linear metallopolymers, and also the metallo-*alt*-copolymer in which n-type and p-type molecules co-alternate in a copolymer. They are processable as expected from literature precedents and can be studied as models for the 3D self-assembled networks which are insoluble as discussed later in Chapter 5.

In Chapter 5, the use of Zn(II)-coordination mechanism to link the 3D core units (p-type and n-type) described in Chapter 2 to form new 3D self-assembled supramolecular networks is discussed. Extended 3D networks were obtained through disassembly (breaking up) of the formed Zn(II)–coordinated networks and then re-assembly by inserting the linear bis(tpy) linkers (p-type or n-type) discussed in Chapter 4. The properties of these new insoluble 3D Zn(II)–coordinated self-assembled supramolecular networks were studied and compared with the 1D linear soluble self-assembled metallosupramolecular polymers shown in Chapter 4. These 3D self-assembled networks were also further investigated for the possibility of accommodating nanoparticles of CdSe and Au (or potentially other materials) within them.

1.4   Scope

Composites of organic and inorganic materials are potential to be used as the active components in electronic devices such as Organic Light Emitting Diodes (OLEDs), Organic Photovoltaics (OPVs), Organic Field Effect Transistors (OFETs). This is because such composites combine the excellent electronic properties of inorganic materials with the processability of organic materials. The formation of ordered assemblies of the inorganic and organic components can be expected to optimize the performance of such composites. The

formation of such ordered structures requires ordered 3D organic macrostructures. Covalently bonded 3D structures can be made but are usually insoluble gels due to the extensive cross-linking within them. Non-covalent self-assembly (metal-coordination in this project) offers an attractive way to prepare processable functional organic macromolecular materials. Besides, large supramolecular architectures can be obtained from small components in solution in mild condition. Furthermore, whereas defects formed during the synthesis of conventional covalently bonded macromolecules are difficult or impossible to remove, metal-coordinated self-assembled materials which held together by non-covalent metal-coordination linkages are potentially self-healing due to their dynamic nature. Thus, in this thesis, new 3D Zn(II)–coordinated supramolecular networks were prepared. Extended 3D networks were obtained through disassembly of the formed Zn(II)–coordinated networks and then re-assembly by inserting the linear bis(tpy) linkers (p-type or n-type). These 3D Zn(II)–coordinated supramolecular networks were studied for their assembly and properties. They were also further investigated for the possibility of accommodating inorganic nanoparticles within them to form new groups of 3D ordered nanocomposites.

1.5   Tools and methods

All of these new organic molecules or self-assembled networks (also composites of organic molecules with inorganic metal particles) were characterized and their structures were confirmed by Nuclear Magnetic Resonance (NMR) spectroscopy, Matrix-Assisted Laser Desorption/Ionization Time-Of-Flight (MALDI-TOF) mass spectroscopy, Elemental Analysis and High Resolution Electrospray[+]-Time-Of-Flight mass spectra (HR ES[+]-TOF MS). Their thermal properties were studied by Thermogravimetric Analysis (TGA) and

Differential Scanning Calorimetry (DSC). Their optical properties were studied by UV-Vis absorption spectroscopy and photoluminescent emission spectroscopy. Their electrochemical properties were evaluated by Cyclic Voltammetry (CV). Their morphology and especially their self-assembly by non-covalent interactions into extended networks (also the degree of order of networks) were studied by means of techniques such as Atomic Force Microscopy (AFM) or X-Ray Diffraction (XRD). Based upon the results obtained, the suitability of these materials to be used as active materials in electronic devices, either alone or as composite with other organic or inorganic materials was assessed. The self-assemblies were also used as possible templates for accommodating inorganic semiconductor nanoparticles to form a new type of nanocomposites which were examined by means of techniques such as Transmission Electron Microscopy (TEM) or X-Ray Diffraction (XRD).

Chapter 2   Synthesis and characterization of 3D conjugated cores for supramolecules

2.1   Review

The power and beauty of spontaneous self-assembly derives from its ability to rapidly and simply generate large, complex and sophisticated "supramolecules" from easily available building blocks with high efficiency. Therefore, supramolecular chemistry has become one of the most interesting fields in modern chemistry. In 1987, Lehn et al. received the Nobel Prize for Chemistry for their pioneering studies in selective host-guest chemistry.[1] Among the approaches to the self-assembly, one efficient way which has been used extensively (e.g. in forming composites of inorganic and organic materials) is metal–ligand coordination. Chelating ligands are of interest since they allow the construction of defined supramolecular architectures and possess increased stability compared to hydrogen bonding.[2]

Self-recognition and self-assembly of functional structures into supramolecular metalloarchitectures through the interactions of third-row transition metal ions and appropriate chelating ligands utilizes the concept of supramolecular chemistry and they afford many intriguing architectures that have gained much attention.[1,3] It is difficult for us to use the directionality of the "weak interaction" (e.g. hydrogen bonding, π–π stacking, etc.) that nature uses for self-assembly processes. In contrast, because of d-orbital involvement, dative metal–ligands bonds are highly directional. Moreover, transition metal–ligands bonds have bond energies of ca. 15–25 kcal/mol, much less than covalent bonds (ca. 60–120

kcal/mol) but stronger than the weak interactions (ca. 0.5–10 kcal/mol) just mentioned. Thus, one dative metal–ligand bond has the strength of several hydrogen bonds in the self-assembly process.[4] Among the advantages of this method are its simplicity, in which large supramolecular architectures can be constructed from small components in solution in a single step under mild conditions, and the avoidance of expensive and sometimes toxic polymerisation catalysts, which are difficult to be removed from the final products. Furthermore, defects that formed during the synthesis of conventional covalently bound molecular macromolecules are difficult or impossible to be removed. However, self-assembled materials held together by non-covalent linkages are potentially self-healing due to their dynamic nature which will offer great potential for the development of future nanotechnology. Last but not least, the use of non-covalent interactions allows the assembly process to be thermodynamically controlled, most often resulting in the formation of single, discrete supramolecules. This literally builds complex molecules from the bottom-up.[5]

In the molecular design of 3D conjugated organic molecules, a species having functionality at the apices (vertices) of a tetrahedron is an attractive building block and thus persistent tetrahedral symmetric of tetraarylmethanes have received considerable interests.[6-10] Galoppini et al.[6] showed that tetraphenylmethane is a useful building block for construction of diamondoid networks with a strong, stiff and 3D structure of covalent bonds that might be translated to a macromolecular system with unusual properties. Langhals et al.[9] have used tetraphenylmethane as the central unit for assembly of highly fluorescent and photostable chromophores using perylene-3,4:9,10-tetracarboxylic bisimides (PTB). They found that the tetrahedral arrangement of chromophores results in an amplification of the absorption, i.e., molar absorptivity of tetrahedral-arranged chromophores (380,000 L mol^{-1} cm^{-1}) is

significantly more than four times the value (88,000 L mol^{-1} cm^{-1}) of the single PTB. This is due to an exciton interaction effect[11] and actually, one is not limited to a certain orientation of the chromophores relative to the light to be absorbed.

Among the composites of inorganic and organic materials, development of new molecular architectures based on polymer blocks containing oligopyridyl ligands and especially their transition metal complexes is of interest. Their reversibility and the behaviour of multinuclear supramolecular interactions cause these metal complexes capable to facilitate the charge carrier generation in polymers.[12] The two most significant factors that determine the obtained supramolecular structure significantly are the shape and size of the individual component-building units. The shape of donor/acceptor's unit is dominated by the turning angle, defined as the angle formed between the open valencies of a ditopic or tritopic donor or acceptor. Furthermore, the size of individual building unit determines the overall size of the self-assembled supramolecular species.[4] The availability of lone pairs of electron on the nitrogen of each pyridine ring enhances the "directional-bonding" between pyridyl molecules and transition metals in the self-assembly by metal-ligand coordination. By carefully designing the component, it allows for the building of supramolecules, e.g. 3D metallacages,[13,14] which can be deposited on highly oriented pyrolytic graphite (HOPG) or Au (111) substrates and studied by scanning tunneling microscopy (STM).[5] In addition, these pyridyl metal complexes are generally thermally and chemically stable.

A lot of interest has focused in recent years on N-heteroaromatic ligands, especially 2,2':6'2''-terpyridines (in short, tpys) and their structural analogs. These are expressed by the large number of scientific publications and patents regarding the synthesis, properties and

applications of tpy-containing systems (June 2010: almost 5500 hits in SciFinder[TM]).[15] Tpys have been used as functional templates in the fields of supramolecular and coordination chemistry (e.g. metal–ligand coordination) as well as materials science.[16-19] Due to their distinct photophysical, electrochemical and catalytic properties, tpys and their complexes have also been studied for a wide range of potential applications covering light-to-electricity conversion,[3,20-24] (electro)luminescent systems (e.g. organic light-emitting diodes) or non-linear optical devices.[25,26] Moreover, ditopic and dendritic tpy ligands may form polymetallic species which can then be used as luminescent or electrochemical sensors.[27-32] Tpys have rich coordination chemistry and generally display remarkably high binding affinity toward most transition metal ions by $d\pi \rightarrow p\pi*$ bonding.[2] In concert with the resulting redox and photophysical properties, this give rise to diverse stable metallosupramolecular architectures and a multitude of potential applications.[17,33] With such chelating properties, tpys are very attractive building blocks for the construction of supramolecular assemblies.[33]

The tpys are molecules containing three near-coplanar nitrogen donor atoms (Fig. 2.1) and can thus act as a tridentate ligand (three interaction sites) to form stable coordination and hydrogen-bonded complexes with a wide range of transition metal ions. Among all tpys compounds, 4'-substituted-tpys are the focus of this project because these derivatives of tpys can be extended or linked together by spacers. A metal-bonded tpy ligand with spacers at C (4') provides a linear communication. Therefore, the electronic communication can occur along the coordination axis, through the path: $M^1 \rightarrow$ tpys$\rightarrow$ spacer$\rightarrow$ tpys$\rightarrow M^2$ (Fig. 2.2). In addition, the insertion of a single substituent in the 4'-position of tpys ligand results in no change to the centrosymmetric nature and no enantiomers are formed (this is by contrast with 2, 2'-bipyridine derivatives). Also, properties of tpy-derivatives bearing π-conjugated

substituents at the 4'-position can be tuned by varying substituents at the 4'-position of the tpys. Besides, the Δ/Δ-chirality problems seen for 2,2'-bipyridines complexed with metal ions do not exist for tpys complexed with metal ions.

The majority of conjugated tpy-containing systems used today are based on the so-called Kröhnke-motif featuring a functionalized phenyl-ring in the 4'-position of the tpy unit, for which the best synthetic approach was reported by Kröhnke in 1976.[34] In general, derivatives of 2-acetylpyridine and a (hetero)aromatic aldehyde are used in a so-called Kröhnke-type condensation reaction yielding 4'-substituted-2,2':6',2''-terpyridines (4'-substituted-tpys). In Kröhnke-type tpys, the phenyl on the 4'-position and the central pyridine rings are twisted on average about 20°–30° due to the unfavorable interaction between the adjacent protons (Fig. 2.3). The nonplanarity between the terpyridyl and the phenyl ring leads to a mismatch between the ground and excited state geometries, thus minimizing the effect of increased delocalization.[35] Relevant research efforts based on 4'-substituted-tpys, especially with metal ion complexes to form supramolecular metallopolymers or supramolecular networks will be explored and discussed further in the review sections in Chapter 4 and Chapter 5.
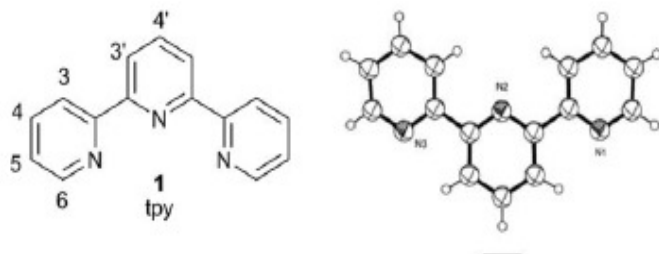
Figure 2.1: Structure of 2,2':6',2''-tpy, together with the solid state crystal structure of tpys showing the trans-confirmation adopted in the solid state by most tpys derivatives. The numbering scheme for substituents in tpys derivatives is also shown.[17]
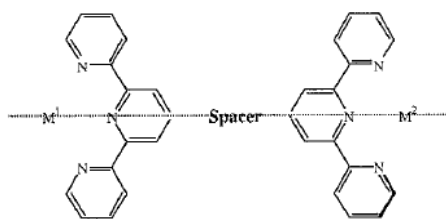
Figure 2.2: Coordination axes across two metal binding 4'-substituted-tpys.[36]
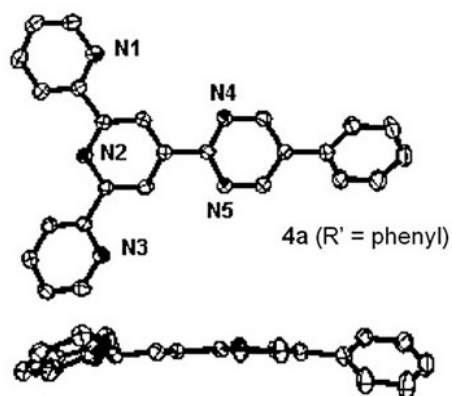
Figure 2.3: ORTEP plot showing two orthogonal views of the crystal structure regarding 20–30° twisting between the phenyl and the central pyridine ring in 4'-substituted-tpys.[35]

Therefore, we report the synthesis (Section 2.2) and characterization (Section 2.3) of two new and novel 3D cores for supramolecules (**1** and **2**) from their subunits. The structures begin from the central tetraphenylmethane, which are then extended through the p-type or n-type conjugated linker units and the four arms end with tpy units. 2,5-bisdodecyloxy-p-phenylene is used as the p-type linker in **1** shown in Fig. 2.4 due to it is being linear and electron rich and thus it is a good electron donor. In the other core **2** shown in Fig. 2.4, 2,1,3-benzothiadiazole (benzo[c][1,2,5]thiadiazole) is used as the n-type linker as it is known to be a good electron acceptor. The purpose of the long alkoxy chain attached on the p-type and n-

type linkers in **1** and **2** respectively is to enhance the solubility of these two cores for 3D

supramolecules.
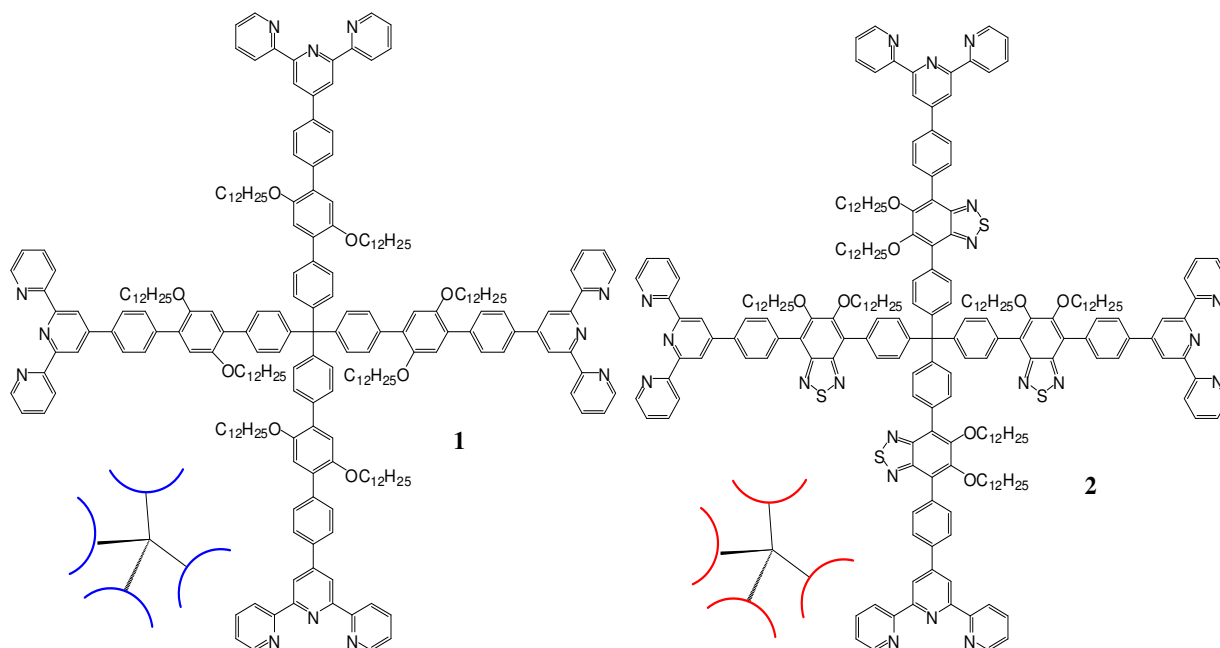
Figure 2.4: Chemical structures of new 3D supramolecules (p-type **1** and n-type **2**).

2.2   Synthesis of new p-type and n-type cores for 3D supramolecules (1 & 2)

Details of synthetic procedures for synthesis of **1** and **2** (including the synthesis of their

intermediates) according to Scheme 2.1–2.3 and the characterization data (including [1]H

NMR, ^{13}C NMR, MALDI-TOF mass spectra, Elemental Analysis and HRMS) are described

in detail in the Experimental Section.

2.2.1 Synthesis of core, terpyridyl and linker monomers

The synthetic steps involved in preparation of core monomer **4** and terpyridyl monomer **6** are outlined in Scheme 2.1. Whereas the synthetic steps involved in preparation of both p-type monomer **7** and n-type linker monomer **12** are outlined in Scheme 2.2.

The para positions of tetraphenylmethane were iodinated using the reagents [bis(trifluoroacetoxy)iodo]benzene and iodine to form the tetrakis(4-iodophenyl)methane **3** as a white solid. The reaction is an electrophilic aromatic substitution by trifluoroacetylhypoiodide, resulting from the interaction of iodine and [bis(trifluoroacetoxy)iodo]benzene.[37] Carbon tetrachloride (CCl_4) is the literature choice of solvent for such halogenations reactions. However, the reaction was conducted in chloroform in this project with lower yield than in the literature as CCl_4 is not available in Singapore. Tetrakis[4-(4',4',5',5'-tetramethyl-1',3',2'-dioxaborolane-phenyl)]methane **4** was formed as a white solid through the palladium-catalyzed Miyaura cross coupling[38] of **3** with bis(pinacolato)diboron. 4'-(4-Bromophenyl)-2,2':6'2''-terpyridine **5** was formed through the reaction of 4-bromobenzaldehyde and 2-acetylpyridine. The enolate of 2-acetylpyridine was generated by KOH under mild conditions, followed by an aldol condensation and a Michael addition. The soluble diketone intermediate was then allowed to form the central pyridine ring with an aqueous ammonia nitrogen source.[39] Using the same method as for **4**, **5** was converted to 4'-(4-pinacolatoboronphenyl)-2,2':6',2''-terpyridine **6**.
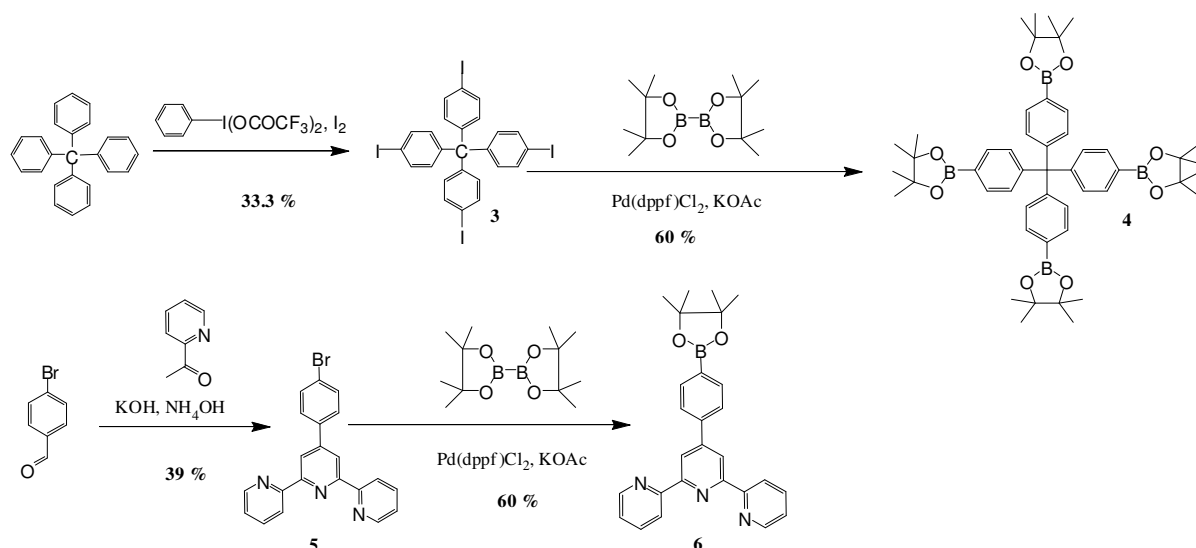
Scheme 2.1: Synthesis of core monomer **4** and terpyridyl monomer **6**.

2,5-Dibromobenzene-1,4-diol (2,5-dibromohydroquinone) was dialkylated to form 1,4-dibromo-2,5-bis(dodecyloxy)benzene **7**, the p-type linker monomer. This reaction is based on the nucleophilic substitution of bromide by phenoxide anions generated in base.[40] The n-type linker monomer **12** was synthesized through a series of reactions. 1,2-Bis(dodecyloxy)benzene **8** was prepared by alkylation of catechol with 1-bromododecane and nitrated with HNO_3 to give the dinitrocompound 1,2-bis(dodecyloxy)-4,5-dinitrobenzene **9** as a yellow solid. Reduction of **9** with tin(II) bromide in HBr gave the diamine as its hydrogen bromide salt **10** which had to be used immediately as it was unstable in air. Treatment of **10** with thionyl bromide with the aid of pyridine produced 5,6-bis(dodecyloxy)benzo[c][1,2,5]thiadiazole **11**, which was immediately brominated with bromine in acid environment to give the 4,7-dibromo-5,6-bis(dodecyloxy)benzo[c][1,2,5]thiadiazole **12** as a white solid. This procedure was adopted as it was discovered that reduction of **9** with tin(II) chloride followed by ring-closure with thionyl chloride as per literature precedents[41] resulted in partial ring chlorination as detected

by NMR and mass spectrometry. Such ring halogenations have not previously been reported from synthesis of benzodiathiazoles using these conditions, but our group have recently obtained halogenated products from the reaction of tetraaminobenzenes with thionyl halides and pyridine under the same conditions.[42]
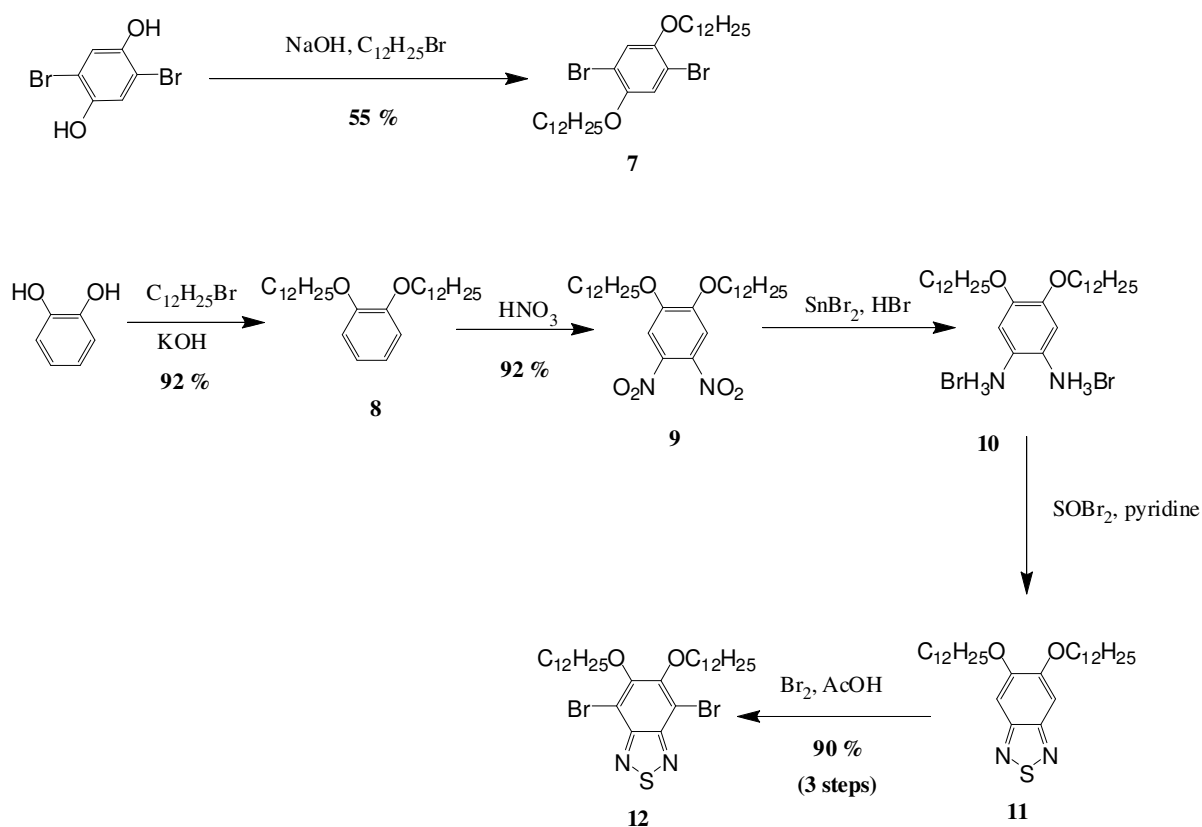
Scheme 2.2: Synthesis of p-type monomer **7** and n-type monomer **12**.

2.2.2 Synthesis of new 3D p-type and n-type cores

The synthetic steps involved in the preparation of the new 3D p-type and n-type cores for supramolecules are outlined in Scheme 2.3, with the presence of monomers **4**, **6**, **7** and **12**. With the aid of Pd (0), 4'-(4-pinacolatoboronphenyl)-2,2':6',2''-terpyridine **6** was Suzuki-coupled with **7** and **12** to produce asymmetric linear monomers **13** and **14** as a white solid

and a light purple solid, respectively. Tetrakis[4-(4',4',5',5'-tetramethyl-1',3',2'-dioxaborolane-phenyl)]methane **4** was then Suzuki-coupled with **13** and **14** with the aid of Pd (0) to produce p-type 3D supramoleculare core **1** as a white glassy solid and n-type 3D supramolecular core **2** as a light purple glassy solid. The structure of **1** and **2** were confirmed by ^{1}H NMR and ^{13}C NMR and their molecular weight were confirmed by MALDI MS. Elemental Analysis of **1** gave too high value for H and might be due to moisture which is unsuccessfully to be removed completely. Elemental Analysis of **2** gave too low value for S (as well as for most of the S-containing materials in this project) and this might be due to incomplete combustion. HRMS data of **1** and **2** are not obtainable as their M_ws are too high for the limit of the machine. **1** and **2** were then used for the metal-coordinated self-assembly to form 3D self-assembled networks. The details (synthesis and characterization) of which will be discussed in Chapter 5.
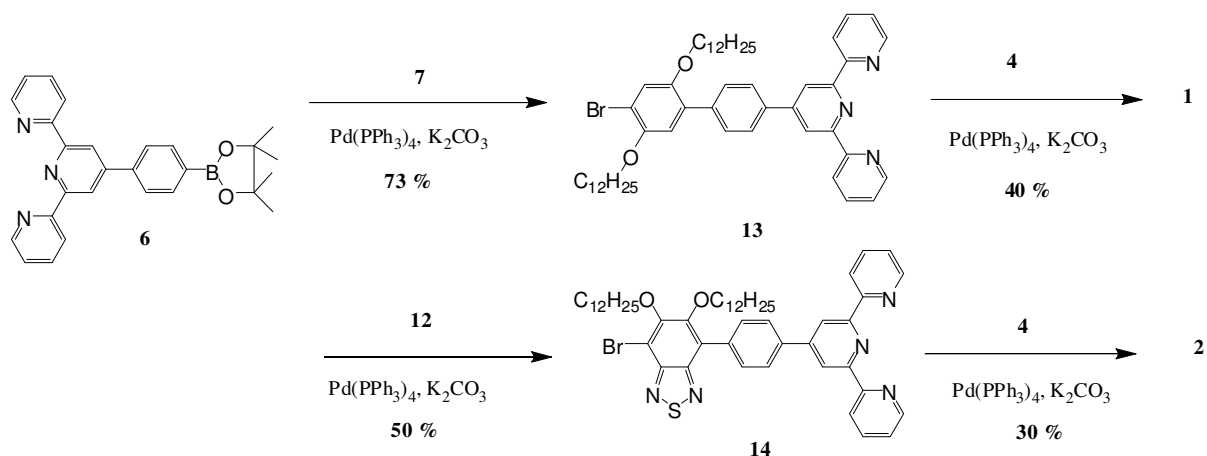
Scheme 2.3: Synthesis of cores for 3D supramolecules (p-type **1** and n-type **2**).

2.3   Characterization of new p-type and n-type 3D cores (1 & 2)

2.3.1   Optical properties of 1 and 2

The spectroscopic data of 3D conjugated cores **1** and **2** in chloroform solution (10^{-5} M) and thin films are summarized in Table 2.1. The absorption spectra and photoluminescence spectra of **1** and **2** in chloroform solution (10^{-5} M) are shown in Fig. 2.5a and Fig. 2.5b, respectively. The absorption spectra and photoluminescence spectra of **1** and **2** in thin films are shown in Fig. 2.6a and Fig. 2.6b, respectively.

Table 2.1: Spectroscopic data of 3D conjugated cores **1** and **2**

		Molecules	
		1	**2**
Chloroform solution	$\lambda_{abs,max}$ (nm)[a]	332	377
	ε_{max} (M^{-1} cm^{-1})[a]	88663	49886
	λ_{onset} (nm)[a]	385	425
	$\lambda_{em,max}$ (nm)[a]	434	477
	Stokes shift (nm)	102	100
	$E_{g,op}$ (eV)[b]	3.22	2.92
Thin Film[c]	$\lambda_{abs,max}$ (nm)	339	379
	λ_{onset} (nm)	395	430
	$\lambda_{em,max}$ (nm)	429	473
	Stokes shift (nm)	90	94
	$E_{g,op}$ (eV)[b]	3.14	2.88

[a]Concentration of 1 x 10^{-5} M in $CHCl_3$; [b]$E_{g,op}$ = (1240/λ_{onset}) (eV); [c]Drop casting from $CHCl_3$ solution.
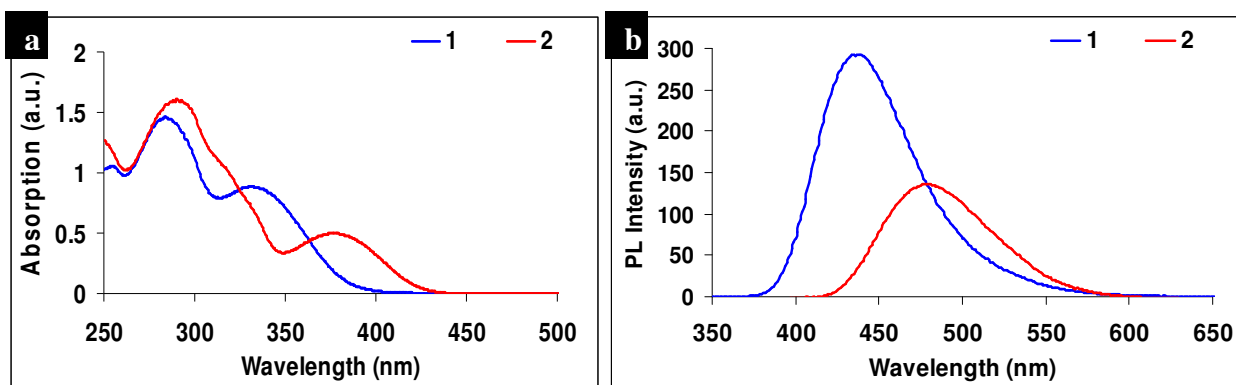
Figure 2.5: (a) UV-vis absorption and (b) photoluminescence spectra of 3D conjugated cores **1** and **2** in CHCl$_3$ solution (10^{-5} M).
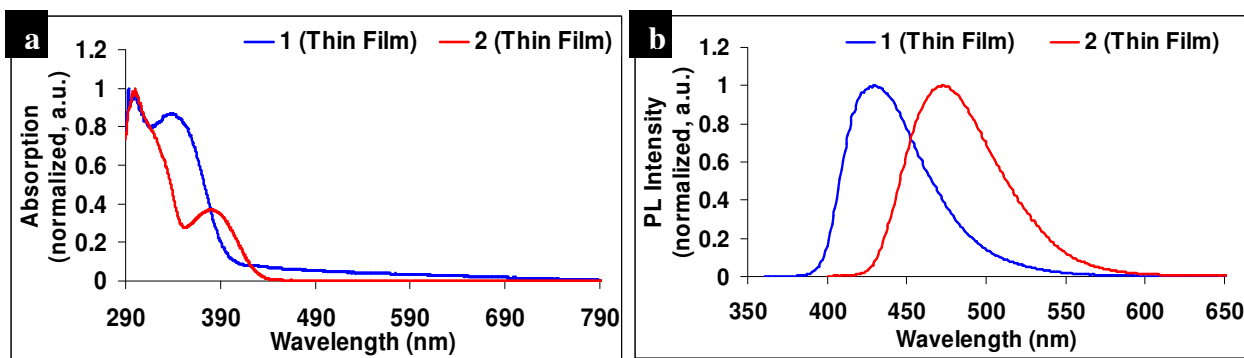
Figure 2.6: (a) UV-vis absorption and (b) photoluminescence spectra of 3D conjugated cores **1** and **2** in thin films.

The absorption maximum ($\lambda_{abs,max}$) (solution) of **1** is at 344 nm, it is red-shifted 33 nm to 377 nm for **2**. The optical bandgap ($E_{g,op}$), is defined by the onset of absorption (λ_{onset}). $E_{g,op}$s (solution) of **1** and **2** are 3.22 eV and 2.92 eV, respectively calculated from the λ_{onset} of 385 nm and 425 nm, respectively. The emission maxima ($\lambda_{em,max}$) (solution) of **1** and **2** are at 434 nm and 477 nm, respectively. Comparing the absorption spectra of solution and solid state, $\lambda_{abs,max}$ of **1** and **2** in the solid state are red-shifted 2–7 nm compared to that in solution state, indicating slight interchain association or aggregation in the solid state. Smaller values of $E_{g,op}$s in thin films of **1** (3.14 eV) and **2** (2.88 eV) are obtained compared to that in solution.

However, $\lambda_{em,max}$ of **1** and **2** in solid state are blue-shifted 4–5 nm compared to that in solution state and this might be due to the twisting in solid state which reduces conjugation.

2.3.2 Thermal behaviour of 1 and 2

Table 2.2: 3% weight loss temperature (T_{3d}) and glass transition temperature (T_g) of 3D conjugated cores **1** and **2**.

Molecules	T_{3d} (°C)[a]	T_g (°C)[b]
1	242	148
2	302	125

[a]T_{3d} = 3% weight loss temperature; [b]T_g = glass transition temperature.

The thermogravimetric analysis (TGA) plots of 3D conjugated cores **1** and **2** are shown in Fig. A32 in Experimental Section. Differential scanning calorimetry (DSC) plots of **1** and **2** are shown in Fig. A33 in Experimental Section. T_{3d} and T_g of **1** and **2** are listed in Table 2.2. Although the T_{3d} of **2** (302 °C) is higher than that of **1** (242 °C), **2** is less stable compared to **1** as it retains about 20% weight when the temperature reach 800 °C compared to **1** which retains about 40% weight (From Fig. A32). **1** and **2** have T_g of 148 °C and 125 °C and both of them are believed to be amorphous materials as no significant exothermic peaks of crystallization temperature (T_c) were observed during the heating cycles in their DSC plots.

2.3.3   Electrochemical properties of 1 and 2

Table 2.3: Redox properties of 3D conjugated cores **1** and **2**.

Molecules	CV					
	$E_{onset,ox}$ (V)	$E_{onset,red}$ (V)	E_{HOMO} (eV)[a]	E_{LUMO} (eV)[b]	$E_{g,ele}$ (eV)[c]	$E_{g,opt}$ (eV)[d]
1	1.15	-0.75	-5.55	-3.65	1.9	3.22
2	0.91	-0.76	-5.31	-3.64	1.67	2.92

[a]E_{HOMO} = -($E_{onset,ox}$ + 4.4) eV; [b]E_{LUMO} = -($E_{onset,red}$ + 4.4) eV; [c]$E_{g,ele}$ = E_{LUMO} - E_{HOMO}; [d]$E_{g,opt}$ [cf. Table 2.1].

The electrochemical behaviour of 3D conjugated cores **1** and **2** was investigated by Cyclic Voltammetry. The plots are shown in Fig. A34 in Experimental Section and the data are listed in Table 2.3. The oxidation onset potentials ($E_{onset,ox}$) of **1** and **2** are 1.15 V and 0.91 V versus Ag/Ag$^+$, respectively. The calculated HOMO values (eV) of **1** and **2** are thus -5.55 and -5.31, respectively. The reduction onset potentials ($E_{onset,red}$) of **1** and **2** are -0.75 V and -0.76 V versus Ag/Ag$^+$, respectively, corresponding to calculated LUMO values (eV) for **1** and **2** of -3.65 and -3.64, respectively. The electrochemical bandgaps ($E_{g,ele}$) of **1** and **2** are thus 1.9 and 1.67 eV, respectively, which are not very close to their $E_{g,opt}$ (3.22 eV and 2.92 eV, respectively). This might due to the inaccuracy when extrapolating data from the CV and UV-vis absorption plots or to other unknown reasons. The difference between optical and electrochemical bandgap energies can be explained in part by the exciton binding energy of organic molecules which is believed to be in the range of ~0.4 eV-1.0 eV.[43,44] The exciton binding is the energy of exciton (electron and hole pair) dissociation, provided by the energy offset between the LUMOs of the donor and acceptor. The larger the exciton binding energy, the harder the electron and hole pairs are to separate.

2.4 Conclusion

In conclusion, new and novel cores for 3D supramolecules with linkers of p-type (**1**) and n-type (**2**) were successfully synthesized. Due to the presence of long solubilizing groups, these tetrahedral symmetric molecules are soluble in common solvents and display blue emission in solution or solid state. They are amorphous and possess good thermal stability (stable above 200 °C). Thus, they can be used to undergo the metal-coordinated self-assembly process in order to form complicated but interesting 3D supramolecular networks which will be further discussed in Chapter 5.

Chapter 3   Synthesis and characterization of new n-type moderate bandgap linear polymers for solar cells

3.1   Review

The n-type monomer **12** not only can be used in the formation of large 3D supramolecules as shown in Chapter 2, it can also be used as an acceptor unit in low bandgap conjugated polymers as will be discussed in this chapter. This was done to show the good electron acceptor (n-type) properties of this unit for comparison with the metal-linked species.

In recent years, considerable efforts have been devoted to the synthesis of conjugated polymers for applications in organic solar cells,[45] organic light emitting diodes (OLEDs),[46] and organic field-effect transistors (OFETs)[47] due to their potentially low production costs as they can be processed from solution, and the possibility of making light weight, flexible large-area devices. Organic solar cells, although still inferior to silicon-based solar cells in terms of power conversion efficiency (PCE) and stability, are still an attractive alternative due to the advantages of low cost and ability to make large-area devices. Among conjugated polymers for use in solar cells, low bandgap ($E_g < 2$ eV) polymers are of particular interest as electron donor materials for solar cell applications as they allow better harvesting of solar energy since they absorb across a wider section of the solar spectrum . Theoretical models suggest that organic cells with the efficiencies above 10% are attainable using polymers with bandgap between 1.3 and 1.8 eV as donors when combined with electron-accepting molecules such as fullerenes in heterojunction (BHJ) devices.[48,49] While such high

efficiencies have yet to be obtained, already very promising PCEs of 5–8% have been achieved from BHJ devices using electron donating conjugated polymers with bandgaps below 2 eV.[41,50-58]

The fullerene derivative, [6,6]-phenyl-C_{61} butyric acid methyl ester (PCBM, **15**) is the most widely used electron acceptor material in polymer solar cells. The absorption of polymer:PCBM solar cells has usually been attributed mainly to the electron donor materials as PCBM absorbs weakly in the visible range,[51] though it has recently been shown that the PCBM does contribute significantly to the overall photocurrent.[59] Hence, the design and synthesis of low bandgap polymers are important in order to improve light harvesting, and so increase the PCE. However, too low a bandgap may result in harvesting more photons with lower energy, accompanied by excessive energy loss from absorbed higher energy photons, producing poorer efficiencies.[60,61]

Low bandgap polymers can be prepared by alternating copolymerization of electron-donating donor (D) and electron-withdrawing acceptor (A) units. The interaction between these units in the resulting donor-acceptor (D–A) copolymers raises the highest occupied molecular orbital (HOMO) energy level and lowers the lowest unoccupied molecular orbital (LUMO) energy level so reducing the bandgap of the polymers.[62,63] The bandgap of a polymer may also be further modified by the attachment of electron-donating or accepting groups as substituents on the chain. Benzo[c][1,2,5]thiadiazole (BT, **16**) is a commonly used acceptor unit in low bandgap conjugated polymers, but the lack of solubilizing units, reduces the solubility and potential molar masses of the polymers containing it. This can be overcome by adding alkoxy groups at the 5- and 6-positions as in **17**.[41] The alkoxy groups will increase the

electron density so **17** might be a poorer acceptor so to confirm its good electron accepting properties we made copolymers with various good donors.

15

16 X = H
17 X = alkoxy

18

19 R = alkyl
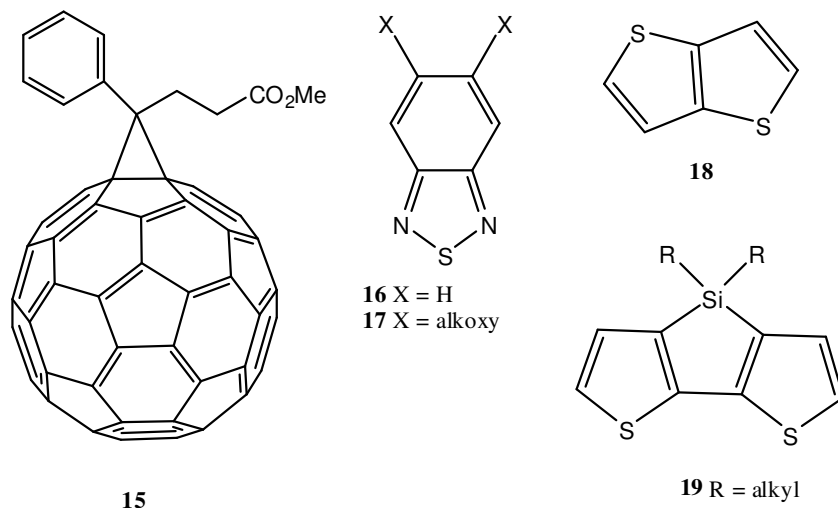
Figure 3.1: PCBM (**15**) and units (**16–19**) to make polymers **P1–P4**.

As the donor moieties in our intended D–A copolymers we choose to use thiophenes and fused thiophene units. Polymers containing fused thiophenes have been extensively investigated as materials for OFETs due to their high charge carrier mobilities assisted by their close solid-state packing.[47] In particular polymers containing thieno [3,2-b]thiophene (TT, **18**) have been shown to have charge carrier mobilities as high as 0.2–0.6 cm^2 V^{-1} s^{-1}.[64] Such high charge carrier mobilities are advantageous in materials for solar cells also as they will assist the collection of charges generated within the cell. Owing to the larger resonance stabilization energy of the TT compared to thiophene, delocalization of electrons from TT into the polymer backbone may be reduced so lowering the polymer's HOMO which enhances stability and also raises the potential V_{oc}. Siloles have been investigated as charge transporting materials due to their good charge carrier mobilities and relatively low

bandgaps.[65] The silicon-fused bithiophene (dithieno[3,2-b:2',3'-d]silole, DTS, **19**) was chosen as a donor unit since it has a notably low bandgap due to the newly formed extended planar π-conjugated tricylic system and σ*–π* conjugation between the σ*-orbit of silicon and π*-orbit of the bithiophene unit.[66-68] DTS-containing polymers have been used in organic solar cells with high efficiencies (around 5%).[51] The silole units in these polymers significantly enhances their hole mobilities, and as a result, the fill factor (FF) and short circuit current (J_{sc}) of these polymer-based device are also enhanced. It is also reported that silole units impart high photochemical stability to conjugated polymers.[69]

In this chapter is shown the synthesis of new copolymers **P1–4** based on alkoxysubstituted BT with different thiophene-based monomers using Stille cross-coupling reaction, the characterization of their optoelectronic properties and some preliminary results from solar cells using them as electron donors.

3.2   Synthesis of monomers and polymers P1–4

Synthetic procedures for synthesis of monomers and polymers according to Scheme 3.1–3.2 and the characterization data (including ^{1}H NMR, ^{13}C NMR, MALDI-TOF mass spectra, Elemental Analysis and HRMS) are described in details in the Experimental Section.
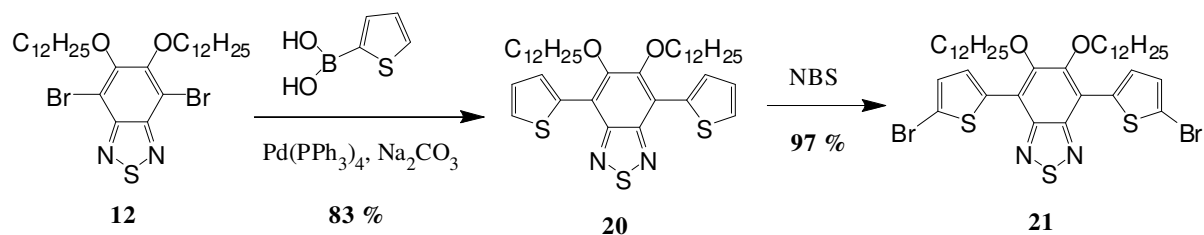
Scheme 3.1: Synthesis of monomers **21** from **12**.

The synthetic steps involved in preparation of monomer **12** are outlined in Scheme 2.2, whereas the synthetic steps involved in preparation of monomer **21** are outlined in Scheme 3.1. Suzuki coupling of 4,7-dibromo-5,6-bis(dodecyloxy)benzo[c][1,2,5]thiadiazole **12** with an excess of thiophene-2-boronic acid produced the dithienyl adduct 5,6-bis(dodecyloxy)-4,7-di(thiophen-2-yl)benzo[c][1,2,5]thiadiazole **20** which was intensely fluorescent in solution. Bromination of **20** with N-bromosuccinimide (NBS) afforded the monomer 4,7-bis(5-bromothiophen-2-yl)-5,6-bis(dodecyloxy)benzo[c][1,2,5]thiadiazole **21** as a reddish-orange solid.
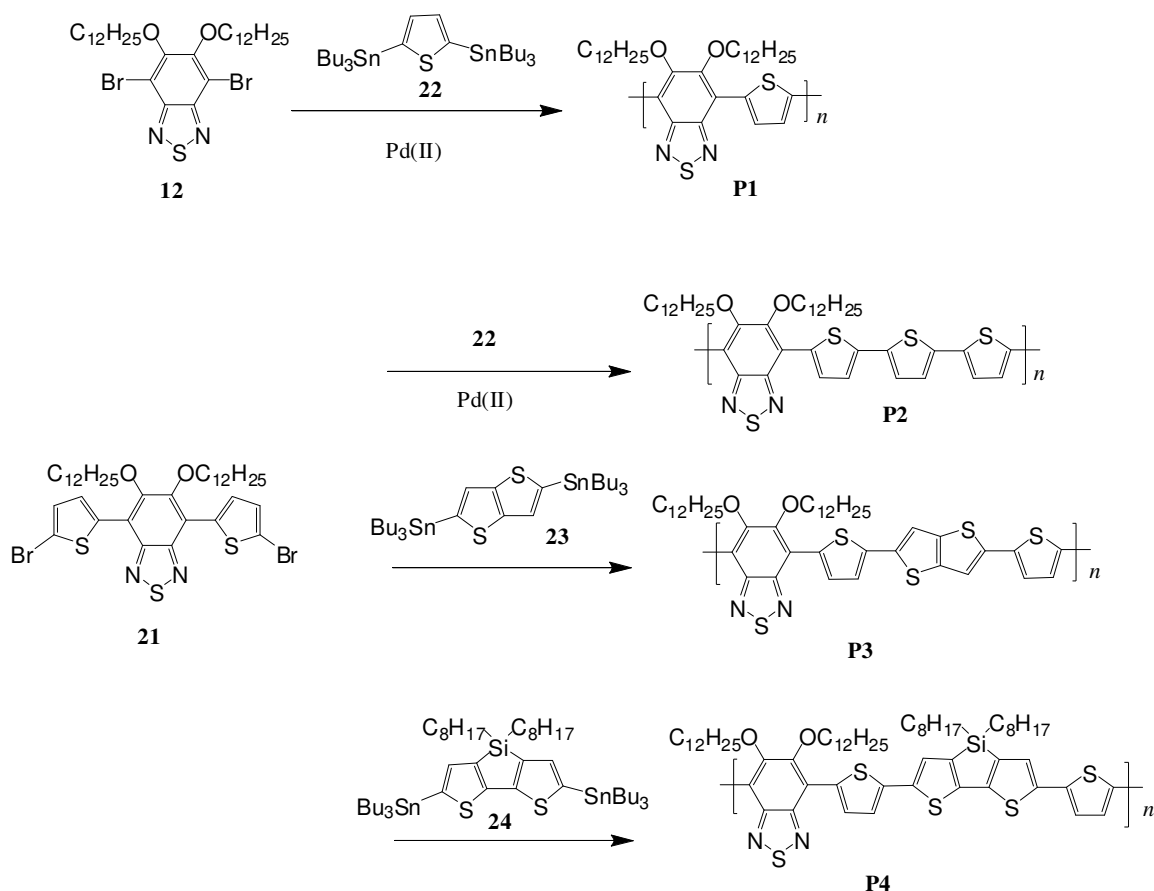
Scheme 3.2: Synthesis of polymer **P1–P4**.

The synthetic steps involved in preparation of polymers **P1–4** are outlined in Scheme 3.2.

Using Pd(II) as catalyst, **12** was coupled with 2,5-bis(tributylstannyl)thiophene **22** to form **P1**.

Coupling of **21** with **22**, 2,5-bis(tributylstannyl)thieno[3,2-b]thiophene **23** and 4,4'-dioctyl-

5,5'-bis(tributyltin)-dithieno[3,2-b:2',3'-d]silole **24** formed respectively **P2**, **P3** and **P4**. These

distannylarenes were all prepared from precursors which were purchased from commercial

sources or prepared by literature methods.[70]

3.3   Charaterization of polymers P1–4

3.3.1   Optical properties of P1–4

The spectroscopic data of polymers **P1–4** in chloroform solution and thin films of polymers

P1–4 are summarized in Table 3.1. The absorption spectra of polymers **P1–4** in chloroform

solution and that of thin films of polymers **P1–4** are shown in Fig. 3.2a and Fig. 3.2b,

respectively. The photoluminescence spectra of polymers **P1–4** in chloroform solution and

that of thin films of polymers **P1–4** are shown in Fig. 3.3a and Fig. 3.3b, respectively.

Table 3.1: Spectroscopic data of polymers **P1–4**.

Poly mer	Chloroform solution					Thin Film				
	$\lambda_{abs (max)}$ (nm)	λ_{onset} (nm)	$\lambda_{em (max)}$ (nm)	Stokes shift (nm)	$E_{g,op}$ (eV)[a]	$\lambda_{abs (max)}$ (nm)	λ_{onset} (nm)	$\lambda_{em (max)}$ (nm)	Stokes shift (nm)	$E_{g,op}$ (eV)[a]
P1	537	630	621	84	1.97	595	710	682	87	1.75
P2	543	638	623	80	1.94	599	712	688	89	1.74
P3	525	625	616	91	1.98	585	708	672	87	1.75
P4	520	627	606	86	1.98	604	715	692	88	1.73

[a] $E_{g,op} = (1240/\lambda_{onset})$ (eV)
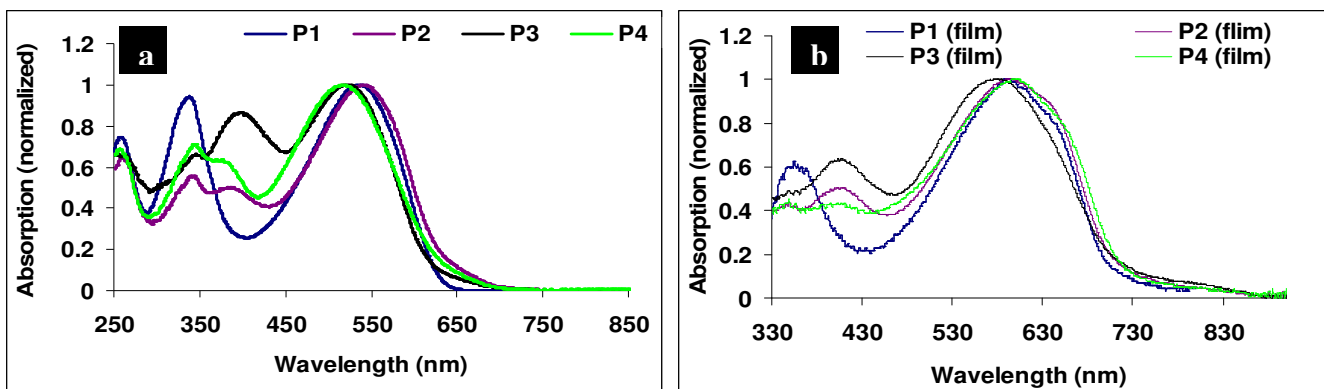
Figure 3.2: UV-vis absorption spectra of (a) polymers **P1–4** in chloroform solution and (b) that of polymers **P1–4** in thin film.
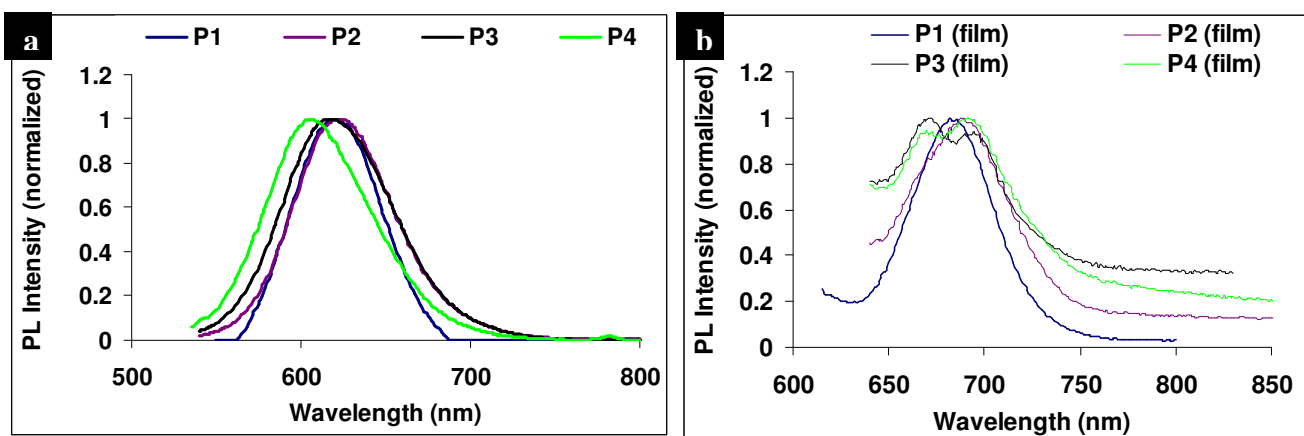
Figure 3.3: Photoluminescence spectra of (a) polymers **P1–4** in chloroform solution and (b) that of polymers **P1–4** in thin films.

The absorption maxima (λ_{max}) of **P1**–**P4** are around 520–543 nm, with the most **P2** red-shifted at 543 nm. Polymers **P2** and **P4** show additional fine vibronic structure around 365 nm. The optical bandgap ($E_{g,op}$), is defined by the onset of absorption (λ_{onset}) and of **P1–4**, **P2** exhibits the lowest $E_{g,op}$ (1.94 eV) with an absorption onset at *ca.* 638 nm. The solid state absorption spectra of polymers **P1–4** in are red-shifted *ca.* 58–84 nm compared to the solution spectra indicating significant interchain association or aggregation in the solid state. The absorption peak at the lower wavelength for **P1–P4** is attributed to the

dialkoxybenzodithiazole units. The optical bandgaps of polymers **P1–4** in thin film are very similar, ranging from 1.73–1.75 eV. The emission maxima ($\lambda_{em,max}$) of polymers **P1–4** in chloroform solution (Fig. 3.3a) range from 606–623 nm, which are red-shifted to 672–692 nm in the solid state (Fig. 3.3b). The Stokes shifts for polymers **P1–4** are all in the range of 80–91 nm (Table 3.1), in both chloroform solution and thin film. The optical properties of **P1–4**, are clearly not significantly influenced by replacing one thiophene in the polymer backbone by a fused thiophene and we therefore deduce that the electron transfer between the BT and the donor units in **P1–4** is much the same.

3.3.2   Molecular weight and thermal behaviour of polymers P1–4

Table 3.2: GPC data of polymers **P1–4**, 3% weight loss temperature (T_{3d}) and glass transition temperature (T_g) of polymers **P1–4**.

Polymer	M_n^a (g/mol)	M_w^b (g/mol)	PDI^c	T_{3d}^d (°C)	T_g (°C)
P1	3606	4888	1.36	216	125
P2	2494	3476	1.39	188	62
P3	1530	1575	1.03	181	119
P4	4400	19899	4.52	237	129

^aM_n = Number-average molecular weight; ^bM_w = Weight-average molecular weight; ^{c}PDI = polydispersity; $^dT_{3d}$ = 3% weight loss temperature; ^eT_g = glass transition temperature.

The TGA plots of **P1**–**4** are shown in Fig. A45 in Experimental Section. DSC plots of **P1–4** are shown in Fig. A46 in Experimental Section. Gel permeation chromatography (GPC) data (e.g. M_n, M_w & PDI) of **P1–4**; T_{3d} and T_g of **P1–4** are listed in Table 3.2. The 3% weight loss temperature *c.a.* 180~240 °C of **P1–4** suggested that the alkoxy chains in the polymer backbone were started to break off. The weight loss exceeds 40% after heating above 400 °C

suggestive of complete dealkylation. Among the polymers, **P2** is the least stable as it suffers 50% weight loss by 300 °C, compared with 390 °C for **P1**, 455 °C for **P3,** and 500 °C for **P4**. This indicated that fused thiophene (thieno[3,2-b]thiophene) in **P3** and the Si-bridged fused thiophene in **P4** are more thermally stable than the thiophenes in **P1** and **P2**. From the DSC analysis, **P1**, **P3** and **P4** have a glass transition temperature T_g around 120°C~130°C whereas the T_g of **P2** is at 62°C. The polymers are believed to be amorphous materials as no significant exothermic peaks of crystallization temperature (T_c) were found during heating cycles in the DSC plots. M_ns of **P1–4** are all less than 5×10^3 g/mol. The low molecular masses for **P2** and **P3** presumably reflect their lower solubility due to their containing fewer solubilising groups. Further optimization of the polymerization conditions, e.g. by using different catalysts or by use of microwave heating, should enable improvement in the molecular masses for **P1–4. P1–3** display very narrow polydispersities whereas **P4** has a high broad polydispersity of 4.52 although the M_w is as high as 20 kg/mol.

3.3.3   Electrochemical properties of polymers P1–4

Table 3.3: Redox properties of polymers **P1–4**.

Polymers	$E_{onset,ox}$ (V)	$E_{onset,red}$ (V)	E_{HOMO} (eV)[a]	E_{LUMO} (eV)[b]	$E_{g,ele}$ (eV)[c]	$E_{g,opt}$ (eV)[d]
P1	1.27	-0.75	-5.67	-3.65	2.02	1.97
P2	0.85	-1.56	-5.25	-2.84	2.41	1.94
P3	0.85	-1.59	-5.25	-2.81	2.44	1.98
P4	0.87	-1.54	-5.27	-2.86	2.41	1.98

[a]$E_{HOMO} = -(E_{onset,ox} + 4.4)$ eV; [b]$E_{LUMO} = -(E_{onset,red} + 4.4)$ eV; [c]$E_{g,ele} = E_{LUMO} - E_{HOMO}$; [d]$E_{g,opt}$ [cf. Table 3.1].

Electrochemical behaviour of **P1–4** was investigated by Cyclic Voltammetry. The plots are shown in Fig. A47 in Experimental Section and the data are listed in Table 3.3. The oxidation

onset potentials ($E_{onset,ox}$) of **P1–4** are 1.27, 0.85, 0.85 and 0.87 V versus Ag/Ag$^+$, respectively. The calculated HOMO values (eV) of **P1–4** are thus -5.67, -5.25, -5.25 and -5.27, respectively. The reduction onset potentials ($E_{onset,red}$) of **P1–4** are -0.75, -1.56, -1.59 and -1.54 V versus Ag/Ag$^+$, respectively, corresponding to calculated LUMO values (eV) for **P1–4** of -3.65, -2.84, -2.81 and -2.86, respectively. The electrochemical bandgaps ($E_{g,ele}$) of **P1–4** are thus 2.02, 2.41, 2.44 and 2.41 eV, respectively. The LUMO energies obtained electrochemically for **P2–P4** appear unusually high compared to that for **P1** – if we use the electrochemically derived HOMO values and the optical bandgaps of *ca*. 1.98 eV (solution) or *ca*. 1.74 eV (film) we derive values of -3.3 to -3.5 eV which are comparable with that obtained for **P1**. These orbital energies suggest that **P1**–**P4** will be able to transfer electrons to fullerene derivatives such as PCBM which has a LUMO energy of about -4.3 eV.

3.3.4 Mobility measurement of P1–4
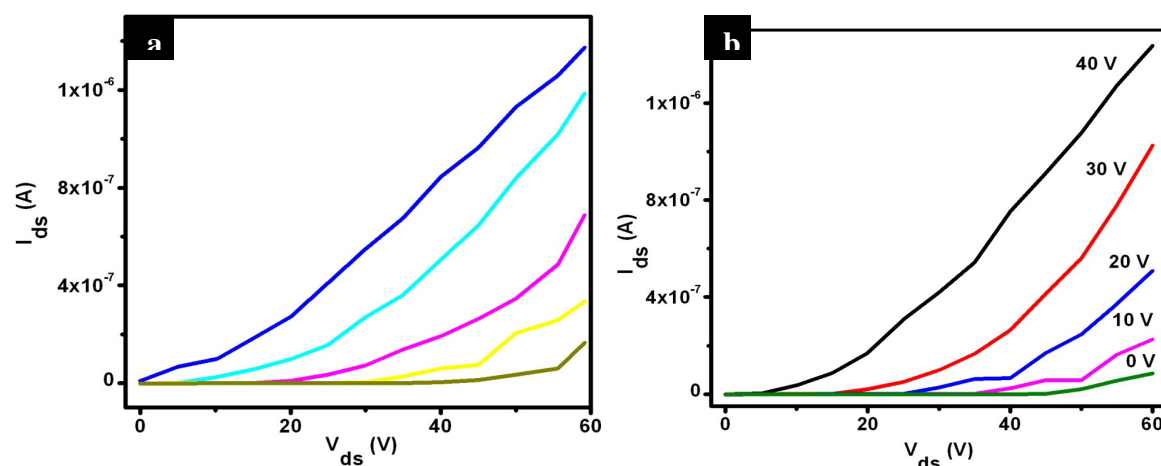
Figure 3.4: Current-voltage I_{ds}_V_{ds} characteristic of (a) **P3** and (b) **P4**. Channel width 1500 μm and channel length 60 μm.

Mobility measurement on the polymers **P1–4** was done by Dr. Manohar Rao N. V. from Energy Research Institute @ NTU (ERIAN). All the devices were fabricated using chlorobenzene and measurements were done in ambient conditions. Concentrations of 15 mg/ml of **P1–4** were used to spin coat on silicon nitride substrates (200 nm dielectric thickness). Gold (thickness ~ 100 nm) were used as the source-drain electrodes instead of aluminum as no Field Effect Transistor (FET) response was obtained when using Al. The current-voltage characteristics (I_{ds} vs. V_{ds}) of the FET devices based on **P3** and **P4** are shown in Fig. 3.4. **P1** and **P2** did not show any FET response, whereas **P3** and **P4** showed n-channel FET response with the electron mobility (μ_e) in the range of 10^{-4} $cm^2V^{-1}s^{-1}$ and this prove at least that **P3** and **P4** are n-type materials. Their I_{ON}/I_{OFF} ratio is quite low due to the high threshold voltages. The μ_e of polymers is not as promising compared to the best value described in the literature[71] and it is lower than the minimum required carrier mobilities (~10^{-3} $cm^2V^{-1}s^{-1}$)[48] to act as a good model to prevent losses in photocurrent and to obtain 10% PCE in OPV devices. However, **P3–4** (μ_e ~10^{-4} $cm^2V^{-1}s^{-1}$ in ambient) are still potential if compared to the copolymer containing carbazole and dialkoxybenzothiadiazole which has the μ_e of 3×10^{-4} $cm^2V^{-1}s^{-1}$ being measured in vacuum.[41] By further optimizing the processing conditions (e.g. in vacuum instead of ambient or using different substrates) or by increasing the M_w of the polymers, μ_e of these polymers in the range of 10^{-3} $cm^2V^{-1}s^{-1}$ could be obtained and their FET performance can be enhanced.

3.3.5   Morphology of polymer P4

P4 exhibited the highest molar mass and as such was the most promising candidate for use in electronic devices as it should produce the best films. Accordingly the topography of films of **P4** cast from chloroform solution was examined by Atomic Force Microscopy (AFM)

operating in tapping mode which was done by Sun Shuangyong in group of Prof. Lam Yeng Ming. As can be seen from Fig. 3.5a, **P4** forms a smooth film, with a low root mean square (RMS) roughness of about 1.4 nm. Some slight undulation was observed which is suggestive of aggregation. The effect of adding PCBM was then investigated. As can be observed from Fig. 3.5b the films of the blend **P4**–PCBM (1:2) cast from chloroform also appear relatively smooth and even, with RMS values comparable to those of the pristine **P4** (about 1.6 nm). This means that **P4** and PCBM mix well to form evenly distributed films, without any apparent large-scale segregation of either **P4** or PCBM. Such a smooth and uniform film morphology is desirable for obtaining good performance in photovoltaic devices as the performance of blends in such devices is severely adversely affected by large-scale phase separation. The performance of blends of **P4** and PCBM in photovoltaic devices was therefore tested and this was done at Newcastle University by Dr. Bofei Xue in group of Prof. Paul C. Dastoor.
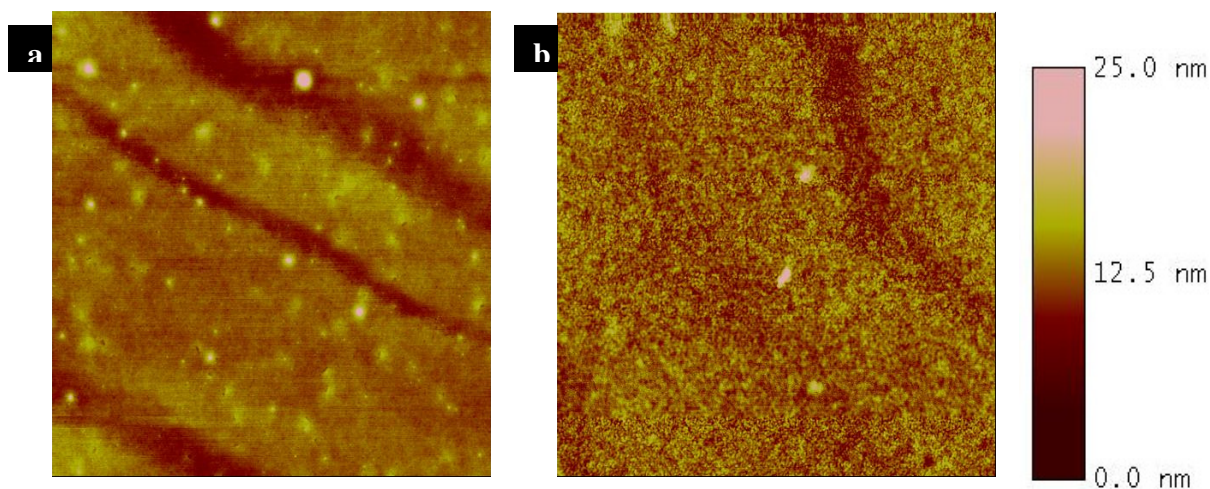
Figure 3.5: Morphology characterization. AFM topography images of film spin-coated from chloroform solution (a) **P4** (10 µm × 10 µm), (b) **P4**–PCBM (1:2) (10 µm × 10 µm). Spin coating rate: 2000 rpm, 60 s. Samples were not annealed.

3.4   Photovoltaic devices using P4

3.4.1   IV performance variation with different P4:PCBM ratios

Table 3.4: J-V performance variation with different **P4**:PCBM ratio (15 mg/ml).

	P4:PCBM Ratio	V_{oc} (mV)	J_{sc} (mA/cm^2)	FF	PCE (%)
15 mg/ml in CHCl$_3$	1:1	639	3.65	0.29	0.68
	1:2	676	4.66	0.34	1.05
	1:3	628	4.78	0.31	0.94
	1:4	656	3.60	0.37	0.88
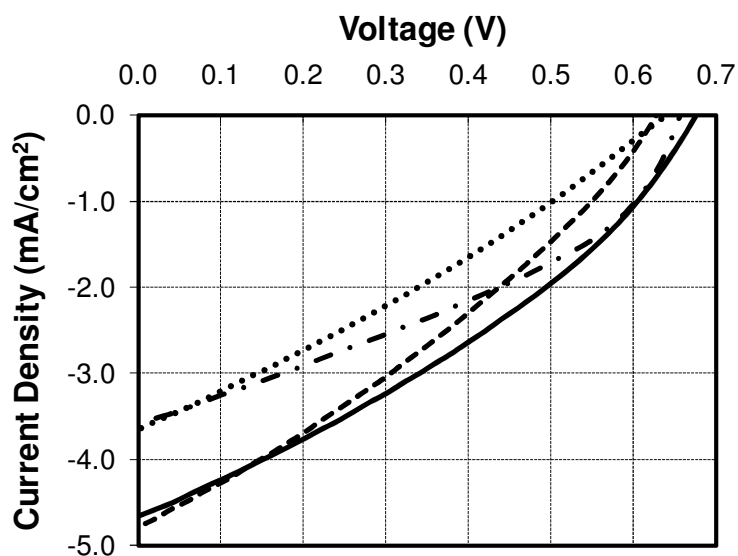
Figure 3.6: Current density-voltage characteristics as a function of **P4**:PCBM ratio. (a) 1:1 (dotted line), (b) 1:2 (solid line), (c) 1:3 (dashed line) and (d) 1:4 (dash dot line).

The concentration of **P4** and PCBM blend solution was kept at 15 mg/ml in chloroform in this study, with the **P4**:PCBM ratio ranging from 1:1 to 1:4. Ratios in the other direction (2:1, 3:1 and so on) were also tried and found to be much worse than 1:1 to 1:4. Device performance data and associated current density – voltage (J-V) curves are shown in Table 3.4 and Fig. 3.6 respectively and reveal that a P4:PCBM ratio of 1:2 ratio gives the best J-V performance and results in OPV devices that are around 1% efficient.

3.4.2   IV performance variation with different P4:PCBM (1:2) concentration in CHCl$_3$

Based on the results of the preceding section, the ratio between **P4** and PCBM was kept at 1:2, whilst the **P4** and PCBM total concentration was varied from 10 mg/ml to 20 mg/ml in CHCl$_3$. The J-V performance data are shown in Table 3.5 and Fig. 3.7 and indicate that the device performance is optimized for concentrations of 15 mg/ml.

Table 3.5: J-V performance variation with different **P4**:PCBM (1:2) concentration in CHCl$_3$.

	Concentration (mg/ml)	V_{oc} (mV)	J_{sc} (mA/cm^2)	FF	PCE (%)
P4:PCBM 1:2	10 mg/ml	605	4.26	0.33	0.86
	15 mg/ml	676	4.66	0.34	1.05
	20 mg/ml	598	5.05	0.30	0.92
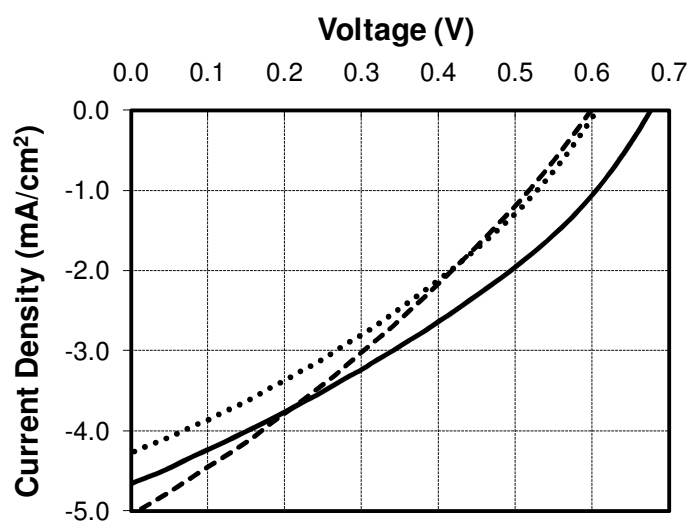
Figure 3.7: Current density-voltage characteristics of **P4**:PCBM (1:2) blend photovoltaic devices as a function of blend concentration in CHCl$_3$: (a) 10 mg/ml (dotted line), (b) 15 mg/ml (solid line), (c) 20 mg/ml (dashed line).

3.4.3　Effect of annealing on the performance

Table 3.6: The effect of annealing on J-V performance on **P4**:PCBM (1:2).

P4:PCBM 1:2 20 mg/ml	Thermal Treatment	V_{oc} (mV)	J_{sc} (mA/cm^2)	FF	PCE (%)
	None	598	5.05	0.30	0.92
	140 °C for 4 min	656	3.11	0.32	0.65
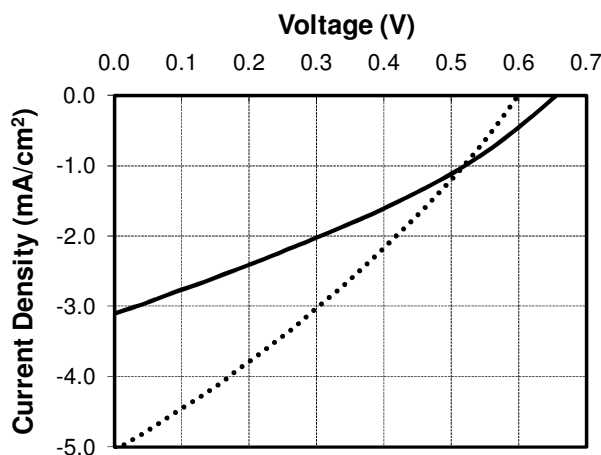
Figure 3.8: Current density-voltage characteristics of **P4**:PCBM (1:2) blend photovoltaic devices as a function of device annealing: (a) unannealed device (dotted line), (b) device annealed at 140 °C for 4 min.

Cells made from **P4**:PCBM (1:2, 20 mg/ml) blend were tested before and after annealing. It is found that annealing at 140 °C for 4 min decreased the IV performance dramatically (Table 3.6 and Fig. 3.8). Cells were also tested at different annealing temperatures (80, 100, 120 °C) and for different times. For all annealing conditions, the IV performance all dropped to different extents (data not shown).

To try and explain this loss in performance upon annealing the morphology of an annealed file of the 1:2 blend was examined by AFM. As can seen by comparison of the unannealed (Fig. 3.9a) and annealed films (Fig. 3.9b), the annealed film shows a much increased surface roughness compared to the unheated film (RMS = 45 nm compared to 1.3 nm). The annealing process thus enhances the aggregation in the polymer blends leading to an unoptimized morphology where exciton dissociation and charge transport becomes more difficult.
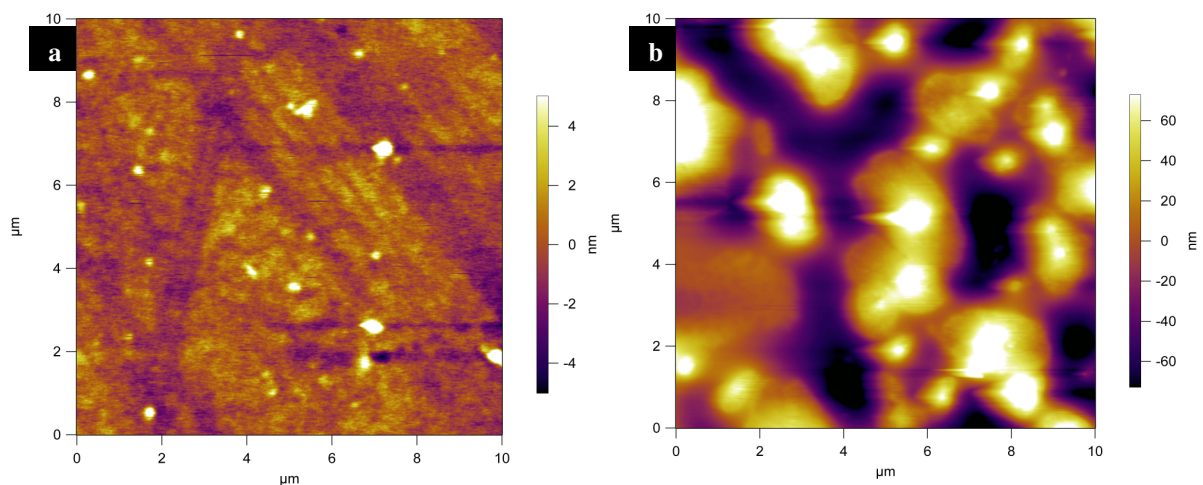
Figure 3.9: Morphology characterization. AFM topography images **P4**–PCBM (1:2) films spin coated from chloroform solution (a) before annealing, (b) after annealing.

3.4.4 P4:PCBM photovoltaic performance

The external quantum efficiency (EQE) of the best cell in Table 3.4 and Table 3.5 (made from **P4**:PCBM 1:2, 15 mg/ml solution) was measured and is shown in Fig. 3.10 together with the absorption curve of an active layer film spun from the same solution. It is clear that EQE spectrum closely resembles that of the absorption curve, with the EQE curve slightly blueshifted, and indicates that light absorbed by **P4** is primarily responsible for the photocurrent generated in the device. The V_{oc} of an organic solar cell (OSC) can be predicted from the HOMO and LUMO energy levels using the model developed by Scharber et al.[48] According to their model, the expected V_{oc} of **P4** based OSC is given by:

$$V_{oc} = \frac{1}{e}\left(\left|E_{HOMO}^{donor}\right| - \left|E_{LUMO}^{acceptor}\right|\right) - 0.3\,\text{V}$$

Substituting in the values for **P4** and PCBM[48] gives a predicted value of V_{oc} of 0.67 V, which is in excellent agreement with the V_{oc} of the best cell in Table 3.5 (0.68 V). This suggests the electrochemically derived HOMO value for **P4** is fairly accurate.
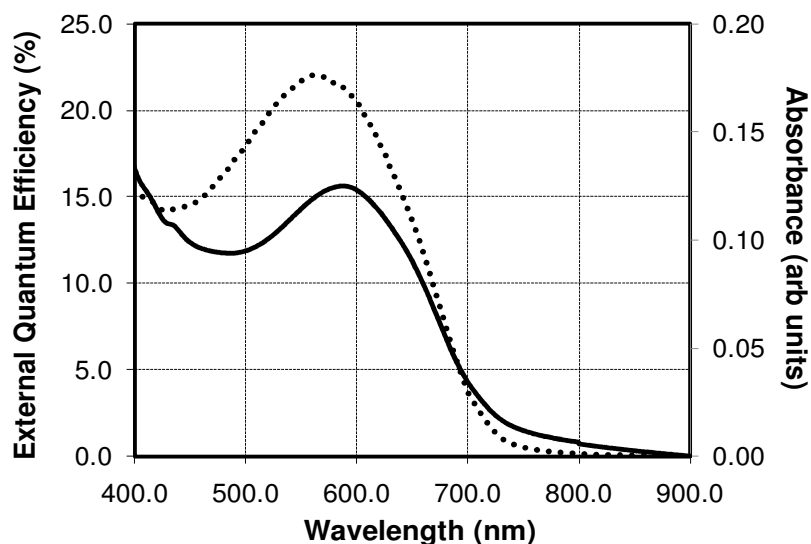
Figure 3.10: Variation of external quantum efficiency (dotted line) and absorption (solid line) as a function of wavelength for a solar cell and the active layer film respectively, both of which are from **P4**:PCBM 1:2, 15 mg/ml solution.

Indeed, based on Scharber's work[48], further comparison between the predicted and experimental values of power conversion efficiency (PCE) for **P4**:PCBM blend devices can be made. In the case of PCE, the efficiency of the **P4**:PCBM devices should be about 2% using $E_{g,ele}$ = 2.41 eV and the electrochemically measured LUMO of -2.86 eV. (This rises to *ca*. 6% if we use the solid state optical bandgap of 1.73 eV and a LUMO value derived from it of -3.52 eV). The best devices (Table 3.5) gave a PCE of about 1%. However, we note that the fill factors of the fabricated cells were quite low (mostly less than 35%). For the best cell in Tables 3.4 and 3.5, if the FF could be improved to 60% (as is assumed for calculating maximum efficiency by Scharber et al.[48]), the efficiency would increase to 1.85%. Further

work on interface engineering is underway at Newcastle University to improve the performance of photovoltaic devices based on **P4** and PCBM. Further if a different acceptor with a higher LUMO energy were to be used so reducing the LUMO offset to below 0.5 eV, theoretical efficiencies close to 10% would be possible according to the model of Scharber, using the optical bandgaps of 1.73-1.98 eV.

3.5 Conclusion

It has been shown that the dialkoxybenzothiadiazole and its derivative can be combined with various electron–donating comonomers to make copolymers **P1–4** with lower bandgap, proving the dialkoxybenzothiadiazole to be a good n-type unit. FET measurements also prove **P3–4** to be n-type materials having μ_e of ~10^{-4} cm^{2}V^{-1}s^{-1}. **P1–4** all display red emission in solution and the solid state. They are amorphous in general and possess reasonable thermal stability (above 160 °C). From the view of morphology, **P4** and PCBM mix well to form evenly distributed films, without any apparent large-scale segregation of either **P4** or PCBM. Such a smooth and uniform film morphology is desirable for obtaining good performance in photovoltaic devices as the performance of blends in such devices is severely adversely affected by large-scale phase separation. An efficiency of over 1% has been obtained from a photovoltaic device using **P4** combined with PCBM and this suggests that with further optimization these materials have considerable promise as active components in organic solar cell. Besides that, these materials can be also tested in other area of organic electronic devices. The properties of these covalently linked polymers will be used for comparison with the metal–linked species with same n-type linker unit in Chapter 4.

Chapter 4   Synthesis and characterization of new linear supramolecular metallopolymers

4.1   Review

As shown in Chapter 3, traditional covalently linked organic conjugated polymers consist of long molecular chains made up of many monomers linked by covalent bonds and the polymers' properties are defined by the nature of the monomers as well as the molar mass. On the other hand, supramolecular polymers are polymeric arrays of monomer units, held together by reversible and sometimes highly directional secondary interactions which are non–covalent bonds.[72] These include hydrogen bonds, metal–ligand bond and others; metal–ligand bonds are focused on this project due to the reasons mentioned in the Review (Section 2.1). Also, conventional polymers become highly viscous when they melt due to the entanglement of their macromolecules. This limits their applications as high temperatures and pressures are typically required to provide a melt of sufficiently low viscosity for processing. But supramolecular polymers combine good material properties with low viscosity melts that are easy to handle.[72]

Metal ions play an important role in modern and materials science, e.g. with respect to electronic applications.[73] Thus, combining these two, organic polymers and metal ions, has proven to be a fruitful approach to producing new functional materials. Among them, polymers with a terpyridine complex in the backbone were initially little investigated by researchers. In 1992, Constable first explored an approach using ditopic tpys as building

blocks for self-assembly with transition metal ions to form metallopolymers and – oligomers.[74] Later in 1995, he discussed, in a review, his original concept of using metallosupramolecular principles to prepare oligomers and polymers by coordination to metal ions.[75] The structures presented by him gave a strong impression of the potential of this strategy in regard to the incorporation of distinctive physical properties and since then, this research area has gained great interest and made metallopolymers one of the fastest developing fields in macromolecular chemistry. The properties of coordinated metallopolymers can be greatly varied due to the availability of a multitude of ions and ligands, both having profound effects on binding strength, reversibility and solubility.[76]

The great interest in these new materials (metallopolymers) is mainly attributed to their special properties, which represent the combination of the properties of $[M(tpy)_2]^{2+}$ complexes (i.e., optical, electrochemical and magnetic properties) with the versatile properties of organic polymers (i.e., mechanical properties, solubility and processability). For this reason, π-conjugated oligomers and polymers, one of the youngest polymer classes which have been developed greatly since the synthesis of polyacetylene almost 40 years ago,[77] are very interesting building blocks for combining with metal complexes. In contrast to the classical covalent polymers which are formed irreversibly, the combination of metal moieties with polymers armed with ligands also ensures the construction of high molar mass coordination polymers. This is achieved by the inherent advantage of reversible supramolecular systems which is their self-healing ability. Furthermore, external stimuli can be applied to the reversible metallopolymers to enable switching from the monomeric state to polymeric state.[15] Besides, after sustaining damage, polymers with the ability to repair

themselves when external stimulus (e.g. light) was applied to them could extend their useful lifetimes in many applications.[78]

These metallopolymers in fact showed outstanding electrical and optical properties and thus have attractive potentials for applications in many fields like organic light-emitting diodes (OLED), polymer light-emitting diodes (PLED) and solar cells, depending on the structure of the polymers.[3,16,23,24,76,79] Due to the advantages discussed in the review in Section 2.1, 4'-substituted-2,2':6',2''-terpyridines will be the our main focus to investigate the bis(tpys) which form linear metallopolymers after coordination with metal ions.

Chemically and thermally stable ditopic bis(tpy) derivatives, where the two tpy units are linked back-to-back with a covalent bond through a spacer, are able to form stable complexes with a large variety of transition metal ions for the design of functional materials.[80,81] In combination with different transition metal ions, the three chelating pyridyl units in tpys offer high binding constants and the formation of distorted octahedral 2:1 ligand–complexes, with properties varying from kinetically inert (e.g. Ru^{II} and Ni^{II}) to labile, but nevertheless thermodynamically stable bonds (e.g. Zn^{II}).[80,82] Zinc (II) will be our main research focus due to its availability, low costs compared with the other potential transition metals and the reversibility of its complexes. During the process of light emission in the metallopolymers, it is confirmed that the phenomenon of metal to ligand charge transfer (MLCT) does not occur in terpyridyl–Zn(II) metallopolymers because of d^{10} Zn(II) species, so only intraligand charge transfer (ILCT) occurs between the coordination sites and chromophores.[83-85] Zinc–tpy metallopolymers have attracted great interest recently due to their well-defined structures and enhanced photoluminescence (i.e., high PL quantum yield) and electroluminescent

properties at room temperature.[23,24,33,86] Therefore Zn[II] containing metallopolymers are promising materials for potential LED applications.
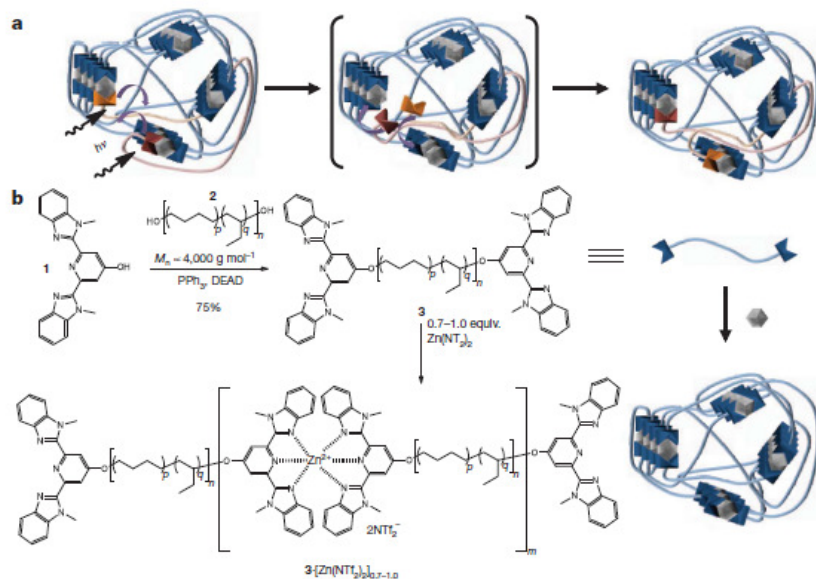
Figure 4.1: Mechanism and synthesis of photohealable metallosupramolecular polymers, a) Proposed optical healing of a metallosupramolecular, phase-separated network, b) Synthesis of macromonomer and polymerization by addition of $Zn(NTf_2)_2$.DEAD, diethyl azodicarboxylate.[87]

In previous works in this field, as shown in Fig. 4.1, Burnworth et al.[87] presented optically healable metallosupramolecular polymers consisting of rubbery and amorphous poly(ethylene-co-butylene) core with 2,6-bis(1'-methylbenzimidazolyl)pyridine (Mebip) ligand end groups that are non-covalently linked through metal ion coordination. These polymers can be healed through exposure to ultraviolet light as the metal–ligand motifs are electronically excited and the absorbed energy is converted to heat. The heat causes temporary disengagement of the metal–ligand motifs, allows the reaction equilibrium to be temporarily shifted to lower-molecular-mass and lower viscosity species, followed by

healing the damaged area through reentanglement of the chains, before the equilibrium is shifted back and the healed metallosupramolecular polymers are formed.

The Würthner group reported the metal–coordinated self-assembly of highly fluorescent tpys bearing perylene bisimide dyes in 4'-position to form photoactive metallopolymers which showed strong red PL emission.[23,84,85] Che and co-workers reported the incorporation of tpy–Zn(II) ions into different main-chain structures to make molecules producing a variety of colours from violet to yellow with high PL quantum yields.[88]

Instead of the metallo-homopolymers that use the same repeating unit coordinated by Zn(II) ions, Chen et al.[24] developed their first light emitting metallo-*alt*-copolymer, which was built up from different ditopic ligands coordinating with Zn(II) species and contained carbazole pendants attached to the C-9 position of fluorene by long alkyl spacers. These metallopolymers exhibited blue PL emissions with decent quantum yields of 11–23% and the PL results revealed that formation of excimers were suppressed by the incorporation of carbazole pendant groups. Besides, their EL results showed green EL emissions with maximum efficiencies of 0.85–1.1 cd A^{-1} and maximum luminances of 1704–2819 cd/m^2.
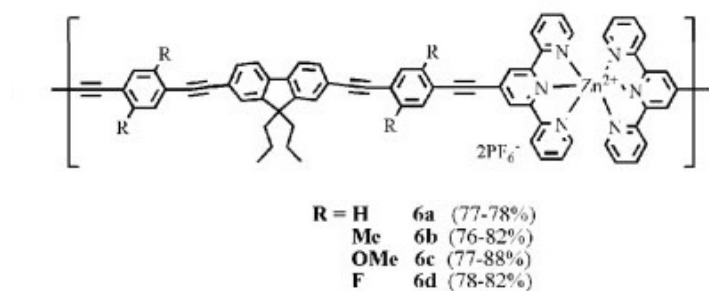
R = H   6a (77-78%)
    Me   6b (76-82%)
    OMe   6c (77-88%)
    F   6d (78-82%)

Figure 4.2: Structure of self-assembled bis(tpy)–Zn(II) based supramolecular polymers.[86]

Chen and Lin[86] later reported a series of self-assembled bis(tpy)–Zn(II) based supramolecular polymers (shown in Fig. 4.2) with various lateral substituents attached to the conjugated bis(tpy) ligands. They declared that their metallopolymers gave green to yellow PL emission (with good PL quantum yields) in films, and showed yellow to orange EL emissions. Besides, they also reported[89] a series of novel metallopolymers containing light-emitting poly(fluorene/ethynylene/(terpyridyl)zinc(II)) backbones and electron-transporting 1,3,4-oxadiazole (OXD) pendants. Enhancement of PL quantum yields by the introduction of 1,3,4-OXD was observed in this literature due to energy transfer happened between the pendants and polymer backbones and by utilization of these new metallopolymers as emitting materials to fabricate PLED devices, green EL emissions and good EL performance (maximum efficiencies of 1.05–1.35 cd A^{-1} and maximum luminances of 2313–3550 cd/m^2) can be obtained.

Schlutter et al.[23] have also synthesized some bis(tpy) building blocks with electron-accepting π-conjugated spacer units, which were combined statistically with established electron-donor units to form supramolecular low bandgap materials, which might be potential photovoltaic materials. The combination of electron acceptors with electron donors leads to a significant decrease of the E_g between the highest occupied molecular orbital (HOMO) of the donor and the lowest unoccupied molecular orbital (LUMO) of the acceptor which results in bathochromic shift (red shift) of the absorption.[45] Furthermore, they mentioned that energy transfer occurred from the excited electron-rich donor part to electron-deficient acceptor part in these statistical metallo-random polymers, which can consequently relax under emission. This proved that the central Zn(II)–tpy ions play a crucial role in the mediation of such a transfer. This is crucial for understanding of the photosynthetic processes and the design of

artificial light-to-energy conversion system. Besides that, an efficient energy transfer process allows long-range information transmission, which could be applied in the development of molecular devices and machines for information technology. [90]
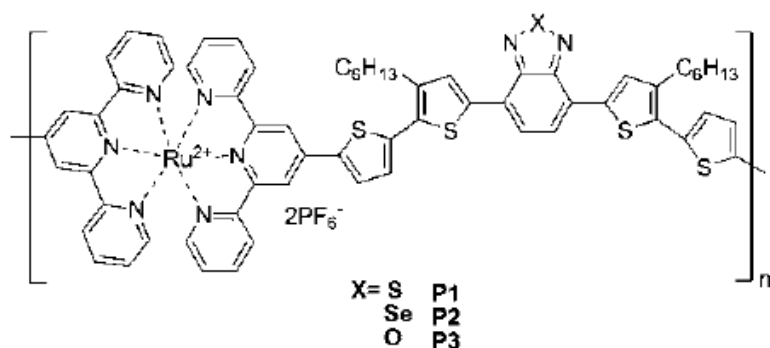
Figure 4.3: Structure of Ru(II)–containing metallopolymers.[3]

Padhly et al.[3] produced a series of π-conjugated bis(tpys) shown in Fig. 4.3 bearing various benzothiazole cores and their corresponding main-chain Ru(II) metallo-polymers. Due to strong intramolecular charge transfer (ICT) interaction and MLCT in Ru(II)-containing metallopolymers, the absorption spectra covered a broad range of 260–750 nm with optical bandgaps of 1.77–1.63 eV. One of these metallopolymers was mixed with PCBM and tested in bulk heterojunction (BHJ) solar cell devices and PCE of 0.45% was obtained, with V_{oc} = 0.61 V, J_{sc} = 2.18 mA cm^{-2}, and FF = 33.1%. Although they used Ru(II) instead of Zn(II) as the metal ions, these show the possibility of metallopolymers to be used in OPV applications.

Therefore, the synthesis (Section 4.2) and characterization (Section 4.3) of two new linear metallo-homopolymers (**P5** and **P6**) and a new linear metallo-*alt*-copolymer (**P7**) from their respectively monomers **26** and **27**, coordinating with Zn(II) ions were investigated in the

current project as processable, linear models for the 3D networks to be discussed in the next chapter.

4.2 Synthesis of new linear bis(tpy) monomers and the related metallopolymers

Details of synthetic procedures for synthesis of linear metallo-homopolymers (**P5** and **P6**) and metallo-*alt*-copolymer (**P7**) (including the synthesis of their monomers) according to Scheme 4.1 and 4.2 and the characterization data (including ^{1}H NMR, ^{13}C NMR, MALDI-TOF mass spectra, Elemental Analysis and HRMS) are given in the Experimental Section.

4.2.1 Synthesis of new linear bis-tpy monomers 26 and 27

The synthetic steps involved in preparation of linear p-type bis(tpy) monomers **26** and linear n-type bis(tpy) monomers **27** are outlined in Scheme 4.1.

2,5-Dibromobenzene-1,4-diol (2,5-dibromohydroquinone) was dialkylated using 2-ethylhexyl bromide to form 1,4-dibromo-2,5-bis(2-ethyhexyloxy)benzene **25** as a light yellow liquid. **25** was then Suzuki-coupled with **6** with the aid of Pd (0) to produce the linear p-type bis(tpy) monomer **26** as a pale yellow solid. Using the same method, **21** was Suzuki-coupled with **6** with the aid of Pd (0) to produce the linear n-type bis(tpy) monomer **27** as a red solid.
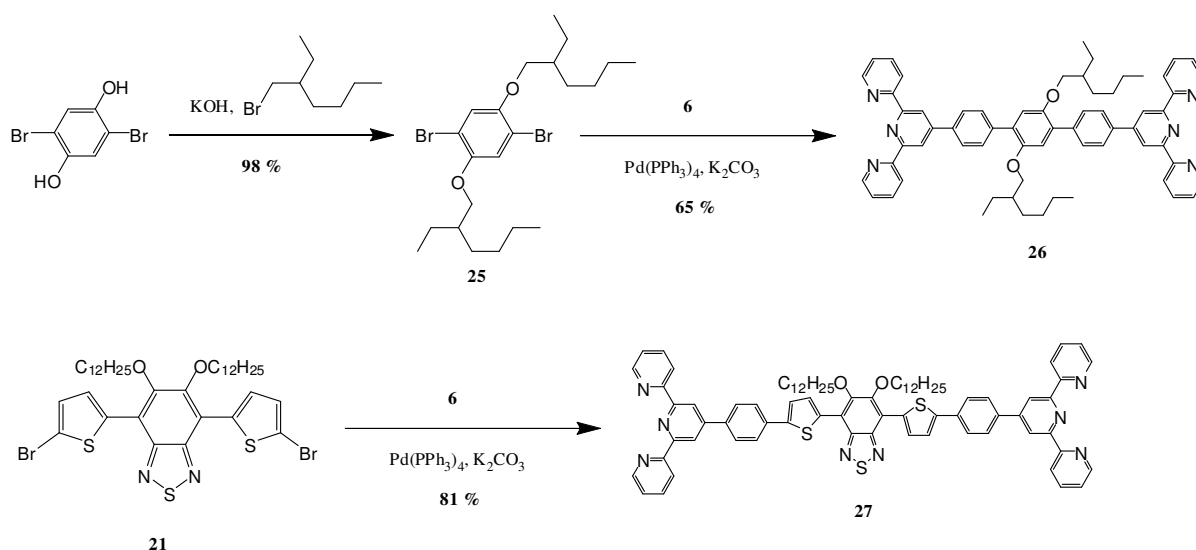
Scheme 4.1: Synthesis of linear p-type bis-tpy monomer **26** and linear n-type bis-tpy monomer **27**.

4.2.2   Synthesis of new linear metallopolymers P5–7

The synthetic steps involved in preparation of new linear p-type metallo-homopolymer **P5**, linear n-type metallo-homopolymer **P6** and linear metallo-*alt*-copolymer (p-type-*alt*-n-type) (**P7**) are outlined in Scheme 4.2.

Metallo-homopolymers **P5** and **P6** were obtained by refluxing respectively, monomers **26** and **27** with zinc acetate $Zn(OAc)_2$ at the stoichiometric ratio of 1:1, in NMP solutions and followed by subsequent anion exchange using excess of NH_4PF_6, as per literature precedents.[24,86,89] The key steps in the combining two different terpyridyl units (**26** and **27**) to form a metallo-*alt*-copolymer were first to complex both terpyridyl units of monomer **26** with $Zn(OAc)_2$ at the ratio of 1:2 to afford complex **28**. Then, complex **28** as an initiator was coordinated with monomer **27** at the ratio of 1:1 (as a sequential-coupling method) to obtain metallo-*alt*-copolymer **P7**.[24,86,89]
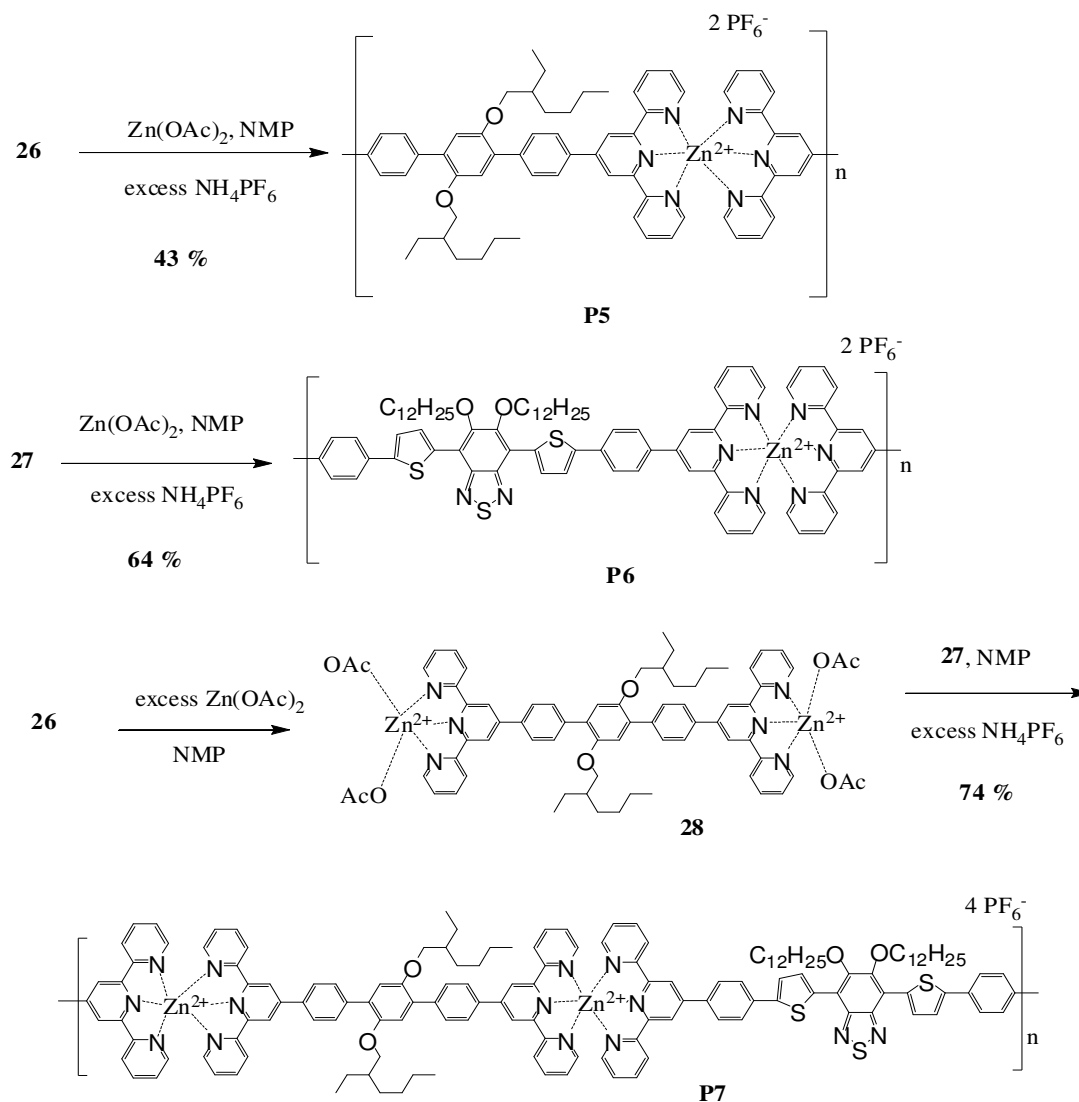
Scheme 4.2: Synthesis of linear metallo-homopolymers (**P5** and **P6**) and linear metallo-*alt*-copolymer **P7**.

Compared to their respective monomers **26** and **27** which are soluble in common organic solvents (e.g. ether, DCM, CHCl$_3$, THF etc.), linear metallopolymers **P5–7** are totally insoluble in those common organic solvents but soluble in highly polar aprotic solvents (e.g. DMSO, DMF, NMP, acetonitrile etc.) at room temperature. This behavior is caused by the highly linear-rigid structure of the metallopolymers' backbone as well as by the charged metal ions.[24,79,85] Therefore, the polymers **P5–7** can be purified and the contaminants

(including unreacted monomers) can be washed away with ether as described in the Experimental Section.

There are three points worthy to be noted for this metal-coordinated polymerization method compared to other polymerization methods, e.g., the Witting or Heck coupling reactions. First, the reactive lability of zinc (II) ions and the stability of six-coordinate bis(tpy) zinc (II) allow self-assembly reactions to take place under relatively mild (refluxing NMP) conditions.[2,19,91] Second, this procedure does not need any toxic polymerization catalysts. Third, the chemical structure of the metallo-copolymers can be controlled by proper stoichiometries of metals and monomers.[24,86]

4.3 Characterization of new linear bis-tpy monomers and the related metallopolymers

4.3.1 ^{1}H NMR analyses

^{1}H NMR spectra of monomers **26** in CD_2Cl_2, **27** in $CDCl_3$ and polymers **P5–7** in DMSO-d_6 were shown in Fig. 4.4. Monomers **26** and **27** revealed well-defined ^{1}H peaks for the terpyridyl units. All polymers **P5–7**, in accordance with literature precedents, exhibited broadening and clear downfield shift (compared with the ^{1}H peaks of terpyridyl units in monomers **26** and **27**) for the ^{1}H peaks of most of the terpyridyl protons i.e. (5,5")-, (4,4")-, (3,3")-, and (3,5')- and upfield shifts for the (6'6")- signals, after coordinating Zn^{2+} ions. [23,24,79,84,85] The formation of homopolymers **P5–6** is clearly indicated by the appearance of new sets of ^{1}H peaks and the absence of some of the original ^{1}H peaks in the terpyridyl units, which belong to uncomplexed monomers **26** and **27**.[23,24,84] To distinguish the molecular

structures between metallo-homopolymer and metallo-*alt*-copolymer, the integrated ratios of

2nd most downfield-shifted ^{1}H peaks in the terpyridyl (***A** for **P6** and ***A'** for **P7**) and the [1]H

peaks of the alkoxy chains (spacer $-CH_2-$ next to oxygen in the alkoxy chain) (**B** for **P6** and

B' for **P7**) of polymers **P6** and **P7** were compared. It reveals that the integrated ratio of ***A/B**

is 1 for homopolymer **P6** and that of ***A'/B'** is 2 for *alt*-copolymer **P7**, which suggests that

the ratio of **26** and **27** in polymers **P7** is 1:1. According to these results, the amount of ligand

blocks can be confirmed.[24]
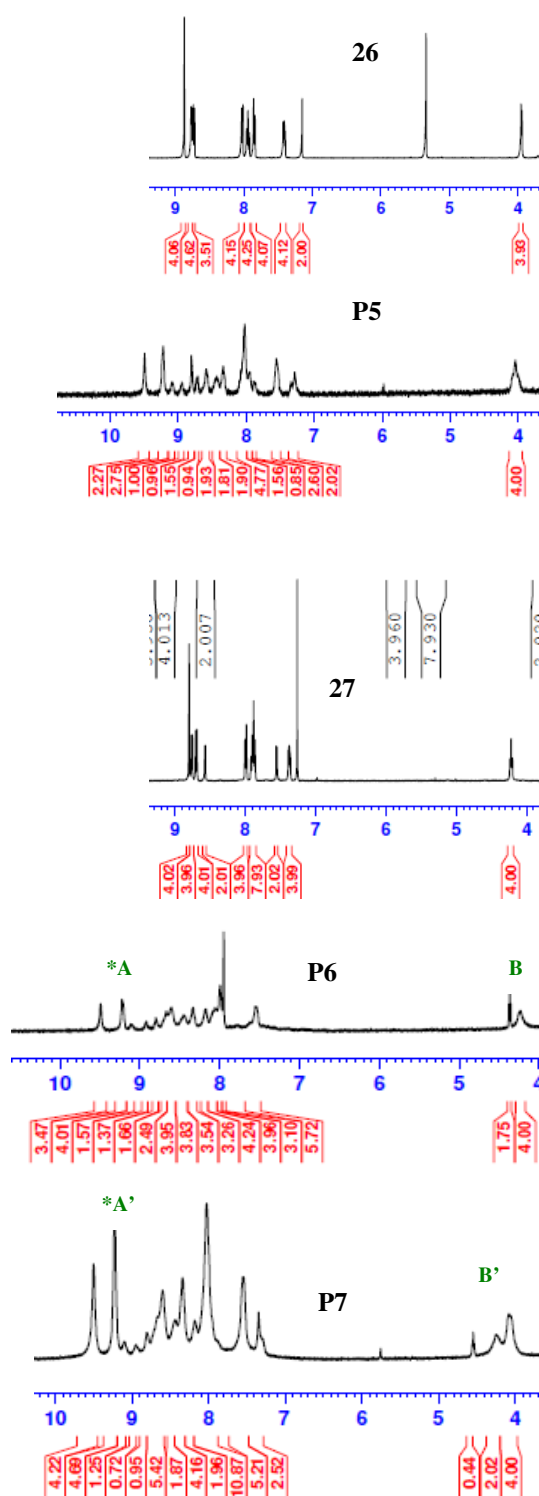
Figure 4.4: ^{1}H NMR spectra of bis-tpy monomer **26** in CD$_2$Cl$_2$, bis-tpy monomer **27** in CDCl$_3$ and metallopolymers **P5–7** in DMSO-d$_6$.

4.3.2 Optical properties of bis(tpy) monomers 26–27 and metallopolymers P5–7

The spectroscopic data of **26–27** in chloroform solution (10^{-5} M) and **P5–7** in DMSO

solution (10^{-5} M) and their results in thin films are summarized in Table 4.1. The absorption

and photoluminescence spectra of **26–27** in chloroform solution (10^{-5} M) and **P5–7** in DMSO

solution (10^{-5} M) are shown in Fig. 4.5a and Fig. 4.5b, respectively. Whereas, the absorption

spectra and photoluminescence spectra of **26–27** and **P5–7** in thin films are shown in Fig.

4.6a and Fig. 4.6b, respectively.

Table 4.1: Spectroscopic data of bis(tpy) monomers **26–27** and metallopolymers **P5–7**.

		Molecules				
		26	**27**	**P5**	**P6**	**P7**
Solution[a]	$\lambda_{abs,max}$ (nm)	324	479	344	484	483
	ε_{max} (M^{-1} cm^{-1})	36569	37383	27103	39131	33861
	λ_{onset} (nm)	396	550	420	564	562
	$\lambda_{em,max}$ (nm)	434	581	466	590	590
	Stokes shift (nm)	110	102	122	106	107
	$E_{g,op}$ (eV)[c]	3.13	2.25	2.95	2.2	2.21
Thin Film[b]	$\lambda_{abs,max}$ (nm)	338	493	354	506	500
	λ_{onset} (nm)	426	590	446	600	604
	$\lambda_{em,max}$ (nm)	437	629	501	630	618
	Stokes shift (nm)	99	136	147	124	118
	$E_{g,op}$ (eV)[c]	2.91	2.1	2.78	2.07	2.05

[a]Recorded in solution (concentration of 1 x 10^{-5} M) of CHCl$_3$ for **26–27** and DMSO for **P5–7**; [b]Drop casting

from solution of CHCl$_3$ for **26–27** and DMSO for **P5–7**; [c]$E_{g,op}$ = (1240/λ_{onset}) (eV).
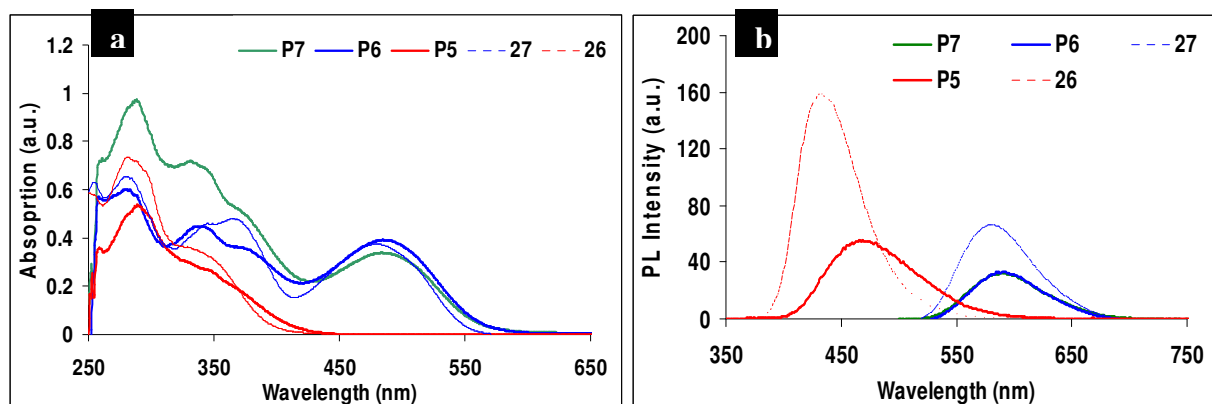
Figure 4.5: (a) UV-vis absorption and (b) photoluminescence spectra of bis(tpy) monomers **26–27** (in CHCl$_3$ solution (10^{-5} M)) and metallopolymers **P5–P7** (in DMSO solution (10^{-5} M)).
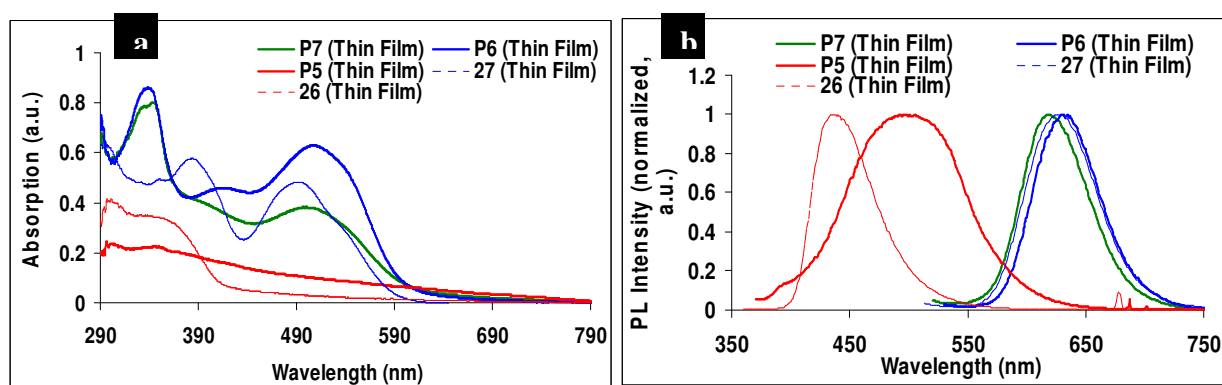
Figure 4.6: Thin films (a) UV-vis absorption and (b) photoluminescence spectra of bis(tpy) monomers **26–27** and metallopolymers **P5–P7**.

Unlike Ru(II), the Zn(II) ions do not participate in the electronic transition due to their filled d^{10} electron shells. The absorption maximum ($\lambda_{abs,max}$) (solution) of **26** is at 324 nm, which is red-shifted 20 nm to 344 nm for **P5**, after coordinating with Zn(II) ion. $\lambda_{abs,max}$ of **P6** is at 484 nm, red-shifted 5 nm compared to that of **27**. Whereas for **P7**, in which Zn(II) coordinates both **26** and **27** in its polymer backbone, it not only absorbs in the same region as **P5**, but also has a $\lambda_{abs,max}$ (483 nm) similar to that of **P6**. The absorption at this specific wavelength is believed due to the unit of dialkoxyBT-dithiophene in the polymer backbone of **P6** and **P7**, which is absent in the absorption spectra of **P5**. $E_{g,op}$s (solution) of **26** and **27** are 3.13 eV and

2.25 eV, respectively corresponding to the λ_{onset} of 396 nm (**26**) and 550 nm (**27**). $E_{g,op}$s (solution) of **P5** is 2.95 eV and that of **P6–7** are about 2.2 eV corresponding to the λ_{onset} of 420 nm (**P5**) and *ca.* 563 nm (**P6–7**). The emission maxima ($\lambda_{em,max}$) (solution) of **26** and **27** are at 434 nm and 581 nm, respectively, which are red-shifted 9–14 nm to 446 nm (**P5**) and 580 nm (**P6–7**). **P7** displays only one emission peak which is the same as the emission peak in **P6** which might be due to the energy transfer from the donor unit to acceptor unit in **P7**. This is currently being investigated by the group of Asst. Prof. Tan Howe-Siang of SPMS in NTU. The nature of the energy transfer in systems like **P7** is of great interest for understanding the properties of natural and artificial light–harvesting systems.

Comparing the absorption spectra of solution and solid state (thin film), $\lambda_{abs,max}$ of **26** and **27** in solid state red-shifted 14 nm and that of **P5–7** in solid state red-shifted 10–22 nm compared to that in solution state, indicating certain degree of interchain association or aggregation in the solid state. A certain degree of aggregation occurs in the **P5** film, causing the quality of the films to decrease. This aggregation may account for the marked red shift between the solution and solid state for PL from **P5**. Its absorption extends all the way from 800 nm to 250 nm, even though the onset of the absorption of **P5** film should be at about 450 nm. The similar phenomena were observed when films were drop-cast for UV characterization. Compared to the $\lambda_{em,max}$ (solution) of **26** (434 nm) and **27** (581 nm), $\lambda_{em,max}$ (thin film) of **26** and **27** are red-shifted to 437 nm and 629 nm, respectively, A similar red-shift phenomena was observed for $\lambda_{em,max}$ (thin film) of **P5** (501 nm) and **P6–7** (630 nm & 618 nm, respectively). Smaller value of $E_{g,op}$s in thin films of **26** (2.91 eV) and **27** (2.1 eV) is obtained compared to that in solution. Among the metallopolymers' thin films, **P7** has the smallest bandgap of 2.05 eV corresponding to the λ_{onset} of 604 nm.

4.3.3 Thermal behaviour of bis(tpy) monomers 26–27 and metallopolymers P5–7

The TGA plots of bis(tpy) monomers **26**–**27** and metallopolymers **P5**–**P7** are shown in Fig. A59 in Experimental Section. Differential scanning calorimetry (DSC) plots of bis(tpy) monomers **26**–**27** and metallopolymers **P5**–**P7** are shown in Fig. A60 in Experimental Section. T_{3d}, T_g and T_m of bis(tpy) monomers **26**–**27** and metallopolymers **P5**–**P7** are listed in Table 4.2.

Table 4.2: 3% weight loss temperature (T_{3d}), glass transition temperature (T_g) and melting temperature (T_m) of bis(tpy) monomers **26**–**27** and metallopolymers **P5**–**P7**.

Molecules	T_{3d} (°C)[a]	T_g (°C)[b]	T_m (°C)[c]
26	368	168	240
27	255	163	212
P5	340	—[d]	—[d]
P6	295	—[d]	—[d]
P7	293	—[d]	—[d]

[a]T_{3d} = 3% weight loss temperature; [b]T_g = glass transition temperature; [c]T_m = melting temperature; [d]relevant data is not found.

P5 has a slightly smaller T_{3d} (340 °C) compared to that of **26** (368 °C), whereas **P6** was observed to have a larger T_{3d} (295 °C) compared to that of **27** (255 °C). **P7** has a T_{3d} (293 °C) larger than that of **27** but smaller than that of **26**. These results do not completely match the thermal stability results reported for other metallopolymers[24,86] for which an increase in the decomposition temperature of metallopolymers in comparison with their monomers was observed. However, it was found that more than 40 wt % of the residual materials were left

upon heating metallopolymers **P5–P7** to 900 °C and upon heating above 600 °C, metallopolymers **P5–P7** are more thermally stable than their monomers (as shown in Fig. A59) which might due to their metal content in **P5–P7**. Also, what is in agreement with literature precedent[86] is that no phase transitions (T_g and T_m) were observed in the DSC measurements of metallopolymers **P5–P7**, unlike the behaviour of the monomers **26** (T_g = 168 °C; T_m = 240 °C) and **27** (T_g = 163 °C; T_m = 212 °C). The metallopolymers **P5–P7** are believed to be amorphous materials as no significant exothermic peaks (T_c) were observed in their DSC plots during heating cycles.

4.3.4   Electrochemical properties of bis(tpy) monomers 26–27 and metallopolymers P5–7

Table 4.3: Redox properties of bis(tpy) monomers **26–27** and metallopolymers **P5–7**.

Molecules	CV					
	$E_{onset,ox}$ (V)	$E_{onset,red}$ (V)	E_{HOMO} (eV)[c]	E_{LUMO} (eV)[d]	$E_{g,ele}$ (eV)[e]	$E_{g,opt}$ (eV)[f]
26[a]	1.03	-0.77	-5.43	-3.63	1.8	3.13
27[a]	1.32	-0.77	-5.72	-3.63	2.09	2.25
P5[b]	-	-0.8	-6.55	-3.6	2.95[g]	2.95
P6[b]	-	-0.89	-5.71	-3.51	2.2[g]	2.2
P7[b]	-	-0.9	-5.71	-3.5	2.21[g]	2.21

[a]**26–27** were measured in DCM; [b]**P5–7** were measured in acetonitrile; [c]E_{HOMO} = -($E_{onset,ox}$ + 4.4) eV for **26–27**, HOMO levels of **P5–7** were estimated from measured optical bandgaps and LUMO levels; [d]E_{LUMO} = -($E_{onset,red}$ + 4.4) eV; [e]$E_{g,ele}$ = E_{LUMO} - E_{HOMO}; [f]$E_{g,opt}$ [cf. Table 4.1]; [g]$E_{g,ele}$ of metallopolymers are the same as $E_{g,opt}$ due to absence of $E_{onset,ox}$.

The electrochemical properties (redox behaviour) of bis(tpy) monomers **26–27** and metallopolymers **P5–7** were investigated by Cyclic Voltammetry to determine their HOMO and LUMO orbital energy values. The plots are shown in Fig. A61 in Experimental Section and the data are listed in Table 4.3.

The oxidation onset potentials ($E_{onset,ox}$) of **26–27** are 1.03 V and 1.32 V versus Ag/Ag$^+$, respectively. The calculated HOMO values (eV) of **26–27** are thus -5.43 and -5.72, respectively. The reduction onset potentials ($E_{onset,red}$) of **26–27** are both at -0.77 V versus Ag/Ag$^+$, corresponding to calculated LUMO values (eV) of -3.63. The electrochemical bandgaps ($E_{g,ele}$) of **26–27** are thus 1.8 eV and 2.09 eV, respectively. **27** has an $E_{g,ele}$ close to its $E_{g,opt}$, but **26**'s $E_{g,ele}$ (1.8 eV) vary from its $E_{g,opt}$ (3.13 eV). The reduction onset potentials ($E_{onset,red}$) of **P5–7** are -0.8 V, -0.89 V and -0.9 V versus Ag/Ag$^+$, respectively, corresponding to calculated LUMO values (eV) of -3.6, -3.51 and -3.5, respectively. All the metallopolymers **P5–7** exhibit quasi-reversible reduction curves and the reduction curves of **P5–7** were attributed to the reduction processes of terpyridines in metal complexes.[86] The absence of oxidation processes (the anodic scans up to 1.5 V) in these metallopolymers was expected, because metal oxidation is extremely difficult to be observed due to the stable d^{10} electron configuration of Zn(II) metal centers.[23,24,86,89] In order to obtain the HOMO levels of the Zn(II)–metallopolymers, the calculated optical bandgap $E_{g,opt}$ and LUMO levels were used for the estimation. HOMO values (eV) of **P5–7** are thus calculated to be -6.55, -5.71 and -5.71, respectively. Note that the bandgap structures of **P6** and **P7** seem identical and this suggests that the BT units dominate the electrochemical as well as the optical properties.

4.4   Quenching effect

Among **P5–7**, **P6–7** are suitable (due to their bandgap structures) to mix with fullerene derivatives such as PCBM as they are able to transfer electrons to the PCBM, which has a HOMO of -6 eV and LUMO of -4.3 eV, in order to test the quenching effect of **P6–7** by PCBM.
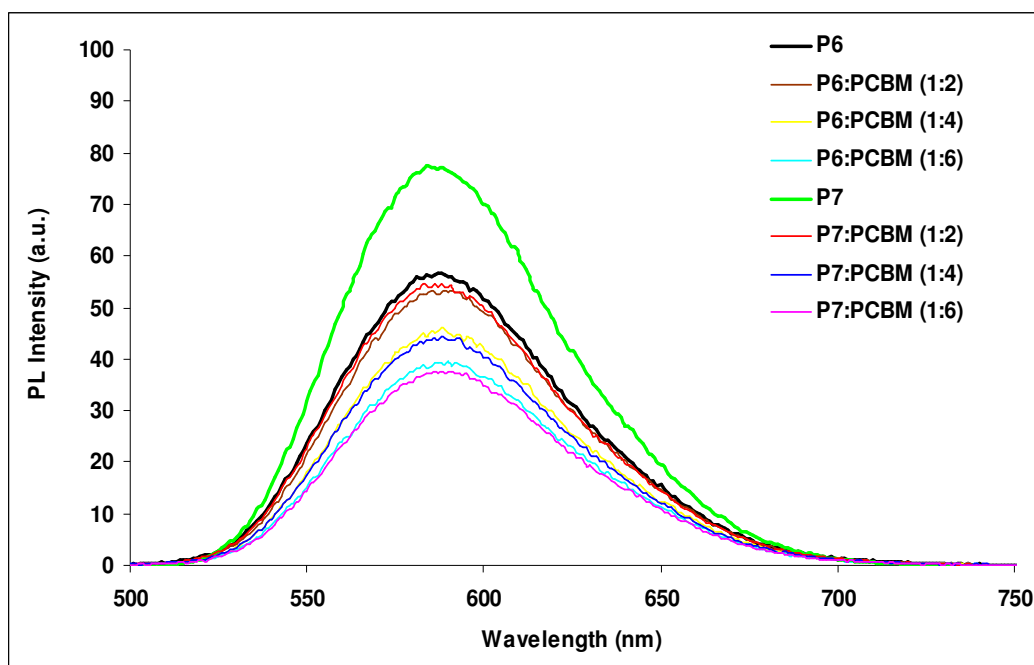
Figure 4.7: photoluminescence spectra of **P6–7** (10^{-5} M) and **P6–7** (10^{-5} M) mixing with PCBM (1:2, 1:4 and 1:6 on weight ratio) in DMF solution.

The photoluminescence spectra (in DMF solution) of **P6–7** and **P6–7** mixed with PCBM in different ratios (1:2, 1:4 and 1:6) are shown in Fig. 4.7. As shown from the PL spectra, $\lambda_{em,max}$ of all the materials are in the small range of around 584–590 nm and the PL intensity does go down as the amount of PCBM increases, for both **P6** and **P7**. This phenomenon is interpreted as electron transfer from **P6** and **P7** to PCBM. The PL data (thin films) of **P6–7**

and **P6–7** mixed with PCBM after spin coating are absent as no PL data could be recorded from the thin films due to the low concentration of the materials in the very thin films obtained by spin coating. But PL could be seen by naked eye from films of only **P6–7** when irradiated by the long wavelength UV light (365 nm) which was not observed for the films of **P6–7** mixed with PCBM. Thus, PCBM, a good electron acceptor, managed to quench the fluorescence of **P6–7** in the solid state.

4.5   Conclusion

In summary, a logical synthesis route for a set of π-conjugated bis(tpy) bearing p-type or n-type spacer units and their corresponding main-chain metallo-homopolymers **P5** (p-type) and **P6** (n-type) was developed. Besides, linear metallo-*alt*-copolymer (p-type-*alt*-n-type) (**P7**) was also developed. The formation of metallopolymers **P5–7** was concluded from the broadened ^{1}H NMR signals. Apparently, the electro-optical properties of the monomers as well as of the metallo-homopolymers are strongly influenced by the nature of the attached π-conjugated spacer unit. Furthermore, **P7**, as a metallo-*alt*-copolymer, from the emission experiment in solution, featured an energy transfer from the donor to the acceptor unit, which is being investigated by the research group of Prof. Tan Howe-Siang. The herein synthesized metallopolymers **P5–7** (homo and random) showed promising properties and they have good potential to be used in opto-electronic applications such as PLED or OPV devices.

Chapter 5 Synthesis and characterization of new 3D supramolecular Zn(II)–coordinated self-assembled organic networks and nanocomposites

5.1 Review

Construction of functional biological systems via the assembly of multiple distinct molecular subunits has been developed by nature. For example, pairs of seven different proteins are assembled to form the proteasome of yeast *Saccharomyces cerevisiae*.[92] In the past two decades, coordination-driven self-assembly has emerged as a strong new tool simulating for nature's own complexity to construct abiological supramolecular architectures with well-defined shape and size.[13,14] Equilibrium between numerous supramolecular structures generally exists for multicomponent coordination-driven self-assembly with more than one metal center or individual donors, resulting in a self-organized mixture via self-recognition and self-selection.[93,94] Thus, it remains challenging for the preparation of a single and discrete supramolecular architecture capable of mimicking the natural systems via multicomponent coordination-driven self-assembly.[95]

Until now, the efficient progress of metallosupramolecules via multicomponent abiological self-assembly has been largely limited to 2D structures.[4,5,93,95-103] However, self-assembled 3D structures are more prevalent and important in nature and science. It is thus novel and interesting to use the mechanism of self-assembly, especially metal–ligand bonding in which

multiple components are selectively recognized and self-assembled to generate only one discrete metal complex in 3D metal-organic networks (MONs). MONs, especially functionalized supramolecular metal-organic assemblies have thus attracted much attention researched on this area due to the interesting geometry, coordination involved and potential uses in a variety of electronic, magnetic, catalytic, photonic, mechanic and sensor applications.[4,13,14,93,98,101,102,104-112]

Functionalities can be readily introduce onto the MONs by employing functional ligands or/and metal corners in the assembly process. Also, cavities created inside the MONs can accommodate guest molecules. MONs which contains transition metals is generally more sensitive and responsive on electro- and photochemical stimuli compared to metal-free organic networks.[101]
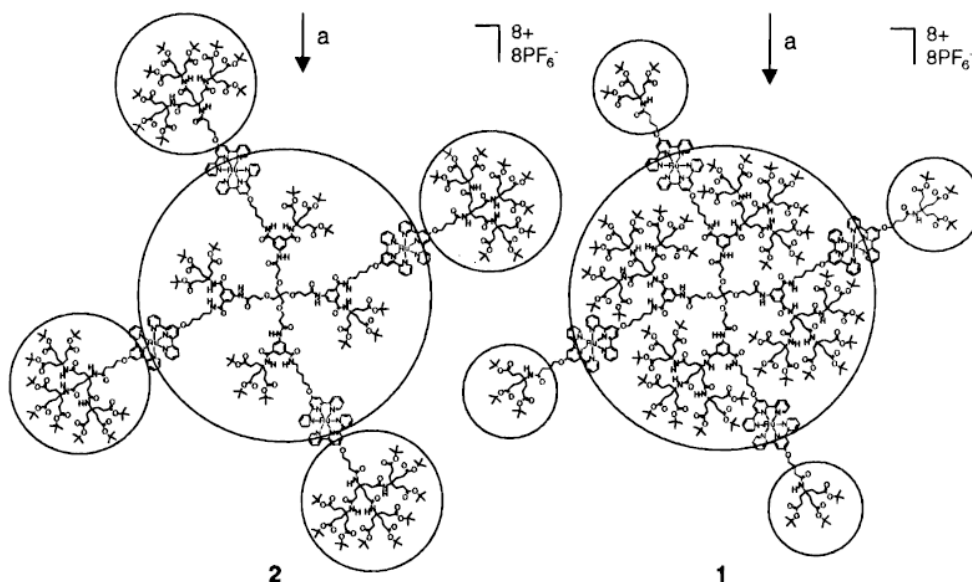
Figure 5.1: Two new tetrahedral isomeric metallomacromolecules using bis(tpy)Ru(II) connectivity.[105]

Among the research efforts in the 3D organic networks involving metal–ligand coordination, Newkome et al.[104] utilized Ru metal centers to connect two independently prepared dendrons in a process that mimicked a key and lock system. Newkome et al.[105] also constructed tetrahedral isomeric metallomacromolecules using a tetrasubstitutional methane core molecule with bis(tpy)Ru(II) connectivity, as shown in Fig. 5.1.
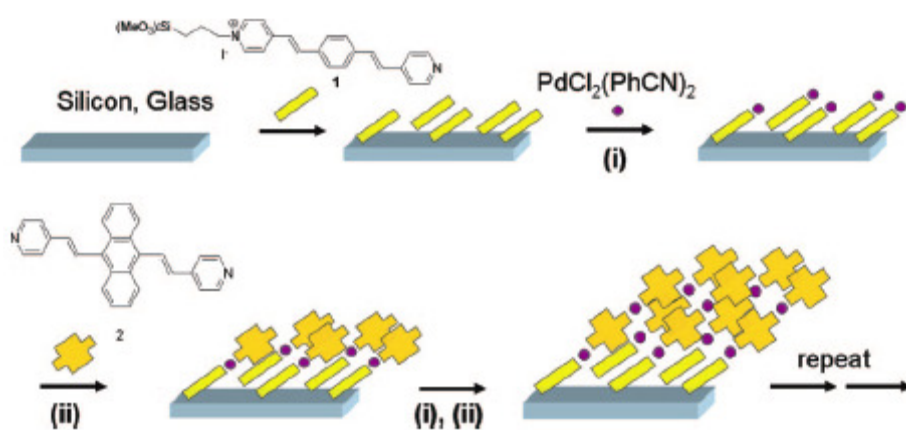
Figure 5.2: 3D-ordered assembly strategy involving metal–ligand coordination between pyridyl-terminated chromophores and PdCl$_2$.[106]

As shown in Fig. 5.2, Altman et al.[106] achieved a 3D-ordered molecular-based multilayer on glass and silicon substrates by a combination of forces including strong metal–ligand coordination. This involves iterative coordination of pyridyl-terminated chromophores and PdCl$_2$ and also π-π interactions and this achievement is believed to be useful in semiconductor-based technologies.

Stang et al.[93,107] focused on the use of square-planar platinum(II) metal acceptors and electron-rich pyridyl donors and investigated the factors that influence and control the self-

assembly of 2D polygons and 3D polyhedral metallosupramolecules via the directional-bonding approach as shown in Fig. 5.3 and 5.4. Steric interactions are observed to be particularly useful control factors for driving such self-organization. Functional groups attached to otherwise identical subunits have been shown to influence self-organization through "second order" effects. The results of their studies help to explain the details of self-organization phenomena and understand the similar organization processes occur in natural and biological systems. In the end highly functional systems (e.g. light-harvesting assemblies) might be prepared simply by mixing a variety of molecular subunits which self-organize into the desired complex assemblies.
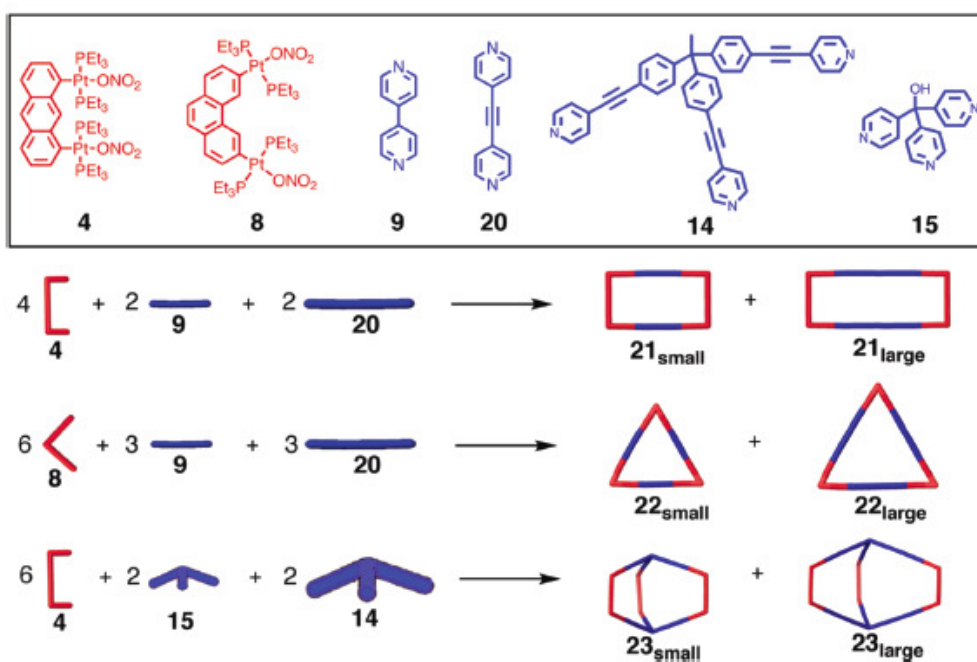
Figure 5.3: Demonstration of the use of different sized molecular components as a means to drive self-organization of 2D and 3D metallosupramolecules.[93]
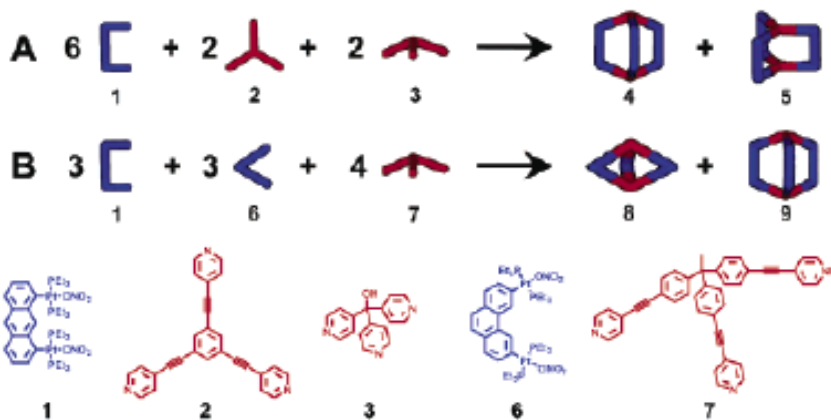
Figure 5.4: Graphical representation of self-recognition in the coordination-driven self-assembly of 3D polyhedra.[107]

Stang et al.[108] presented the multicomponent coordination-driven self-assembly of discrete 3D tetragonal prisms by the reaction of two donors and one metal acceptor in the proper stiochiometric ratios without the use of any templates. Such molecules may have applications in host–guest chemistry or as new micro-reactors.
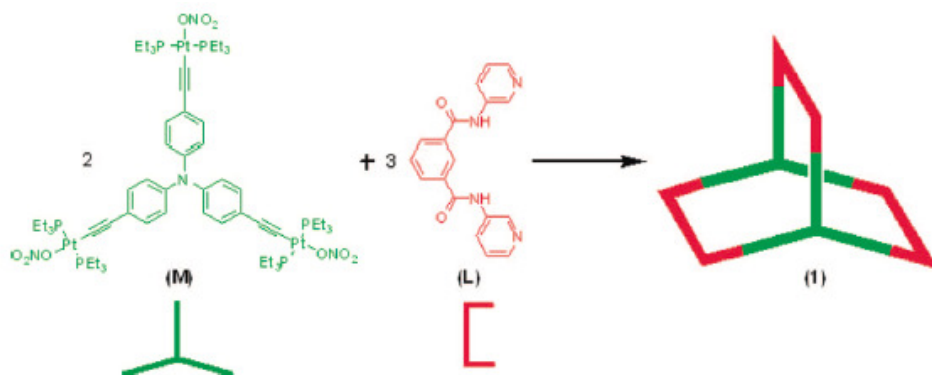
Figure 5.5: Self-assembly of 3D trigonal cage prism.[109]

As shown in Fig. 5.5, Ghosh and Mukherjee[109] reported the synthesis and characterization of 3D trigonal cage prisms by formation of a M_2L_3 system (M = tridentate acceptor and L =

bidentate donor) prepared via directional self-assembly of a new organometallic Pt$_3$ plannar

acceptor and an organic clip-type donor. They reported preliminary fluorescence quenching

results in which the solution fluorescence of the 3D cage prism was quenched by oxidative

nitroaromatics, which are chemical signatures for explosives.

Furthermore, Würthner et al.[84,85] showed that by adding more metal ions into their linear

metallopolymers, coordination complexes can be dissociated again in favour of an open form

with the zinc ion only attached to one tpy unit and its other coordination sites are presumably

saturated by solvent molecules. This assumption of reversible self-assembly and disassembly

of bis(tpy) Zn(II) coordination polymers upon addition of an excess of Zn(II) ions was

supported by DOSY NMR spectroscopy as well as fluorescence anisotropy measurements

and will be useful also for the 3D self-assembly and disassembly.
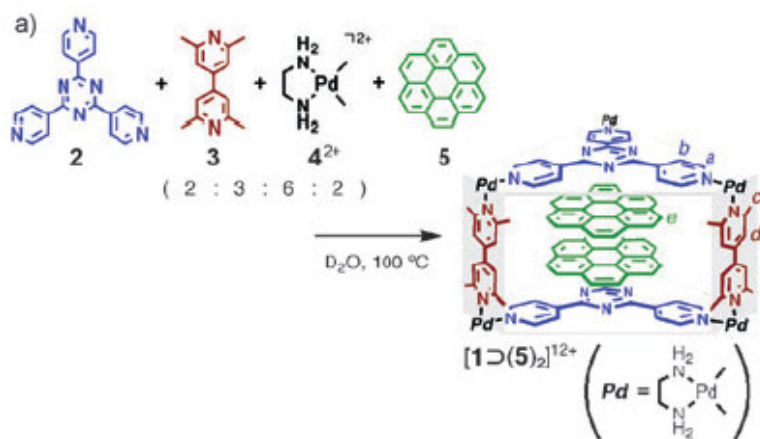
Fig. 5.6: 3D organic pillared coordination cages encapsulating large aromatic molecules.[111]

As shown in Fig. 5.6, Fujita et al.[111,112] demonstrated the facile, selective self-assembly of

metal-hinged, organic-pillared 3D trigonal prisms by mixing palladium (II) acceptors with di-

and tritopic pyridyl ligands with a large cavity that can intercalate two or more large π-conjugated molecules, which are expected to change the physical and chemical properties of the encapsulated materials significantly.

Similarly, Zheng et al.[98] combined a 90° Pt(II) acceptor and a carboxylate ligand with pyridyl donors in a proper ratio, allowing selective self-assembly formation of a variety of multicomponent supramolecular 3D prisms. Such multicomponent, selective self-assembly processes are directed, in part, by a charge separation effect, whereby a negative carboxylate ligand and a neutral pyridyl donor favor heteroleptic motif upon coordination with Pt(II) centers. Triphenylene can be encapsulated in one of the 3D cages, as shown in Fig. 5.7.
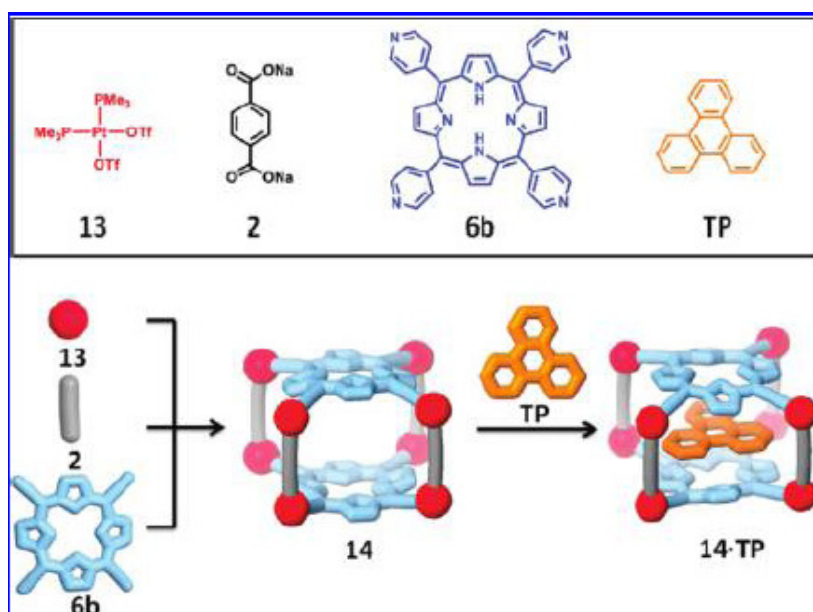
Figure 5.7: 3D multicomponent porphyrin cage encapsulating triphenylene (TP).[98]

However, to date tpy–Zn(II) coordinated self-assembled organic 3D networks have not been investigated compared to either 1D or 2D assemblies; this might be because of the difficulty

in synthesis and isolation of the original uncomplexed high molecular weight molecules. We hypothesised that by using the same technique, the formed 3D supramolecular self-assembled networks can be dissociated and different linear bis(tpys) can be inserted in between the original 3D networks so that new extended 3D supramolecular Zn(II)–coordinated self-assembled networks can be formed. Thus, by using the 3D tetrahedral cores (**1** and **2**) introduced in Chapter 2 and combining them with the Zn(II) ions that was successfully used to form linear metallopolymers in Chapter 4, we here introduce two new 3D supramolecular Zn(II)–coordinated self-assembled networks **S1–2** and through dissociating original networks **S1–2** with more Zn(II) ions followed by inserting with linear bis(tpys) (**26** or **27**) introduced in Chapter 4, new 3D supramolecular Zn(II)–coordinated self-assembled extended networks **S3–6** have been made.

5.2   Synthesis of new 3D Zn(II)–coordinated self-assembled networks

Details of synthetic procedures for synthesis of new 3D Zn(II)–coordinated self-assembled supramolecular networks **S1–2** according to Scheme 5.1 and new 3D Zn(II)–coordinated self-assembled extended supramolecular networks **S3–6** according to Scheme 5.2 are described in the Experimental Section.

3D Zn(II)–coordinated self-assembled networks **S1** and **S2** were obtained by refluxing their 3D monomers **1** and **2** respectively, with zinc acetate Zn(OAc)$_2$ at the stoichiometric ratio of 1:2, in NMP solutions followed by anion exchange using an excess of NH$_4$PF$_6$. Compared to their respective 3D monomers (**1** and **2**) which are soluble in common organic solvents (e.g. ether, DCM, CHCl$_3$, THF etc.), 3D networks **S1–2** are not only insoluble in those common

organic solvents but, unlike the linear metallopolymer **P5–7**, also are insoluble in highly polar aprotic solvents (e.g. DMSO, DMF, NMP, acetonitrile etc.) at room temperature. This behavior is believed to be caused by the highly crosslinked or interpenetrated structure of the 3D networks. Therefore, all the unwanted byproducts (including any unreacted starting material **1–2**) can be washed away by using ether to get the final solid of **S1–2** as shown in Experimental Section.

1

Dark blue fluorescent colourless soluble solid

Zn(OAc)$_2$, NMP

excess NH$_4$PF$_6$

92 %

4 PF$_6^-$

S1

Dark yellow fluorescent yellow insoluble solid

2

Sky blue fluorescent light yellow soluble solid

Zn(OAc)$_2$, NMP

excess NH$_4$PF$_6$

58 %

4 PF$_6^-$

S2

Light green fluorescent light yellow insoluble solid
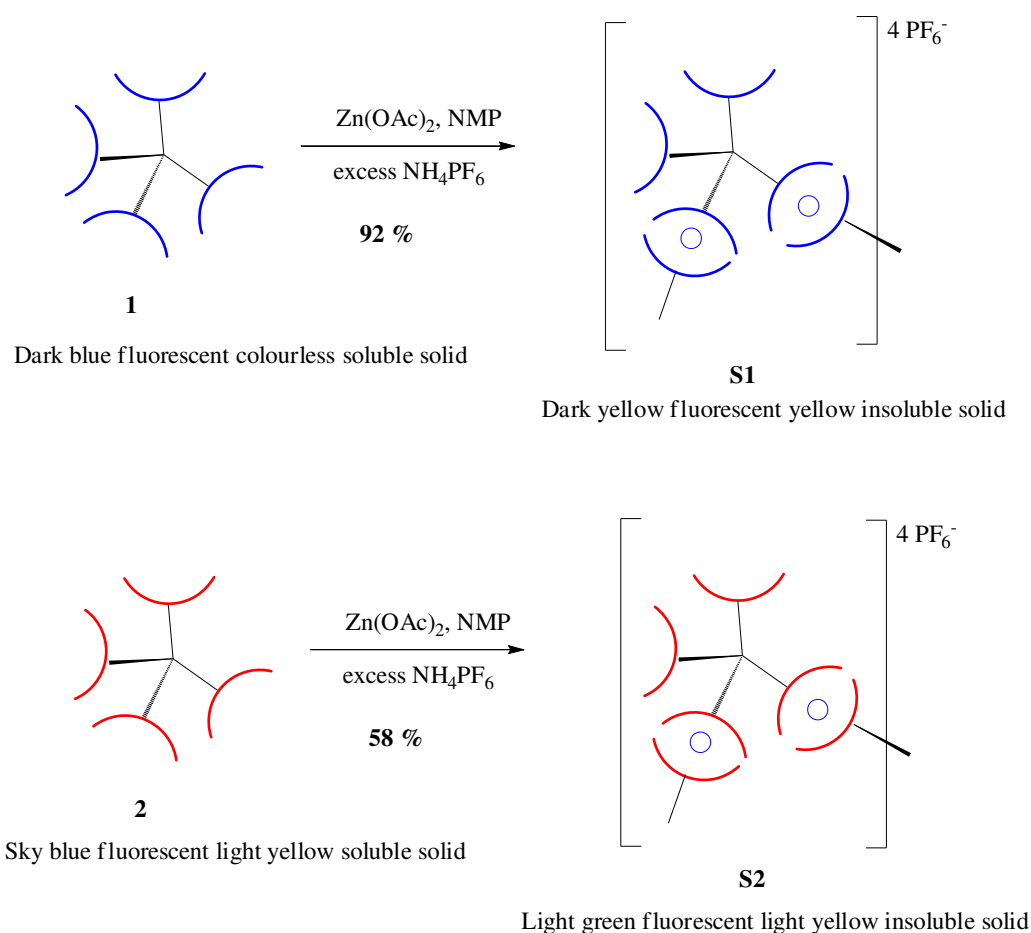
Scheme 5.1: Synthesis of 3D Zn(II)-coordinated self-assembled supramolecular networks **S1–2**

The same insoluble behaviour was found for the 3D extended networks **S3–6**. **S3** (p-type core with p-type linker) and **S4** (p-type core with n-type linker) were obtained by refluxing

3D network **S1** with zinc acetate $Zn(OAc)_2$ at the stoichiometric ratio of 1:2 in NMP solution to break the network, followed by inserting the linear bis(tpy) monomers **26** and **27** in between the 3D molecules, respectively, to form the 3D extended networks **S3–4** after anion exchange using an excess of NH_4PF_6. Using the same method, **S5** (n-type core with p-type linker) and **S6** (n-type core with n-type linker) were obtained by refluxing 3D network **S2** with zinc acetate $Zn(OAc)_2$ at the stoichiometric ratio of 1:2 in NMP solutions to break the network, followed by inserting **26** and **27** in between the 3D molecules, respectively, and form the 3D extended networks **S5–6** after anion exchange using an excess of NH_4PF_6. After forming networks **S3–6**, any residual 3D starting monomers (**1** and **2**) and the linear bis(tpy) monomers (**26** and **27**) are washed away by ether.

By adding more metal ions into the 3D networks **S1–2**, coordination complexes can be dissociated again in favour of an open form with each zinc ion only attached to one tpy unit and its other coordination sites presumably saturated by solvent molecules. The assumption of reversible disassembly followed by re-self-assembly of extended 3D networks **S3–6** was supported by following observations: original 3D networks **S1–2** were not totally soluble in the NMP solution at 105 °C and the colour of solution was light brown at that moment, after adding 2 equivalents of $Zn(OAc)_2$ in NMP, the insoluble solid gradually dissolved in the solution and the colour of solution gradually changed to light yellow before adding the linear bis(tpy) linkers **26** or **27**. All the new 3D Zn(II)–coordinated self-assembled supramolecular networks **S1–6** were obtained in decent yields (> 55%).
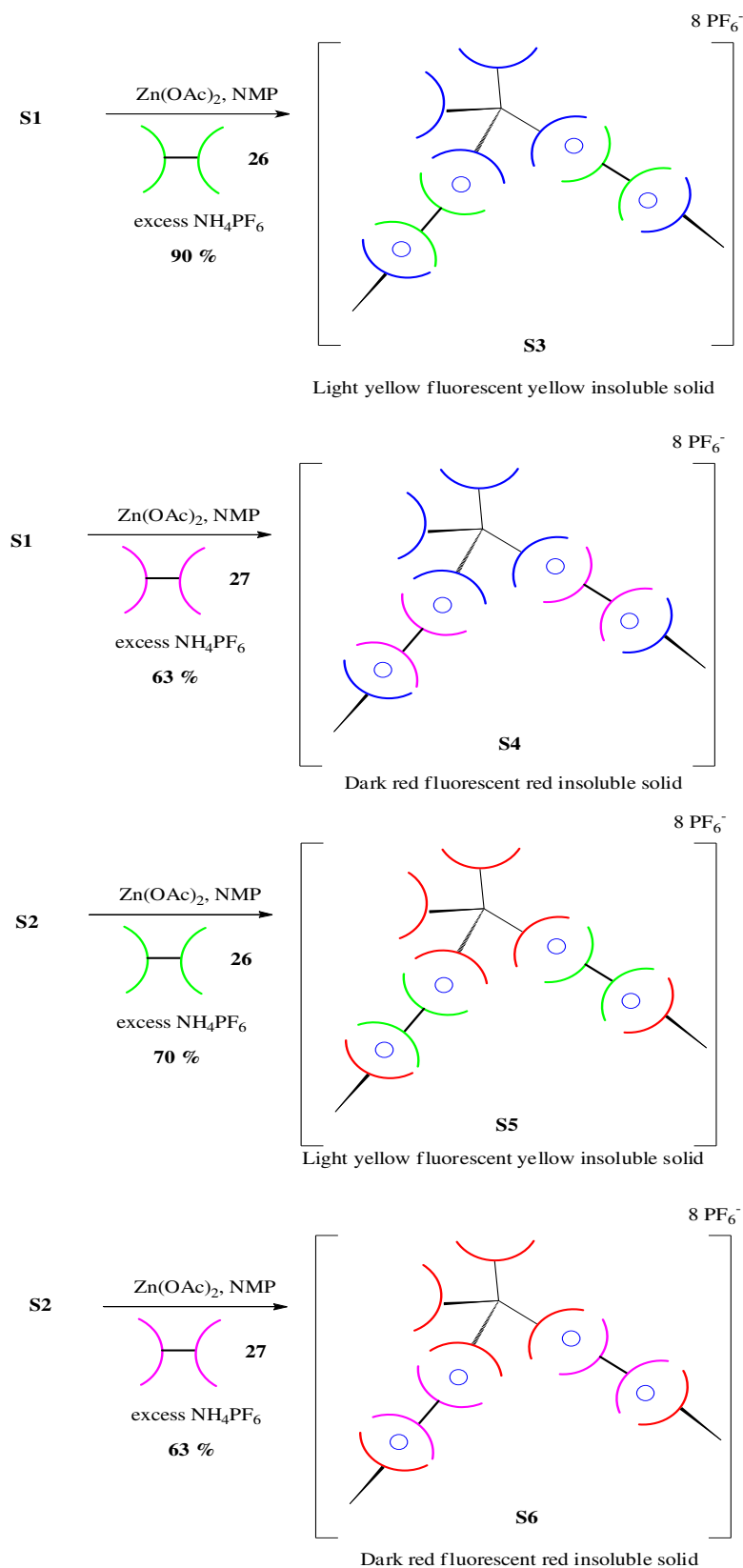
Scheme 5.2: Synthesis of 3D Zn(II)–coordinated self-assembled extended supramolecular networks **S3–6**.

5.3 Characterization of new 3D Zn(II)–coordinated self-assembled networks

5.3.1 Optical properties of 3D Zn(II)–coordinated self-assembled supramolecular networks S1–6

The spectroscopic data (absorption and photoluminescence) of 3D networks **S1–6** in solution are not obtainable as they are not soluble in organic solvent unlike their respective monomers **1–2** and **26–27** which are soluble in common organic solvents and the metallopolymer polymer **P5–7** which are soluble in highly polar aprotic organic solvents. Solid state absorption spectra of **S1–6** are also unobtainable. Images of the appearance and solid state fluorescence under excitation of long wavelength UV light of **S1–6** are shown in Fig. 5.8. Solid state photoluminescence spectra and data of **S1–6** are shown in Fig. 5.9 and summarized in Table 5.1, respectively.

Compared to soluble 3D starting materials **1**–(an off-white glassy solid) and **2**–(a light purple glassy solid), the appearance of the insoluble solids **S1–6** is as follows: **S1** is a yellow solid, **S2** is a light yellow solid, **S3** is a yellow solid, **S4** is a red solid, **S5** is a yellow solid and **S6** is a red solid, as shown in Fig. 5.8a. Comparing the fluorescence of the solids, 3D starting materials **1** and **2** display dark blue and sky blue fluorescence, respectively, whereas, network **S1–2** show red-shifted fluorescence of dark yellow and light green, respectively, as shown in Fig. 5.8b. By putting p-type extended linker **26** and n-type extended linker **27** in between the 3D network **S1** (p-type core), **S3** and **S4** show light yellow and red fluorescence, whereas

compared to 3D network **S2** (n-type core), p-type extended linker **26** and n-type extended linker **27** cause **S5** and **S6** to have fluorescence colours of light yellow and red. Due to lower bandgap of linker **27** in **S4** and **S6**, energy transfer phenomena happened in **S4** and **S6** which the unit predominantly emitting being **27** in **S4** and **S6** which show red fluorescence similar to that **27** in **P6** and **P7**. Therefore, it can be seen that Zn(II)–coordinated 3D networks are reversible allowing disassembly and re-self-assembly process by controlling the ratio of metal ions in the networks and that the optical properties of the networks can be adjusted by inserting different types of linkers into the extended networks.
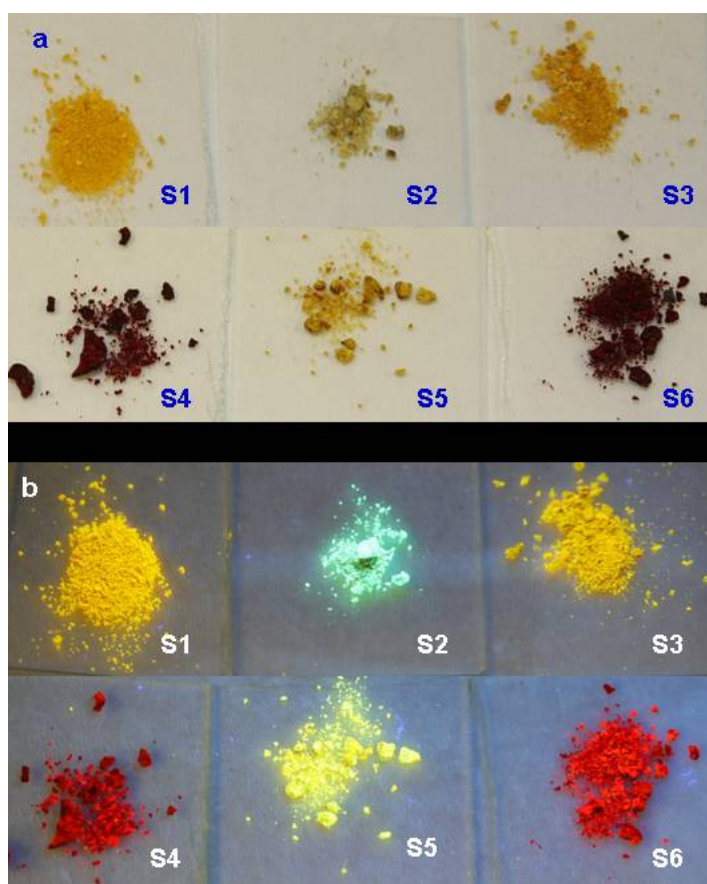
Figure 5.8: (a) Solid appearance and (b) solid fluorescence of 3D networks **S1–6**.

The emission maxima ($\lambda_{em,max}$) (solid state) of **S1** and **S2** are at 522 nm and 479 nm, respectively. Among the extended networks **S3–6**, $\lambda_{em,max}$ of **S4** and **S6** red-shifted more than 100 nm to 625 nm and 644 nm, in comparison to the original unextended networks **S1** and **S2**. This again shows the effect of inserted n-type extended linker **27** which has lower bandgap and acted as sole emissive unit to produce red fluorescence. Whereas the $\lambda_{em,max}$ of **S3** (513 nm) and **S5** (502 nm), which are having the same p-type extended linker **26** are similar to the $\lambda_{em,max}$ (thin film) of **P5** (501 nm) which has the same p-type linker **26**.
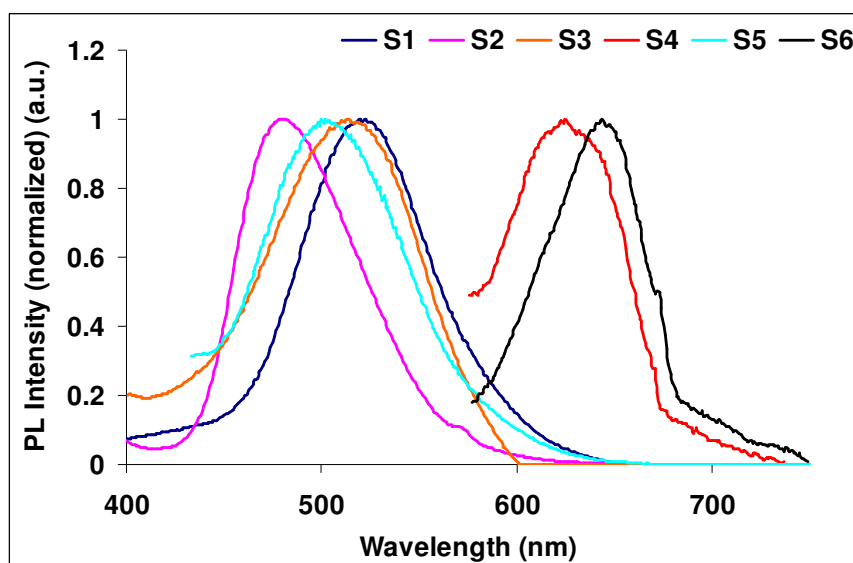
Figure 5.9: Solid state photoluminescence spectra of 3D networks **S1–6**.

Table 5.1: Solid state photoluminescence data of 3D networks **S1–6**.

Molecules	$\lambda_{em,\,max}$ (nm)
S1	522
S2	479
S3	513
S4	625
S5	502
S6	644

5.3.2 Thermal behaviour of 3D Zn(II)–coordinated self-assembled supramolecular networks S1–6

Thermogravimetric analysis (TGA) plots of 3D networks **S1–6** (including 3D conjugated cores **1–2**) are shown in Fig. A62 in Experimental Section. Differential scanning calorimetry (DSC) plots of 3D networks **S1–6** are shown in Fig. A63 in Experimental Section. T_{3d}, T_g and T_m of 3D networks **S1–6** are listed in Table 5.2.

Table 5.2: 3% weight loss temperature (T_{3d}), glass transition temperature (T_g) and melting temperature (T_m) of 3D conjugated cores **1–2** and 3D networks **S1–6**.

Networks	T_{3d} (°C)[a]	T_g (°C)[b]	T_m (°C)[c]
1	242	148	–[d]
2	302	125	–[d]
S1	365	–[d]	–[d]
S2	315	–[d]	–[d]
S3	326	–[d]	–[d]
S4	294	–[d]	–[d]
S5	233	–[d]	–[d]
S6	300	–[d]	–[d]

[a]T_{3d} = 3% weight loss temperature; [b]T_g = glass transition temperature; [c]T_m = melting temperature; [d]relevant data is not found.

According to Table 5.2, 3D metal–coordinated supramolecular networks **S1–6** have similar or slightly higher T_{3d} compared to their respectively 3D starting materials **1–2** (except for **S5**). Besides that, **S1–6** are generally more thermally stable compared **1–2** as more than 40% (except for **S2**) of materials of **S1–6** remain after heating to 900 °C. Thus, Zn(II)– coordination to some degree helps to improve the thermal stability of the Zn(II)–coordinated

networks. Similar to the results for **P5–7**, no phase transitions (T_g and T_m) were observed in the DSC measurements for **S1–6**. Also, 3D Zn(II)–coordinated supramolecular networks **S1–6** are believed not to be crystalline materials as no significant exothermic peaks (T_c) were seen during the heating cycles in their DSC plots.

5.3.3 Crystallographic information of 3D Zn(II)–coordinated self-assembled supramolecular networks S1–6

Crystallographic information of **1–2**, **S1–6** and pure Zn powders are shown in the XRD plots (5° to 120°) in Fig. 5.10. In comparison with the XRD pattern of the pure Zn powders, it is confirmed that amorphous (most likely hyperbranched) network instead of clear crystalline network are believed to be the structures for **1–2** and **S1–6** as there is no significant sharp peak being observed in their XRD patterns. This is in agreement with the DSC results of **1–2** and **S1–6** in which no crystalline temperatures (T_c) could be found. Furthermore their XRD patterns are more or less similar to each other although their intensity (PSD counts) varies which can be due to the varying amounts of solid used for XRD scans. The sharp peaks seen in the pure Zn XRD pattern are not found in the XRD patterns of **S1–6**, indicating the absence of Zn particles and lack of regular crystalline pattern. Thus, in conclusion, XRD scanning from (5° to 120°) is not able to produce useful information to show the variation of XRD patterns by changing the core units (p-type or n-type) as well as extended linker units (p-type or n-type) which are coordinated through the metal ions.
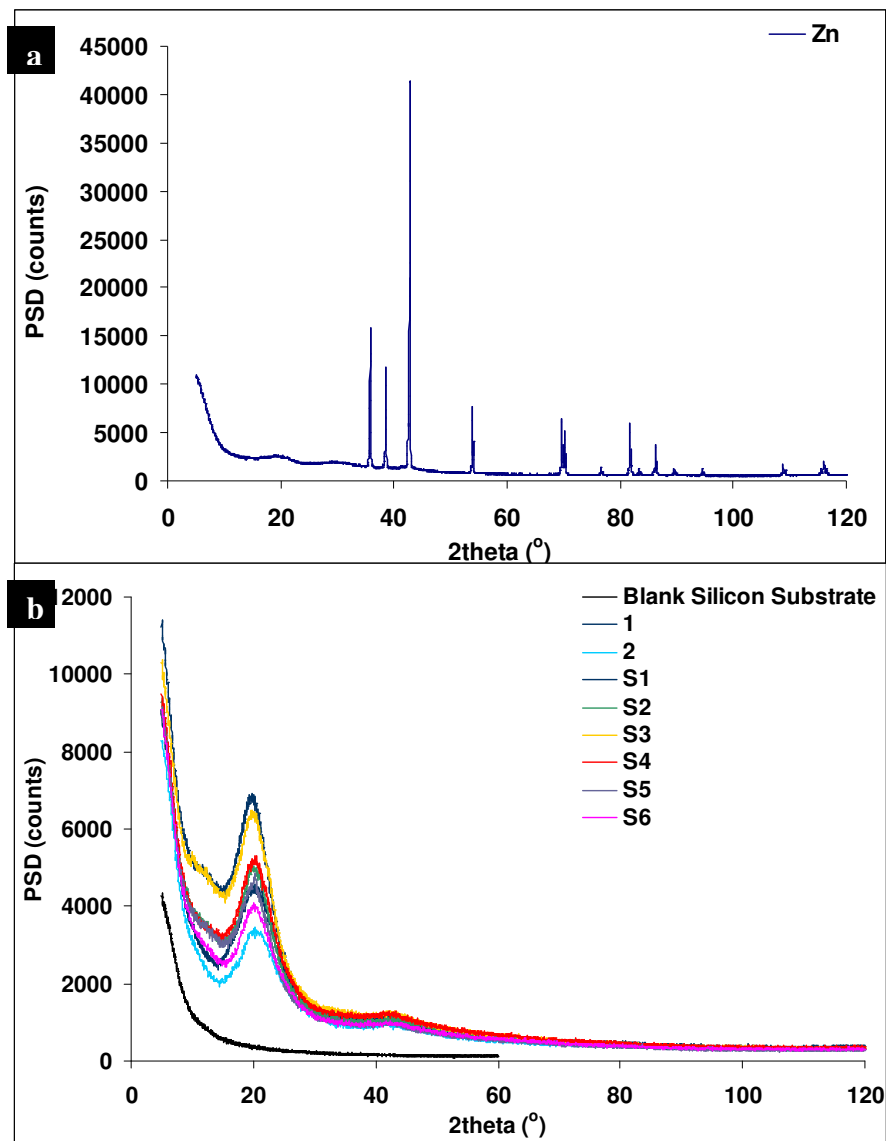
Figure 5.10: XRD plots (5° to 120°) of (a) pure Zn, (b) 3D conjugated cores **1–2** and 3D networks **S1–6**.

5.4   Quenching effect

S1 and **S6** were used, as representative of insoluble solids **S1–6**, to mix with PCBM in

weight ratio of 1:3 in order to see the quenching effect if any on 3D self-assembled networks

by PCBM. **S1** and **S6** were dispersed in DMF separately and added with PCBM. The reaction

mixture was stirred overnight in order to mix the networks **S1** and **S6** with PCBM

homogeneously and effectively. However PL could still be seen by naked eye from the insoluble solids (**S1** and **S6**) when irradiated by the long wavelength UV light (365 nm). Thus, PCBM did not quench the fluorescence of **S1** and **S6**. It is expected the same will be seen for the other networks **S2–5**. The reason for these phenomenon is deduced to be that the PCBM was not able to penetrate into the networks and thus not able to mix with the networks sufficiently to quench the fluorescence of the networks completely. This is consistent with the data for porosity and surface area of these 3D self-assembled networks given in next section.

5.5 Porosity and surface area measurement of the 3D Zn(II)– coordinated self-assembled organic networks

The porosity and the surface area of the 3D Zn(II)–coordinated self-assembled networks **S1– 6** were investigated by sorption analyses using nitrogen. The results are shown in Fig. 5.11 and summarized in Table 5.3.

Table 5.3: Nitrogen sorption analysis of 3D networks **S1–6**.

Networks	S_{BET} [m^{2}g^{-1}][a]	S_{micro} [m^{2}g^{-1}] (t_{plot})[b]	V_{micro} [cm^{3}g^{-1}][b]	Pore Size$_{ad}$[c] (Å)	Pore Size$_{de}$[d] (Å)
S1	0.1963 (0.2365)	2.1218	0.000988	*	*
S2	0.0151 (0.0172)	1.1938	0.000539	*	*
S3	0.9938 (1.2585)	3.5068	0.001546	824.219	382.4371
S4	0.8247 (1.0696)	2.4798	0.00112	59.5412	9.3259
S5	0.6769 (0.8804)	1.8604	0.000852	600.2537	45.473
S6	2.092 (2.8906)	0.9549	0.000387	118.3048	92.0758

[a]Surface area calculated from the N_2 adsorption isotherm using the Brunauer–Emmett–Teller method (the number in parentheses is the Langmuir surface area being calculated); [b]The micropore surface area and micropore volume using t-plot method based on the Halsey thickness equation; [c]Adsorption average pore width (4V/A by BET); [d]Desorption average pore width (4V/A by BET);*relevant data is not found.
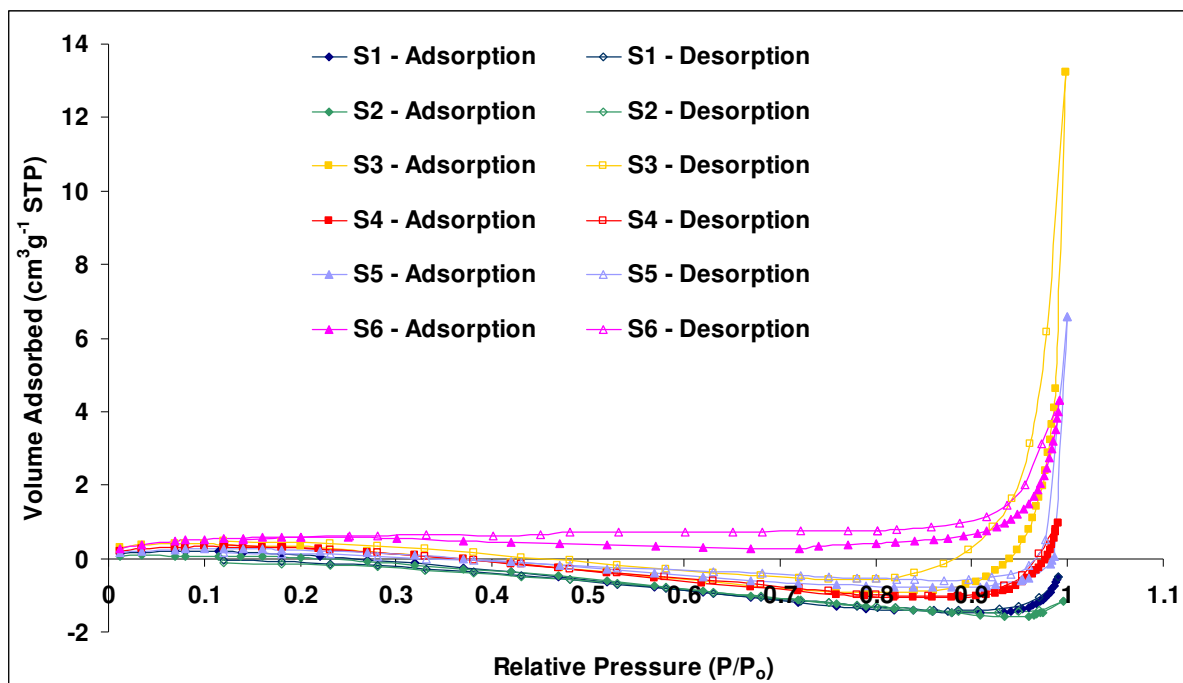
Figure 5.11: Nitrogen adsorption–desorption isotherms of 3D networks **S1–6** measured at 77.3 K (adsorption branch is labeled with filled symbols whereas desorption branch is labeled with empty symbols).

The surface areas of these networks are essentially small (< 2.1 m^2g^{-1}) as compared to the value (> few hundred m^2g^{-1}) obtained from the conjugated bonded organic microporous networks based on tetraphenylmethane by other researchers.[113-116] All the values are well within the experimental error of the equipment. The uptake for some materials at higher pressure (P/P_o > 0.8) will be due to the macro-porosity, inter-particulate pores and surface condensation and not due to the microporosity of the networks. Besides, the negative dip for most of the networks is likely due to small sample size. These materials are thus believed to be highly interpenetrating networks, and hence no order and no porosity was found in these 3D Zn(II)–coordinated self-assembled networks. This again explains why PCBM is not able to penetrate into the networks and thus not able to mix with the networks well enough to

quench the fluorescence of the networks completely. Acknowledgement is given to Dr. Abbie Trewin from University of Liverpool for her comments which assisted in evaluating the porosity and surface area results of networks **S1–6**. Dr. Trewin is currently attempting to develop a model of these materials to understand their non-porosity.

5.6 Incorporation of CdSe nanoparticles and Au nanoparticles (in situ) in the 3D Zn(II)–coordinated self-assembled organic networks forming nanocomposites

5.6.1 Synthesis of 3D self-assembled nanocomposites

The synthetic steps involved in preparation of new 3D Zn(II)–coordinated self-assembled composites **S3 (with CdSe)** and **S4 (with CdSe)** are outlined in Scheme 5.3 and described in details in the Experimental Section. The in situ synthesis of gold nanoparticles in 3D Zn(II)–coordinated self-assembled networks forming composites **S3 (with Au) (1)/(2)** and **S4 (with Au) (1)/(2)** are outlined in Scheme 5.4 and Scheme 5.5, respectively and described in detail in the Experimental Section.

Extra Zn(II) was added into the NMP mixture of **S1** to break the assembly of **S1**. Red CdSe particles (provided by Mr. Lek Jun Yan from the group of Prof. Lam Yeng Ming) which are *ca.* 4 nm in diameter were then added into the reaction mixture. After the CdSe particles were completely dispersed in NMP, **26** and **27** was added into the reaction mixture to close the networks and encapsulate the CdSe particles to form the nanocomposites **S3 (with CdSe)** and **S4 (with CdSe)**, respectively.
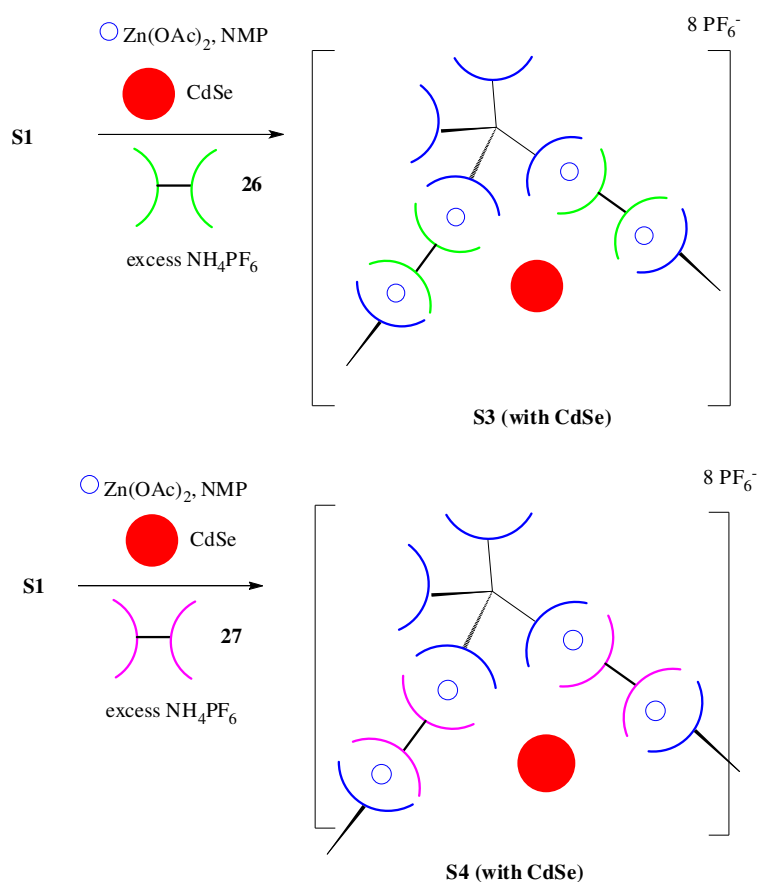
Scheme 5.3: Synthesis of 3D Zn(II)–coordinated self-assembled composites **S3 (with CdSe)** and **S4 (with CdSe)**.

Following the method in the literature,[117] **S3** and **S4** were dispersed in toluene and treated with tetrachloroauric acid (HAuCl$_4$•3H$_2$O) to let the Au^{3+} ions penetrate into the cavity of the networks. The reaction mixture was treated with hydrazine monohydrate to reduce the Au^{3+} ions to form elemental Au particles in situ in the 3D Zn(II)–self-assembled networks to form new composites **S3 (with Au) (1)** and **S4 (with Au) (1)**.

However, insoluble solid was not obtained. It is believed that the hydrazine monohydrate not only reduces the Au^{3+} in the reaction mixture but also binds to the Zn^{2+} ions which link the networks and hence breaks up the networks **S3** and **S4**, giving back the respective monomers, which are soluble in toluene. Thus, the incorporation of the Au nanoparticles (in situ) through this method is not successful. The filtrate of **S3 (with Au) (1)** contains starting materials **1** ($M_w = 3328.75$ g/mol) and **26** ($M_w = 949.23$ g/mol) whereas the filtrate of **S4 (with Au) (1)** contains starting materials **1** ($M_w = 3328.75$ g/mol) and **27** ($M_w = 1283.75$ g/mol), respectively according to the TLC results and MALDI-TOF results (Fig. A64 and Fig. A65).
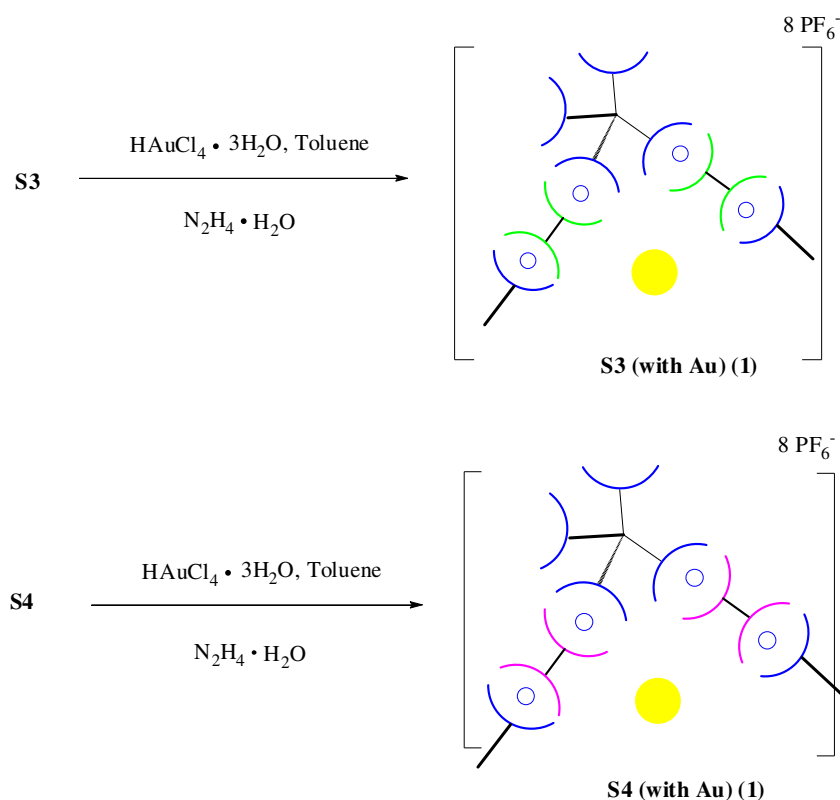
Scheme 5.4: In situ synthesis of gold nanoparticles in 3D Zn(II)–coordinated self-assembled networks forming composites **S3 (with Au) (1)** and **S4 (with Au) (1)**.

Using the method pioneered by Turkevich,[118] sodium citrate dihydrate solution was used to replace the hydrazine monohydrate in order to reduce the Au^{3+} in the boiling reaction mixture. However, it also binds to the Zn^{2+} and hence breaks up the networks **S3** and **S4** in the end, giving back the respective monomers, which are soluble in organic solvents. Thus, the incorporation of the Au nanoparticles (in situ) through this method is also not successful. The filtrate of **S3 (with Au) (2)** contains starting materials **1** (M_w = 3328.75 g/mol) and **26** (M_w = 949.23 g/mol) whereas the filtrate of **S4 (with Au) (2)** contains starting materials **1** (M_w = 3328.75 g/mol) and **27** (M_w = 1283.75 g/mol), respectively according to the TLC results and MALDI-TOF results (Fig. A66 and Fig. A67).
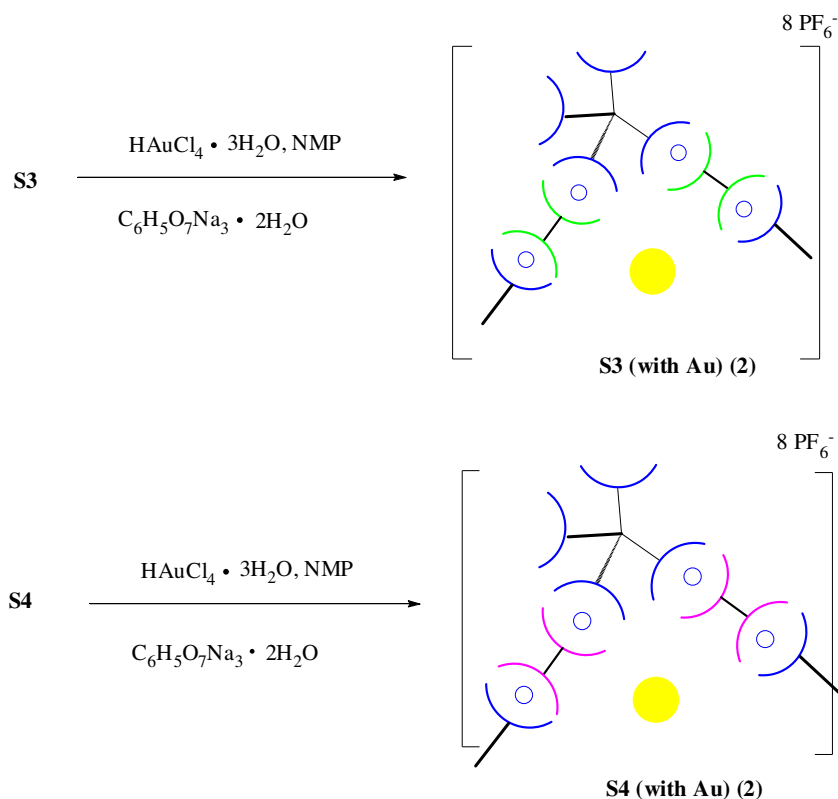
Scheme 5.5: In situ synthesis of gold nanoparticles in 3D Zn(II)–coordinated self-assembled networks forming composites **S3 (with Au) (2)** and **S4 (with Au) (2)**.

The unsuccessful reduction of Au^{3+} by reducing agents mentioned above can be explained by comparing the binding constants (also formation constants) of Zn^{2+}–tpy complexes (log K_1 ~ 5–8)[119,120] and that of zinc citrate (log K_1 ~ 4)[121] and zinc hydrazine (log K_1 ~ 3–4)[122] complexes from literatures. Larger binding constants means that the compound binds less strongly and thus this explains why both reducing agents hydrazine and citrate bind well to the Zn^{2+}, which break up the networks in the end.

5.6.2 Optical properties of 3D self-assembled nanocomposites

The solution and solid state spectroscopic data (absorption and photoluminescence) of 3D Zn(II)–coordinated self-assembled composites **S3 (with CdSe)** and **S4 (with CdSe)** are not obtainable as they are not soluble in organic solvents Images of the appearance and solid state fluorescence under excitation of long wavelength UV light of **S3 (with CdSe)** and **S4 (with CdSe)** are shown in Fig. 5.12.
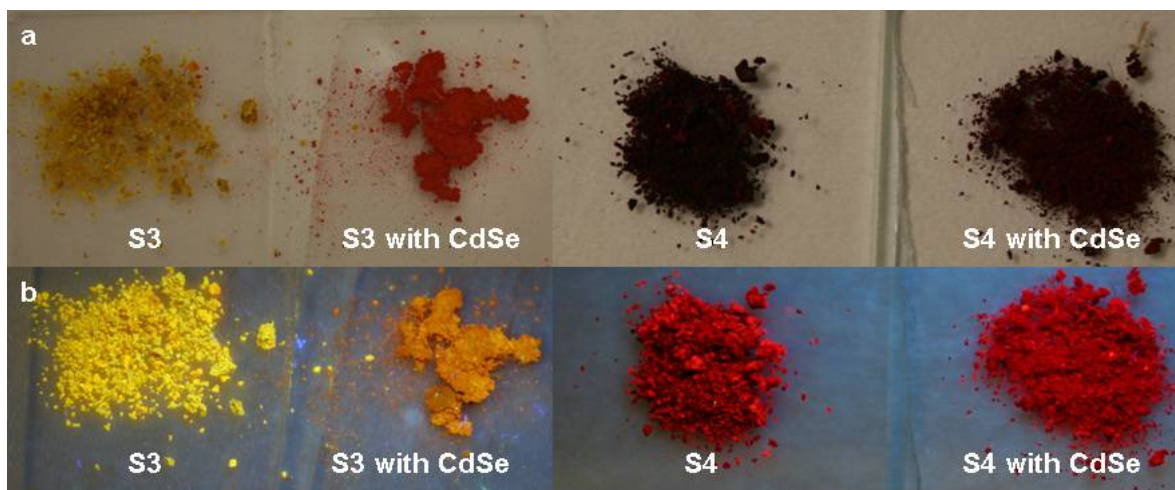
Figure 5.12: (a) Solid appearance and (b) solid fluorescence of **S3**, **S4**, **S3 (with CdSe)** and **S4 (with CdSe)**.

The appearance of the insoluble solids **S3**, **S4**, **S3 (with CdSe)** and **S4 (with CdSe)** is as follow: **S3** is a yellow solid, **S4** is a red solid, **S3 (with CdSe)** is a dark orange solid and **S4 (with CdSe)** is a red solid, as shown in Fig. 5.12a. Comparing the fluorescence of the solids, **S3** displays light yellow fluorescence, **S4** displays red fluorescence, **S3 (with CdSe)** displays red-shifted fluorescence of weak orange compared to that of **S3,** and **S4 (with CdSe)** displays red fluorescence, as shown in Fig. 5.12b. Thus not only the colour of the composite **S3 (with CdSe)** is changed by red CdSe particles to orange compared to yellow **S3**, its fluorescence is also red-shifted compared to that of **S3**. However, the colour (appearance and fluorescence) of the nanocomposite **S4 (with CdSe)** is not affected by CdSe if compared to that of **S4**.

5.6.3   TEM characterization of 3D self-assembled nanocomposites
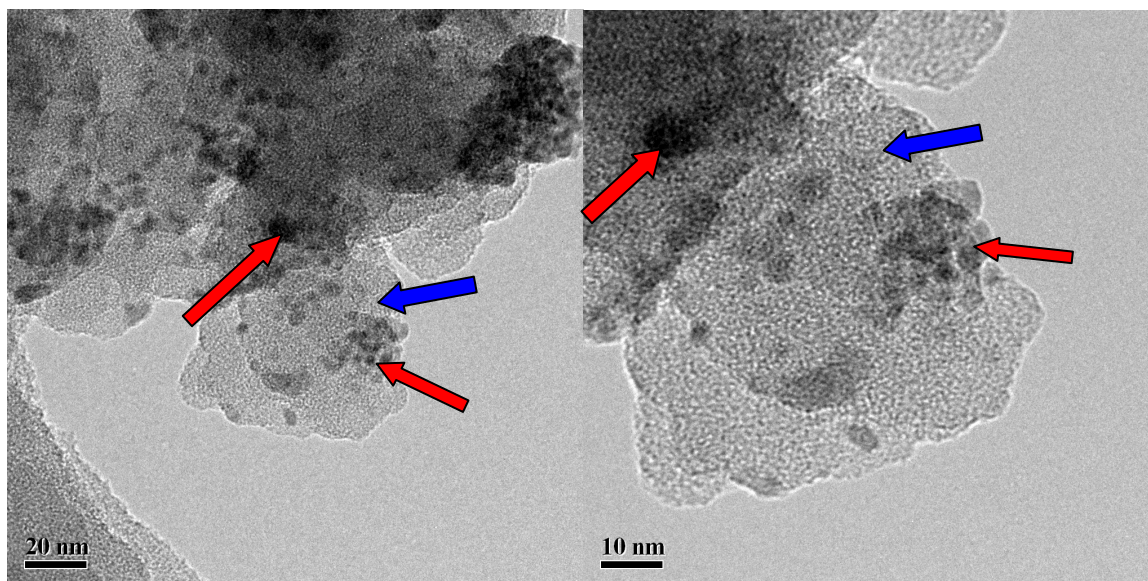
Figure 5.13: TEM images of nanocomposite **S3 (with CdSe)**. Inorganic nanoparticles CdSe observed as black dots (red arrows); organic parts (blue arrows).
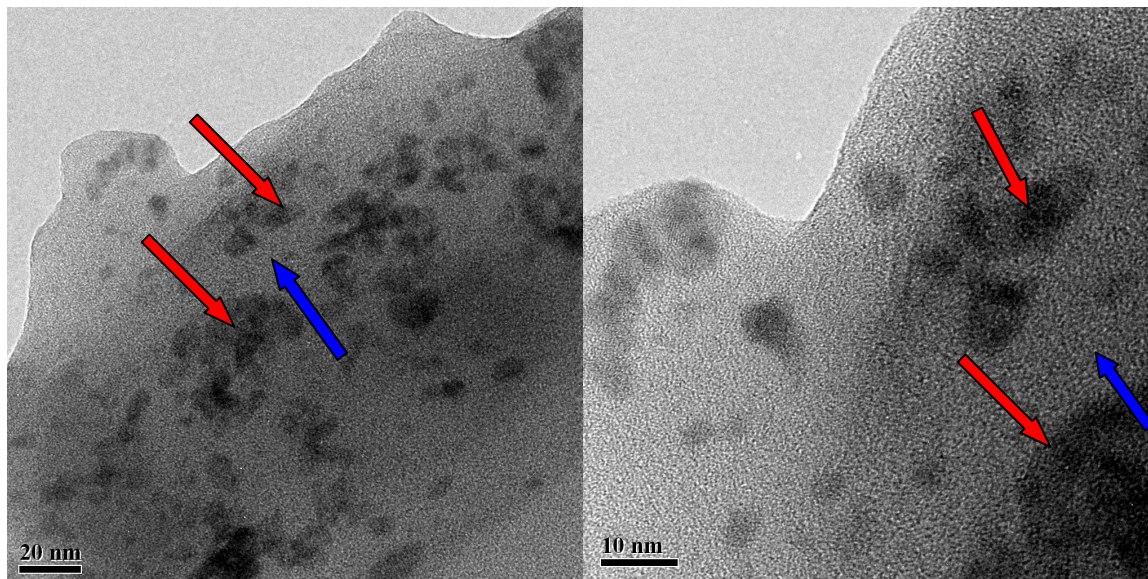
Figure 5.14: TEM images of nanocomposite **S4 (with CdSe)**. Inorganic nanoparticles CdSe observed as black dots (red arrows); organic parts (blue arrows).

TEM characterization of the nanocomposites **S3 (with CdSe)** and **S4 (with CdSe)** was performed by Mr. Lek Jun Yan from the group of Prof. Lam Yeng Ming. The TEM images of nanocomposites **S3 (with CdSe)** and **S4 (with CdSe)** are shown in Fig. 5.13 and Fig. 5.14, respectively.

Clear black dots (red arrows) were observed in the TEM images and they are believed to be the CdSe nanoparticles being surrounded by the organic parts (blue arrows) which are shallower in colour in the TEM images. The size of CdSe nanoparticles is estimated to be *ca.* 4 nm in diameter according to the TEM images. The CdSe nanoparticles are not evenly distributed in the organic networks and some of them aggregate among themselves. From the TEM images, it is difficult to tell whether the CdSe nanoparticles are fully trapped inside the networks, due to the limitation of 2D images as projections of 3D object. But it is clear that the nanocomposites are successfully synthesized as both organic and inorganic parts are

clearly seen in the TEM images and the nanoparticles are at least attached to or partially encapsulated by the organic networks. These preliminary results show the possibility of the 3D metal–coordinated self-assembled networks accommodating nanoparticles or even other materials within them.

5.6.4 XRD characterization of 3D self-assembled nanocomposites

Crystallographic information of 3D networks **S3–4** (extracted from Fig. 5.10), 3D nanocomposites **S3 (with CdSe)** and **S4 (with CdSe)** and pure CdSe are shown in the XRD plots (5° to 120°) in Fig. 5.15.

The XRD pattern of pure CdSe (bottom in Fig. 5.15) was obtained from Joint Committee on Powder Diffraction Standards (JCPDS) Data File No. 00-019-0191 in 2011 International Centre for Diffraction Data. The peaks (red dotted circles at *ca.* 25°, 42° and 50°) in the XRD pattern of **S3 (with CdSe)** and **S4 (with CdSe)** match perfectly with the XRD pattern of pure CdSe. Thus CdSe was proved to exist in the nanocomposites **S3 (with CdSe)** and **S4 (with CdSe)**. Lower intensity of CdSe peaks in nanocomposite **S4 (with CdSe)** comparing to nanocomposite **S3 (with CdSe)** is believed to be because the amount of CdSe included in **S4 (with CdSe)** (especially on the surface of the solid) is less. The peak (sky blue dotted circle at *ca.* 20°) for organic networks **S3** and **S4** alone is barely observed in the XRD pattern of **S3 (with CdSe)** and **S4 (with CdSe)** (very low intensity) and this is believed to be due to the CdSe nanoparticles disrupting the networks, causing the nanocomposites **S3 (with CdSe)** and **S4 (with CdSe)** to be more amorphous compared to pure organic networks **S3** and **S4**.

Therefore, the intensity from the organic network in nanocomposites **S3 (with CdSe)** and **S4**

(with CdSe) is too low to be observed.
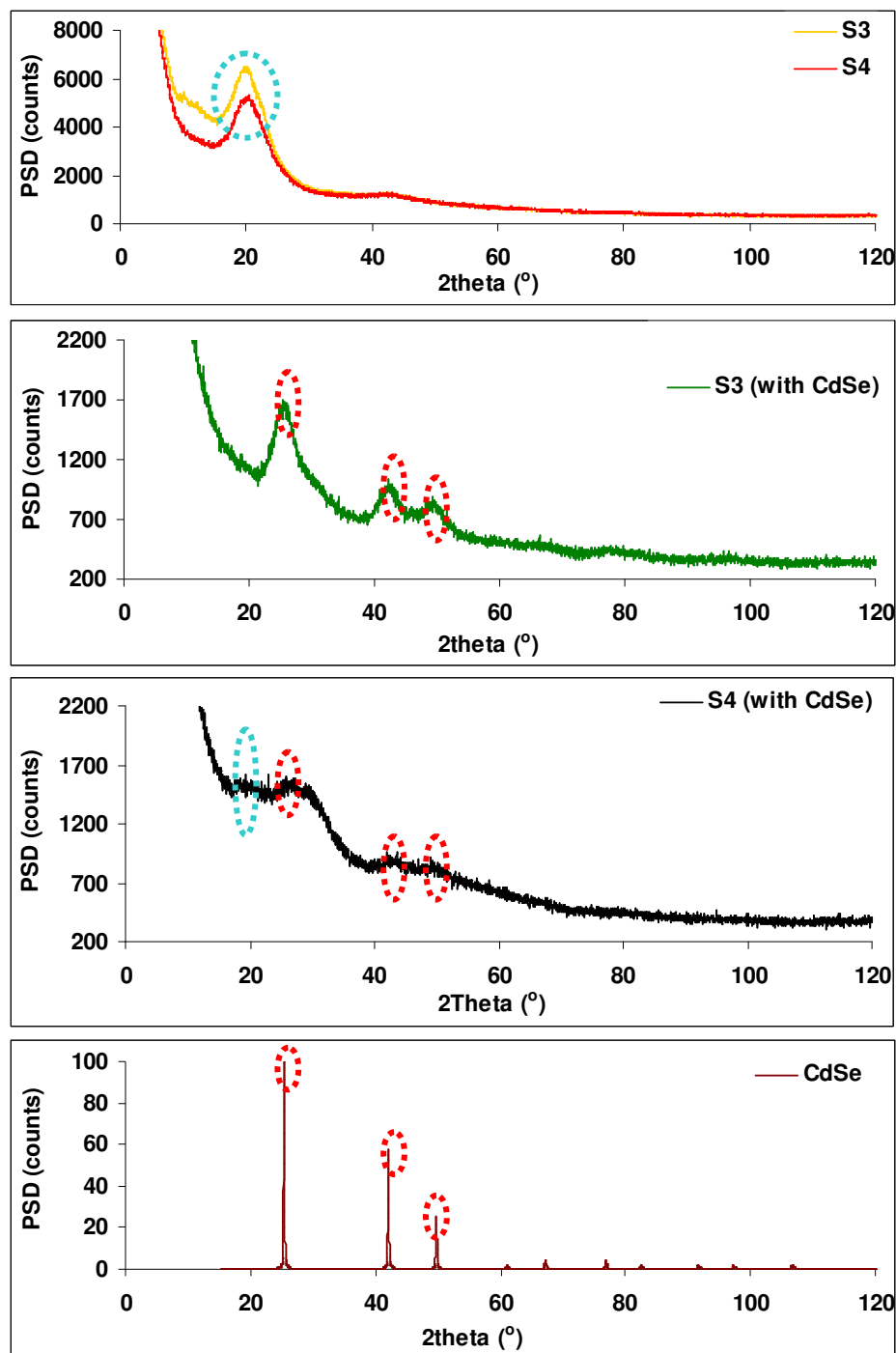
Figure 5.15: XRD plots (5° to 120°) of 3D networks **S3–4** (top), 3D nanocomposites **S3 (with CdSe)** and **S4 (with CdSe)** (middle), pure CdSe (bottom)

5.7   Conclusion

In summary, several insoluble 3D Zn(II)–coordinated self-assembled supramolecular networks (including the extended networks) **S1–6** were successfully synthesized from the tetrahedral core molecules (n-type and p-type) described in Chapter 2. Although no useful crystallographic information could be obtained in order to differentiate them, they show reversible disassembly in which the original formed coordination complexes can be dissociated again by adding extra metal ions followed by re-self-assembly with different potential p-type or n-type linkers being inserted to expand the networks. This is important as by modifying the assembly procedure in metal–ligands coordination, not only could the size and morphology of the networks be modified, but their properties (e.g. optical) could also be varied. This can be seen from the energy transfer phenomena seen in **S4** and **S6** which emit red fluorescent from the lower bandgap n-linker inserted compared to the their respective analogues **S3** and **S5** with a p-type linker inserted. Thus, this new research topic (self-assembly) can have a lot of different opportunities and possibilities to be considered in order to develop various useful organic networks that can be studied and applied in organic electronics as in general, they are found to be more thermal stable compared to uncomplexed species especially at very high temperature due to the effect of metal–coordination bonding. Furthermore, the key idea is hopefully through the metal–coordinated self-assembly we can prepare ordered (3D) arrays of chromophores which to data have not been reported. However in the end through the XRD and BET studies, no order and no porosity were found in these amorphous (highly interpenetrating) networks **S1–6**.

Due to the 2D viewing limitation of the current techniques (especially TEM), it is difficult to tell whether the CdSe nanoparticles are being fully encapsulated inside the networks. But it is clear that the incorporation of nanoparticles CdSe in the 3D Zn(II)–coordinated self-assembled networks **S3** and **S4** is considered successful according to TEM and XRD results. Both organic and inorganic parts are clearly seen in the TEM images and at least the nanoparticles are being attached (or partially encapsulated) by the organic networks. Thus, the nanocomposites are successfully synthesized. The in situ growing of Au nanoparticles using the 3D Zn(II)–coordinated self-assembled networks as a nanoreactor's templates was not successful due to the binding of the Zn(II) ions to the reducing agents which were used to reduce Au^{3+}. However, by choosing the correct reaction condition, these Zn(II)–coordinated self-assembled networks have potential to be used as a template for different application such as host-guest chemistry catalysis,[123,124] supramolecular catalysis[125,126] etc.

These preliminary results show the possibility of the 3D metal–coordinated self-assembled networks accommodating nanoparticles or even other materials within them. In order to analyze how well the incorporation of nanoparticles (e.g. CdSe) in these networks, advanced 3D characterization methods can be used to visualize the tomography of these nanocomposites in three dimensions since TEM "only" provide a 2D projection of a 3D object. Possible candidates of these techniques could be Annular Dark-Field Transmission Electron Microscopy (ADF-TEM) tomography,[127] High-Angle Annular Dark-Field Scanning Transmission Electron Microscopy (HAADF-STEM) tomography or Energy-Filtered Transmission Electron Microscopy (EFTEM) tomography.[128] However, these techniques are not available currently in the School of Materials Science and Engineering. Thus,

collaboration with other researchers who have these equipments or techniques in the future is

needed to study these nanocomposites.

Chapter 6 Synthesis of new 2-components 3D self-assembled adamantane cages and new 3D expanded conjugated cores for supramolecules

6.1 Synthesis of new p-type & n-type cores for 2-components 3D self-assembled adamantane cages

6.1.1 Synthesis of core monomers

The synthetic steps involved in preparation of core monomers **30** and **32** are outlined in Scheme 6.1. Details of synthetic procedures for synthesis of **30** and **32** (including the synthesis of their subunits **29** and **31**, respectively) according to Scheme 6.1 and the characterization data (including ^{1}H NMR, ^{13}C NMR, MALDI-TOF mass spectra, Elemental Analysis and HRMS) are described in detail in the Experimental Section.
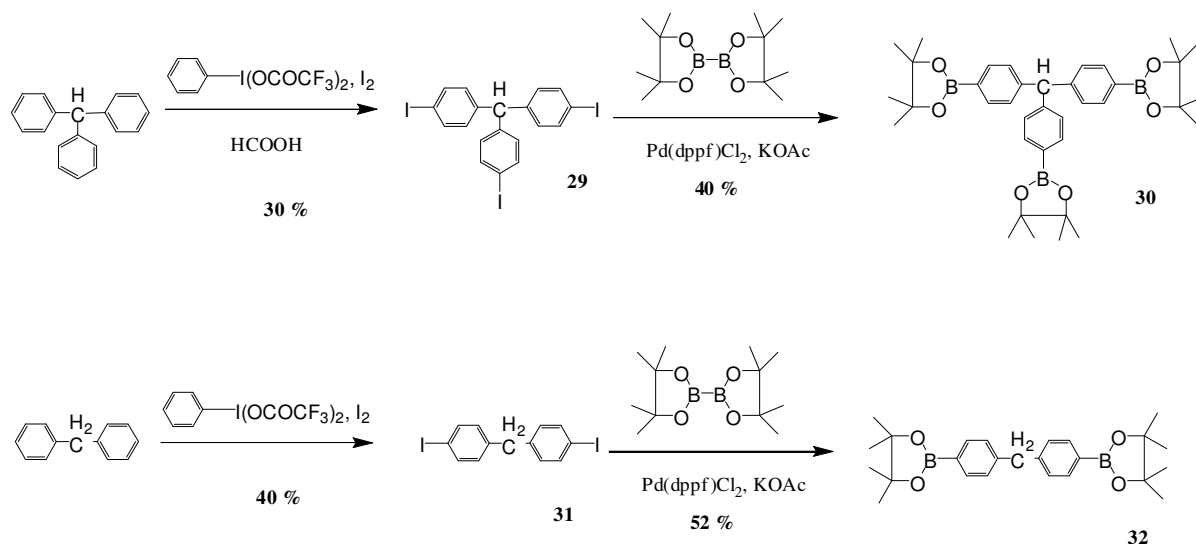
Scheme 6.1: Synthesis of core monomers **30** and **32**.

The para positions of triphenylmethane were iodinated using the reagents [bis(trifluoroacetoxy)iodo]benzene and iodine to form a mixture of tris(4-iodophenyl)methanol as the major product and tris(4-iodophenyl)methane **29** as the minor product. The crude mixture was refluxed in formic acid in order to convert OH group to H group [129]. Impure **29** was obtained as a light yellow solid which include **29** as the major product with minor impurity of tris(4-iodophenyl)methanol. **29** was reacted with bis(pinacolato)diboron through the palladium-catalyzed Miyaura cross coupling to form tris(4-(4,4,5,5-tetramethyl-1,3,2-dioxaborolan-2-yl)phenyl)methane **30**. Diphenylmethane was iodinated to form bis(4-iodophenyl)methane **31** which was then become bis(4-(4,4,5,5-tetramethyl-1,3,2-dioxaborolan-2-yl)phenyl)methane **32**.

6.1.2 Synthesis of p-type & n-type cores for 2-components 3D self-assembled adamantane cages

The synthetic steps involved in preparation of n-type and p-type cores **33–36** for 2-components 3D self-assembled adamantane cages are outlined in Scheme 6.2. Due to time limitation, the synthesis of the p-type and n-type cores will be studied and continued by future students. **30** and **32** will react with either **13** or **14** through Suzuki coupling under the aid of Pd (0) to form new n-type and p-type cores **33–36** for 2-components 3D self-assembled adamantane cages.
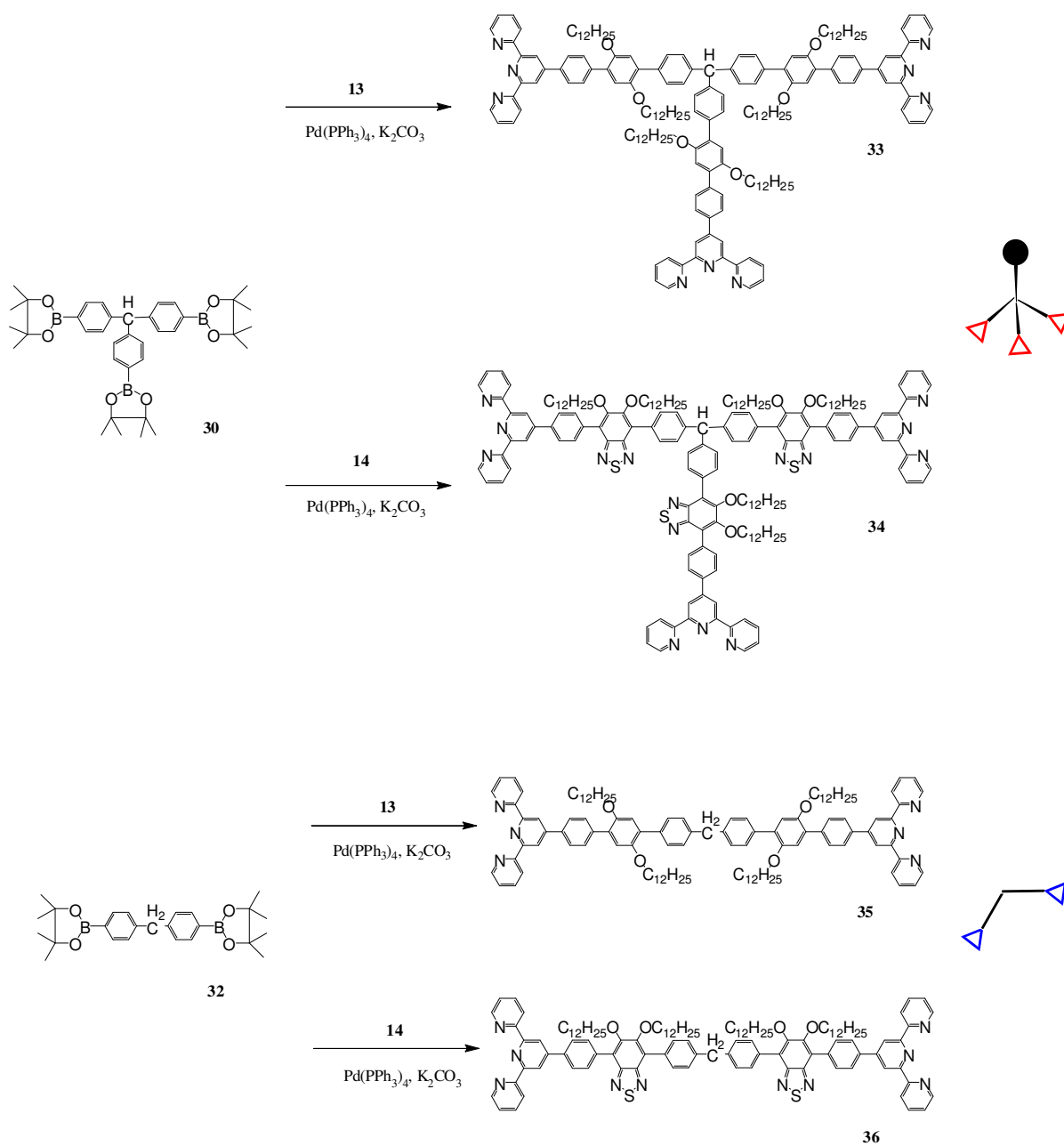
Scheme 6.2: Synthesis of n-type (**33** and **35**) and p-type (**34** and **36**) cores.

6.1.3   Self-assembly of 2-components 3D self-assembled adamantane cages
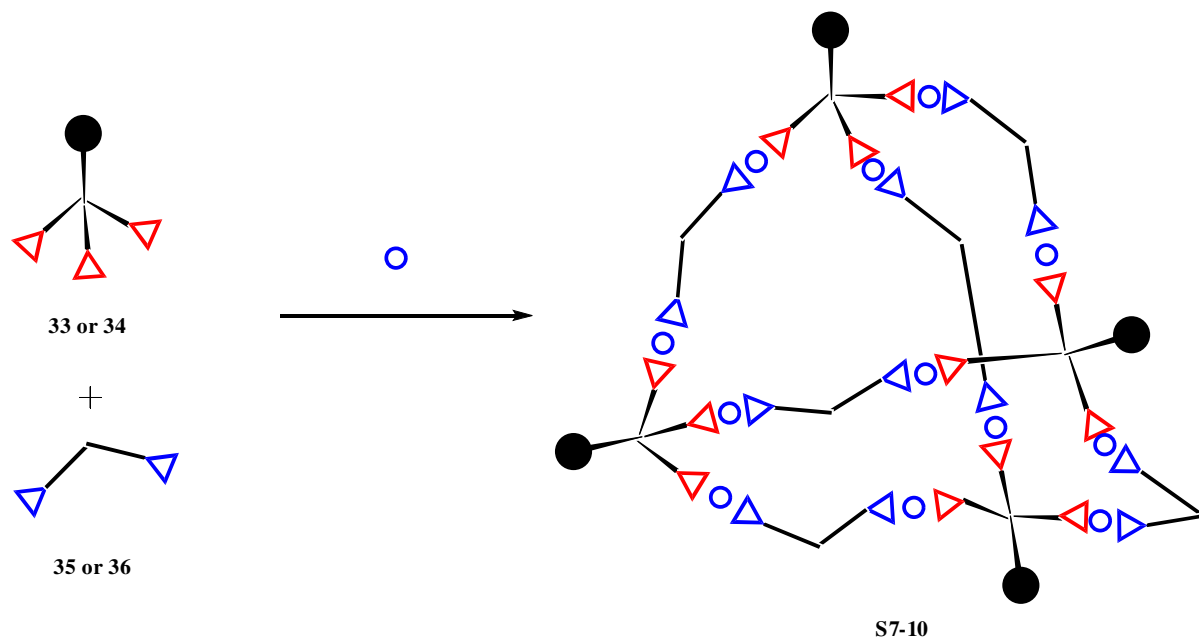
Scheme 6.3: Self-assembly of 2-components 3D adamantane cages.

With the presence of **33–36**, they can have different combinations (**33** with **35**, **33** with **36**, **34** with **35** and **34** with **36**) in the self-assembly using metal–coordination forming **S1–6** as shown in Chapter 5 to form **S7–10** as shown in Scheme 6.3. These 3D self-assembled adamantane cages will also be further investigated for their structure, properties and the possibility of accommodating nanoparticles or even other materials within them. Due to time limitation, these studies will be continued by future students.

6.2   Synthesis of new 3D expanded conjugated core for supramolecules

In order to try to increase the porosity of our networks **S1–6** described in Chapter 5, the synthesis of one of the new conjugated cores expanded as compared to cores **1–2** mentioned in Chapter 2 by ethynyl linkers was attempted to be synthesized. Ethynes are very versatile

functional groups for connecting building blocks because they possess rigid-rod geometry[130]

and can expand the cores into larger structures while retaining π-conjugation.

6.2.1 Synthesis of terpyridyl and p-type linker monomers

The synthetic steps involved in preparation of terpyridyl and p-type linker monomers **38** and

40 are outlined in Scheme 6.4. Details of synthetic procedures for synthesis of **38** and **40**

(including the synthesis of intermediates **37** and **39**, respectively) according to Scheme 6.4

and the characterization data (including ^{1}H NMR, ^{13}C NMR, MALDI-TOF mass spectra,

Elemental Analysis and HRMS) are described in detail in the Experimental Section.
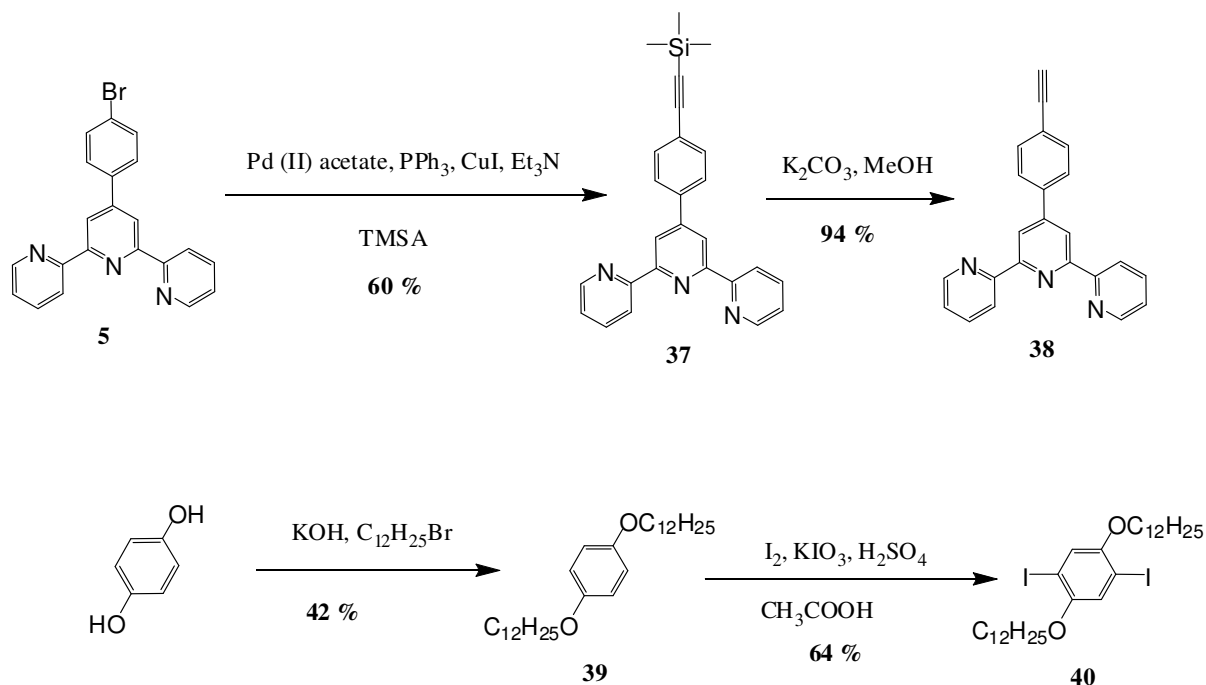
Scheme 6.4: Synthesis of terpyridyl monomer **38** and p-type linker **40**.

5 was Sonogashira coupled with trimethylsilylacetylene (TMSA) with the aid of co-catalysts (Pd(II) complex and Cu(I) salt) in a basic reaction medium to form 4'-[4-(trimethylsilylethynyl)phenyl]-2,2':6',2''-terpyridine **37** as a brown solid. By using K_2CO_3 as base and MeOH as alcoholic aqueous co-solvent, **37** was then base-catalyzed deprotected to form 4'-(4 -ethynylphenyl) -2,2':6',2''-terpyridine **38** as a white solid.

Hydroquinone was dialkylated to form 1,4-bis(dodecyloxy)benzene **39** as an off-white solid. **39** was then iodinated using iodine in acetic acid environment to form 1,4-bis(dodecyloxy)-2,5-diiodobenzene **40** as a white solid.

6.2.2   Synthesis of asymmetric p-type monomer

The synthetic steps involved in preparation of asymmetric p-type monomer **43** are outlined in Scheme 6.5. Details of synthetic procedures for synthesis of **43** (including the synthesis of its intermediates **41** and **42**, respectively) according to Scheme 6.5 and the characterization data (including ^{1}H NMR, ^{13}C NMR, MALDI-TOF mass spectra, Elemental Analysis and HRMS) are described in detail in the Experimental Section.

1 equivalent of **40** was Sonogashira coupled with 1 equivalent of **38** to form **41** as a light yellow solid. **41** was then coupled with TMSA in a Sonogashira coupling to form **42** as a white solid, which was deprotected to form **43**, the asymmetric p-type monomer as a white solid.
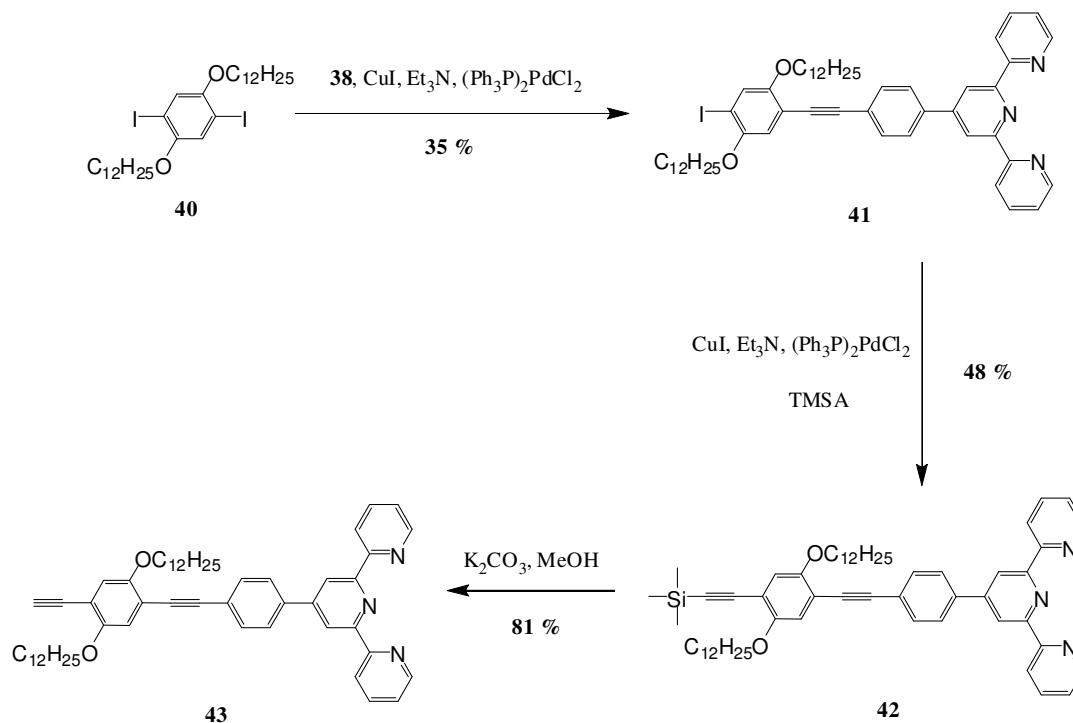
Scheme 6.5: Synthesis of asymmetric p-type monomer **43**.

6.2.3 Synthesis of new 3D expanded conjugated p-type core

The synthetic step involved in preparation new 3D expanded conjugated p-type core **44** is outlined in Scheme 6.6. Details of synthetic procedures for synthesis of **44** according to Scheme 6.6 are described in the Experimental Section.

4 equivalents of **43** were Sonogashira coupled with 1 equivalent of **3**, intended to form the new 3D expanded conjugated p-type core **44** for supramolecules. However, based on MALDI-TOF mass spectra of the reaction mixture, incomplete addition was found in the reaction mixture, i.e. only monoadduct (M_w = 1497.35 g/mol) and diadduct (M_w = 2170.97 g/mol) were found. Due to lack of the material (especially **43**) and time limitation, the remaining studies will be continued by future students.

43

3 | CuI, Et₃N, (Ph₃P)₂PdCl₂

44
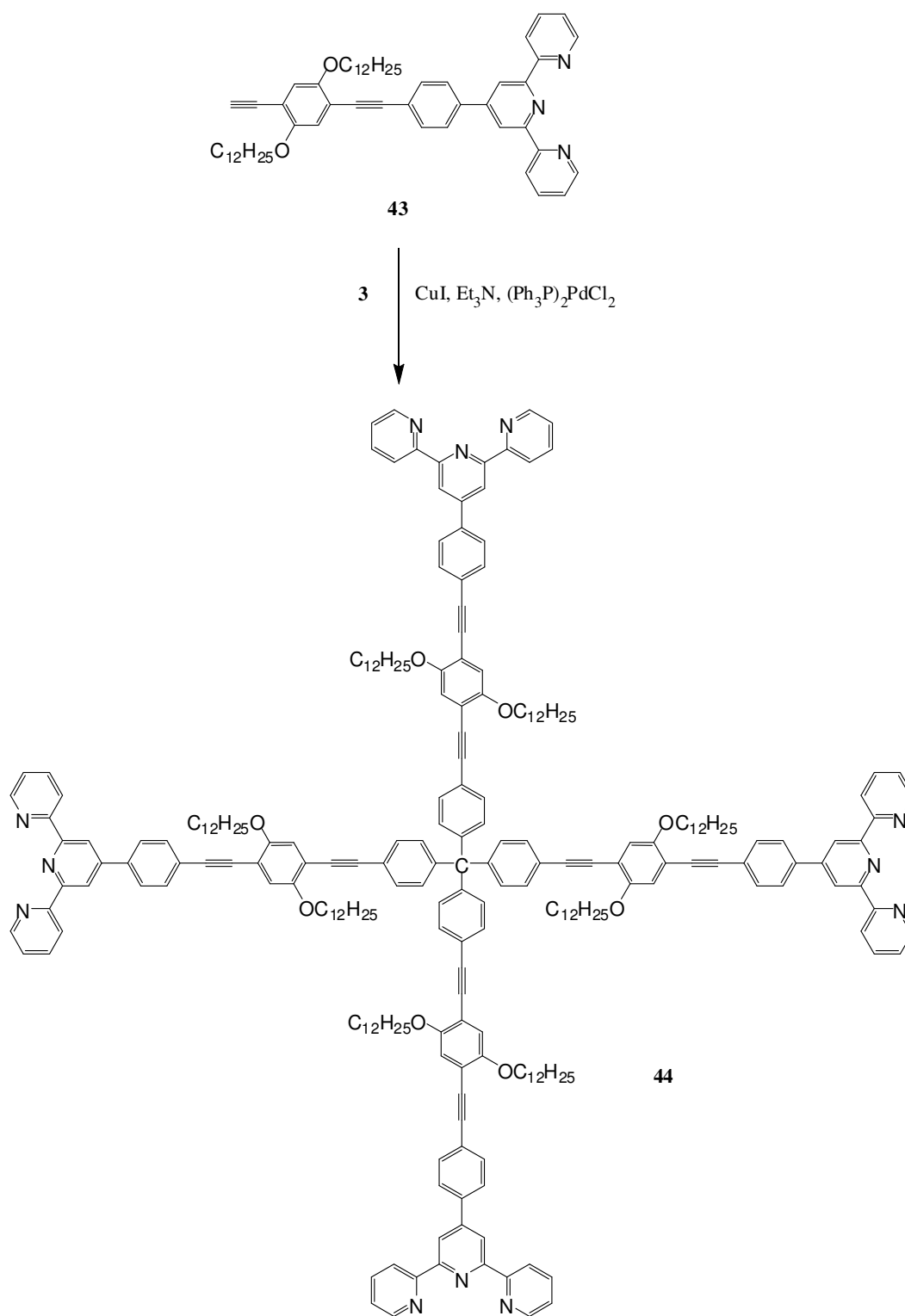
Scheme 6.6: Synthesis of new 3D expanded conjugated p-type core **44** for supramolecules.

Alternatively method is shown in Scheme 6.7 which might help to reduce the time for

preparation (especially the purification time) of the final p-type core **44**. **3** was coupled with

TMSA based on Sonogashira coupling to form **45** which can be deprotected to form **46**. **46**

can thus be Sonogashira coupled with more than 4 equivalents of **41** to form new 3D

expanded conjugated p-type core **44**.
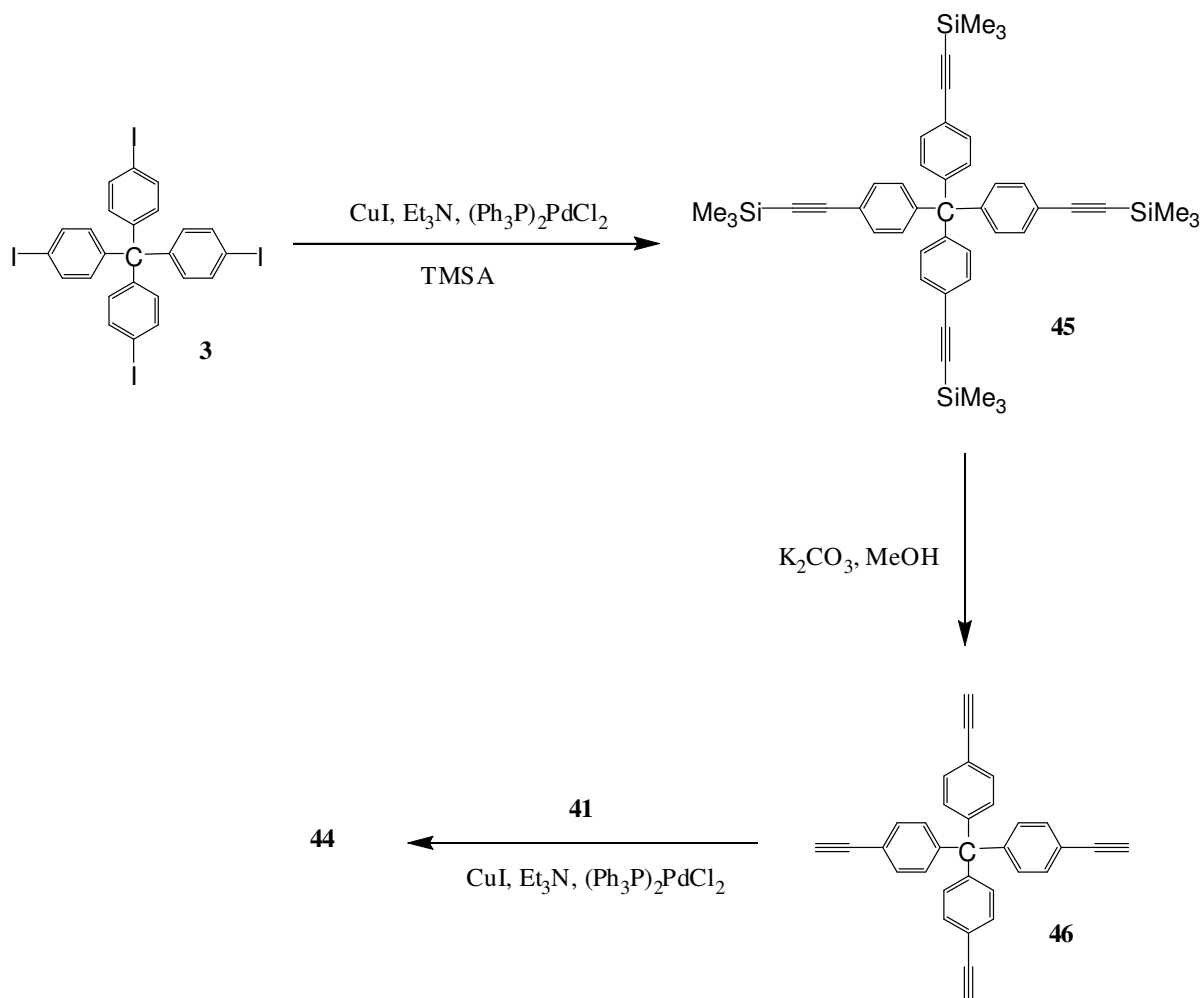
Scheme 6.7: Alternative method to prepare new 3D expanded conjugated p-type core **44**.

Once the **44** is successfully synthesized, similar reaction paths can be used to prepare the new

3D expanded conjugated n-type core (similar to **13**) in which the n-type linker can be the

dialkoxybenzothiadiazole. These new 3D expanded cores can also be used for metal–coordination self-assembly to form new networks and nanocomposites similar to what had been done for **S1–6**. These studies will be continued by future students.

Chapter 7   Conclusion and future works

7.1   Conclusion

Different p-type or n-type groups of organic molecules, that display potential for active roles in electronic devices, were synthesized and investigated in this project. Synthesis and characterization of two new cores for 3D organic supramolecules (p-type **1** and n-type **2**) were discussed in Chapter 2. These tetrahedral symmetric molecules, with long solubilizing groups, are soluble in common solvents. They display blue emission in solution or solid state. We anticipate that processability problem will be encountered after **1** and **2** were self-assembled through Zn(II) ions to form new 3D supramolecular networks. Thus several 1D linear supramolecular metallopolymers were formed by Zn(II)–coordinating π-conjugated bis(2,2':6',2''-terpyridine) molecules which the 4'-positions are linked to different p-type or n-type spacer units (similar to the p-type or n-type spacer units in the cores in Chapter 2). These 1D linear metallopolymers were processable according to the literature precedents and thus could be used as models to compare and study the assembly and properties of the 3D self-assembled networks synthesized subsequently.

The n-type linker units, dialkoxybenzothiadiazole which were used in the cores (n-type) described in Chapter 2, was proven to be a good electron acceptor by combining it with different types of thiophene-based monomers (donors, D) under Stille cross-coupling reaction to form new D–A covalently linked π-conjugated organic copolymers **P1–4** as shown in Chapter 3. **P1–4** have decent low optical bandgaps which confirm that

dialkoxybenzothiadiazole is a good n-type unit. **P1–4** are all purple solids and display red emission in solution and the solid state. One of these copolymers **P4** was then mixed with PCBM to test its performance in OPV devices as it and PCBM mix well to form evenly distributed films. Such smooth and uniform film morphology is desirable for obtaining good performance in photovoltaic devices as the performance of blends in such devices is severely adversely affected by large-scale phase separation. Efficiency (PCE) of over 1% has been obtained from a photovoltaic device using **P4** combined with PCBM and this suggests that with further optimization these materials have considerable promise as active components in organic solar cell. These materials might be also tested in other area of organic electronic devices such as OLEDs given their strong luminescence.

Several linear supramolecular metallopolymers **P5–7** were then formed as shown in Chapter 4. These linear metallopolymers include p-type (**P5**) and n-type linear metallopolymers (**P6**), and also the metallo-*alt*-copolymer in which n-type and p-type molecules co-exist in the alternating copolymer (**P7**). The electro-optical properties of the monomers as well as of the metallo-homopolymers are strongly influenced by the nature of the attached π-conjugated spacer units (p-type or n-type). Furthermore, **P7**, as a metallo-*alt*-copolymer, featured an energy transfer from the donor to the acceptor unit (benzothiadiazole unit) and this acceptor unit is in charge of the emitting role in the metallo-*alt*-copolymer due to its lower bandgap. These new groups of metallopolymers **P5–7** have good potential to be used in opto-electronic applications such as OPV or PLED devices. The energy transfer phenomena in **P7** are being further investigated by the research group of Prof. Tan Howe-Siang.

1 and **2** were then self-assembled in Chapter 5 through Zn(II)–coordination to form new 3D supramolecular networks **S1** and **S2**. These metal–coordinated networks can be disassembled by adding more metal ions and re-self-assembled to form extended 3D networks **S3–6** after inserting linear bis(tpy) linkers (p-type **26** or n-type **27**). Energy transfer phenomena were observed in **S4** and **S6** which the benzothiadiazole linker unit (n-type) is in charge of the emitting role in the whole networks due to its lower bandgap. **S1–6** are amorphous (most likely hyperbranched) network instead of clear crystalline network according to their XRD patterns. They are also examined to have no order and no porosity according to the BET results and hence are amorphous materials from highly interpenetrating networks. PCBM is thus not able to penetrate into the networks and thus not able to mix with the networks well to quench the fluorescence of the networks completely.

The incorporation of CdSe nanoparticles in the 3D Zn(II)–coordinated self-assembled networks **S3** and **S4** is considered successful according to TEM and XRD results. Further advanced 3D characterization methods can be used to visualize the tomography of these nanocomposites to examine how well the CdSe nanoparticles are being encapsulated or attached in the networks.

Thus, these display the theory and the functionality of self-assembly, especially the metal–coordination (metal–ligand), is in principle attainable in constructing different organic networks or organic systems that are worth investigating to control their crystallographic structure, morphology, and properties (e.g. electro-optical, thermal, etc.).

Regarding the 2-components 3D self-assembled adamantane cages as shown in Chapter 6, preliminary synthesis has been done (synthesis of monomers **30** and **32**). Due to time limitation, they will be used by the future students to make new n-type and p-type cores **33–36** in order to self-assemble **33–36** into new 2-components 3D self-assembled adamantane cages (**S7–10**), which could act as models for **S1–6**.

Incomplete addition of asymmetric p-type linker **43** to **3** was found in the last step of preparation of new 3D expanded conjugated p-type core **44** based on the MALDI-TOF mass spectra. Due to time limitation and lack of the material **43**, the preparation of **44** will be continued by future students either following Scheme 6.6 or the alternative method in Scheme 6.7.

7.2 Future works

In summary, the energy transfer phenomena of **P7**, **S4** and **S6** will be further investigated by the research group of Prof. Tan Howe-Siang at NTU. Modeling simulation on 3D Zn(II)–coordinated self-assembled networks **S1–6** to understand their non-porosity is being done by Dr. Abbie Trewin from University of Liverpool. Also, the synthesis, characterization and application of the 2-components 3D self-assembled adamantane cages (**S7–10**) in forming new nanocomposites or devices will be continued by future students. Besides, preparation of new 3D expanded conjugated p-type core **44** and new 3D expanded n-type core based on the n-type linker dialkoxybenzothiadiazole will be continued by future students. These new 3D expanded cores can also be used for metal–coordination self-assembly to form new networks

and nanocomposites similar to what had been done for **S1–6**. The remaining studies will be continued by future students.

The problem of the metal–ligand coordination, especially in 3D self-assembled networks is the insolubility in room temperature which limit their characterization and application in the organic electronic devices. This is believed to be caused by the highly rigid and interpenetrating structure of the metal–coordinated 3D networks. In order to solve this problem and in the same time continue the studies of the non-covalent self-assembled 3D networks, other approaches of non-covalent self-assembly (e.g. acid-base interactions, electrostatic interactions between cations and anions, and specific hydrogen bonding) can be used to replace the endgroups (tpys ligands) in this project.

As for the conventional organic conjugated polymers, different acceptor unit (e.g. benzo[1,2-c;4,5-c']bis[1,2,5]thiadiazole) can be used to replace BT unit due to its lower bandgap to mix with the thiophene based donor units in order to improve the PCE. Besides that, in order to improve the PCE of these polymers, it is better to completely quench their fluorescence in the solid state. This largely depends on the π-π stacking of the films made of the polymers mixed with PCBM when they are made into OPV devices. Therefore, by choosing other donor unit compared to those mentioned in Chapter 3 (e.g. thiophene-based pyrrole, DTP) and mix it with BT unit, it might help to have better morphology of the polymer:PCBM films which reduce or quench its fluorescence to have better PCE results in the OPV devices.

References

(1)   Lehn, J.-M. *Supramolecular Chemistry, Concepts and Perspectives*, 1995.

(2)   Hofmeier, H.; Schubert, U. S. *Chemical Society Reviews* **2004**, *33*, 373.

(3)   Padhy, H.; Sahu, D.; Chiang, I. H.; Patra, D.; Kekuda, D.; Chu, C.-W.; Lin, H.-C. *Journal of Materials Chemistry* **2011**, *21*, 1196.

(4)   Stang, P. J. *The Journal of Organic Chemistry* **2009**, *74*, 2.

(5)   Li, S.-S.; Northrop, B. H.; Yuan, Q.-H.; Wan, L.-J.; Stang, P. J. *Accounts of Chemical Research* **2009**, *42*, 249.

(6)   Galoppini, E.; Gilardi, R. *Chem. Commun.* **1999**, 173.

(7)   Weil, T.; Wiesler, U. M.; Herrmann, A.; Bauer, R.; Hofkens, J.; De Schryver, F. C.; Mullen, K. *Journal of the American Chemical Society* **2001**, *123*, 8101.

(8)   Grimsdale, A. C.; Bauer, R.; Weil, T.; Tchebotareva, N.; Wu, J.; Watson, M.; Mullen, K. *Synthesis* **2002**, 1229.

(9)   Langhals, H.; Wagner, C.; Ismael, R. *New Journal of Chemistry* **2001**, *25*, 1047.

(10)   Wilson, L. M.; Griffin, A. C. *J. Mater. Chem.* **1993**, *3*, 991.

(11)   Davydov, A. S. *Theory of Molecular Excitations*; McGraw Hill: New York, 1962.

(12)   Duprez, V.; Biancardo, M.; Krebs, F. C.; International Society for Optical Engineering, Bellingham WA, WA 98227-0010, United States: San Diego, CA, United States, 2005; Vol. 5938, p 1.

(13)   Leininger, S.; Olenyuk, B.; Stang, P. J. *Chemical Reviews* **2000**, *100*, 853.

(14)   Seidel, S. R.; Stang, P. J. *Accounts of Chemical Research* **2002**, *35*, 972.

References

(15)   Wild, A.; Winter, A.; Schlutter, F.; Schubert, U. S. *Chemical Society Reviews* **2011**, *40*, 1459.

(16)   Schubert, U. S.; Hofmeier, H.; Newkome, G. R. *Modern Terpyridine Chemistry*; 1st ed.; WILEY-VCH Verlag GmbH & Co. KGaA: Weinheim, Germany, 2006.

(17)   Constable, E. C. *Chemical Society Reviews* **2007**, *36*, 246.

(18)   Cooke, M. W.; Hanan, G. S. *Chemical Society Reviews* **2007**, *36*, 1466.

(19)   Andres, P. R.; Schubert, U. S. *Advanced Materials* **2004**, *16*, 1043.

(20)   O'Regan, B.; Gratzel, M. *Nature* **1991**, *353*, 737.

(21)   Krebs, F. C.; Biancardo, M. *Solar Energy Materials and Solar Cells* **2006**, *90*, 142.

(22)   Duprez, V.; Biancardo, M.; Spanggaard, H.; Krebs, F. C. *Macromolecules* **2005**, *38*, 10436.

(23)   Schlutter, F.; Wild, A.; Winter, A.; Hager, M. D.; Baumgaertel, A.; Friebe, C.; Schubert, U. S. *Macromolecules* **2010**, *43*, 2759.

(24)   Chen, Y.-Y.; Tao, Y.-T.; Lin, H.-C. *Macromolecules* **2006**, *39*, 8559.

(25)   Uyeda, H. T.; Zhao, Y.; Wostyn, K.; Asselberghs, I.; Clays, K.; Persoons, A.; Therien, M. J. *Journal of the American Chemical Society* **2002**, *124*, 13806.

(26)   Dumur, F.; Mayer, C. R.; Hoang-Thi, K.; Ledoux-Rak, I.; Miomandre, F.; Clavier, G.; Dumas, E.; Méallet-Renault, R.; Frigoli, M.; Zyss, J.; Sécheresse, F. *Inorganic Chemistry* **2009**, *48*, 8120.

(27)   Zhang, Y.; Murphy, C. B.; Jones, W. E. *Macromolecules* **2002**, *35*, 630.

(28)   Meier, M. A. R.; Schubert, U. S. *Chemical Communications* **2005**, 4610.

(29)   Schubert, U. S.; Newkome, G. R.; Manners, I.; Tew, G. N., Aamer, K. A., Shunmugam, R., Eds.; American Chemical Society: 2006; Vol. 928, p 126.

(30)   Manuela, C.; Michael, A. R. M.; Johannes, M. K.; Ulrich, S. S. *Macromolecular Chemistry and Physics* **2007**, *208*, 679.

(31)   Bonnet, S.; Collin, J. P.; Koizumi, M.; Mobian, P.; Sauvage, J. P. *Advanced Materials* **2006**, *18*, 1239.

(32)   Banjoko, V.; Xu, Y.; Mintz, E.; Pang, Y. *Polymer* **2009**, *50*, 2001.

(33)   Vellis, P. D.; Mikroyannidis, J. A.; Lo, C.-N.; Hsu, C.-S. *Journal of Polymer Science Part A: Polymer Chemistry* **2008**, *46*, 7702.

(34)   Kröhnke, F. *Synthesis* **1976**, 1.

(35)   Fang, Y.-Q.; Taylor, N. J.; Laverdière, F.; Hanan, G. S.; Loiseau, F.; Nastasi, F.; Campagna, S.; Nierengarten, H.; Leize-Wagner, E.; Van Dorsselaer, A. *Inorganic Chemistry* **2007**, *46*, 2854.

(36)   Fallahpour, R.-A. *Synthesis* **2003**, 155.

(37)   Merkushev, E. B.; Simakhina, N. D.; Koveshnikova, G. M. *Synthesis* **1980**, 486.

(38)   Aspley, C. J.; Williams, J. A. G. *New Journal of Chemistry* **2001**, *25*, 1136.

(39)   Wang, J. J. *Synlett* **2005**, 1251.

(40)   Baskar, C.; Lai, Y. H.; Valiyaveettil, S. *Macromolecules* **2001**, *34*, 6255.

(41)   Qin, R.; Li, W.; Li, C.; Du, C.; Veit, C.; Schleiermacher, H.-F.; Andersson, M.; Bo, Z.; Liu, Z.; Inganas, O.; Wuerfel, U.; Zhang, F. *Journal of the American Chemical Society* **2009**, *131*, 14612.

(42)   Tam, T. L.; Li, H.; Wei, F.; Tan, K. J.; Kloc, C.; Lam, Y. M.; Mhaisalkar, S. G.; Grimsdale, A. C. *Organic Letters* **2010**, *12*, 3340.

(43)   Scheblykin, I. G.; Yartsev, A.; Pullerits, T.; Gulbinas, V.; Sundström, V. *The Journal of Physical Chemistry B* **2007**, *111*, 6303.

(44)   Sariciftci, N. S. *Primary Photoexcitations In Conjugated Polymers: Molecular Exciton Versus Semiconductor Band Model*; World Scientific: Singapore, 1997.

(45)   Cheng, Y.-J.; Yang, S.-H.; Hsu, C.-S. *Chemical Reviews* **2009**, *109*, 5868.

(46)   Grimsdale, A. C.; Leok Chan, K.; Martin, R. E.; Jokisz, P. G.; Holmes, A. B. *Chemical Reviews* **2009**, *109*, 987.

(47)   Arias, A. C.; MacKenzie, J. D.; McCulloch, I.; Rivnay, J.; Salleo, A. *Chemical Reviews* **2010**, *110*, 3.

(48)   Scharber, M. C.; Mühlbacher, D.; Koppe, M.; Denk, P.; Waldauf, C.; Heeger, A. J.; Brabec, C. J. *Advanced Materials* **2006**, *18*, 789.

(49)   Dennler, G.; Scharber, M. C.; Brabec, C. J. *Advanced Materials* **2009**, *21*, 1323.

(50)   Kim, J. Y.; Lee, K.; Coates, N. E.; Moses, D.; Nguyen, T.-Q.; Dante, M.; Heeger, A. J. *Science* **2007**, *317*, 222.

(51)   Hou, J.; Chen, H.-Y.; Zhang, S.; Li, G.; Yang, Y. *Journal of the American Chemical Society* **2008**, *130*, 16144.

(52)   Peet, J.; Kim, J. Y.; Coates, N. E.; Ma, W. L.; Moses, D.; Heeger, A. J.; Bazan, G. C. *Nat Mater* **2007**, *6*, 497.

(53)   Wang, E.; Wang, L.; Lan, L.; Luo, C.; Zhuang, W.; Peng, J.; Cao, Y. *Applied Physics Letters* **2008**, *92*, 033307.

(54)   Park, S. H.; Roy, A.; Beaupre, S.; Cho, S.; Coates, N.; Moon, J. S.; Moses, D.; Leclerc, M.; Lee, K.; Heeger, A. J. *Nat Photon* **2009**, *3*, 297.

(55)   Chen, H.-Y.; Hou, J.; Zhang, S.; Liang, Y.; Yang, G.; Yang, Y.; Yu, L.; Wu, Y.; Li, G. *Nat Photon* **2009**, *3*, 649.

(56)   Zhou, H.; Yang, L.; Stuart, A. C.; Price, S. C.; Liu, S.; You, W. *Angewandte Chemie International Edition* **2011**, *50*, 2995.

(57)   Chu, T.-Y.; Lu, J.; Beaupre, S.; Zhang, Y.; Pouliot, J.-R.; Wakim, S.; Zhou, J.; Leclerc, M.; Li, Z.; Ding, J.; Tao, Y. *Journal of the American Chemical Society* **2011**, *133*, 4250.

(58)   Price, S. C.; Stuart, A. C.; Yang, L.; Zhou, H.; You, W. *Journal of the American Chemical Society* **2011**, *133*, 4625.

(59)   Nicolaidis, N. C.; Routley, B. S.; Holdsworth, J. L.; Belcher, W. J.; Zhou, X.; Dastoor, P. C. *The Journal of Physical Chemistry C* **2011**, *115*, 7801.

(60)   Bundgaard, E.; Krebs, F. C. *Macromolecules* **2006**, *39*, 2823.

(61)   Lenes, M.; Morana, M.; Brabec, C. J.; Blom, P. W. M. *Advanced Functional Materials* **2009**, *19*, 1106.

(62)   He, Y.; Wang, X.; Zhang, J.; Li, Y. F. *Macromolecular Rapid Communications* **2009**, *30*, 45.

(63)   Zhou, H.; Yang, L.; Stoneking, S.; You, W. *ACS Applied Materials & Interfaces* **2010**, *2*, 1377.

(64)   McCulloch, I.; Heeney, M.; Bailey, C.; Genevicius, K.; MacDonald, I.; Shkunov, M.; Sparrowe, D.; Tierney, S.; Wagner, R.; Zhang, W.; Chabinyc, M. L.; Kline, R. J.; McGehee, M. D.; Toney, M. F. *Nat Mater* **2006**, *5*, 328.

(65)   Yamaguchi, S.; Tamao, K. *Polysiloles and related silole-containing polymers*; John Wiley & Sons, Ltd: Chichester, U.K., 2001.

(66)   Tamao, K.; Uchida, M.; Izumizawa, T.; Furukawa, K.; Yamaguchi, S. *Journal of the American Chemical Society* **1996**, *118*, 11974.

(67)   Ohshita, J.; Nodono, M.; Kai, H.; Watanabe, T.; Kunai, A.; Komaguchi, K.; Shiotani, M.; Adachi, A.; Okita, K.; Harima, Y.; Yamashita, K.; Ishikawa, M. *Organometallics* **1999**, *18*, 1453.

(68)   Yamaguchi, S.; Tamao, K. *Bulletin of the Chemical Society of Japan* **1996**, *69*, 2327.

(69)   Manceau, M.; Bundgaard, E.; Carle, J. E.; Hagemann, O.; Helgesen, M.; Sondergaard, R.; Jorgensen, M.; Krebs, F. C. *Journal of Materials Chemistry* **2011**, *21*, 4132.

(70)   Usta, H.; Lu, G.; Facchetti, A.; Marks, T. J. *Journal of the American Chemical Society* **2006**, *128*, 9034.

(71)   Zhao, X.; Zhan, X. *Chemical Society Reviews* **2011**, *40*, 3728.

(72)   de Greef, T. F. A.; Meijer, E. W. *Nature* **2008**, *453*, 171.

(73)   Ulbricht, C.; Beyer, B.; Friebe, C.; Winter, A.; Schubert, U. S. *Advanced Materials* **2009**, *21*, 4418.

(74)   Constable, E. C.; Thompson, A. M. W. C. *Journal of the Chemical Society, Chemical Communications* **1992**, 617.

(75)   Constable, E. C. *Macromolecular Symposia* **1995**, *8*, 50.

(76)   Manners, I. *Science* **2001**, *294*, 1664.

(77)   Shirakawa, H.; Louis, E. J.; MacDiarmid, A. G.; Chiang, C. K.; Heeger, A. J. *Journal of the Chemical Society, Chemical Communications* **1977**, 578.

(78)   Blaiszik, B. J.; Kramer, S. L. B.; Olugebefola, S. C.; Moore, J. S.; Sottos, N. R.; White, S. R. *Annual Review of Materials Research* **2010**, *40*, 179.

(79)   Winter, A.; Friebe, C.; Chiper, M.; Hager, M. D.; Schubert, U. S. *Journal of Polymer Science Part A: Polymer Chemistry* **2009**, *47*, 4083.

(80)   Dobrawa, R.; Würthner, F. *Journal of Polymer Science Part A: Polymer Chemistry* **2005**, *43*, 4981.

(81)   Sauvage, J. P.; Collin, J. P.; Chambron, J. C.; Guillerez, S.; Coudret, C.; Balzani, V.; Barigelletti, F.; De Cola, L.; Flamigni, L. *Chemical Reviews* **1994**, *94*, 993.

(82)   Flores-Torres, S.; Hutchison, G. R.; Soltzberg, L. J.; Abruna, H. D. *Journal of the American Chemical Society* **2006**, *128*, 1513.

(83)   Wang, X.-y.; Del Guerzo, A.; Schmehl, R. H. *Chemical Communications* **2002**, 2344.

(84)   Dobrawa, R.; Würthner, F. *Chemical Communications* **2002**, 1878.

(85)   Dobrawa, R.; Lysetska, M.; Ballester, P.; Grune, M.; Wurthner, F. *Macromolecules* **2005**, *38*, 1315.

(86)   Yi-Yu, C.; Hong-Cheu, L. *Journal of Polymer Science Part A: Polymer Chemistry* **2007**, *45*, 3243.

(87)   Burnworth, M.; Tang, L.; Kumpfer, J. R.; Duncan, A. J.; Beyer, F. L.; Fiore, G. L.; Rowan, S. J.; Weder, C. *Nature* **2011**, *472*, 334.

(88)   Yu, S. C.; Kwok, C. C.; Chan, W. K.; Che, C. M. *Advanced Materials* **2003**, *15*, 1643.

(89)   Chen, Y.-Y.; Lin, H.-C. *Polymer* **2007**, *48*, 5268.

(90)   Santoni, M.-P.; Medlycott, E. A.; Hanan, G. S.; Hasenknopf, B.; Proust, A.; Nastasi, F.; Campagna, S.; Chiorboli, C.; Argazzi, R.; Scandola, F. *Dalton Transactions* **2009**, 3964.

(91)   Schubert, U. S.; Eschbaumer, C. *Angewandte Chemie International Edition* **2002**, *41*, 2892.

References

(92)   Groll, M.; Ditzel, L.; Löwe, J.; Stock, D.; Bochtler, M.; Bartunik, H. D.; Huber, R. *Nature* **1997**, *386*, 463.

(93)   Northrop, B. H.; Zheng, Y.-R.; Chi, K.-W.; Stang, P. J. *Accounts of Chemical Research* **2009**, *42*, 1554.

(94)   Zheng, Y.-R.; Northrop, B. H.; Yang, H.-B.; Zhao, L.; Stang, P. J. *The Journal of Organic Chemistry* **2009**, *74*, 3554.

(95)   De, S.; Mahata, K.; Schmittel, M. *Chemical Society Reviews* **2010**, *39*, 1555.

(96)   Lee, J.; Ghosh, K.; Stang, P. J. *Journal of the American Chemical Society* **2009**, *131*, 12028.

(97)   Mahata, K.; Schmittel, M. *Journal of the American Chemical Society* **2009**, *131*, 16544.

(98)   Zheng, Y.-R.; Zhao, Z.; Wang, M.; Ghosh, K.; Pollock, J. B.; Cook, T. R.; Stang, P. J. *Journal of the American Chemical Society* **2010**, *132*, 16873.

(99)   Hwang, S.-H.; Wang, P.; Moorefield, C. N.; Godinez, L. A.; Manriquez, J.; Bustos, E.; Newkome, G. R. *Chemical Communications* **2005**, 4672.

(100)   Kaminker, R.; Motiei, L.; Gulino, A.; FragalaÌ€, I.; Shimon, L. J. W.; Evmenenko, G.; Dutta, P.; Iron, M. A.; van der Boom, M. E. *Journal of the American Chemical Society* **2010**, *132*, 14554.

(101)   Wurthner, F.; You, C.-C.; Saha-Moller, C. R. *Chemical Society Reviews* **2004**, *33*, 133.

(102)   Lee, S. J.; Hupp, J. T. *Coordination Chemistry Reviews* **2006**, *250*, 1710.

(103)   Jin-Liang, W.; Yi-Tsu, C.; Charles, N. M.; Jian, P.; David, A. M.; Natalie, C. R.; George, R. N. *Macromolecular Rapid Communications* **2010**, *31*, 850.

(104)   Newkome, G. R.; Güther, R.; Moorefield, C. N.; Cardullo, F.; Echegoyen, L.; Pérez-Cordero, E.; Luftmann, H. *Angewandte Chemie International Edition in English* **1995**, *34*, 2023.

(105)   Newkome, G. R.; He, E.; Godínez, L. A. *Macromolecules* **1998**, *31*, 4382.

(106)   Altman, M.; Zenkina, O.; Evmenenko, G.; Dutta, P.; van der Boom, M. E. *Journal of the American Chemical Society* **2008**, *130*, 5040.

(107)   Yang, H.-B.; Ghosh, K.; Northrop, B. H.; Stang, P. J. *Organic Letters* **2007**, *9*, 1561.

(108)   Wang, M.; Zheng, Y.-R.; Ghosh, K.; Stang, P. J. *Journal of the American Chemical Society* **2010**, *132*, 6282.

(109)   Ghosh, S.; Mukherjee, P. S. *Organometallics* **2008**, *27*, 316.

(110)   Prakash, M. J.; Lah, M. S. *Chemical Communications* **2009**, 3326.

(111)   Yoshizawa, M.; Nakagawa, J.; Kumazawa, K.; Nagao, M.; Kawano, M.; Ozeki, T.; Fujita, M. *Angewandte Chemie International Edition* **2005**, *44*, 1810.

(112)   Kumazawa, K.; Biradha, K.; Kusukawa, T.; Okano, T.; Fujita, M. *Angewandte Chemie International Edition* **2003**, *42*, 3909.

(113)   Jiang, J.-X.; Su, F.; Trewin, A.; Wood, C. D.; Campbell, N. L.; Niu, H.; Dickinson, C.; Ganin, A. Y.; Rosseinsky, M. J.; Khimyak, Y. Z.; Cooper, A. I. *Angewandte Chemie International Edition* **2007**, *46*, 8574.

(114)   Tozawa, T.; Jones, J. T. A.; Swamy, S. I.; Jiang, S.; Adams, D. J.; Shakespeare, S.; Clowes, R.; Bradshaw, D.; Hasell, T.; Chong, S. Y.; Tang, C.; Thompson, S.; Parker, J.; Trewin, A.; Bacsa, J.; Slawin, A. M. Z.; Steiner, A.; Cooper, A. I. *Nat Mater* **2009**, *8*, 973.

(115)   Jiang, J.-X.; Su, F.; Trewin, A.; Wood, C. D.; Niu, H.; Jones, J. T. A.; Khimyak, Y. Z.; Cooper, A. I. *Journal of the American Chemical Society* **2008**, *130*, 7710.

(116)   Chen, Q.; Luo, M.; Wang, T.; Wang, J.-X.; Zhou, D.; Han, Y.; Zhang, C.-S.; Yan, C.-G.; Han, B.-H. *Macromolecules* **2011**, *44*, 5573.

(117)   Leong, W. L.; Lee, P. S.; Lohani, A.; Lam, Y. M.; Chen, T.; Zhang, S.; Dodabalapur, A.; G. Mhaisalkar, S. *Advanced Materials* **2008**, *20*, 2325.

(118)   Turkevich, J.; Stevenson, P. C.; Hillier, J. *Discussions of the Faraday Society* **1951**, *11*, 55.

(119)   Benniston, A. C.; Harriman, A.; Lawrie, D. J.; Mayeux, A.; Rafferty, K.; Russell, O. D. *Dalton Transactions* **2003**, 4762.

(120)   Goze, C.; Ulrich, G.; Charbonnière, L.; Cesario, M.; Prangé, T.; Ziessel, R. *Chemistry – A European Journal* **2003**, *9*, 3748.

(121)   Wyrzykowski, D.; Chmurzyński, L. *Journal of Thermal Analysis & Calorimetry* **2010**, *102*, 61.

(122)   Rebertus, R. L.; Laitinen, H. A.; Bailar, J. C. *Journal of the American Chemical Society* **1953**, *75*, 3051.

(123)   Northrop, B. H.; Yang, H.-B.; Stang, P. J. *Chemical Communications* **2008**, 5896.

(124)   Fiedler, D.; Leung, D. H.; Bergman, R. G.; Raymond, K. N. *Accounts of Chemical Research* **2005**, *38*, 349.

(125)   Pluth, M. D.; Bergman, R. G.; Raymond, K. N. *Accounts of Chemical Research* **2009**, *42*, 1650.

(126)   Lee, J.; Farha, O. K.; Roberts, J.; Scheidt, K. A.; Nguyen, S. T.; Hupp, J. T. *Chemical Society Reviews* **2009**, *38*, 1450.

(127)   Bals, S.; Van Tendeloo, G.; Kisielowski, C. *Advanced Materials* **2006**, *18*, 892.

(128)   Midgley, P. A.; Weyland, M. *Ultramicroscopy* **2003**, *96*, 413.

(129)   Papamicaël, C. A.; Mongin, O.; Gossauer, A. *Monatshefte für Chemie / Chemical Monthly* **2007**, *138*, 791.

(130)   Stang, P. J.; Diederich, F. *Modern Acetylene Chemistry*; Wiley-VCH, 1995.

Experimental Section

General

All starting materials (chemicals) used in this project were purchased from commercial sources, e.g. Sigma Aldrich, Alfa Aesar et al. All reactions were carried out under inert N_2 atmosphere, unless otherwise stated. Analytical Thin Layer Chromatography (TLC) was performed on aluminum or Polyethylene terephthalate (PET) sheets pre-coated with silica gel or Aluminum Oxide (with fluorescent indicator 254 nm). Visualization was accomplished with UV light. Purification of reaction mixture using column chromatography was done on the silica gel 60 Geduran (Merck) or neutral Aluminum oxide (Brockmann Grade I, 58 angstroms).

Nuclear Magnetic Resonance (NMR) spectra (^1H and ^{13}C) were recorded on a Bruker Advance 400 spectrometer. The solvent used in the NMR characterization was deuterated- chloroform ($CDCl_3$), unless otherwise stated. Chemical shifts are given δ in units of ppm referenced to residual proton signals in $CDCl_3$. Coupling constants (J) are reported Hertz (Hz). NMR splitting patterns are designated as s, singlet; d, doublet; t, triplet; q, quartet; AB, pair of doublet which is mirror image to each other; m, multiplet; and br, broad.

Mass spectra were recorded using Shimadzu Axima Matrix-Assisted Laser Desorption/Ionization Time-Of-Flight (MALDI-TOF) mass spectrometer. Molecular weight of polymers was determined by Gel Permeation Chromatography (GPC) method in chloroform, which was performed on Agilent GPC 1100 series model G1311A. In this method, column of PL gel 5 micron, MIXED-C was used and polystyrene was used as a

standard.

Absorption spectra were taken on a UV-Vis recording spectrophotometer (Shimadzu UV-2501PC). Fluorescent measurements were taken on a spectrofluorophotometer (Shimadzu RF-5301PC).

Thermogravimetric Analysis (TGA) experiments were performed on TA TGA-Q500 with a dynamic heat rate (10 °C/min) under N_2 atmosphere (50 ml/min) in the temperature range 25–900 °C. Differential Scanning Calorimetry (DSC) measurements were performed on TA DSC-Q10 with dynamic heating and cooling rate (5 °C/min) under N_2 atmosphere (50 ml/min) in the temperature range 0–300 °C.

The electrochemical Cyclic Voltammetry (CV) was conducted on a frequency response analyzer (Solartron 1255B) with a sweep rate 100 mV/s by a platinum working electrode. Gold was used as counter electrode. Ag/Ag^+ was used as reference electrode and DCM containing 0.1 M tetra-n-butylammonium hexafluorophosphate (Bu_4NPF_6) was used as electrolyte in electrochemical measurements. Thin films were made by Spin Coater model P6700 series with 1250 rpm for 1.5 min.

XRD scanning (5° to 120°) was studied by Bruker AXS D8 Advance X-Ray diffractometer. Elemental Analysis and High Resolution Electrospray[+]-Time-Of-Flight Mass Spectra (HR ES[+]-TOF MS) were done by Mr. Yang Yifan and Asst. Prof. So Cheuk Wai from School of Physical and Mathematical Sciences (Division of Chemistry & Biological Chemistry), Nanyang Technological University. Elemental Analysis was done on the EuroEA Elemental Analyser with calibration type of K-Factor. HR ES[+]-TOF MS was done on the Water Q-TOF Premier Mass Spectrometer.

The porous properties of the networks were investigated by nitrogen adsorption at 77.3 K

using ASAP Chemisorption Accelerated Surface Area and Porosimetry Analyzer (Micromeritics Instrument Corporation). Samples were degassed at 100 °C for 6 h under vacuum (10^{-5} bar) before analysis.

Solar Cells Fabrication and Characterization.

This was done at Newcastle University by Dr. Bofei Xue in group of Prof. Paul C. Dastoor.

PEDOT:PSS (Clevios P, filtered by 0.45 µm PTFE filter) films were spin-coated (4000 rpm) on pre-cleaned patterned ITO glass slides. The PEDOT:PSS films were transferred into a glove box with dry N_2 atmosphere and annealed at 120 °C for 20 min to eliminate water in the films. Different weight ratios were used for **P4** and PCBM (Luminescence Tech. Corp., Taiwan) blends. The **P4**:PCBM blend solution (different concentration in chloroform) was sonicated for 30 min and then used to spin-coat the active layers in an inert atmosphere glove box at 2000 rpm for 1 min. Thickness of these active layers were measured by a KLA Tencor profilometer These active layers were then transferred into a vacuum chamber for electrode evaporation. The aluminium (Al) electrodes were evaporated on the active layers in vacuum (2×10^{-6} Torr). The thickness of Al layers was measured to be about 80 nm by a KLA Tencor profilometer and the area of each cell was 5 mm^2.

The photocurrent density-voltage (J-V) measurements were conducted using a Newport Class A solar simulator with an AM 1.5 spectrum filter to illuminate the full cells. The light intensity was measured to be 100 mW cm^{-2} by a silicon reference solar cell (Newport) and the J-V data were recorded by a Keithley 2400 source meter. The cells

were tested after Ca-Al evaporation. Post-evaporation annealing at different temperature and duration was also carried out to study the J-V performance of these cells after annealing.

Synthesis and characterization

List of abbreviations

DCM = Dichloromethane

DI = Deionized

DMSO = Dimethyl sulfoxide

EA = Ethyl acetate

EtOH = Ethanol

MeOH = Methanol

NBS = N-Bromosuccinimide

NMP = N-Methyl-2-pyrrolidone

RBF = Round bottom flask

RT = Room temperature

$PdCl_2(dppf)$ = [1,1-Bis(diphenylphosphino)ferrocene]dichloropalladium(II)

$Pd(PPh_3)_4$ = Tetrakis(triphenylphosphine)palladium

$(Ph_3P)_2PdCl_2$ = Bis(triphenylphosphine)palladium(II) dichloride

THF = Tetrahydrofuran

Tetrakis(4-iodophenyl)methane (3). Tetraphenylmethane (0.5 g, 1.56 mmol), I_2 (0.84 g, 3.3 mmol) and bis[(trifluoroacetoxy)iodo]benzene (1.55 g, 3.6 mmol) were dissolved in

CHCl$_3$ (10 ml) in a RBF and the reaction mixture was heated at 55 °C until the colour of iodine disappeared. The reaction mixture was then concentrated under reduced pressure to remove solvent. Residual solid was washed with EtOH and acetone and purified by recrystallization from THF to give **3** as a white solid (0.43 g, 33.3%). **^{1}H NMR (CDCl$_3$):** δ 7.58 (d, *J* = 4.4 Hz, 2 H), 6.877 (d, *J* = 4.4 Hz, 2 H). **^{13}C NMR (CDCl$_3$):** δ 145.05, 137.08, 132.60, 92.44, 64.02.
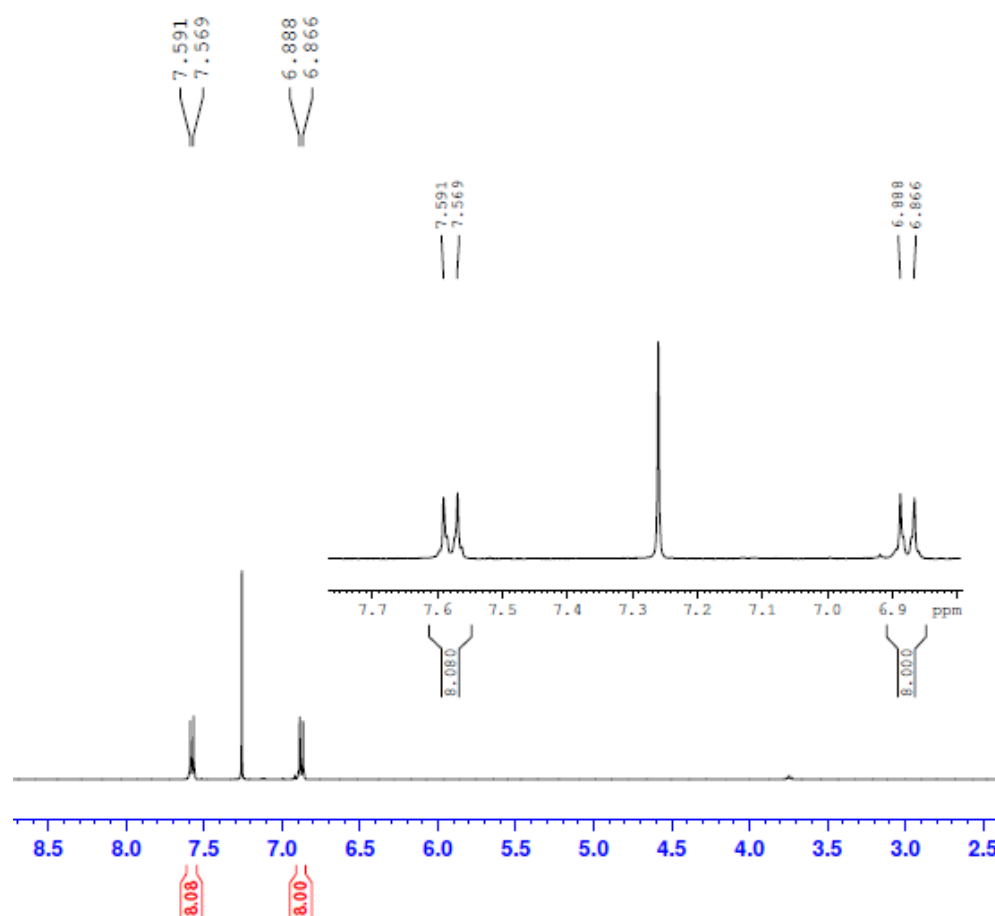
Figure A1 ^{1}H NMR spectrum of tetrakis(4-iodophenyl)methane **(3)**
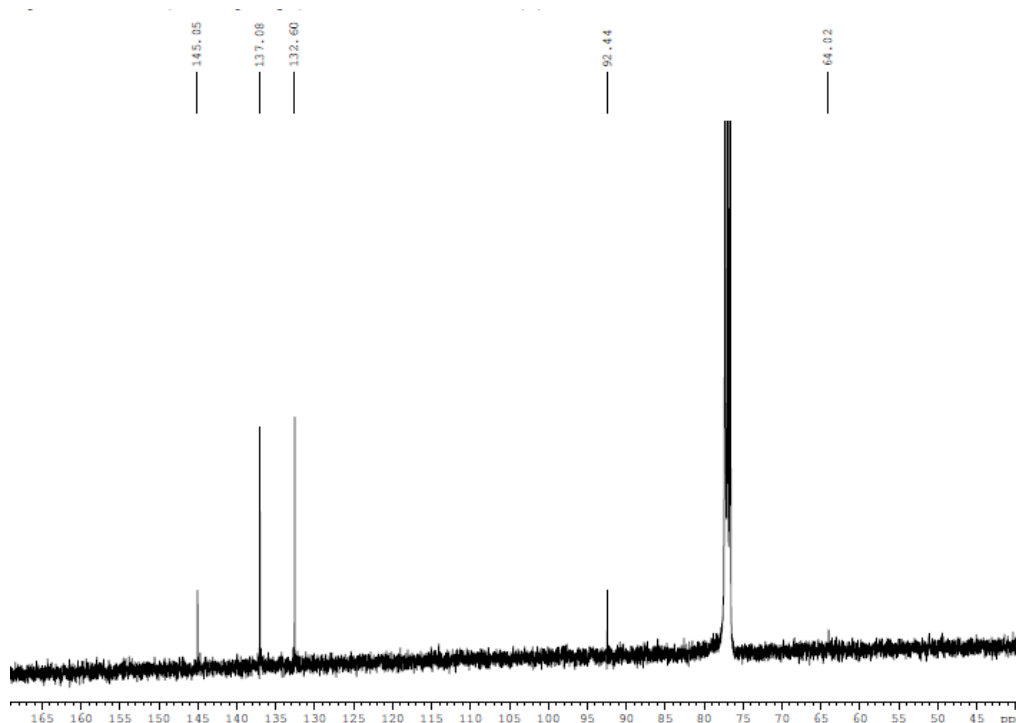
Figure A2 ¹³C NMR spectrum of tetrakis(4-iodophenyl)methane **(3)**

Tetrakis[4-(4',4',5',5'-tetramethyl-1',3',2'-dioxaborolane-phenyl)]methane **(4).** **3** (0.412 g, 0.5 mmol), bis(pinacolato)diborane (0.77 g, 3 mmol), potassium acetate (0.75 g, 7.5 mmol) and $PdCl_2$(dppf) (50 mg, 0.06 mmol) were dissolved in anhydrous DMSO (10 ml) and the reaction mixture was degassed. Reaction mixture was stirred at 80 °C for 12 h, cooled to RT, and then poured into ice water. The mixture was then extracted with $CHCl_3$ and water. The combined organic layers were dried over anhydrous $MgSO_4$. After the solvent was evaporated, the residue was washed with cold hexane. The solid residue was then recrystallized from MeOH-THF to afford **4** as a white solid (0.23 g, 60%). **¹H NMR (CDCl₃):** δ 7.652 (d, J = 8.4 Hz, 8 H), 7.27 (d, J = 8.4 Hz, 8 H), 1.314 (s, 48 H). **¹³C NMR (CDCl₃):** δ 149.48, 134.14, 130.30, 83.72, 67.69, 24.86.
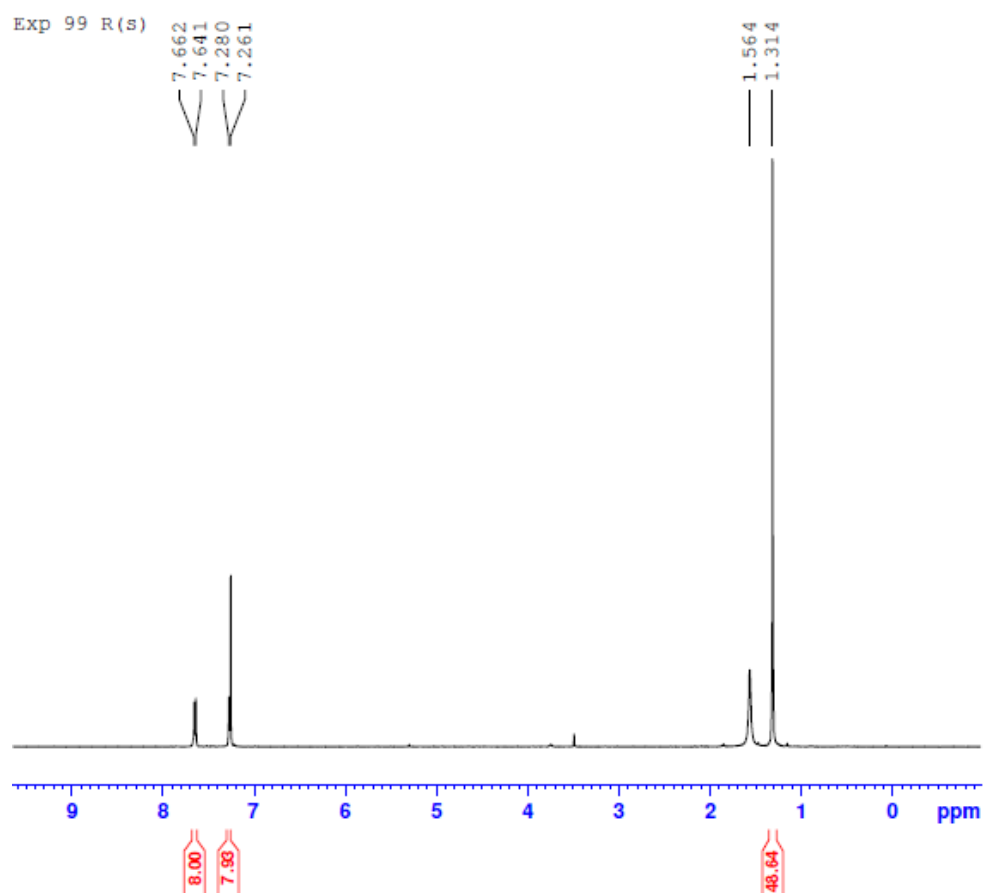
Figure A3 ^{1}H NMR of Tetrakis[4-(4',4',5',5'-tetramethyl-1',3',2'-dioxaborolane-phenyl)]methane **(4)**
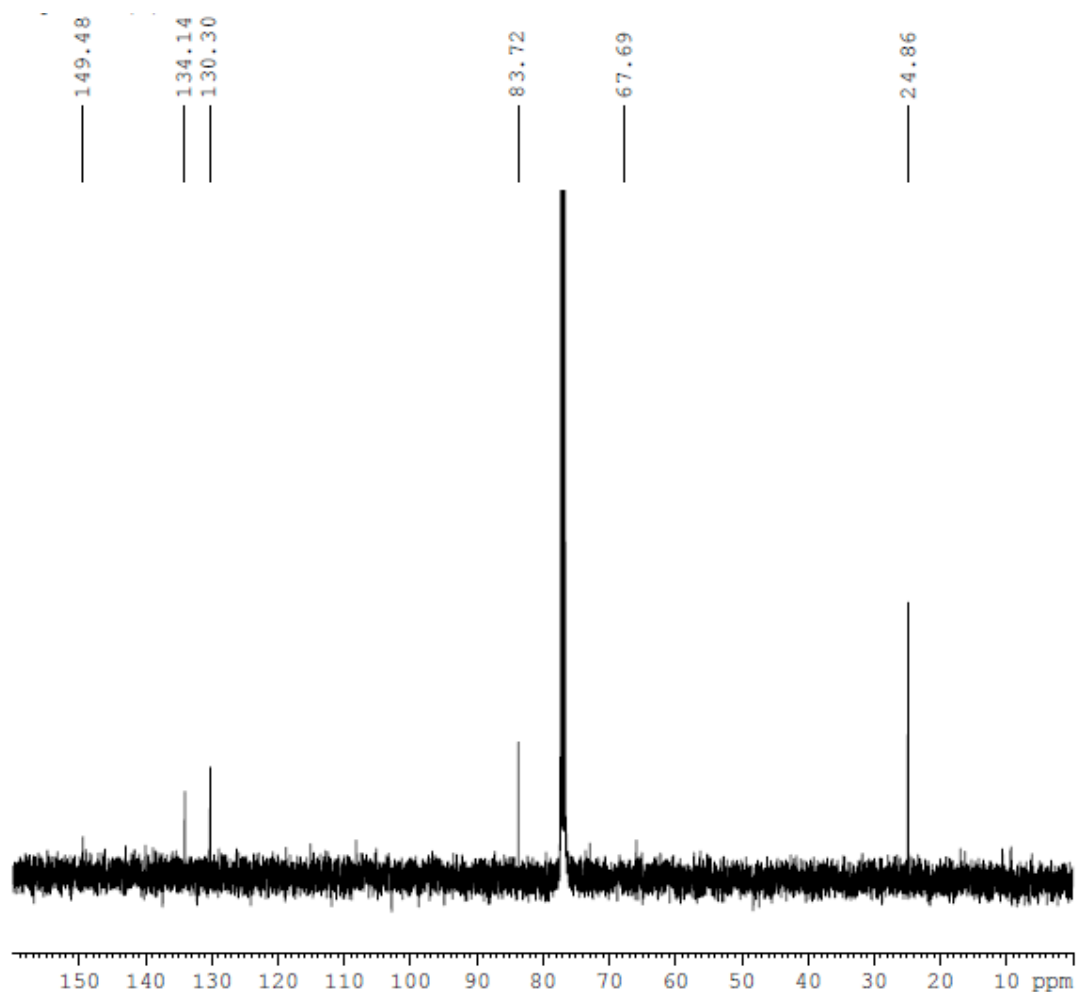
Figure A4 ^{13}C NMR of Tetrakis[4-(4',4',5',5'-tetramethyl-1',3',2'-dioxaborolane-phenyl)]methane **(4)**

4'-(4-Bromophenyl)-2,2':6'2''-terpyridine (5). 2-acetylpyridine (18 ml, 160 mmol) was added to a solution of 4-bromobenzaldehyde (14.8 g, 80 mmol) and EtOH (400 ml) in RBF. Potassium hydroxide (12.32 g, 220 mmol) and aqueous ammonia (280 ml, 200 mmol) were then added to the reaction mixture. The reaction mixture was then stirred for 3 h at 40 °C. The reaction mixture was then filtered and washed with EtOH to get crude product as a solid. Recrystallization of the crude solid from MeOH–CHCl$_3$ afforded **5** as a white solid (12.14 g, 39.1%). **^{1}H NMR (CDCl$_3$):** δ 8.723 (d, $J = 4.4$ Hz , 2 H), 8.691 (s, 2 H), 7.633 and 7.772 (AB q, $J = 8.4$ Hz, 4 H), 7.88 (td, $J = 8$ Hz, 2 H), 7.356 (t, $J = 6$ Hz, 2

H), 8.662 (d, J = 8 Hz, 2 H). ^{13}C NMR (CDCl₃): δ 156.05, 149.14, 136.94, 132.11, 128.90, 123.95, 121.40, 118.57. MALDI TOF MS: m/z 390 (M+2H).

Exp 38 4'-(4-bromophenyl)-2,2':6',2"-tpy
PROTON

**Figure A5** ^{1}H NMR of 4'-(4-Bromophenyl)-2,2':6'2''-terpyridine (**5**)
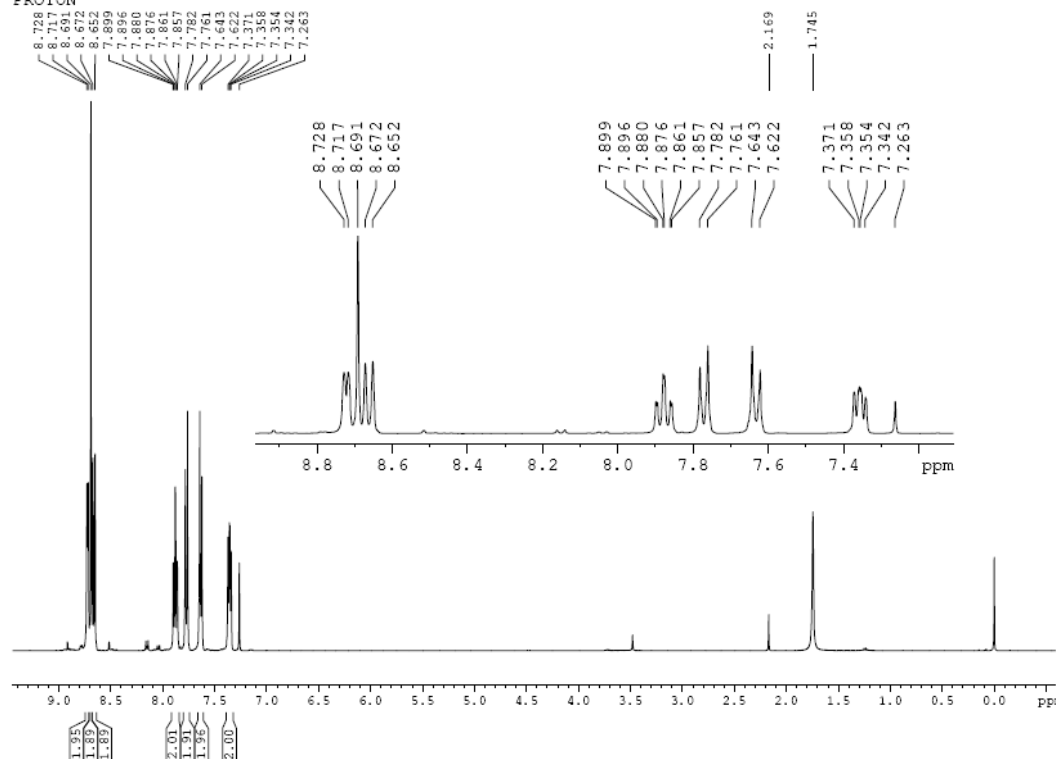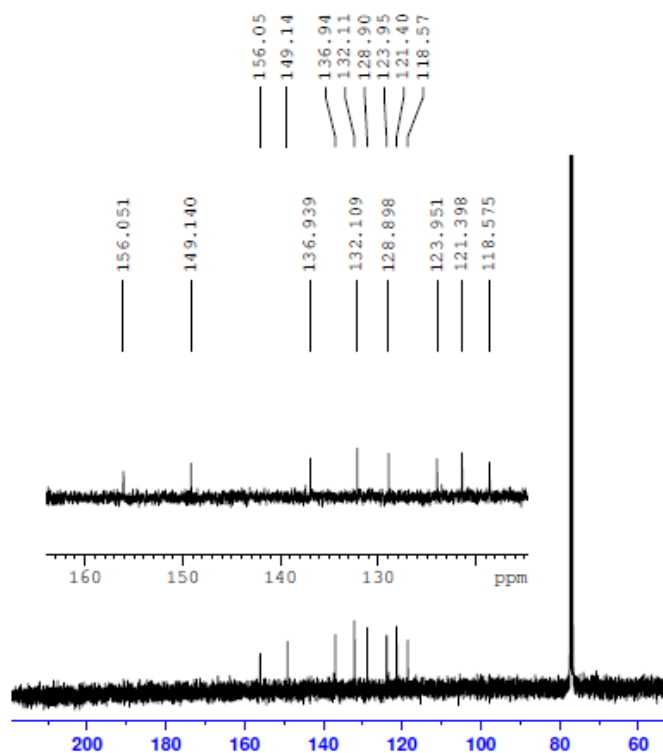
Figure A6 ^{13}C NMR of 4'-(4-Bromophenyl)-2,2':6'2''-terpyridine **(5)**
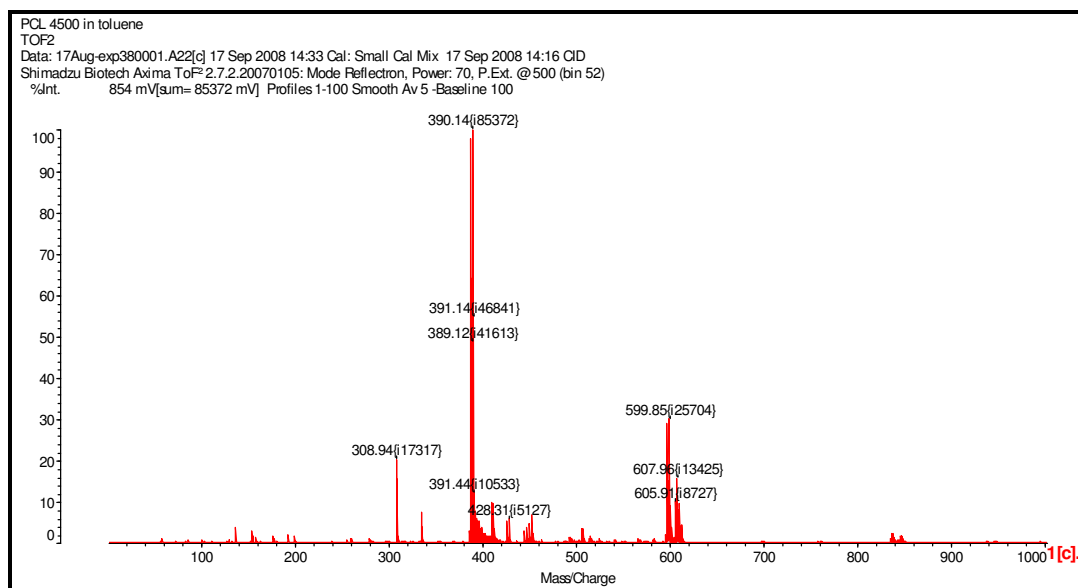
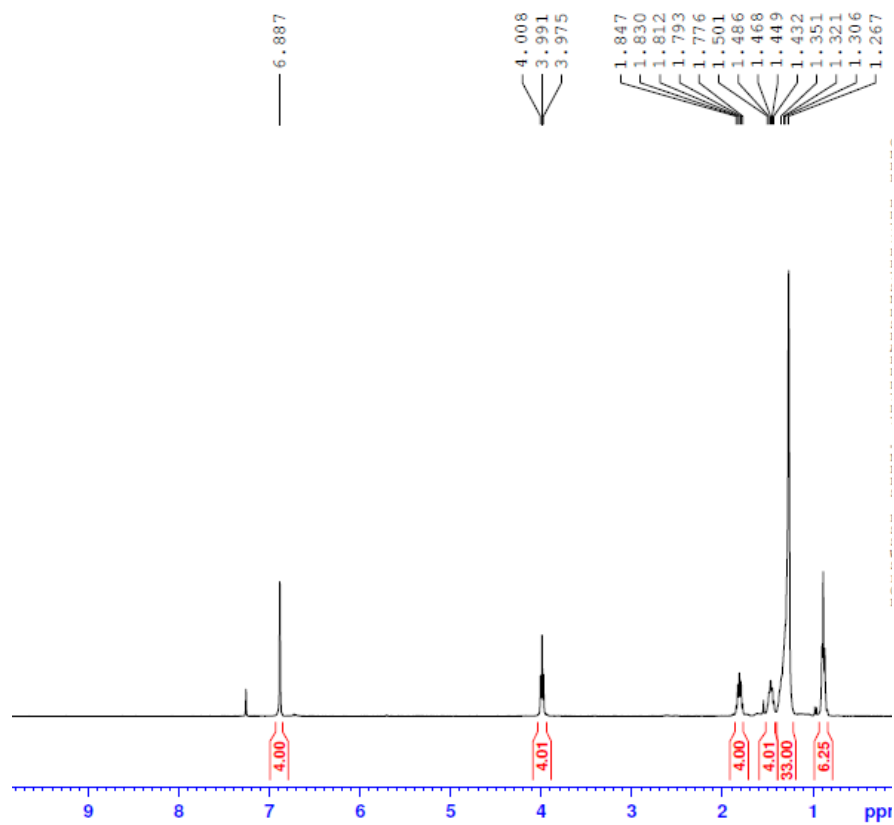**Figure A7** MALDI-TOF mass spectra of 4'-(4-Bromophenyl)-2,2':6'2''-terpyridine **(5)**

4'-(4-Pinacolatoboronphenyl)-2,2':6',2''-terpyridine (6). A RBF which contained

Pd(dppf)Cl$_2$ (2.1 g, 2.58 mmol), potassium acetate (7.6 g, 77.4 mmol),

bis(pinacolato)diboron (7.2 g, 28.4 mmol) and **5** (10 g, 25.8 mmol) was degassed thoroughly with N_2 before adding DMSO (250 ml). The reaction mixture was then stirred at 80 °C overnight. After cooling down to RT, the reaction mixture was poured into ice water to form precipitate. The solid of precipitate was collected through filtration, followed by extraction in DCM and water. The aqueous layer was purple at this stage, presumably due to complexation of some terpyridine to ions released on decomposition of the catalyst. The DCM layer was then dried over $MgSO_4$ and concentrated using a rotary evaporator. Through column chromatography on silica gel with 30% EA in hexane followed by recrystallization in MeOH–THF, **6** was obtained as a white solid (6.27 g, 60%). **^{1}H NMR (CDCl$_3$):** δ 8.800 (s, 2 H), 8.771 (d, *J* = 4.4 Hz, 2 H), 8.717 (d, *J* = 4 Hz, 2 H), 7.95–7.914 (m, 6 H), 7.398 (t, *J* = 6 Hz, 2 H), 1.384 (s, 12 H). **^{13}C NMR (CDCl$_3$):** δ 155.52, 155.28, 150.39, 148.53, 140.60, 137.74, 135.43, 126.62, 124.10,121.86, 119.42, 83.99, 24.92. **MALDI TOF MS:** m/z 436 (M+1H).
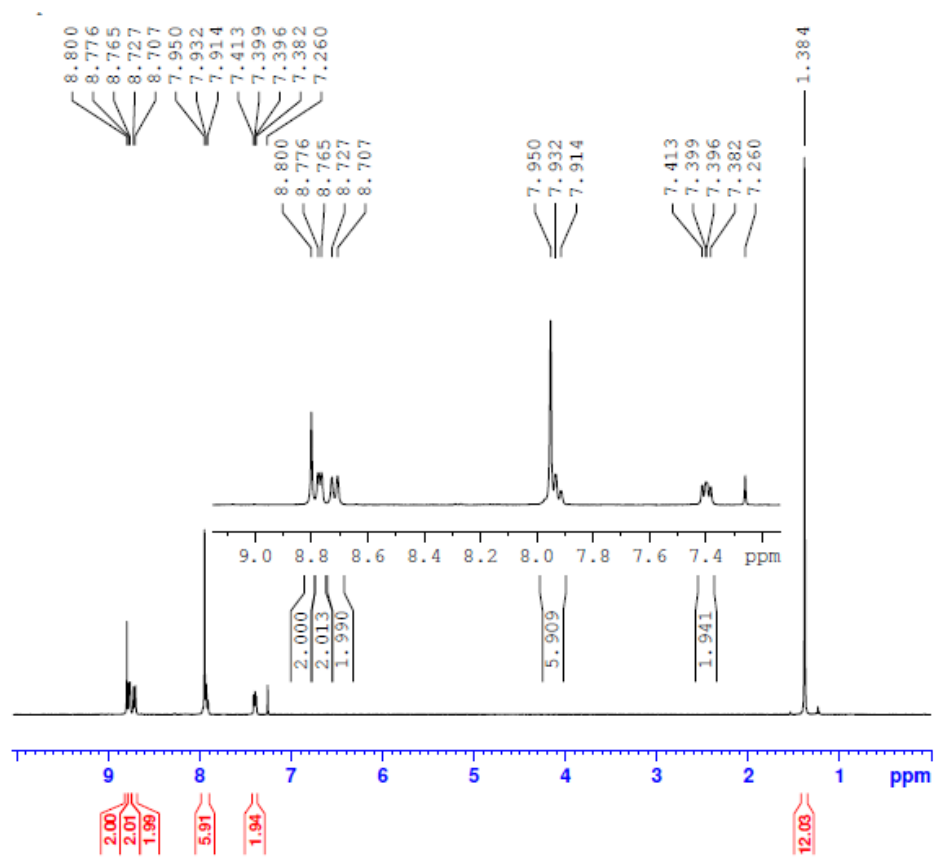
Figure A8   ¹H NMR of 4'-(4-Pinacolatoboronphenyl)-2,2':6',2''-terpyridine (**6**)
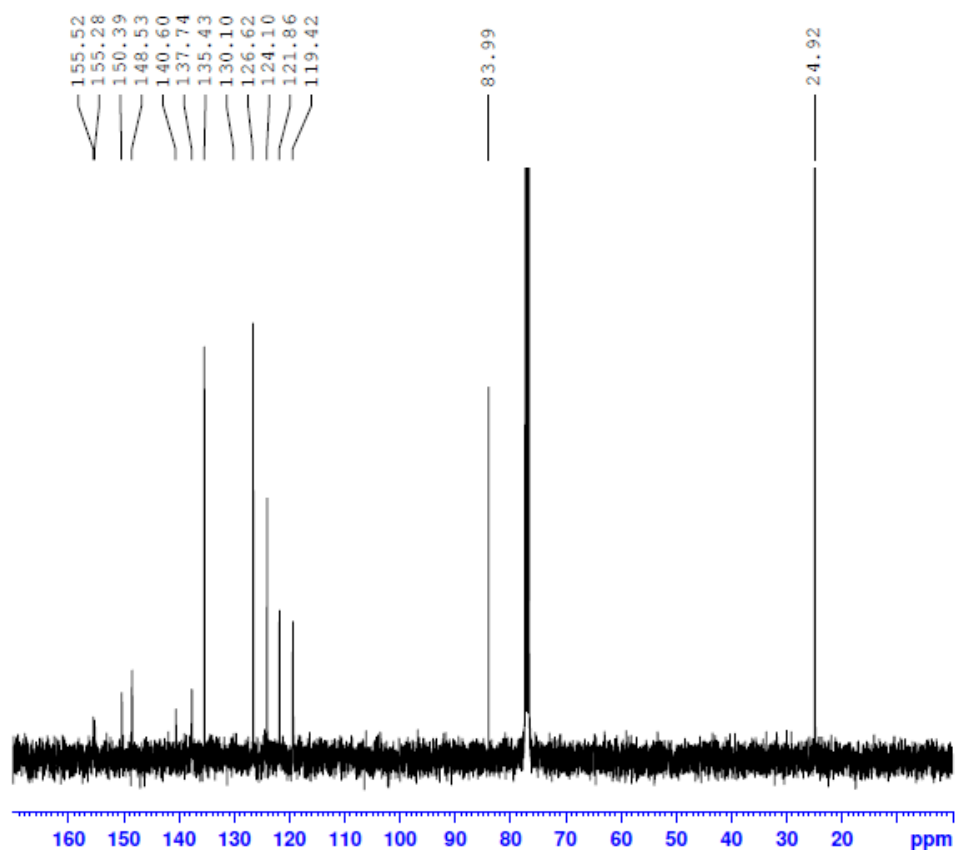
Figure A9 ^{13}C NMR of 4'-(4-Pinacolatoboronphenyl)-2,2':6',2''-terpyridine (**6**)
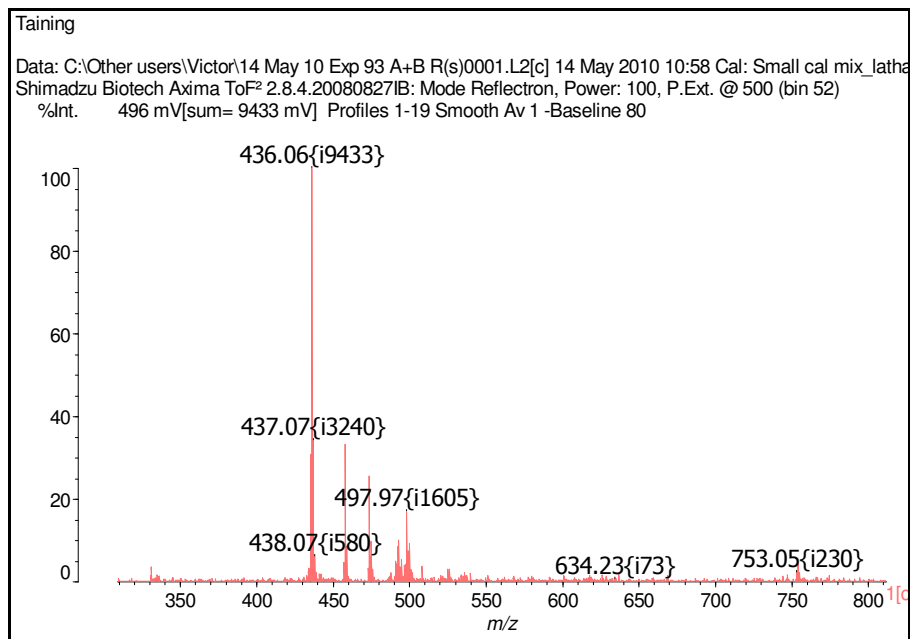
Figure A10 MALDI-TOF mass spectra of 4'-(4-Pinacolatoboronphenyl)-2,2':6',2''-terpyridine (**6**)

1,4-dibromo-2,5-bis(dodecyloxy)benzene (7). 2,5-Dibromohydroquinone (4 g, 15.06 mmol) was dissolved in absolute EtOH (150 ml) containing sodium hydroxide (0.92 g, 23 mmol) at RT under N_2. The reaction mixture was heated to 80 °C with constant stirring, the colour of solution changed from colourless to reddish brown. Dodecylbromide (7.2 ml, 30 mmol) was then added dropwise. After 24 h stirring under N_2, the reaction mixture was cooled to RT and filtered, and the precipitate was washed with MeOH to give **7** as a white solid (5.04 g, 55.4%). **^{1}H NMR (CDCl$_3$):** δ 7.082 (s, 2 H), 3.942 (t, J = 6.4 Hz, 4 H), 1.831–1.761 (m, 4 H), 1.547–1.452 (m, 4 H), 1.364–1.262 (br, 32 H), 0.879 (t, J = 6.8 Hz, 6 H). **^{13}C NMR (CDCl$_3$):** δ 150.09, 118.48, 111.14, 70.32, 31.94, 29.67, 29.66, 29.59, 29.56, 29.37, 29.31, 29.13, 25.94, 22.71, 14.14.
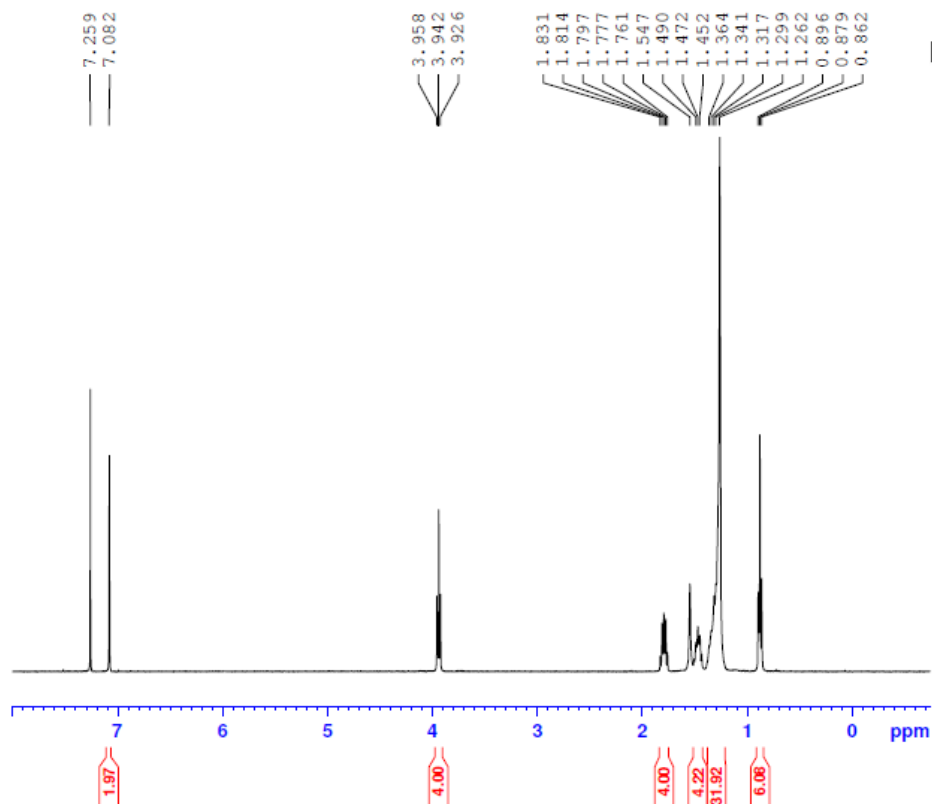
Figure A11 ^{1}H NMR of 1,4-dibromo-2,5-bis(dodecyloxy)benzene **(7)**

Figure A12 ^{13}C NMR of 1,4-dibromo-2,5-bis(dodecyloxy)benzene **(7)**

1,2-bis(dodecyloxy)benzene (8). Potassium hydroxide (19 g, 340.57 mmol) was added to

a solution of catechol (15 g, 136.23 mmol) in EtOH (150 ml). After stirring at 60 °C for

30 min, 1-bromododecane (82 ml, 340.57 mmol) was added dropwise into the reaction

mixture and the reaction mixture was stirred at 60 °C overnight. After cooling down to RT,

EtOH was removed on a rotary evaporator and the residue was extracted with DCM and

water. The organic layer was then dried over MgSO$_4$ and concentrated. The residue was

washed with MeOH to completely remove remaining 1-bromododecane and dried to give

8 as a white solid (56 g, 92%). **^{1}H NMR (CDCl$_3$):** δ 6.887 (s, 4 H), 3.991 (t, J = 6.8 Hz, 4

H), 1.776–1.847 (m, 4 H), 1.432–1.501 (m, 4 H), 1.267–1.351 (br, 32 H), 0.882 (t, J = 6.4

Hz, 6 H). **^{13}C NMR (CDCl$_3$):** δ 149.91, 121.66, 114.79, 69.95, 32.60, 30.38, 30.34, 30.32,

134

30.12, 30.04, 30.02, 26.73, 23.37, 14.79.

Figure A13 ^{1}H NMR spectrum of 1,2-bis(dodecyloxy)benzene **(8)**
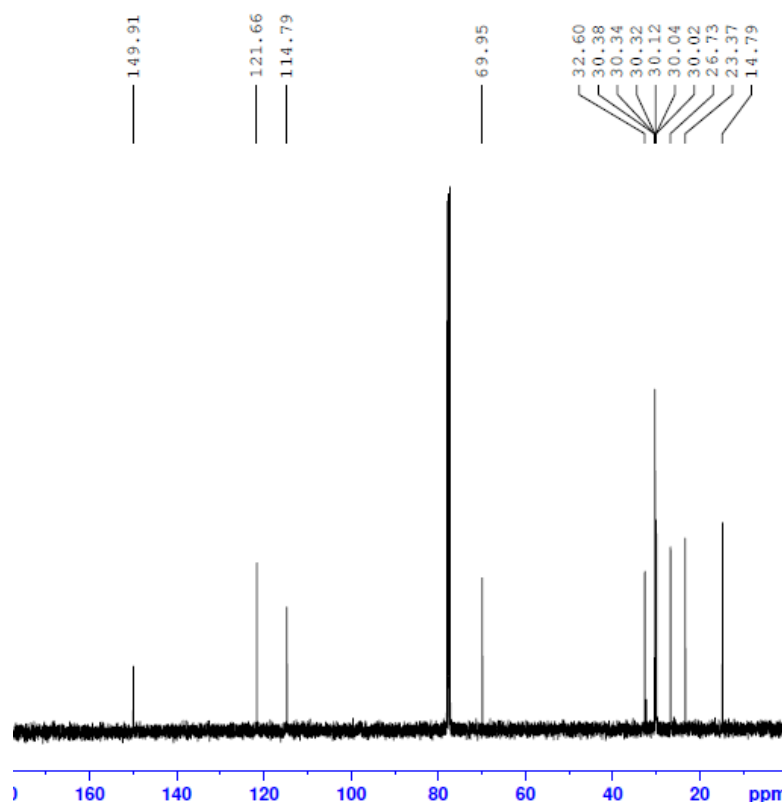
Figure A14 ^{13}C NMR spectrum of 1,2-bis(dodecyloxy)benzene **(8)**

1,2-bis(dodecyloxy)-4,5-dinitrobenzene (9). 8 (12 g, 27 mmol) was added in portions slowly to a mixture of 65% HNO_3 (80 ml) and 100% HNO_3 (50 ml) in an ice bath. The reaction mixture was then stirred overnight at RT. The reaction mixture was then poured into an ice-water mixture. The precipitate was collected by vacuum filtration, washed with water, and recrystallized using EtOH to afford **9** as a yellow solid (13.14 g, 92%).[1]**H NMR (CDCl₃):** δ 7.289 (s, 2 H), 4.092 (t, *J* = 6.4 Hz, 4 H), 1.829–1.898 (m, 4 H), 1.434–1.505 (m, 4 H), 1.240–1.259 (br, 32 H), 0.892 (t, *J* = 6.4 Hz, 6 H). [13]**C NMR (CDCl₃):** δ 151.79, 136.48, 107.88, 70.20, 31.93, 29.68, 29.66, 29.58, 29.55, 29.37, 29.24, 29.08, 28.69, 25.82, 22.70, 14.12.

7.289
7.259

4.108
4.092
4.075
3.747
3.730
3.712
3.695
1.898
1.882
1.864
1.845
1.829
1.505
1.489
1.471
1.451
1.434
1.259
1.240
0.892

7.289   7.259

7.30   7.25   ppm

2.000

2.00   3.82   3.63   3.93   47.68   7.31

9   8   7   6   5   4   3   2   1   ppm
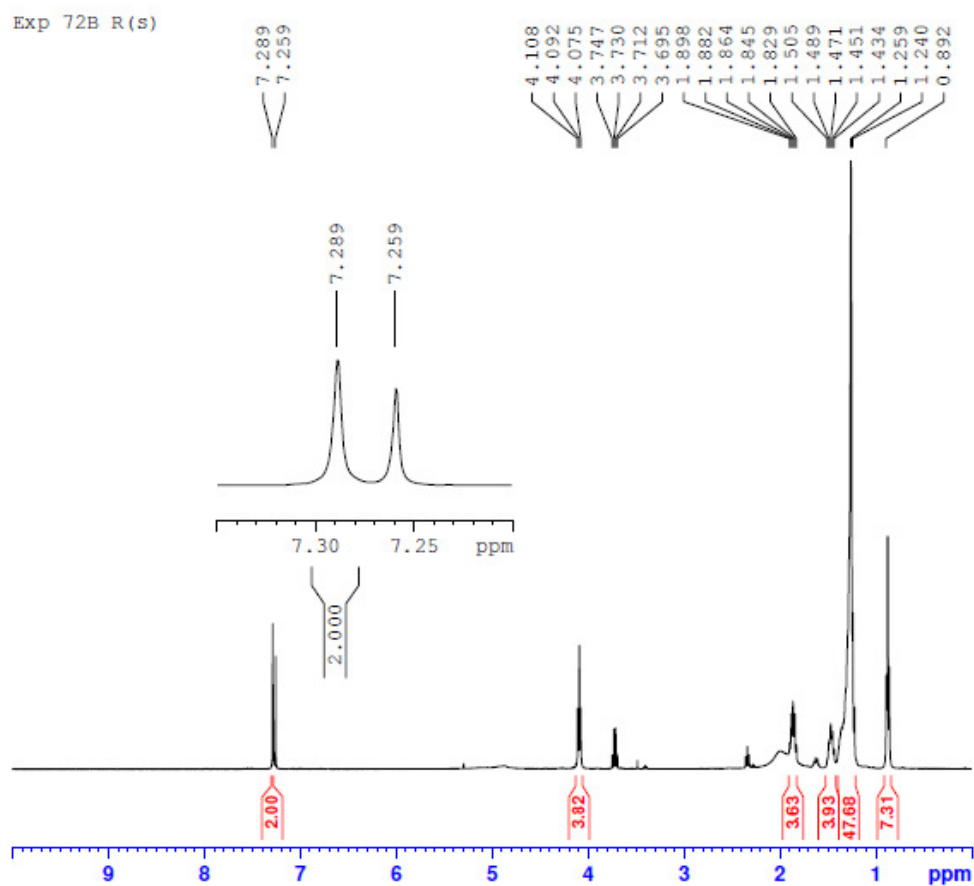
Figure A15   ^{1}H NMR spectrum of 1,2-bis(dodecyloxy)-4,5-dinitrobenzene **(9)**
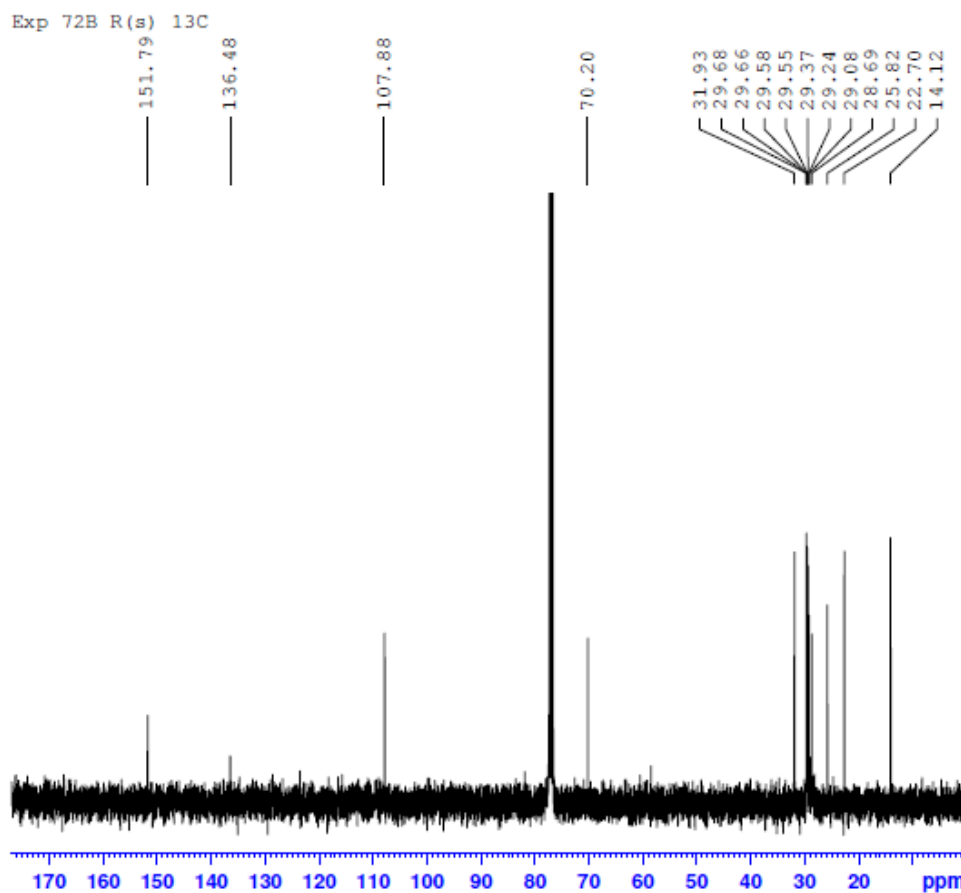
Figure A16 ^{13}C NMR spectrum of 1,2-bis(dodecyloxy)-4,5-dinitrobenzene **(9)**

4,7-dibromo-5,6-bis(dodecyloxy)benzo[c][1,2,5]thiadiazole (12).   Sn(II)Br$_2$ (5.7 g, 20.4 mmol) and **9** (1.5 g, 2.79 mmol) were dissolved in EtOH (40 ml) and concentrated hydrobromic acid (21 ml) in RBF and the reaction mixture was stirred at 100 ^{o}C for 18 h. After cooling to RT, the precipitate was collected by vacuum filtration and rinsed with hexane in order to give crude 4,5-bis(dodecyloxy)benzene-1,2-diamine dihydrobromide **10** as an air-sensitive purple solid. This solid was then transferred into an ice-cooled RBF, into which was injected anhydrous chloroform (15 ml) and thionyl bromide (2.16 ml, 27.9 mmol) followed by anhydrous pyridine (3.6 ml, 41.85 mmol). The temperature of the reaction mixture was then gradually raised to RT, followed by heating and stirring at

138

70 °C overnight. After cooling down to RT, the reaction mixture was then counter-extracted with 5% $NaHCO_3$ aqueous solution until neutralized, the $CHCl_3$ layer was then dried over $MgSO_4$, and concentrated, to give crude **11** which was contaminated with brominated derivatives. To a solution of the impure **11** (2.2 g, 4.35 mmol) in a mixture of DCM (100 ml) and acetic acid (52 ml) was added bromine (1.7 ml, 33.15 mmol). The resulting mixture was stirred in the dark for 2 days at 40 °C. The mixture was then poured in water, extracted with DCM, washed sequentially with water, saturated $NaHCO_3$ (aq), and 1M $Na_2S_2O_3$ (aq) and the organic layer was then dried over $MgSO_4$ and concentrated using a rotary evaporator. The residue mixture was subjected to column chromatography on silica gel eluting with 5% EA in hexane to obtain **12** as a white solid (2.6 g, 90%). **^{1}H NMR (CDCl$_3$):** δ 4.157 (t, J = 6.8 Hz, 4 H), 1.844–1.915 (m, 4 H), 1.494–1.563 (m, 4 H), 1.267 (br, 32 H), 0.878 (t, J = 6.8 Hz, 6 H). **^{13}C NMR (CDCl$_3$):** δ 154.52, 150.38, 106.27, 75.16, 31.94, 30.28, 29.70, 29.67, 29.64, 29.62, 29.45, 29.38, 26.00, 22.71, 14.13. **MALDI TOF MS**: m/z 666.46 (M+4). **Anal. Calcd.** for $C_{30}H_{50}Br_2N_2O_2S$: C, 54.38; H, 7.61; Br, 24.12; N, 4.23; O, 4.83, S, 4.84. Found: C, 54.80; H, 8.23; N, 4.23; S, 3.24. **HR ES$^+$-TOF MS**: calculated m/z: 663.2018 (M$^+$), found: m/z 663.2042 (M$^+$).

Figure A17   MALDI MS of crude 5,6-bis(dodecyloxy)benzo[c][1,2,5]thiadiazole **(11)**

Figure A18 ^{1}H NMR spectrum of 4,7-dibromo-5,6-bis(dodecyloxy)benzo[c][1,2,5]thiadiazole **(12)**
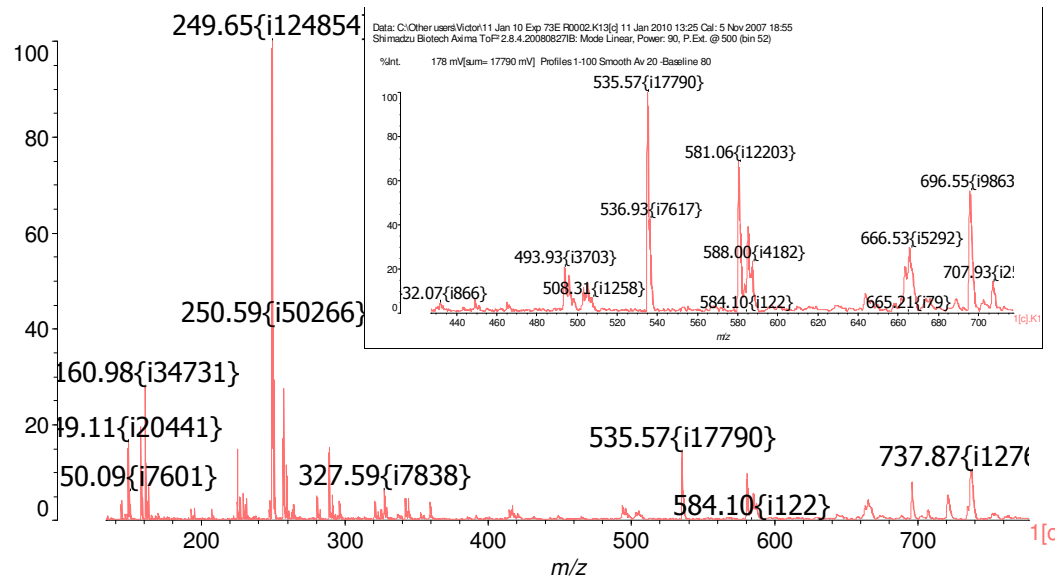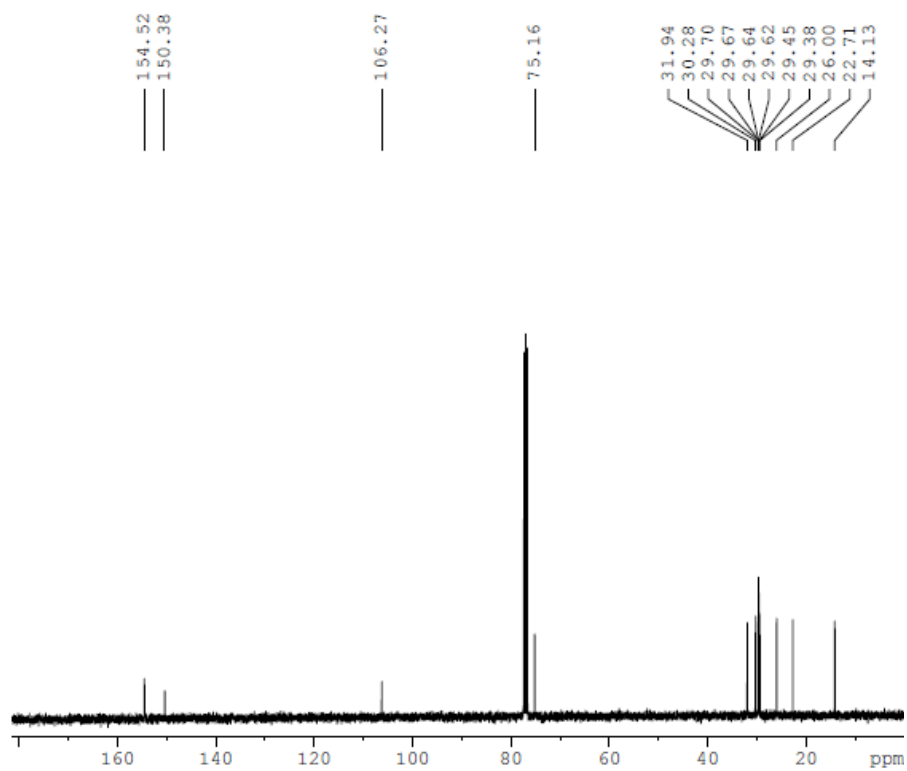
Figure A19 ^{13}C NMR spectrum of 4,7-dbromo-5,6-bis(dodecyloxy)benzo[c][1,2,5]thiadiazole **(12)**
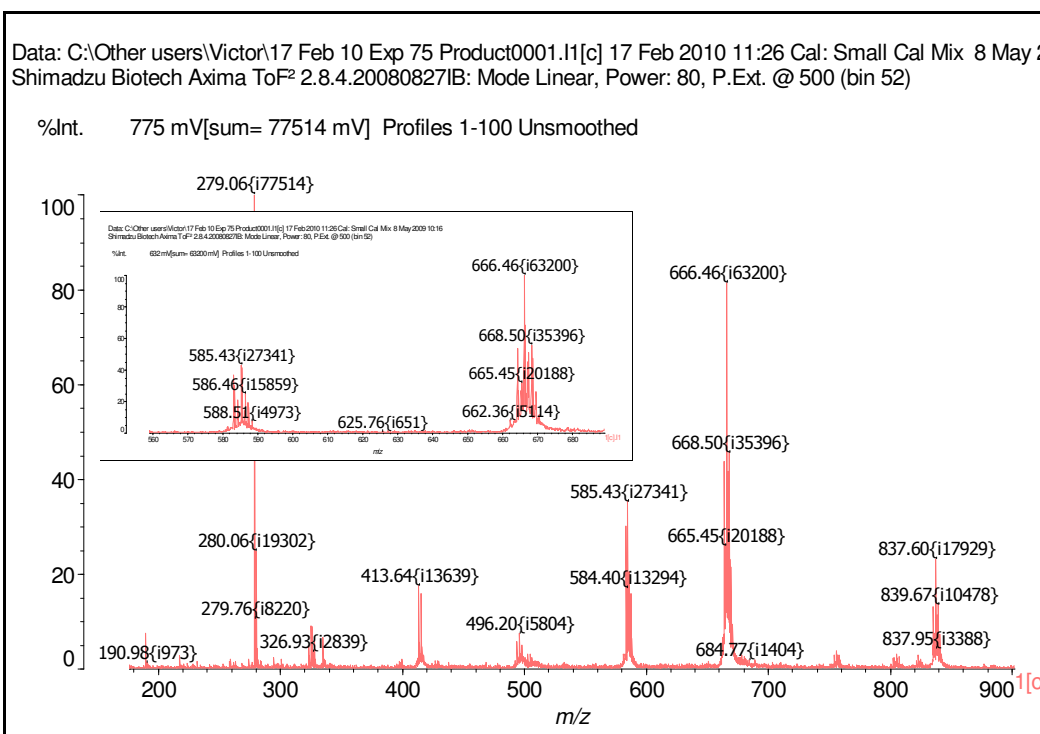
Figure A20   MALDI MS of 4,7-dbromo-5,6-bis(dodecyloxy)benzo[c][1,2,5]thiadiazole **(12)**

Monoadduct of 4'-(4-Pinacolatoboronphenyl)-2,2':6',2''-terpyridine with 1,4-dibromo-2,5-bis(dodecyloxy)benzene (13). 7 (0.42 g, 0.69 mmol), **6** (0.1 g, 0.23 mmol) and Pd(PPh$_3$)$_4$ (0.016 g, 0.014 mmol) were put into RBF and degassed using N$_2$. Aqueous K$_2$CO$_3$ (2 M, 10 ml) and THF (30 ml) were degassed using N$_2$ and then injected into the RBF. The reaction mixture was then stirred in the dark at 80 °C overnight. The reaction mixture was cooled to RT and THF was removed using a rotary evaporator. The reaction mixture was then extracted with DCM and water. The DCM layer was dried over MgSO$_4$, concentrated and the residue mixture was purified by column chromatography on alumina eluting with 10% EA in hexane. **13** was obtained as a white solid (140 mg, 50%).

^{1}H NMR (CDCl$_3$): δ 8.907 (s, 2 H), 8.804 (d, *J* = 4.4 Hz, 2 H), 8.771 (d, *J* = 4 Hz, 2 H), 8.042–7.978 (m, 4 H), 7.695 (d, *J* = 8.4 Hz, 2 H), 7.451 (t, *J* = 6.8 Hz, 2 H), 4.037 (t, *J* = 6.4 Hz, 2 H), 3.904 (t, *J* = 6.4 Hz, 2 H), 1.741–1.671 (m, 2 H), 1.546–1.473 (m, 2 H),

1.471–1.195 (br, 36 H), 0.877 (m, 6 H). ^{13}C NMR (CDCl$_3$): δ 155.19, 150.51, 150.28,

149.99, 148.19, 139.05, 138.24, 136.44, 130.13, 130.06, 127.02, 125.53, 124.22, 122.07,

119.46, 118.48, 116.28, 111.77, 70.38, 69.78, 31.93, 31.88, 29.66, 29.61, 29.37, 29.33,

29.26, 29.19, 26.03, 22.70, 22.67, 14.13, 14.11. **MALDI TOF MS**: m/z 832.19 (M),

755.06 (M-Br). **Anal. Calcd.** for C$_{51}$H$_{66}$BrN$_3$O$_2$: C, 73.54; H, 7.99; Br, 9.59; N, 5.04; O,

3.84. Found: C, 73.80; H, 10.63; N, 4.97. **HR ES$^+$-TOF MS**: calculated m/z: 832.4417

(M$^+$), found: m/z 832.4398 (M$^+$).
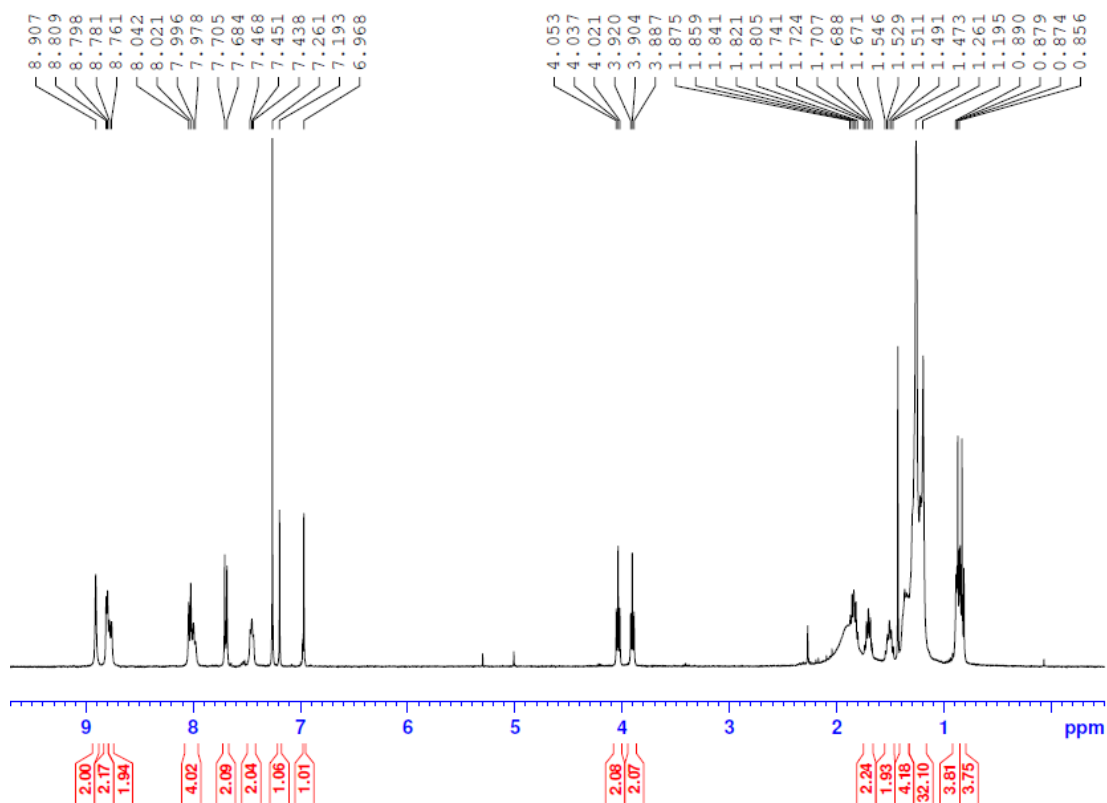
Figure A21 ^{1}H NMR spectrum of **13**
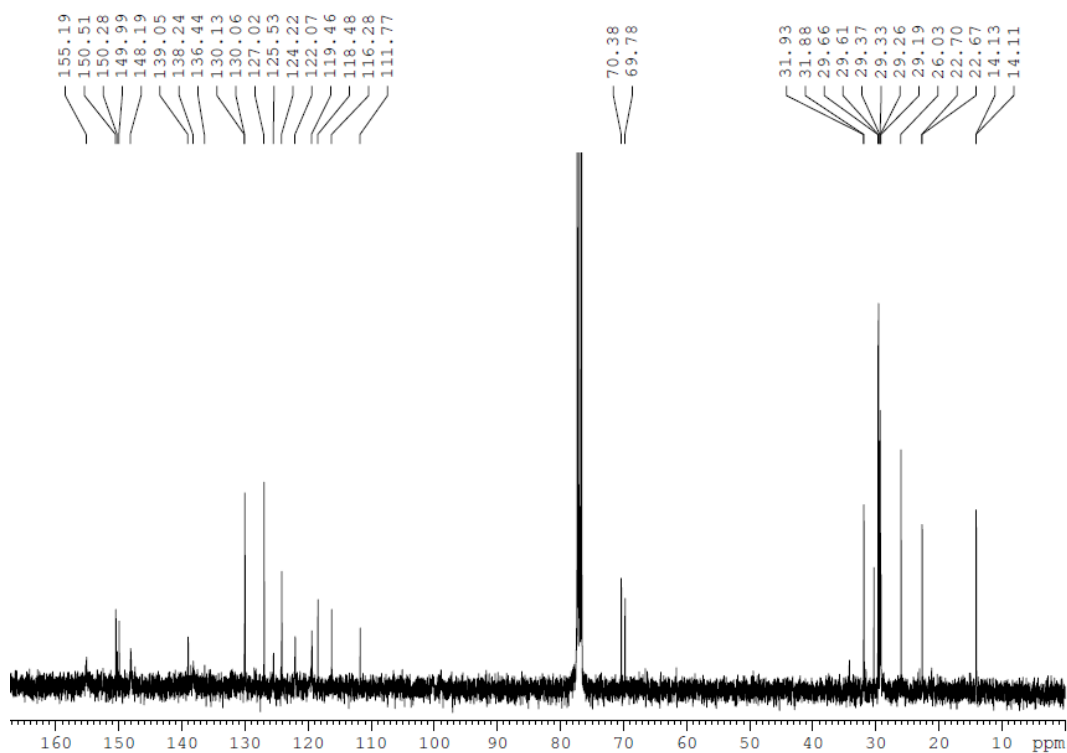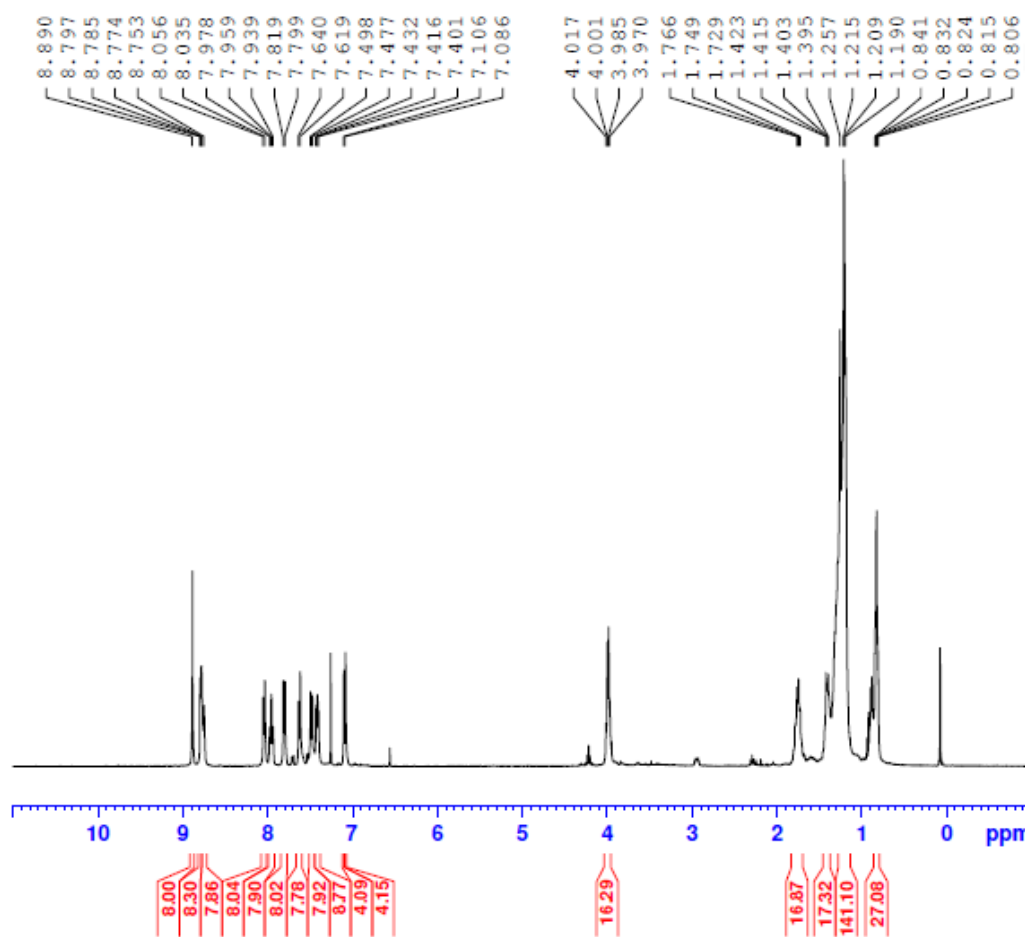
Figure A22 ^{13}C NMR spectrum of **13**
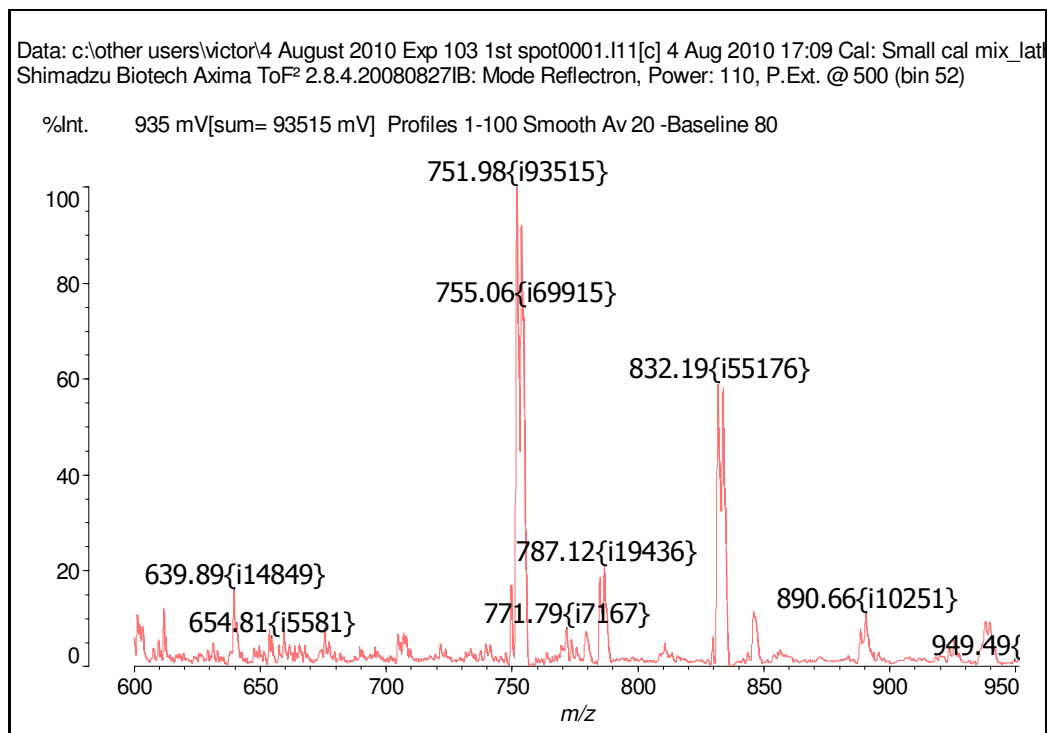
Figure A23   MALDI MS of **13**
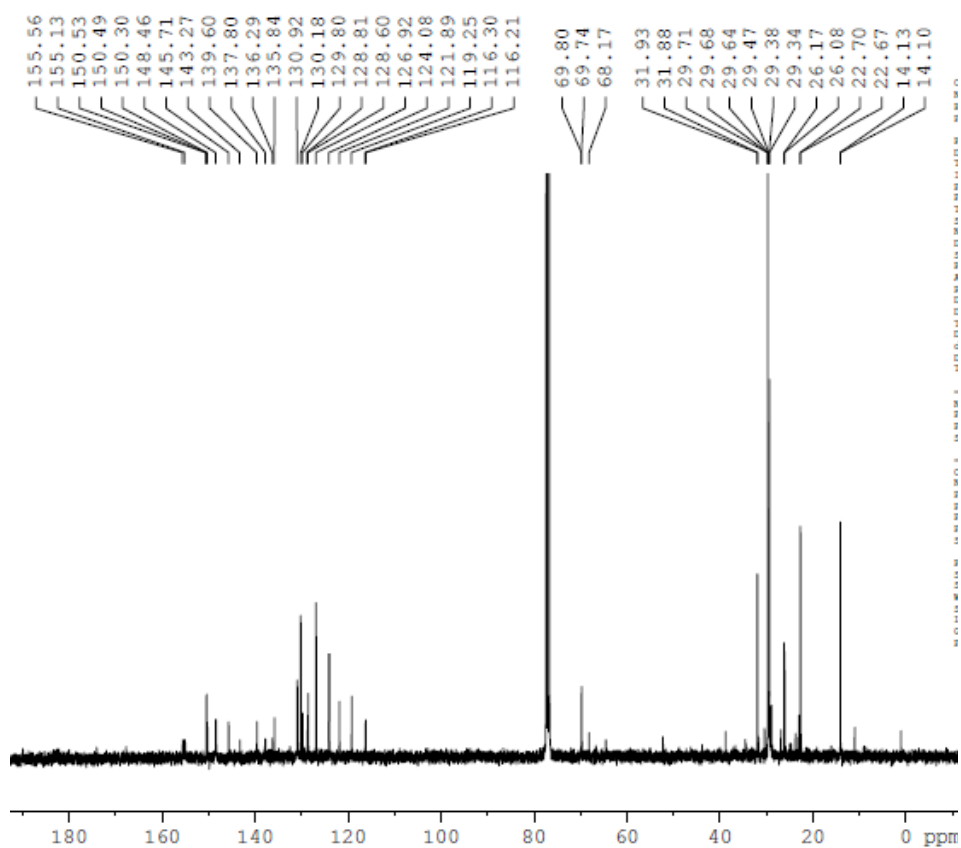
Monoadduct of 4'-(4-Pinacolatoboronphenyl)-2,2':6',2''-terpyridine with 4,7-dibromo-5,6-bis(dodecyloxy)benzo[c]thiadiazole (14). 12 (0.3 g, 0.46 mmol), **6** (0.08 g, 0.18 mmol) and Pd(PPh$_3$)$_4$ (0.021 g, 0.018 mmol) were put into a RBF and degassed using N$_2$. Aqueous K$_2$CO$_3$ (2 M, 10 ml) and THF (30 ml) were degassed using N$_2$ and then injected into the RBF. The reaction mixture was then stirred in the dark at 80 °C overnight. The reaction mixture was cooled to RT and THF was removed using a rotary evaporator. The reaction mixture was then extracted with DCM and water. The DCM layer was dried over MgSO$_4$, concentrated and the residue mixture was purified by column chromatography on alumina eluting with 10% EA in hexane. **14** was obtained as a light purple solid (80 mg, 50%). **^{1}H NMR (CDCl$_3$):** δ 8.920 (s, 2 H), 8.797–8.786 (m, 4 H), 8.128 (d, *J* = 8 Hz, 2 H), 7.986 (t, *J* = 7.6 Hz, 2 H), 7.853 (d, *J* = 8 Hz, 2 H), 7.435 (t, *J* = 6.4 Hz, 2 H), 4.255 (t, *J* = 6.8 Hz, 2 H), 3.852 (t, *J* = 6.8 Hz, 2 H), 1.618–1.514 (m, 4 H), 1.618–1.121 (br, 36 H), 0.880 (t, *J* = 7.2 Hz, 3 H), 0.820 (t, *J* = 7.2 Hz, 3 H). **^{13}C NMR (CDCl$_3$):** δ 155.96, 155.77, 154.63, 153.34, 151.32, 151.24, 149.86, 148.93, 138.18, 137.17, 134.00, 131.31, 127.09, 124.32, 123.94, 121.52, 119.02, 105.75, 75.01, 74.91, 31.95, 31.88, 29.65, 29.39, 29.32, 26.10, 25.91, 22.71, 22.67, 14.15, 14.11. **MALDI TOF MS**: m/z 896.45 (M+5). **Anal. Calcd.** for C$_{51}$H$_{64}$BrN$_5$O$_2$S: C, 68.74; H, 7.24; Br, 8.97; N, 7.86; O, 3.59; S, 3.60. Found: C, 68.73; H, 8.03; N, 7.58, S, 2.44. **HR ES$^+$-TOF MS**: calculated m/z: 890.4042 (M$^+$), found: m/z 890.4017 (M$^+$).
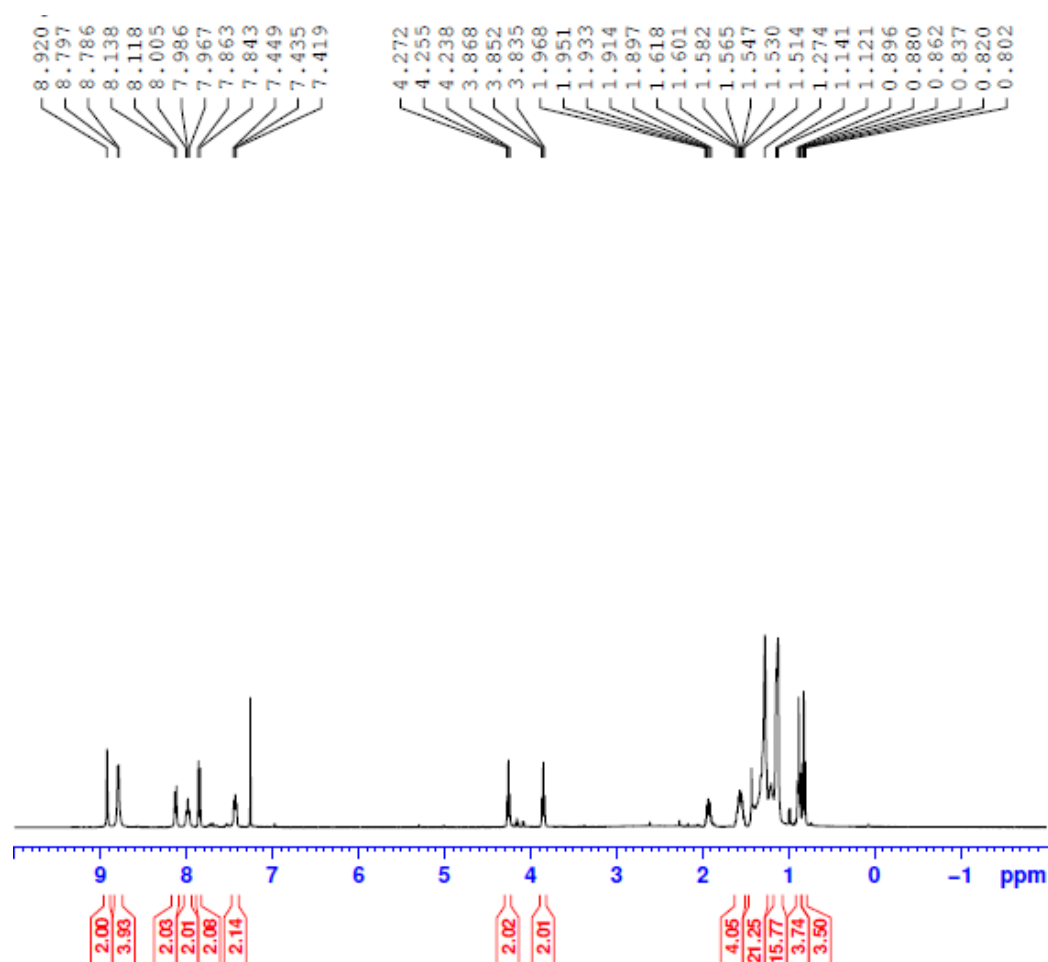
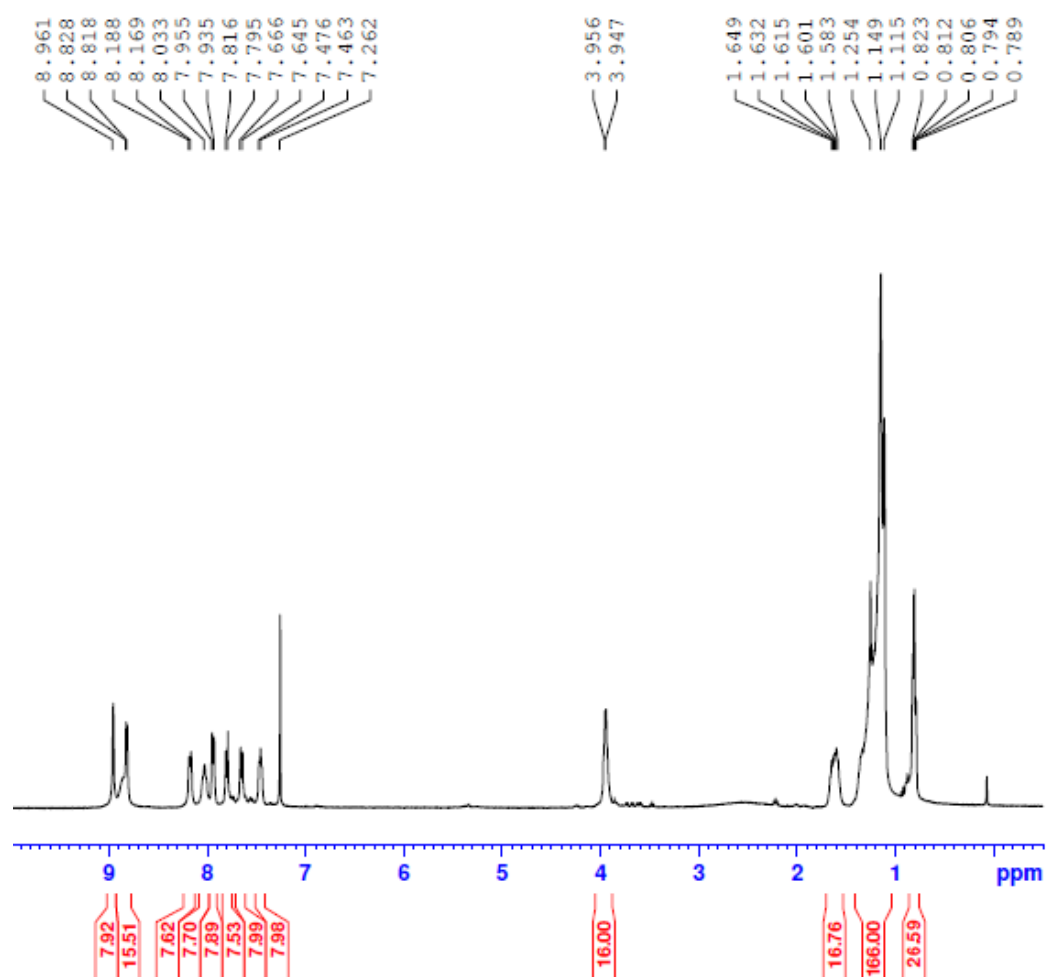**Figure A24** ^{1}H NMR spectrum of **14**
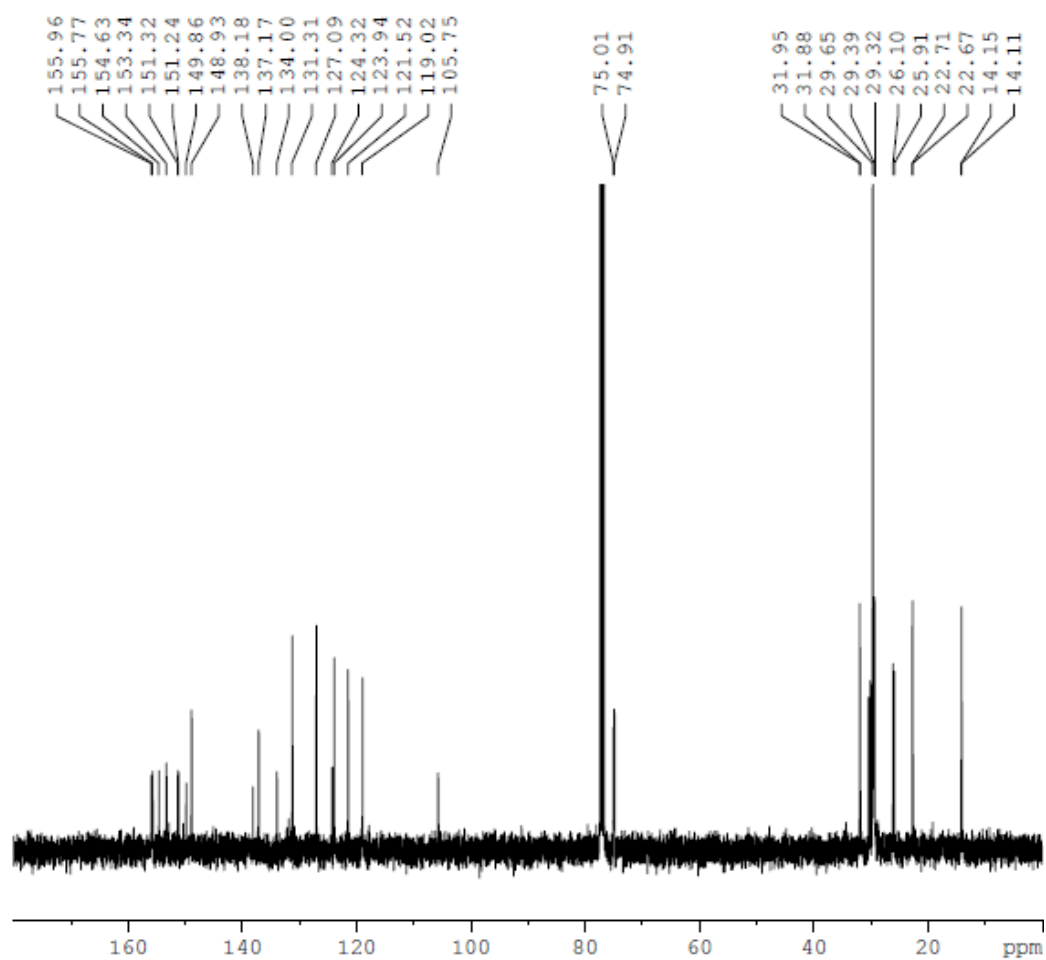
Figure A25 ^{13}C NMR spectrum of **14**
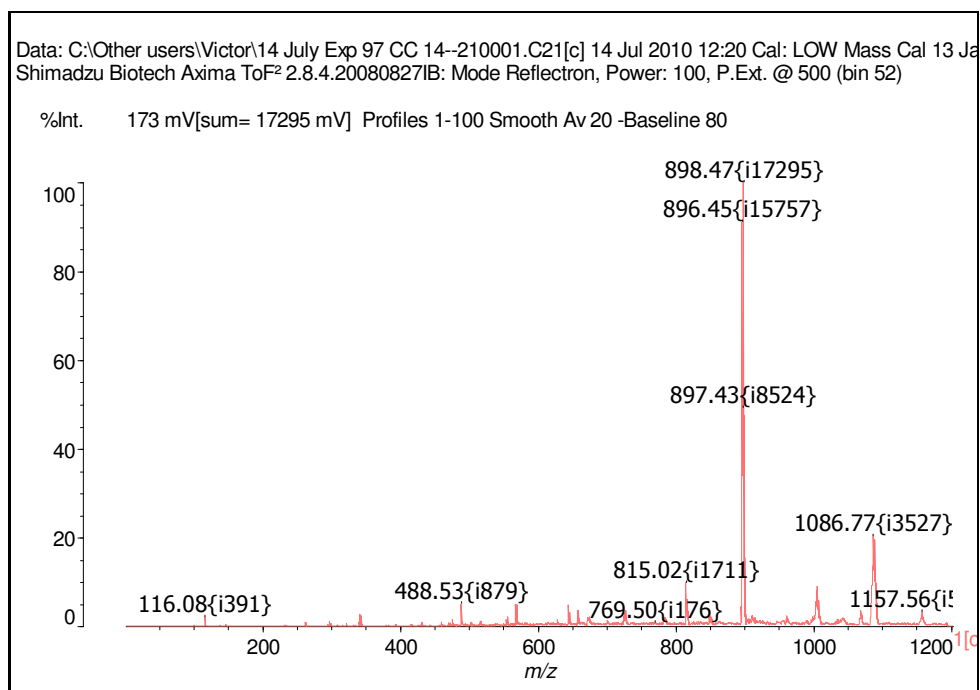
Figure A26   MALDI MS of **14**

Tetraadduct of (Monoadduct of 4'-(4-Pinacolatoboronphenyl)-2,2':6',2''-terpyridine with 1,4-dibromo-2,5-bis(dodecyloxy)benzene) with Tetrakis[4-(4',4',5',5'-tetramethyl-1',3',2'-dioxaborolane-phenyl)]methane (1). **4** (0.45 g, 0.54 mmol), **13** (2.8 g, 3.35 mmol) and Pd(PPh$_3$)$_4$ (0.063 g, 0.054 mmol) were put into RBF and degassed using N$_2$. Aqueous K$_2$CO$_3$ (2 M, 60 ml) and toluene (100 ml) were degassed using N$_2$ and then injected into the RBF. The reaction mixture was then stirred in the dark at 88 °C for 3 days. The reaction mixture was cooled to RT and toluene was removed using a rotary evaporator. The reaction mixture was then extracted with DCM and water. The DCM layer was dried over MgSO$_4$, concentrated and the residue mixture was purified by column chromatography on alumina eluting with 20% EA in hexane. **1** was obtained as an off-white glassy solid (700 mg, 40%). **^{1}H NMR (CDCl$_3$):** δ 8.890 (s, 8 H), 8.797–8.753 (m, 16 H), 8.036 (d, *J* = 8 Hz, 8 H), 7.959 (t, *J* =8 Hz, 8 H),

7.809 (d, *J* = 8 Hz, 8 H), 7.630 (d, *J* = 8 Hz, 8 H), 7.488 (d, *J* = 8 Hz, 8 H), 7.416 (t, *J* =8

Hz, 8 H), 7.106 (s, 4 H), 7.086 (s, 4 H), 3.993 (t, *J* = 9.6 Hz, 16 H), 1.766–1.729 (m, 16

H), 1.423–1.395 (m, 16 H), 1.257–1.190 (br, 128 H), 0.841–0.806 (m, 24 H). ^{13}**C NMR**

(CDCl$_3$): δ 155.56, 155.13, 150.53, 150.49, 150.30, 148.46, 145.71, 143.27, 139.60,

137.80, 136.29, 135.84, 130.92, 129.80, 128.81, 128.60, 126.92, 124.08, 121.89, 119.25,

116.30, 116.21, 69.80, 69.74, 68.17, 31.93, 31.88, 29.71, 29.68, 29.64, 29.47, 29.38,

29.34, 26.17, 26.08, 22.70, 22.67, 14.13, 14.10. **MALDI TOF MS**: m/z 3328.6 (M).

Anal. Calcd. for C$_{229}$H$_{280}$N$_{12}$O$_8$: C, 82.63; H, 8.48; N, 5.05; O, 3.85. Found: C, 82.15; H,

11.71; N, 5.17.

Figure A27 ^{1}H NMR spectrum of **1**

Figure A28 ^{13}C NMR spectrum of **1**

Data: C:\Other users\Victor\15 Sep Exp 106 4th spot0001.B10[c] 15 Sep 2010 10:52 Cal: Small cal mix_latha 1
Shimadzu Biotech Axima ToF² 2.8.4.20080827IB: Mode Reflectron, Power: 112, P.Ext. @ 3328 (bin 115)

%Int.   9.6 mV[sum= 1156 mV] Profiles 1-120 Smooth Av 80 -Baseline 120
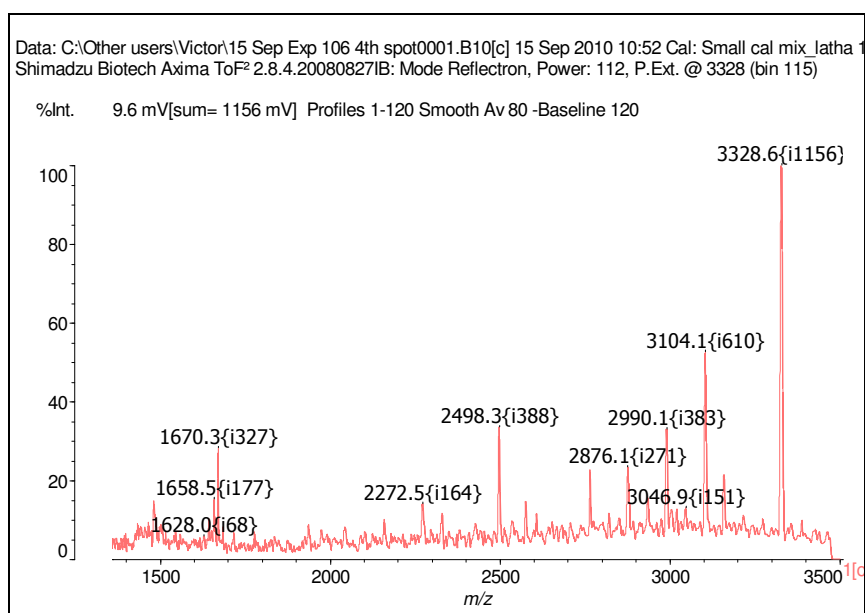
Figure A29   MALDI MS of **1**

Tetraadduct of (Monoadduct of 4'-(4-Pinacolatoboronphenyl)-2,2':6',2''-terpyridine with 4,7-dibromo-5,6-bis(dodecyloxy)benzo[c]thiadiazole) with Tetrakis[4-(4',4',5',5'-tetramethyl-1',3',2'-dioxaborolane-phenyl)]methane (2). **4** (0.45 g, 0.54 mmol), **14** (2.9 g, 3.29 mmol), $Pd(PPh_3)_4$ (0.063 g, 0.054 mmol) were put into RBF and degassed using N_2. Aqueous K_2CO_3 (2 M, 60 ml) and toluene (100 ml) were degassed using N_2 and then injected into the RBF. The reaction mixture was then stirred in the dark at 88 °C for 3 days. The reaction mixture was cooled to RT and toluene was removed using a rotary evaporator. The reaction mixture was then extracted with DCM and water. The DCM layer was dried over $MgSO_4$, concentrated and the residue mixture was purified by column chromatography on alumina eluting with 20% EA in hexane. **2** was obtained as a light purple glassy solid (550 mg, 30%). **^{1}H NMR (CDCl$_3$):** δ 8.961 (s, 8 H), 8.828–8.818 (m, 16 H), 8.179 (d, J = 7.6 Hz, 8 H), 8.033 (s, 8 H), 7.945 (d, J = 8 Hz, 8 H), 7.806 (d, J = 8.4 Hz, 8 H), 7.656 (d, J = 8 Hz, 8 H), 7.47 (s, 8 H), 3.952 (s, 16 H), 1.649–1.583 (m, 16 H), 1.254–1.115 (br, 144 H), 0.823–0.789 (m, 24 H). **^{13}C NMR (CDCl$_3$):** δ 155.20, 153.47, 153.44, 152.15, 150.16, 148.41, 146.34, 137.88, 135.04, 131.83, 131.54, 131.28, 129.99, 127.06, 124.58, 124.15, 123.87, 121.95, 119.35, 74.78, 74.68, 65.11, 31.91, 31.87, 30.30, 29.70, 29.67, 29.56, 29.46, 29.36, 29.31, 26.03, 22.67, 22.65, 14.11, 14.09. **Anal. Calcd.** for $C_{229}H_{272}N_{20}O_8S_4$: C, 77.24; H, 7.70; N, 7.87; O, 3.59; S, 3.60. Found: C, 77.19; H, 7.83; N, 7.56; S, 1.88.

Figure A30   ¹H NMR spectrum of **2**
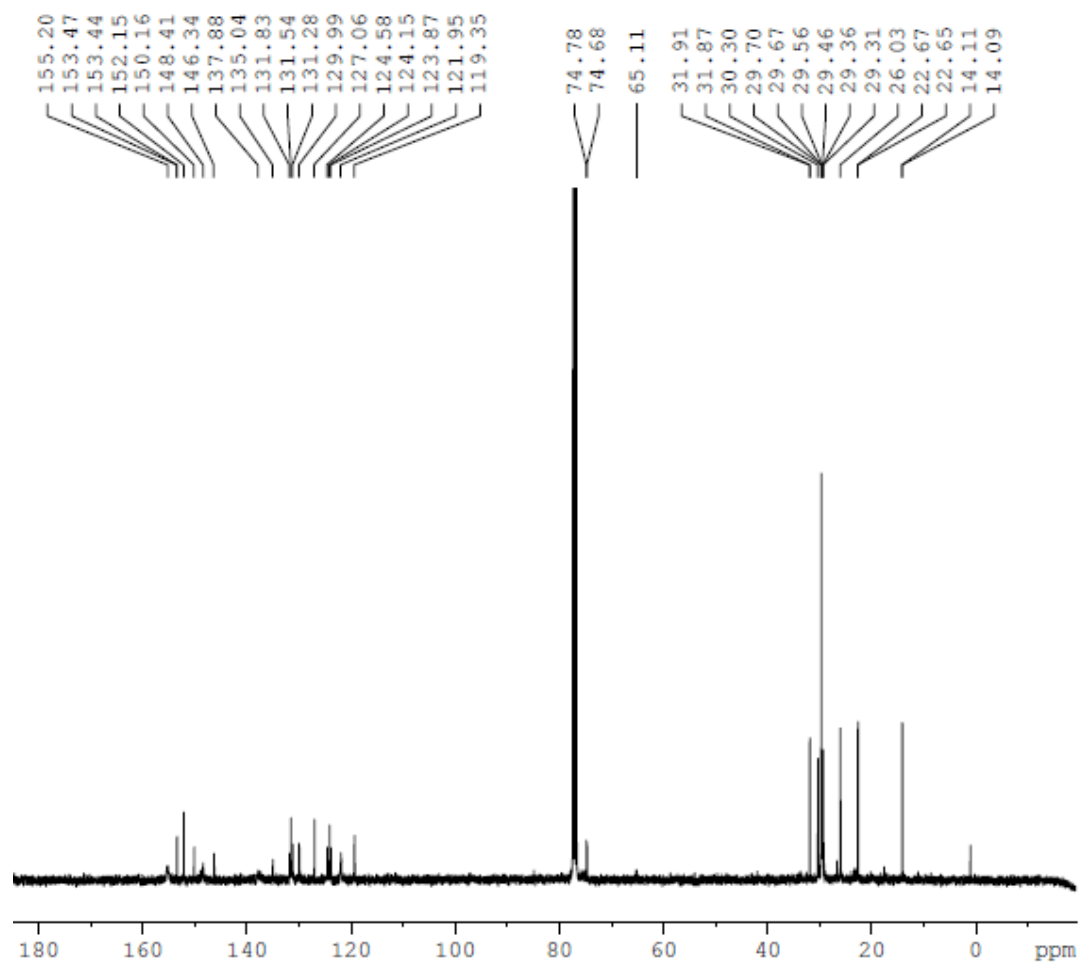
Figure A31 ^{13}C NMR spectrum of **2**
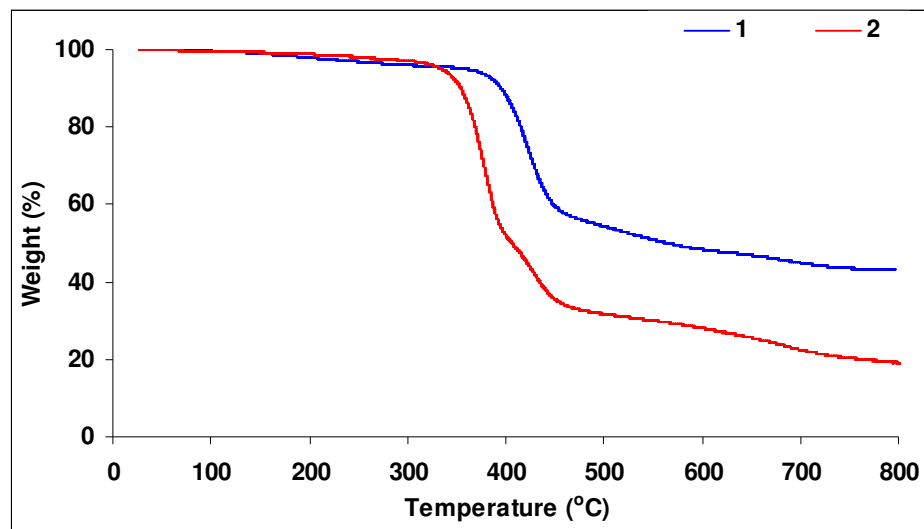
Figure A32   TGA scans of **1** and **2**
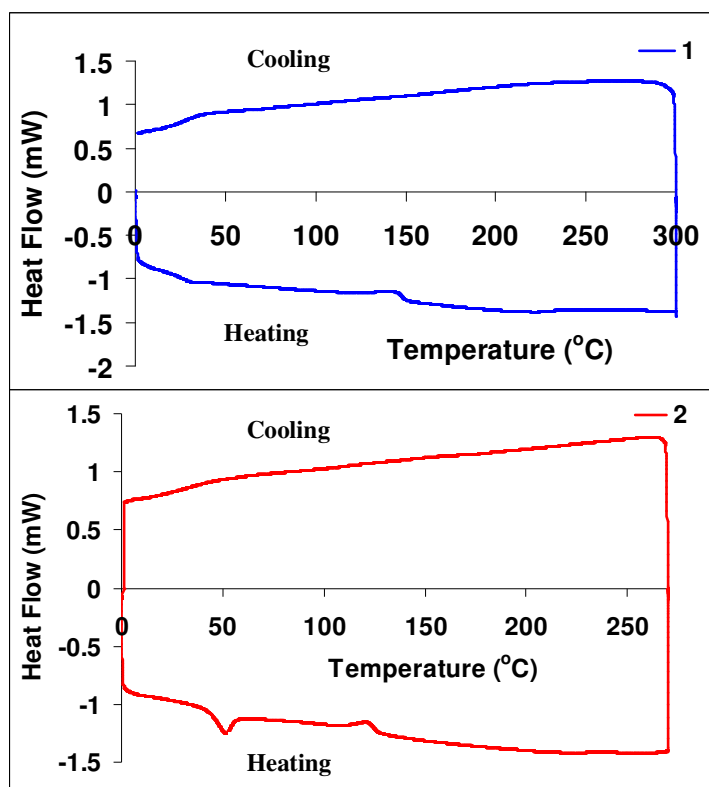
Figure A33   DSC scans of **1** and **2**
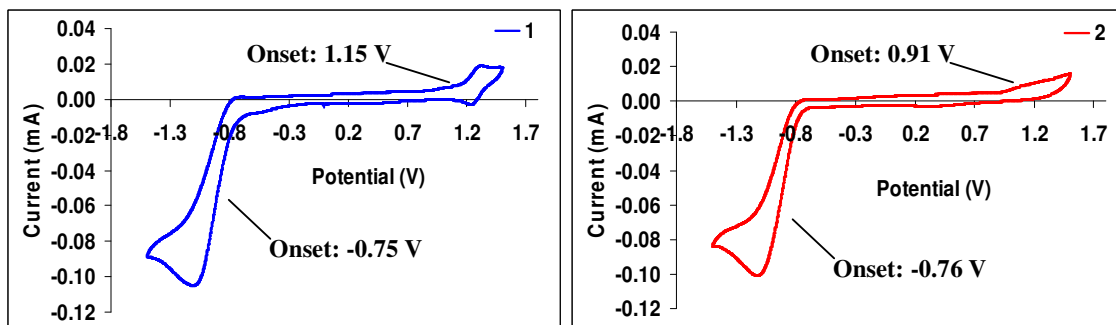
Figure A34   Cyclic voltammograms of **1** and **2** on a platinum electrode (wire) in 0.1 M Bu$_4$NPF$_6$, DCM

solution with a sweep rate of 100 mV/s

5,6-bis(dodecyloxy)-4,7-di(thiophen-2-yl)benzo[c][1,2,5]thiadiazole (20). 12 (2.6 g,

3.94 mmol), thiophene-2-boronic acid (1.3 g, 9.8 mmol) and Pd(PPh$_3$)$_4$ (0.48 g, 0.394

mmol) were put into RBF and degassed using N$_2$. Aqueous Na$_2$CO$_3$ (2 M, 80 ml) and

THF (120 ml) were degassed using N$_2$ and then injected into the RBF. The reaction

mixture was stirred in the dark at 80 °C. After 48 h, more thiophene-2-boronic acid (0.7 g) and Pd(PPh$_3$)$_4$ (0.48 g) were added to the mixture and the reaction was continued for another 24 h. The reaction mixture was cooled to RT and THF was removed using a rotary evaporator. The reaction mixture was then extracted with CHCl$_3$ and water. The CHCl$_3$ layer was dried over MgSO$_4$ and concentrated using a rotary evaporator. The residue mixture was subjected to column chromatography on silica gel with a solvent mixture of 20% DCM in hexane to obtain **20** as a yellow-green oily-solid (2.2 g, 83%).

^{1}H NMR (CDCl$_3$): δ 8.466 (d, J = 3.2 Hz, 2 H), 7.504 (d, J = 4.8 Hz, 2 H), 7.234 (t, J = 4.6 Hz, 2 H), 4.106 (t, J = 7.2 Hz, 4 H), 1.881-1.954 (m, 4 H), 1.432-1.452 (m, 4 H), 1.271 (br, 32 H), 0.884 (t, J = 6.8 Hz, 6 H). **^{13}C NMR (CDCl$_3$):** δ 151.983, 151.016, 134.127, 130.548, 127.310, 126.764, 117.634, 74.38, 31.95, 30.34, 29.72, 29.68, 29.65, 29.57, 29.39, 25.97, 22.71, 14.13. **MALDI TOF MS**: m/z 671.51 (M+2H). **Anal. Calcd. for** C$_{38}$H$_{56}$N$_2$O$_2$S$_3$: C, 68.22; H, 8.44; N, 4.19; O, 4.78; S, 14.38. Found: C, 68.55; H, 9.22; N, 4.21; S, 9.39. **HR ES$^+$-TOF MS**: calculated m/z: 669.3582 (M$^+$), found: m/z 669.3564 (M$^+$).
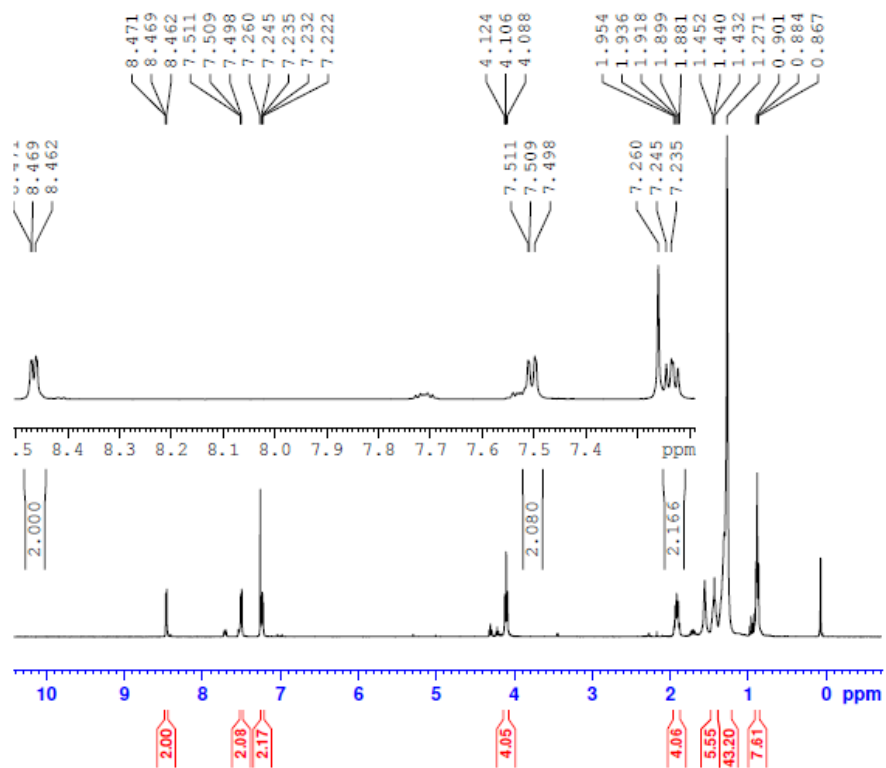
Figure A35 ^{1}H NMR spectrum of 5,6-bis(dodecyloxy-4,7-di(thiophen-2-yl)-benzo[c][1,2,5]thiadiazole

(20)

Figure A36 ^{13}C NMR spectrum of 5,6-bis(dodecyloxy)-4,7-di(thiophen-2-yl)benzo[c][1,2,5]thiadiazole

(20)

Figure A37 MALDI MS of 5,6-bis(dodecyloxy)-4,7-di(thiophen-2-yl)benzo[c][1,2,5]thiadiazole **(20)**

157

4,7-bis(5-bromothiophen-2-yl)-5,6-bis(dodecyloxy)benzo[c][1,2,5]thiadiazole (21). 20 (0.31 g, 0.47 mmol) was dissolved in THF (20 ml). The reaction mixture was then placed in an ice bath and was added with NBS (0.21 g, 1.175 mmol). The reaction mixture was then stirred for 18 h, with the temperature being gradually raised to RT. The reaction mixture was then extracted with DCM and water. The DCM layer was dried over $MgSO_4$ and concentrated to give **21** as a reddish orange solid (0.38 g, 97%). **^{1}H NMR (CDCl$_3$):** δ 8.364 (d, J = 4.4 Hz, 2 H), 7.172 (d, J = 4.4 Hz, 2 H), 4.120 (t, J = 7.2 Hz, 4 H), 1.92–1.957 (m, 4 H), 1.422–1.442 (m, 4 H), 1.262–1.275 (br, 32 H), 0.884 (t, J = 6 Hz, 6 H). **^{13}C NMR (CDCl$_3$):** δ 151.497, 150.411, 135.708, 131.015, 129.689, 117.010, 115.466, 74.59, 31.95, 30.28, 29.73, 29.69, 29.65, 29.53, 29.45, 29.40, 25.94, 22.72, 14.14. **MALDI TOF MS**: m/z 828.43 (M+2H). **Anal. Calcd.** for $C_{38}H_{54}Br_2N_2O_2S_3$: C, 55.20; H, 6.58; Br, 19.33; N, 3.39; O, 3.87; S, 11.63. Found: C, 54.89; H, 6.85; N, 3.10; S, 12.07.
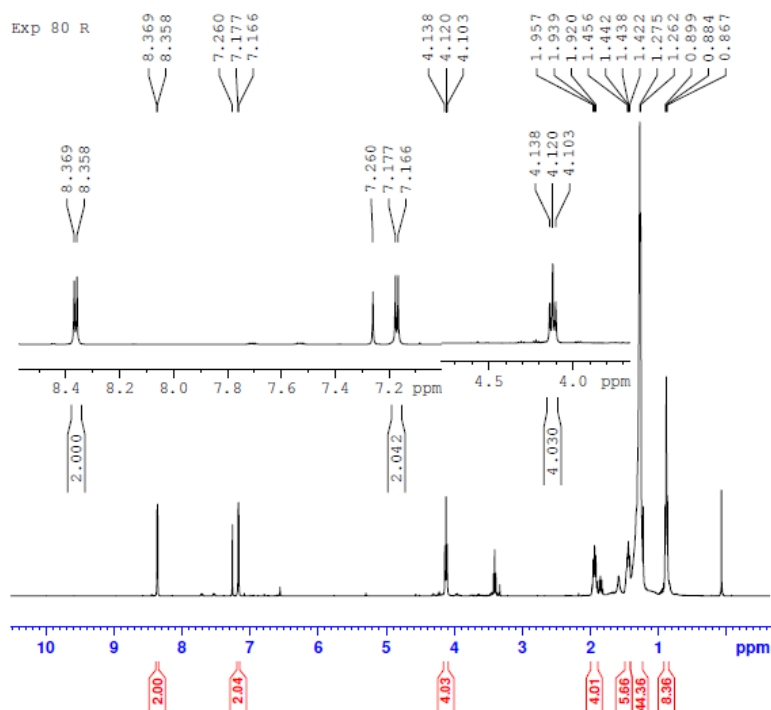
Figure A38 ^{1}H NMR spectrum of

4,7-bis(5-bromothiophen-2-yl)-5,6-bis(dodecyloxy)benzo[c][1,2,5]thiadiazole **(21)**
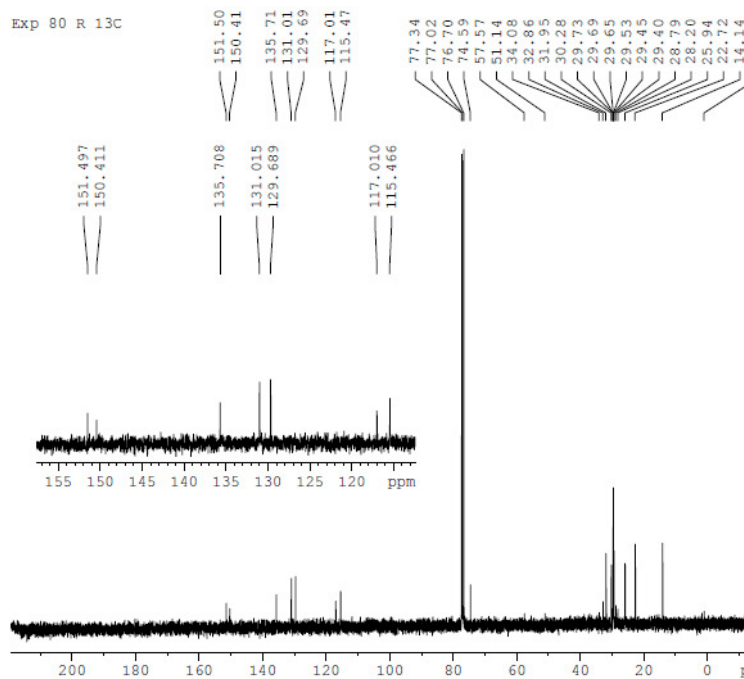
Figure A39 ^{13}C NMR spectrum of 4,7-bis(5-bromothiophen-2-yl)-5,6-bis(dodecyloxy)-

benzo[c][1,2,5]thiadiazole **(21)**
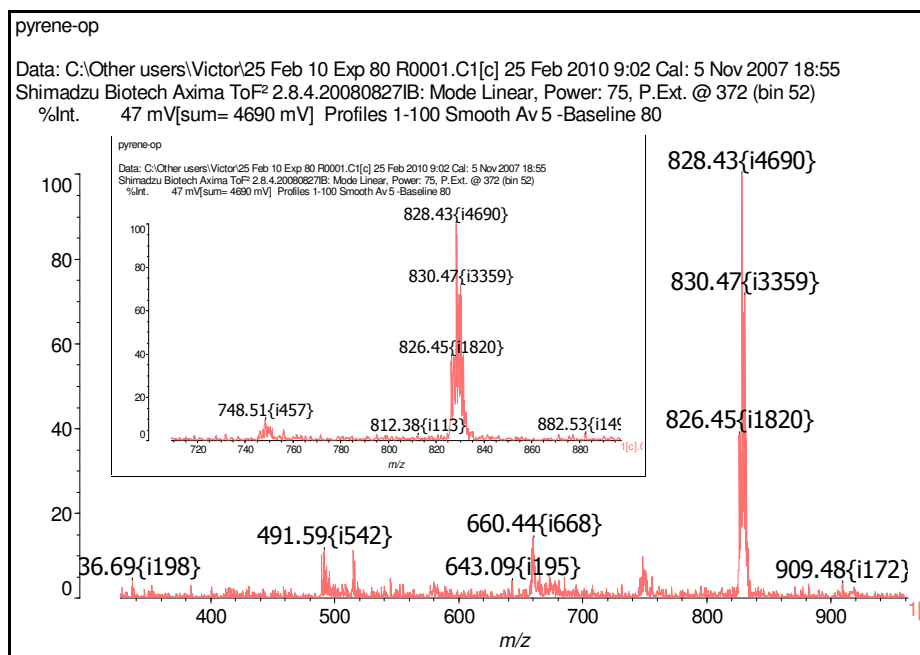
Figure A40 MALDI MS of

4,7-bis(5-bromothiophen-2-yl)-5,6-bis(dodecyloxy)benzo[c][1,2,5]thiadiazole **(21)**

2,5-bis(tributylstannyl)thiophene (22). 2,5-dibromothiophene (1 ml, 8.88 mmol) was injected dropwise into a solution of dry THF (15 ml) and 1.6 M BuLi in hexane (17 ml, 26.62 mmol) at -78 °C under N_2. The reaction mixture was then stirred at -78 °C for 10 min under N_2. The temperature of the reaction mixture was then gradually raised to RT (white suspension gradually formed), then was stirred at -78 °C again for 10 min. Tributyl tin chloride (7.2 ml, 26.62 mmol) was injected dropwise into the reaction mixture and it was stirred at -78 °C for 30 min. The reaction mixture was then stirred at RT overnight. The reaction mixture was extracted (one time) with ether (100 ml) and DI water (400 ml) and the ether layer was concentrated. The bis-tin **22** was obtained as a light brown liquid which was immediately put inside fridge for storage and used for polymer synthesis without purification.

2,5-bis(tributylstannyl)thieno[3,2-b]thiophene (23). Thieno[3,2-b]thiophene (1.5 g, 10.69 mmol) in a dry THF (7 ml) solution was injected dropwise into a solution of dry THF (20 ml) and 1.6 M BuLi in hexane (20 ml, 35 mmol) at -78 °C under N_2. The reaction mixture (light yellow) was then stirred at -78 °C for 10 min. The temperature of the reaction mixture was then gradually raised to RT (white suspension gradually formed), which stirred at -78 °C again for 10 min. Tributyl tin chloride (9 ml, 32 mmol) was injected dropwise into the reaction mixture and it was stirred at -78 °C for 30 min. The reaction mixture was then stirred at RT overnight. The reaction mixture was extracted (one time) with ether (100 ml) and DI water (800 ml) and the ether layer was concentrated. **23** was obtained as a light green liquid which was immediately put inside fridge for storage and used for polymer synthesis without purification.

4,4'-dioctyl-5,5'-bis(tributyltin)-dithieno[3,2-b:2',3'-d]silole **(24).**

4,4'-Dioctyl-dithieno[3,2-b:2',3'-d]silole (5 g, 12 mmol) in a dry THF (10 ml) solution was injected dropwise into a solution of dry THF (20 ml) and 1.6 M BuLi in hexane (22 ml, 36 mmol) at -78 °C under N_2. The reaction mixture was then stirred at -78 °C for 10 min. The temperature of the reaction mixture was then gradually raised to RT, which stirred at -78 °C again for 10 min. Tributyl tin chloride (10 ml, 36 mmol) was injected dropwise into the reaction mixture and it was stirred at -78 °C for 30 min. The reaction mixture was then stirred at RT overnight. The reaction mixture was extracted (one time) with ether (100 ml) and DI water (800 ml) and the ether layer was concentrated. **24** was

obtained as a brown liquid which was immediately put inside fridge for storage and used for polymer synthesis without purification.

Poly {5,6-bis(dodecyloxy)-4-(thiophen-2-yl)benzo[c][1,2,5]thiadiazole} (P1). 12 (0.3 g, 0.45 mmol), crude **22** (0.3 g, 0.45 mmol) and $(Ph_3P)_2PdCl_2$ (0.032 g, 0.045 mmol) were put inside RBF with balloon degassing using N_2. 1,4-Dioxane (30 ml) was injected into the reaction mixture. The reaction mixture was then heated at 80 °C for 3 days. During 2nd day, more crude **22** (0.3 g, 0.45 mmol) was added into the mixture. $CHCl_3$ and dilute aqueous HCl were added to the reaction mixture and the reaction mixture was stirred at RT overnight. The reaction mixture was then extracted with water and $CHCl_3$. The $CHCl_3$ layer was dried over $MgSO_4$, concentrated by a rotary evaporator and the reaction mixture was stirred in MeOH (to remove starting material or oligomers) at RT. After 2 days of stirring, MeOH was decanted off. Acetone was added (to remove oligomers and low M_w polymer) and the reaction mixture was stirred at RT overnight. Acetone was then decanted off. The remaining insoluble solid was dissolved in DCM, followed by filtration and the filtrate was collected and concentrated by using a rotary evaporator. **P1** (160 mg) was collected as a dark purple solid. GPC ($CHCl_3$): M_w = 4888, PDI = 3606.

P1b (Stille)
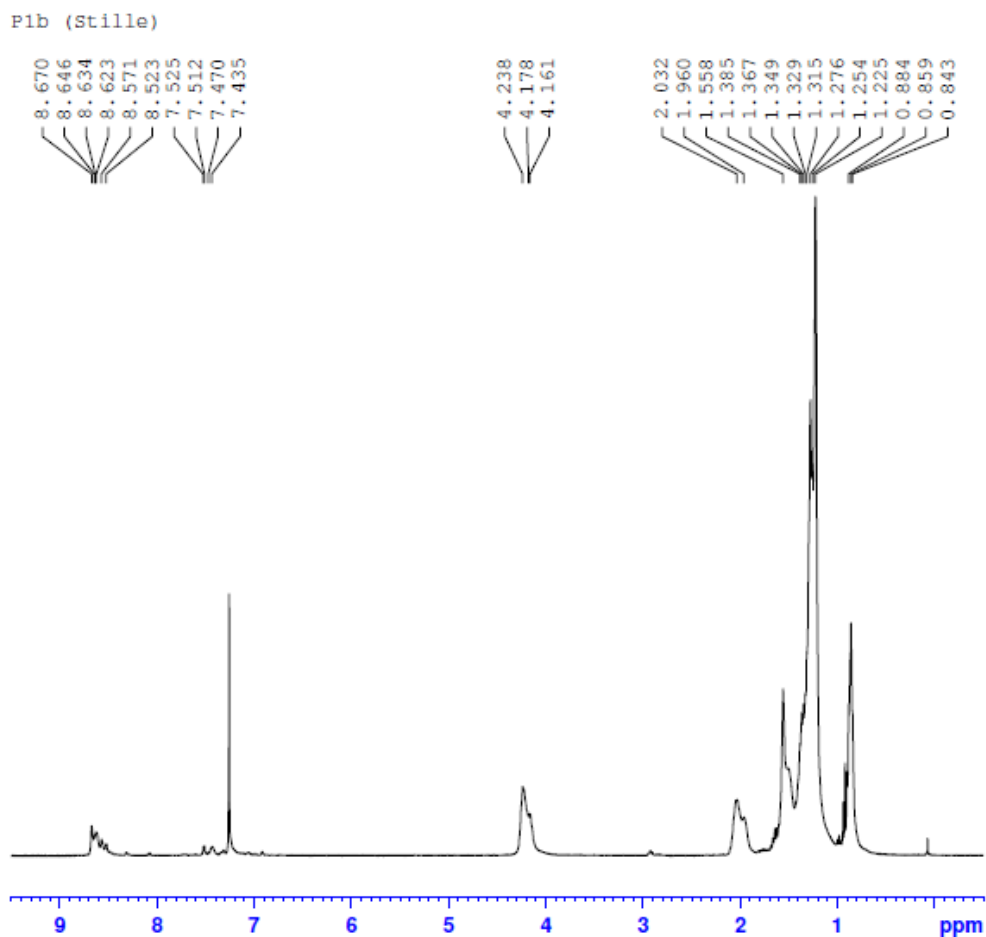
Figure A41 ^{1}H NMR spectrum of **P1**

Poly{4-(2,2'-bithiophen-5-yl)-5,6-bis(dodecyloxy)-7-(thiophen-2-yl)benzo[c][1,2,5]thi

adiazole} (P2). 21 (0.3 g, 0.36 mmol), crude **22** (0.384 g, 0.58 mmol) and $(Ph_3P)_2PdCl_2$

(0.027 g, 0.036 mmol) were put inside RBF with balloon degassing using N_2.

1,4-Dioxane (20 ml) was injected into the reaction mixture. The reaction mixture was

then heated at 80 °C for 3 days. During 2nd day, more crude **22** (0.384 g, 0.58 mmol) was

added into the reaction mixture. $CHCl_3$ and dilute aqueous HCl were added to the

reaction mixture and the mixture was stirred at RT overnight. The mixture was then

extracted with water and $CHCl_3$. The $CHCl_3$ layer was dried over $MgSO_4$, concentrated

by a rotary evaporator and the residue mixture was stirred in MeOH (to remove starting

163

material or oligomers) at RT overnight. After 2 days of stirring, MeOH was decanted off.

Acetone was added (to remove oligomers and low M_w polymer) and the reaction mixture

was stirred at RT overnight. Acetone was then decanted off, remaining insoluble solid was

dissolved in DCM, followed by filtration and the filtrate was collected and concentrated

by using a rotary evaporator. **P2** (130 mg) was obtained as a dark purple solid. M_w = 3476,

PDI = 1.39.
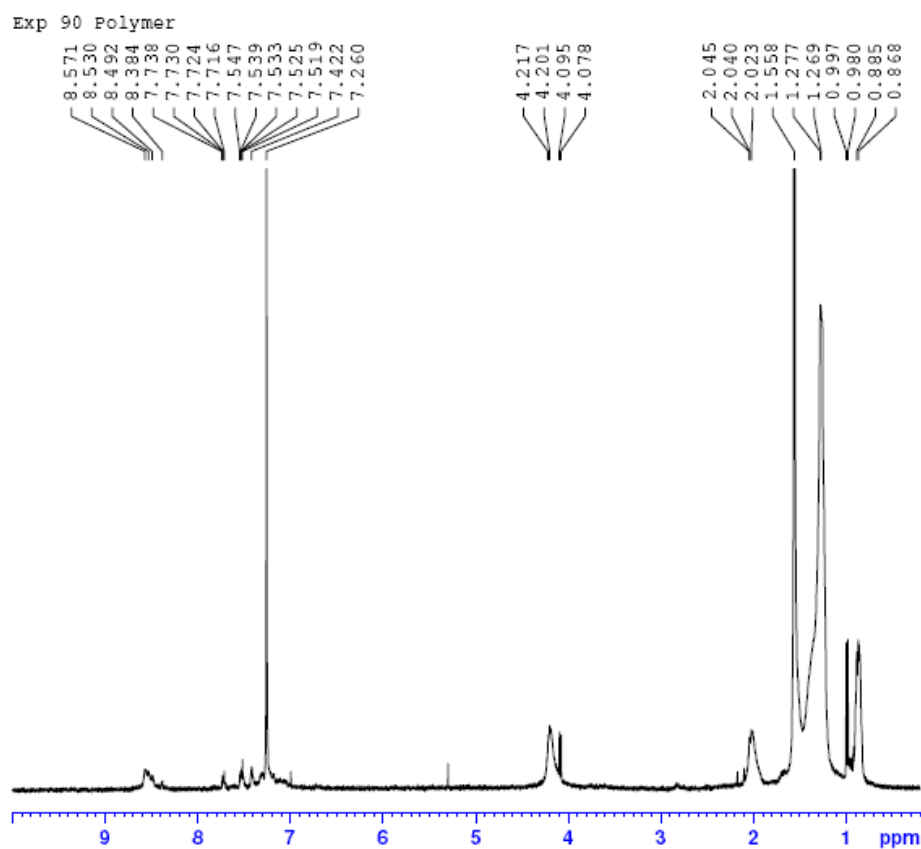
Figure A42 ^{1}H NMR spectrum of **P2**

Poly

{(thieno[3,2-b]thiophene)-2,5-diyl-alt-(4,7-bis(2-thienyl)-5,6-bis(dodecyloxy)benzo[c]

[1,2,5]thiadiazole)-5,5'-diyl} (P3). 21 (0.3 g, 0.36 mmol), crude **23** (0.258 g, 0.36 mmol)

and $(Ph_3P)_2PdCl_2$ (0.027 g, 0.036 mmol) were put inside RBF with balloon degassing using N_2. THF (30 ml) was injected into the reaction mixture. The reaction mixture was then heated at 80 °C for 3 days. During 2nd day, more crude **23** (0.258 g, 0.36 mmol) was added into the reaction mixture. The reaction mixture was then cooled to RT and THF was concentrated by a rotary evaporator. $CHCl_3$ and dilute aqueous HCl were added to the reaction mixture and the mixture was stirred at RT for 2 h. The mixture was then extracted with water and $CHCl_3$. The $CHCl_3$ layer was dried over $MgSO_4$, concentrated by a rotary evaporator and the residue mixture was stirred in MeOH at RT (to remove any starting material or oligomers). After 2 days stirring, MeOH was decanted off. Acetone was added (to remove low M_w oligomers and polymer) and the reaction mixture was then stirred for another day at RT. Acetone was then decanted off and the remaining insoluble solid was dissolved in DCM, filtered and the filtrate was collected and concentrated by using a rotary evaporator. **P3** (70 mg) was obtained as a dark purple solid. GPC ($CHCl_3$): $M_w = 1575$, PDI = 1.03.
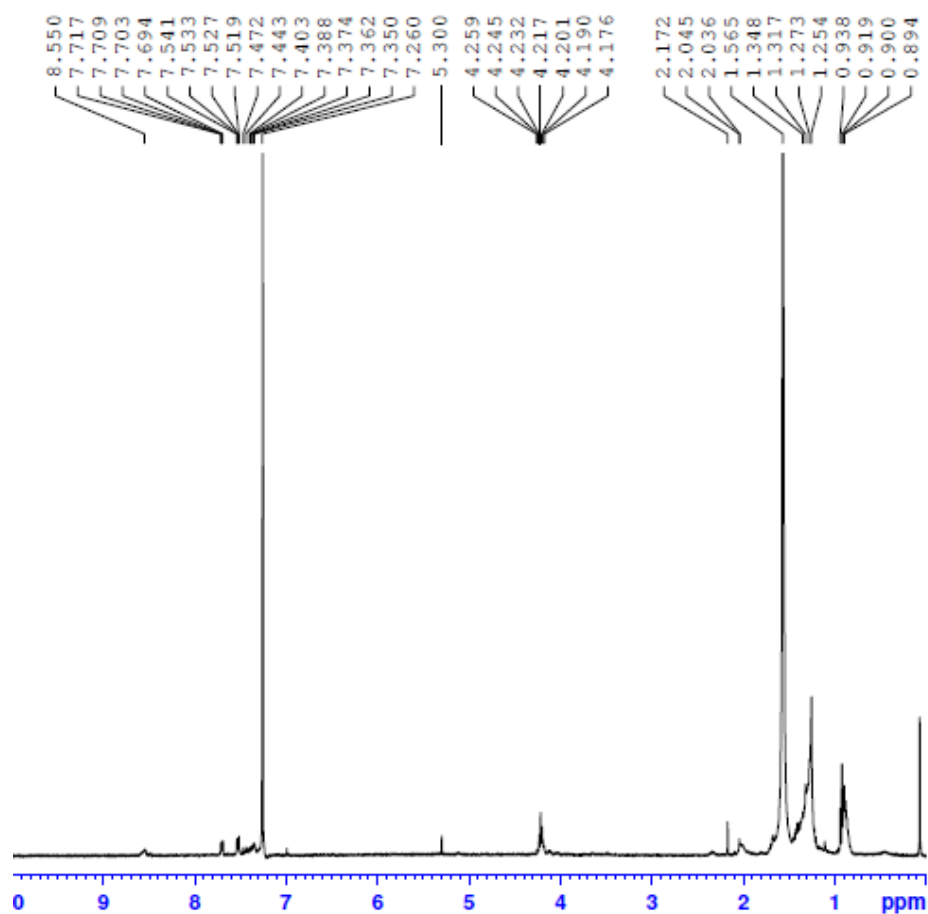
**Figure A43** ^{1}H NMR spectrum of **P3**

Poly

{(4,4'-dioctyldithieno[3,2-b:2',3'-d]silole)-2,6-diyl-alt-(4,7-bis(2-thienyl)-5,6-bis(dode

cyloxy)benzo[c][1,2,5]thiadiazole)-5,5'-diyl} (P4). 21 (0.3 g, 0.36 mmol), (Ph$_3$P)$_2$PdCl$_2$

(0.027 g, 0.036 mmol) and crude **24** (0.51 g, 0.514 mol) were put inside RBF with

balloon degassing using N$_2$. 1,4-Dioxane (30 ml) was injected into the reaction mixture.

The reaction mixture was then heated at 80 °C for 3 days. During 2nd day, more crude **24**

(0.51 g, 0.514 mol) was added into the reaction mixture. CHCl$_3$ and dilute aqueous HCl

were added to the reaction mixture and the reaction mixture was stirred at RT overnight.

The reaction mixture was then extracted with water and CHCl$_3$. The CHCl$_3$ layer was

dried over MgSO$_4$, concentrated by a rotary evaporator and the residual mixture was stirred in MeOH (to remove starting material or oligomers) at RT. After 2 days of stirring, MeOH was decanted off. Acetone was added (to remove oligomers and low M$_w$ polymer) and the reaction mixture was stirred at RT overnight. Acetone was then decanted off, remaining insoluble solid was dissolved in DCM, followed by filtration and the filtrate was collected. DCM of filtrate was concentrated by using a rotary evaporator. Acetone was added and the reaction mixture was stirred for another 2 h at RT (to remove any low M$_w$ polymer completely). Acetone was decanted off and remaining insoluble solid was dissolved in DCM. After adding MgSO$_4$, it was filtered and the filtrate was collected and concentrated by using a rotary evaporator. **P4** (290 mg) was obtained as a dark purple solid. GPC (CHCl$_3$): M_w = 19899, PDI = 4.52.
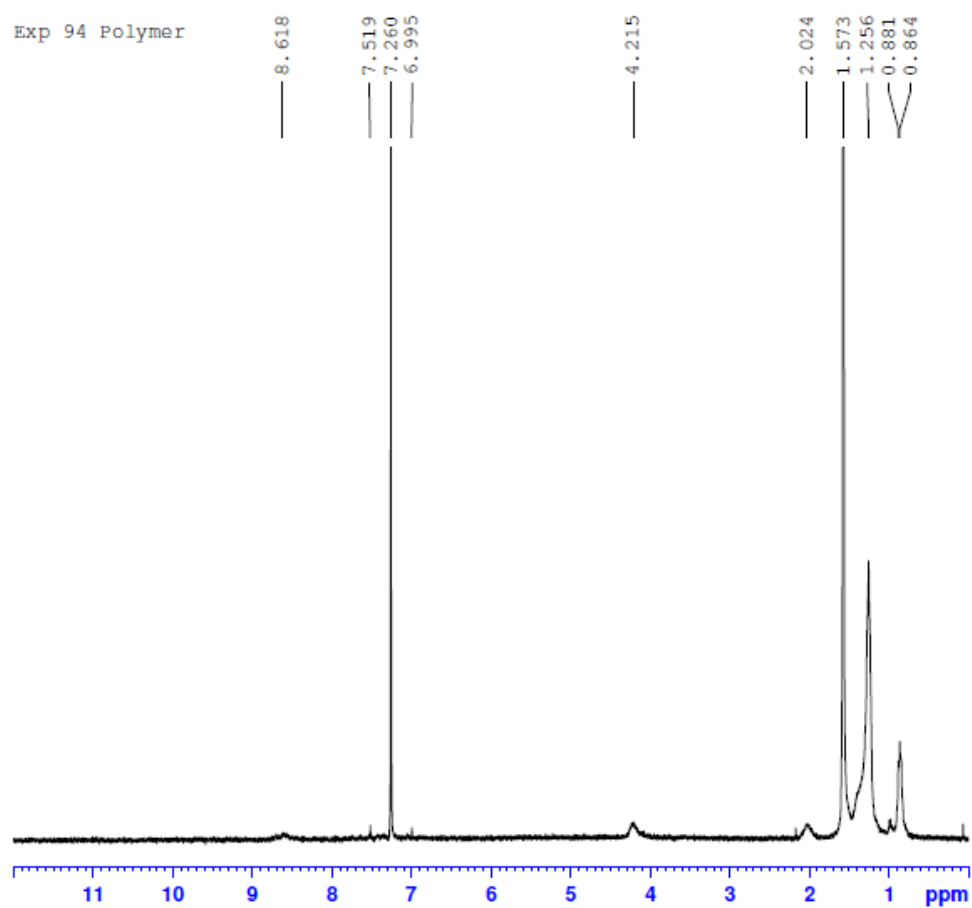
Figure A44   ^{1}H NMR spectrum of **P4**
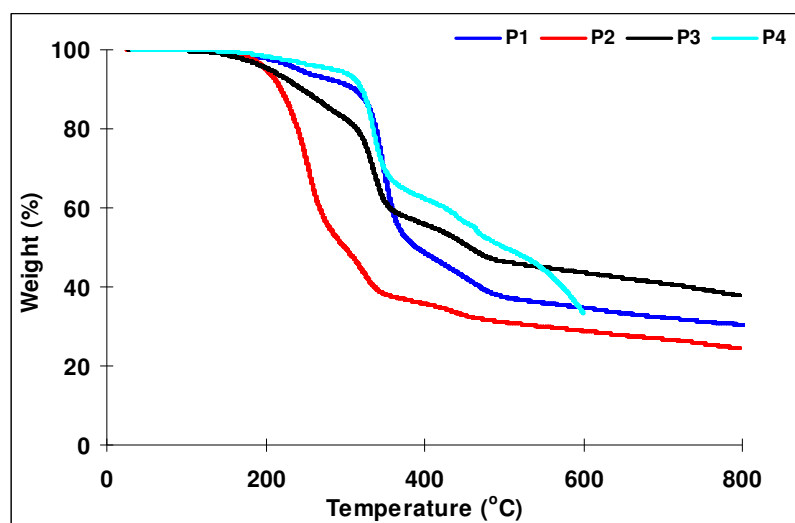
Figure A45   TGA scans of polymers **P1–P4**
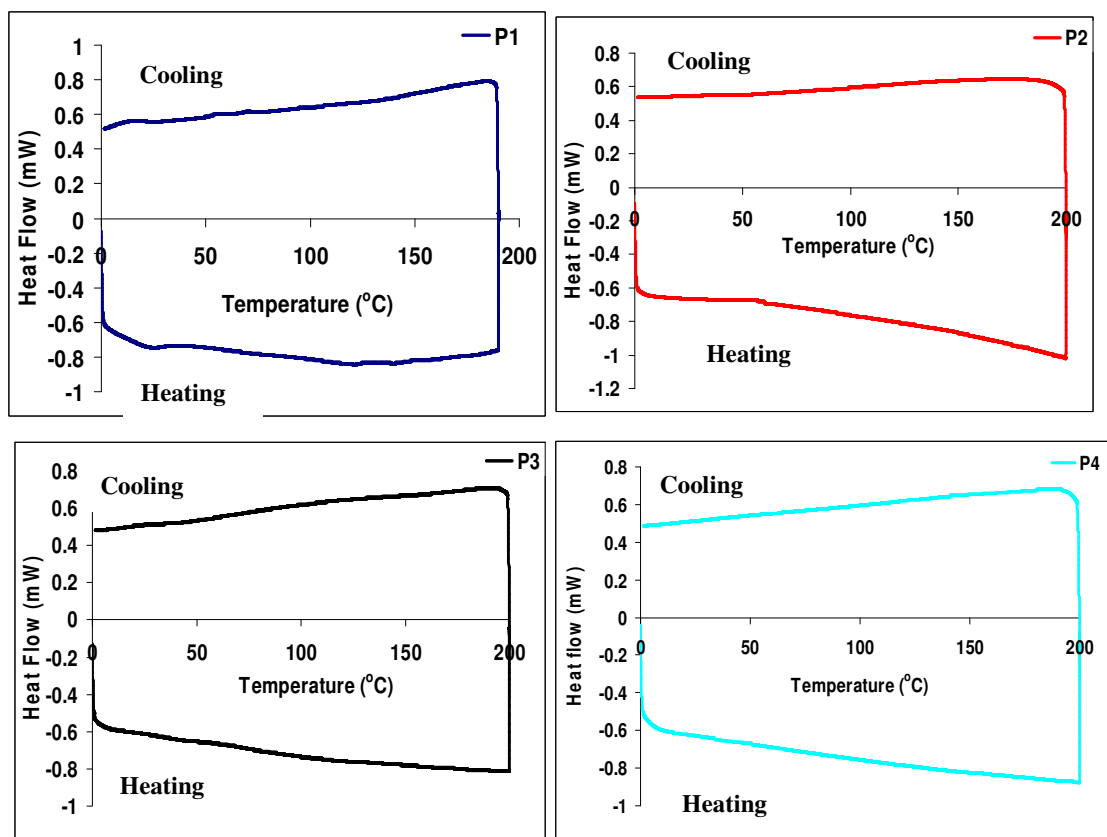
Figure A46 DSC scans (second cycle) of polymers **P1–P4**
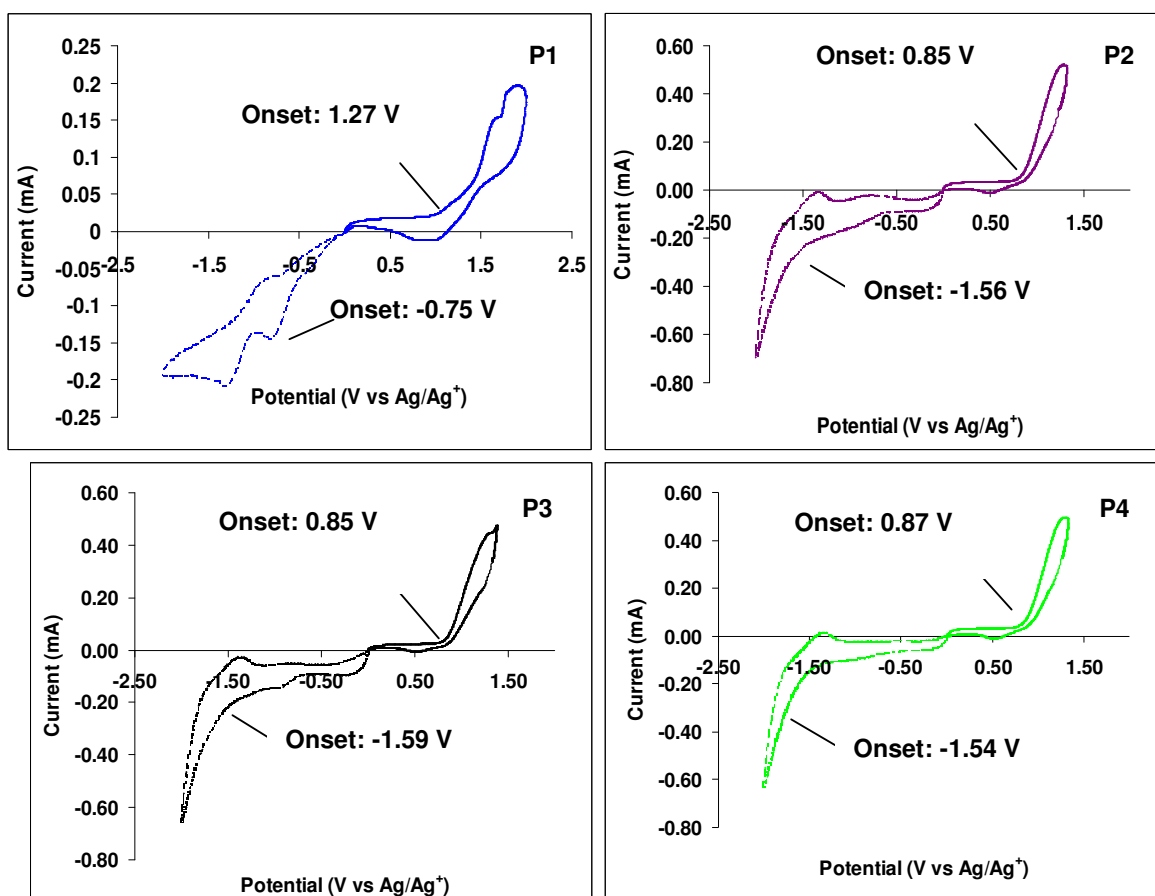
Figure A47   Cyclic voltammograms of polymer **P1–P4** on a platinum electrode (wire) in 0.1 M Bu₄NPF₆,

DCM solution with a sweep rate of 100 mV/s

1,4-dibromo-2,5-bis(2-ethyhexyloxy)benzene (**25**). Potassium hydroxide (2.62 g, 46.65

mmol) was added into a solution of 2,5-dibromo-1,4-diol (5 g, 18.66 mmol) in EtOH (60

ml). After 30 min of stirring at 60 °C, 2-ethylhexyl bromide (8.3 ml, 46.65 mmol) was

added dropwise into the reaction mixture and the reaction mixture was stirred at 60 °C

overnight. After cooling down to RT, the EtOH in the reaction mixture was removed

using a rotary evaporator and the remaining reaction mixture was extracted with DCM

and water. The organic layer was then dried over MgSO₄, concentrated and subjected to

column chromatography on silica gel eluting with a solvent mixture of 20% DCM in

hexane to obtain **25** as a light yellow liquid (9 g, 9%). **^{1}H NMR (CDCl₃):** δ 7.077 (d, *J* =

3.2 Hz, 2 H), 3.831 (t, J = 4.8 Hz, 4 H), 1.746–1.736 (m, 2 H), 1.550–1.323 (m and br, 16 H), 0.956–0.929 (m, 12 H). ^{13}C NMR (CDCl$_3$): δ 150.20, 118.20, 111.07, 72.55, 39.44, 30.46, 29.04, 23.88, 23.03, 14.08, 11.16. HR ES$^+$-TOF MS: calculated m/z: 491.1160 (M$^+$), found: m/z 491.1157 (M$^+$).

Figure A48 ^{1}H NMR spectrum of 1,4-dibromo-2,5-bis(2-ethyhexyloxy)benzene (**25**)
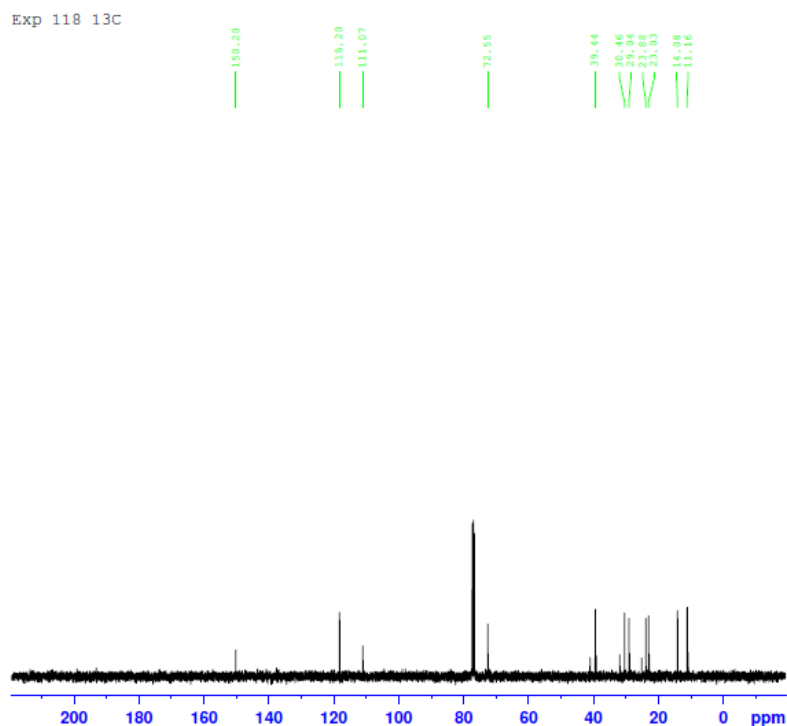
Figure A49   ^{13}C NMR spectrum of 1,4-dibromo-2,5-bis(2-ethyhexyloxy)benzene **(25)**

Diadduct of 1,4-dibromo-2,5-bis(2-ethyhexyloxy)benzene with 4'-(4-Pinacolatoboronphenyl)-2,2':6',2''-terpyridine (26). 25 (0.5 g, 1.02 mmol), **6** (1.11 g, 2.54 mmol) and Pd(PPh$_3$)$_4$ (0.12 g, 0.102 mmol) were put into RBF and degassed using N$_2$. Aqeuous K$_2$CO$_3$ (2 M, 20 ml) and THF (50 ml) were degassed using N$_2$ and then injected into the RBF. The reaction mixture was then stirred in the dark at 80 °C for 2 days. The reaction mixture was cooled to RT and THF was removed using a rotary evaporator. The reaction mixture was then extracted with DCM and water. The DCM layer was dried over MgSO$_4$ and concentrated using a rotary evaporator. Recrystallization from MeOH–THF gave **26** as a faint yellow solid (0.63 g, 65%). **^{1}H NMR (CD$_2$Cl$_2$):** δ 8.868 (s, 4 H), 8.763 (d, *J* = 4.8 Hz, 4 H), 8.729 (d, *J* = 8 Hz, 4 H), 8.023 (d, *J* = 8 Hz, 4 H), 7.960–7.921 (m, 4 H), 7.846 (d, *J* = 8 Hz, 4 H), 7.426–7.396 (m, 4 H), 3.944 (t, *J* =

5.6 Hz, 4 H), 1.740–1.681 (m, 2 H), 1.512–1.430 (m, 8 H), 1.307–1.289 (m, 8 H), 0.926–0.879 (m, 12 H). **^{13}C NMR (CD$_2$Cl$_2$):** δ 156.17, 156.05, 150.55, 149.79, 149.18, 139.42, 136.91, 136.84, 130.24, 130.16, 126.67, 123.88, 112.11, 118.50, 115.64, 71.76, 39.63, 30.60, 29.02, 23.96, 23.06, 13.85, 10.87. **MALDI TOF MS**: m/z 949.18 (M). **Anal. Calcd.** for C$_{64}$H$_{64}$N$_6$O$_2$: C, 80.98; H, 6.80; N, 8.85; O, 3.37. Found: C, 79.44; H, 7.68; N, 8.90. **HR ES$^+$-TOF MS**: calculated m/z: 949.5169 (M$^+$), found: m/z 949.5167 (M$^+$).
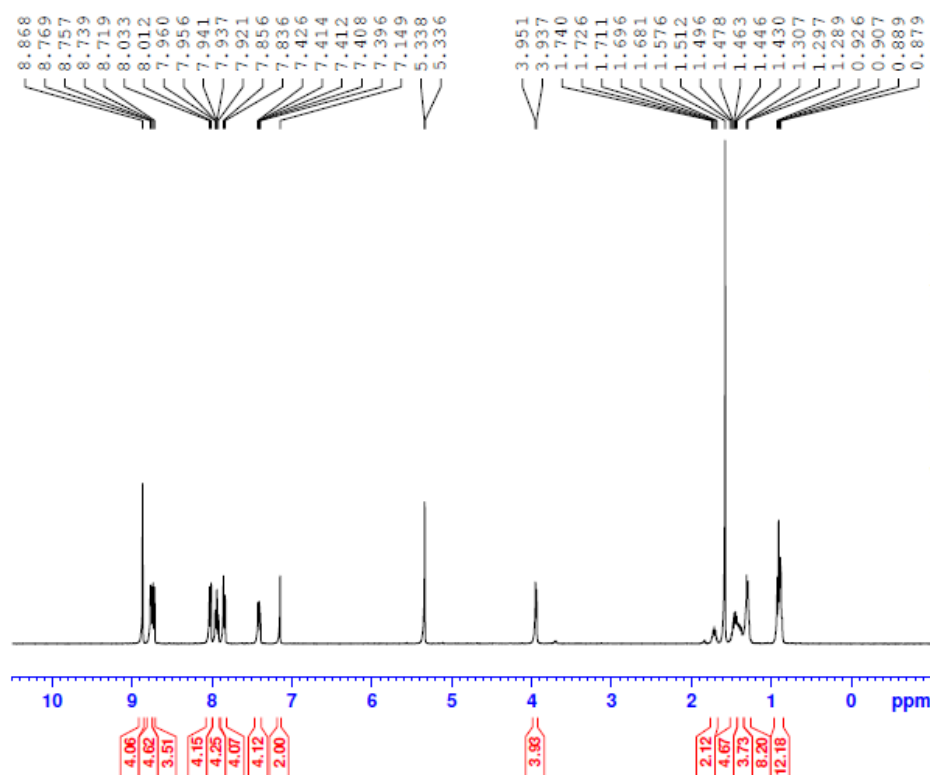
Figure A50 ^{1}H NMR spectrum of **26**
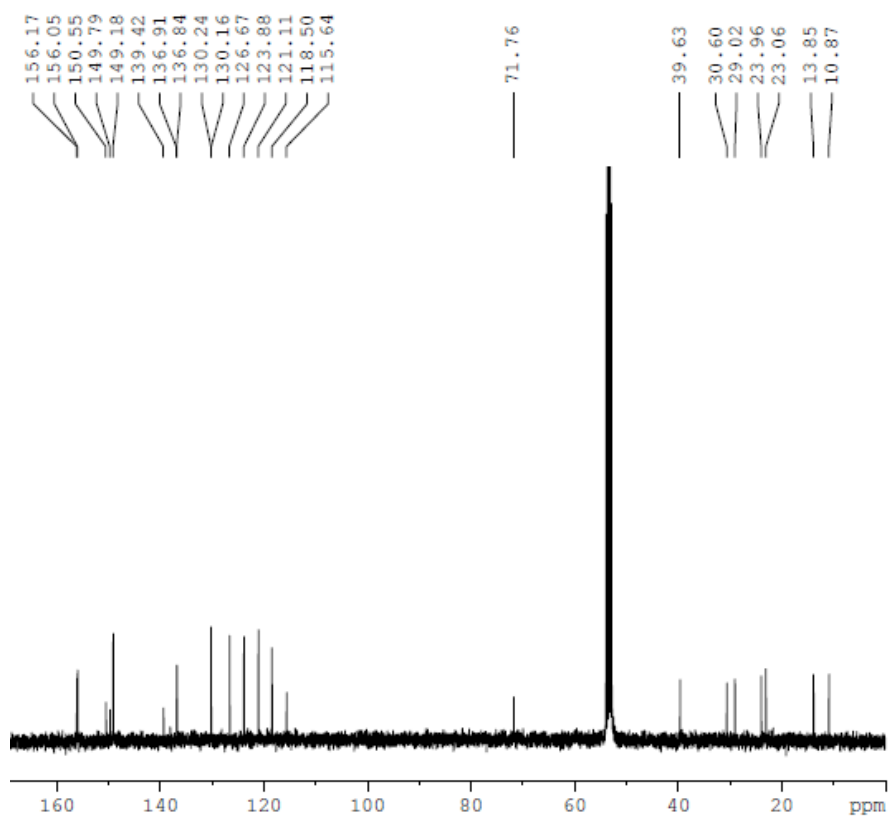
Figure A51 ^{13}C NMR spectrum of **26**

Data: C:\Other users\Victor\24 Nov Exp 119 P0001.N5[c] 24 Nov 2010 15:09 Cal: TOFMIX_23Nov10 23 Nov 2010 13:42
Shimadzu Biotech Axima ToF² 2.8.4.20080827IB: Mode Reflectron, Power: 70, P.Ext. @ 949 (bin 72)

%Int.   130 mV[sum= 1425 mV] Profiles 1-11 Smooth Av 50 -Baseline 100
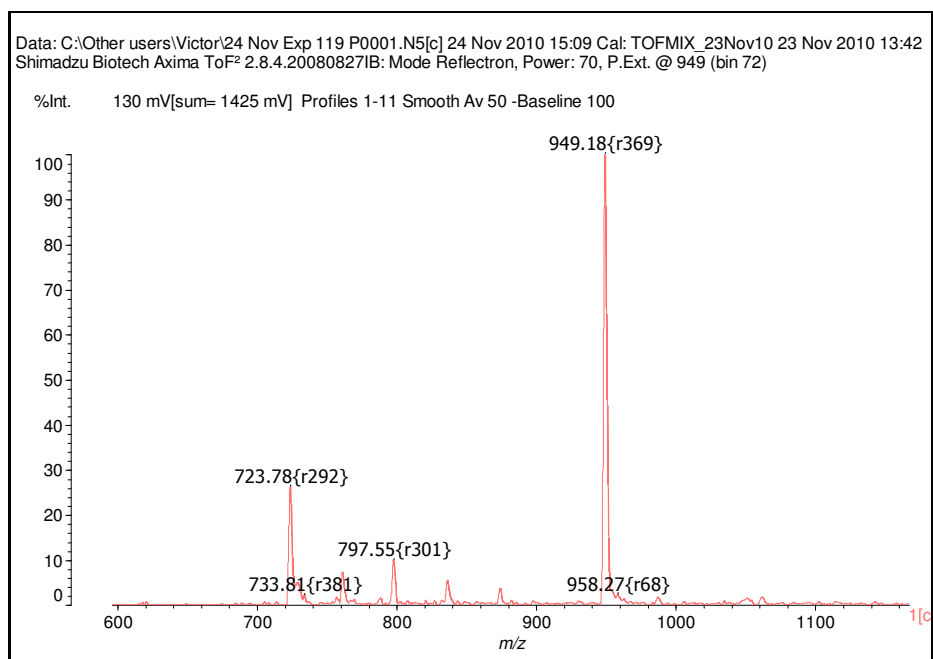
Figure A52   MALDI MS of **26**
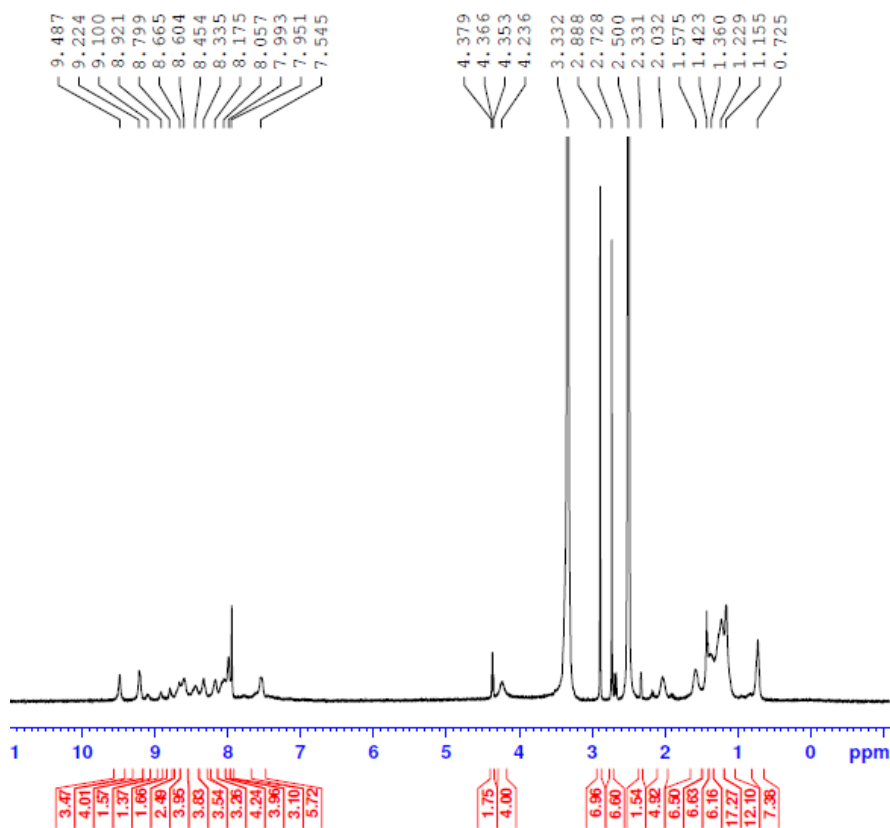
Diadduct   **of**

**4,7-bis(5-bromothiophen-2-yl)-5,6-bis(dodecyloxy)benzo[c][1,2,5]thiadiazole   with**

4'-(4-Pinacolatoboronphenyl)-2,2':6',2''-terpyridine (27). 21 (0.2 g, 0.24 mmol), **6**

(0.22 g, 0.5 mmol) and $Pd(PPh_3)_4$ (0.03 g, 0.024 mmol) were put into RBF and degassed

using N_2. Aqueous K_2CO_3 (2 M, 20 ml) and THF (35 ml) were degassed using N_2 and

then injected into the RBF. The reaction mixture was then stirred in the dark at 80 °C for

2 days. The reaction mixture was then cooled to RT and THF was removed using a rotary

evaporator. The reaction mixture was then extracted with DCM and water. The DCM

layer was dried over $MgSO_4$, concentrated and subjected to column chromatography on

silica gel eluting with a solvent mixture of 3% triethylamine in DCM to give **27** as a red

solid (0.25 g, 81%). **^{1}H NMR (CDCl$_3$):** δ 8.800 (s, 4 H), 8.759 (d, *J* = 4 Hz, 4 H), 8.696

(d, *J* = 8 Hz, 4 H), 8.573 (d, *J* = 4 Hz, 2 H), 7.994 (d, *J* = 4 Hz, 4 H), 7.920–7.860 (m, 8

H), 7.555 (d, *J* = 3.6 Hz, 2 H), 7.374 (t, *J* = 6.4 Hz, 4 H), 4.221 (t, *J* = 6.8 Hz, 4 H),

2.061–1.988 (m, 4 H), 1.431–1.231 (br, 36 H), 0.830 (t, *J* = 6.4 Hz, 6 H). **^{13}C NMR

(CDCl$_3$):** δ 156.28, 156.04, 151.93, 150.91, 149.17, 144.84, 136.90, 135.16, 134.29,

132.06, 127.86, 126.23, 123.86, 123.62, 121.40, 118.51, 117.56, 74.62, 31.93, 29.75,

29.70, 29.38, 22.67, 14.10. **MALDI TOF MS**: m/z 1283.38 (M). **Anal. Calcd.** for

$C_{80}H_{82}N_8O_2S_3$: C, 74.85; H, 6.44; N, 8.73; O, 2.49; S, 7.49. Found: C, 71.70; H, 5.57; N,

7.57; S, 7.40. **HR ES$^+$-TOF MS**: calculated m/z: 1283.5801 (M$^+$), found: m/z 1283.5780

(M$^+$).
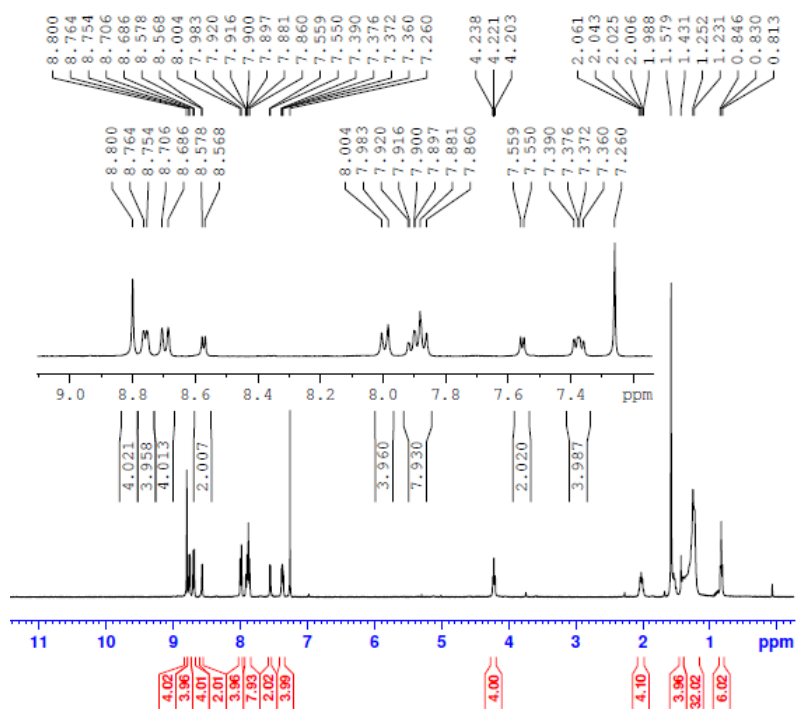
Figure A53 ^{1}H NMR spectrum of **27**
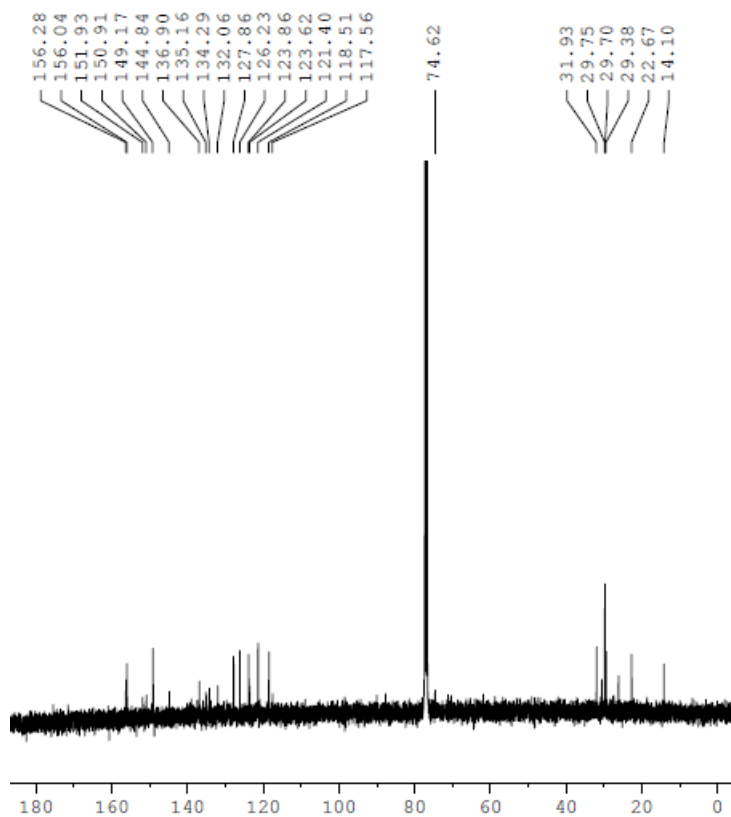
Figure A54 ^{13}C NMR spectrum of **27**
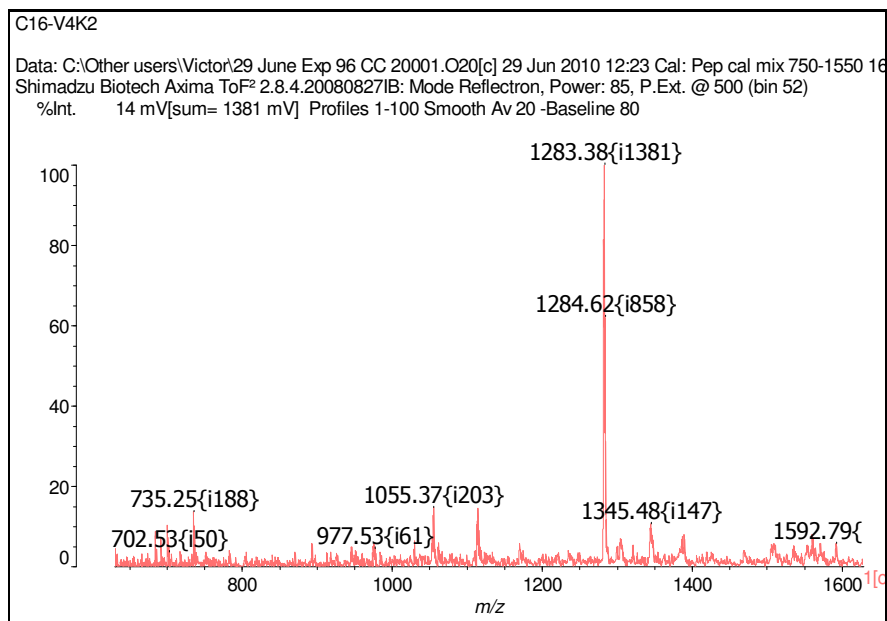
Figure A55   MALDI MS of **27**

**Poly   {Diadduct   of   1,4-dibromo-2,5-bis(2-ethyhexyloxy)benzene   with 4'-(4-Pinacolatoboronphenyl)-2,2':6',2''-terpyridine}   (P5).** Zinc(II) acetate dihydrate (12 mg, 0.053 mmol) in NMP (2 ml) was added dropwise into a solution of **26** (50 mg, 0.053 mmol) in NMP (10 ml). The reaction mixture was then stirred at 105 °C under N_2 for 24 h. An excess of NH_4PF_6 was added into the hot solution and the stirring was continued for 30 min. After cooling down to RT, the reaction mixture was poured into MeOH. The precipitate was filtered off and washed with MeOH. Precipitate was redissolved with NMP followed by reprecipitation of the solid by adding ether. The precipitate was dried at 50 °C under vacuum for 24 h to give **P5** as a yellow solid (30 mg, 43%).

177
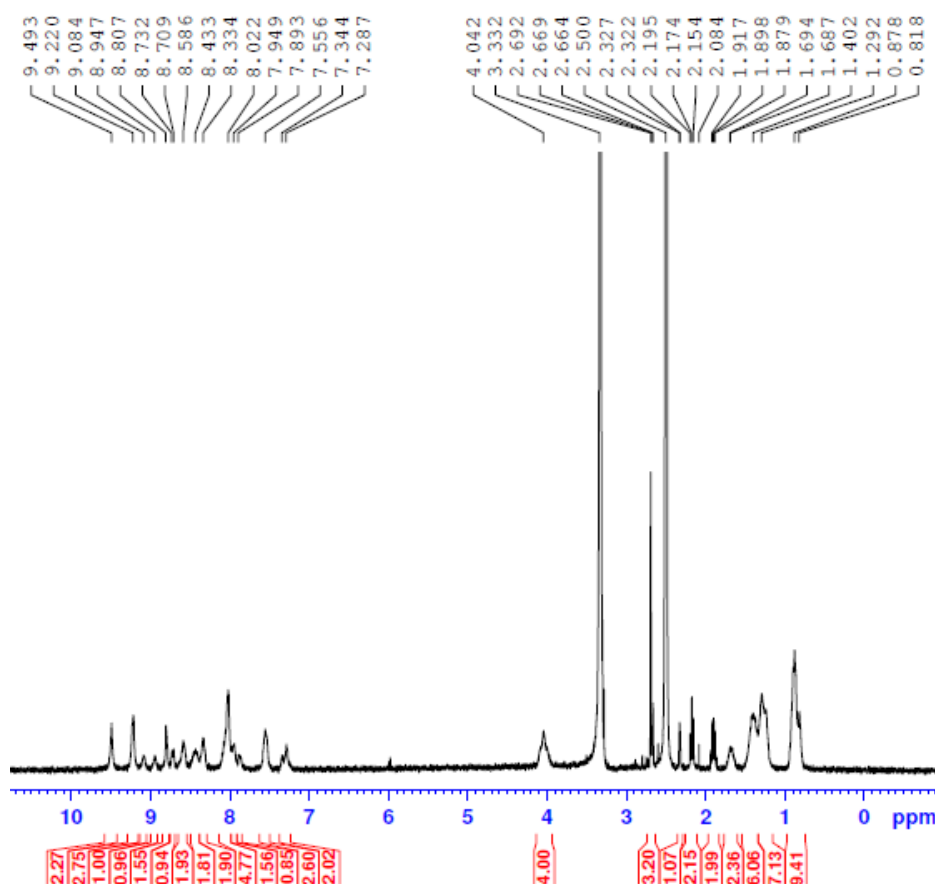
Figure A56 ^{1}H NMR spectrum of **P5**

Poly {Diadduct of 4,7-bis(5-bromothiophen-2-yl)-5,6-bis(dodecyloxy)benzo[c][1,2,5]thiadiazole with 4'-(4-Pinacolatoboronphenyl)-2,2':6',2''-terpyridine} (P6). Zinc(II) acetate dihydrate (8.6 mg, 0.039 mmol) in NMP (2 ml) was added dropwise into a solution of **27** (50 mg, 0.039 mmol) in NMP (10 ml). The reaction mixture was stirred at 105 °C under N_2 for 24 h. An excess of NH_4PF_6 was added into the hot solution and the stirring was continued for 30 min. After cooling down to RT, reaction mixture was poured into MeOH. The precipitate was filtered off and washed with MeOH. Precipitate was redissolved with NMP followed by reprecipitation of the solid by adding ether. The precipitate was dried at 50 °C under vacuum for 24 h to give **P6** as a red solid (41 mg, 43%).

Figure A57 ^{1}H NMR spectrum of **P6**

Poly {{Diadduct of 1,4-dibromo-2,5-bis(2-ethyhexyloxy)benzene with 4'-(4-Pinacolatoboronphenyl)-2,2':6',2''-terpyridine}-*alt*-{Diadduct of 4,7-bis(5-bromothiophen-2-yl)-5,6-bis(dodecyloxy)benzo[c][1,2,5]thiadiazole with 4'-(4-Pinacolatoboronphenyl)-2,2':6',2''-terpyridine}} (P7). 26 (50 mg, 0.053 mmol) in NMP (10 ml) was added dropwise into a solution of zinc(II) acetate dihydrate (24 mg, 0.11 mmol) in NMP (5 ml). The reaction mixture was then stirred at RT for 2 h, and a solution of **27** (68 mg, 0.053 mmol) in NMP (10 ml) was added dropwise into the reaction mixture. The reaction mixture was then heated at 105 °C under N_2 for 24 h. An excess of NH_4PF_6 was added into the hot solution and the stirring was continued for 30 min. After

cooling down to RT, the reaction mixture was poured into MeOH. The precipitate was filtered off and washed with MeOH. Precipitate was redissolved with NMP followed by reprecipitation of the solid by adding ether. The precipitate was dried at 50 °C under vacuum for 24 h to give **P7** as a red solid (115 mg, 74%).
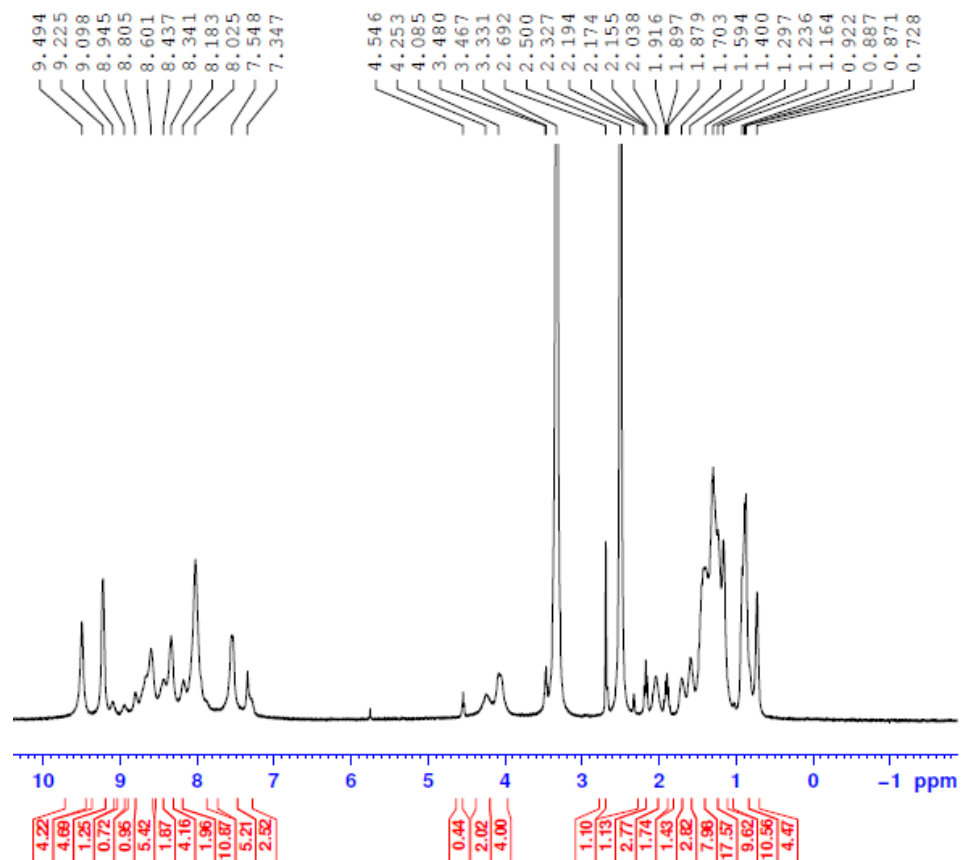
Figure A58 ^{1}H NMR spectrum of **P7**
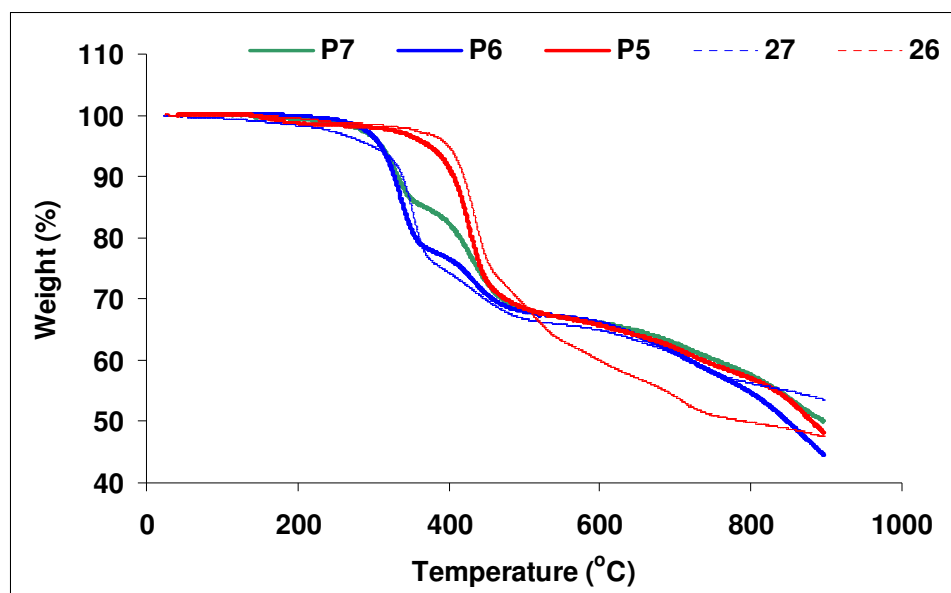
Figure A59   TGA scans of bis(tpys) monomers **26–27** and metallopolymers **P5–P7**
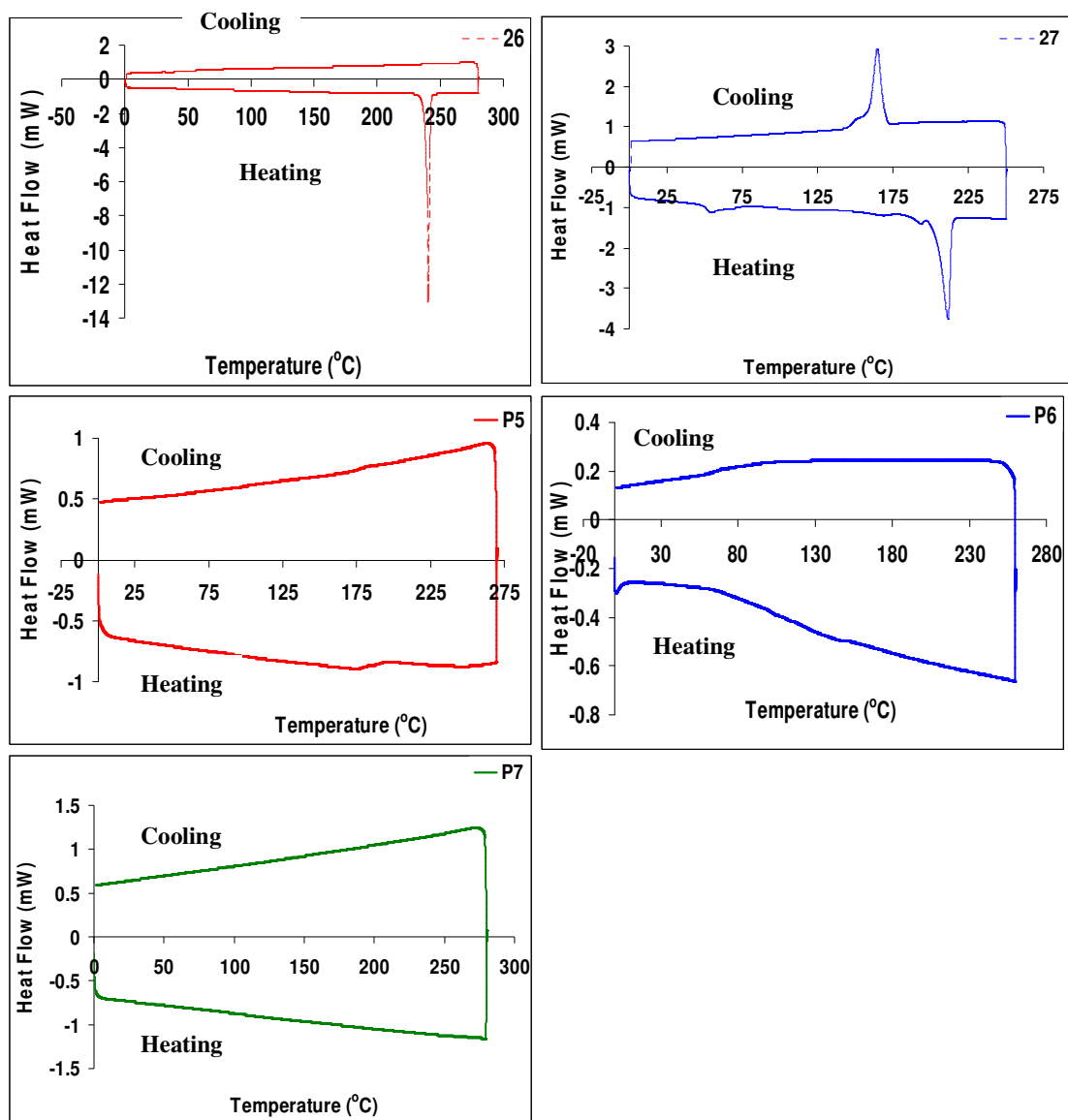
Figure A60   DSC scans of bis(tpys) monomers **26**–**27** and metallopolymers **P5**–**P7**
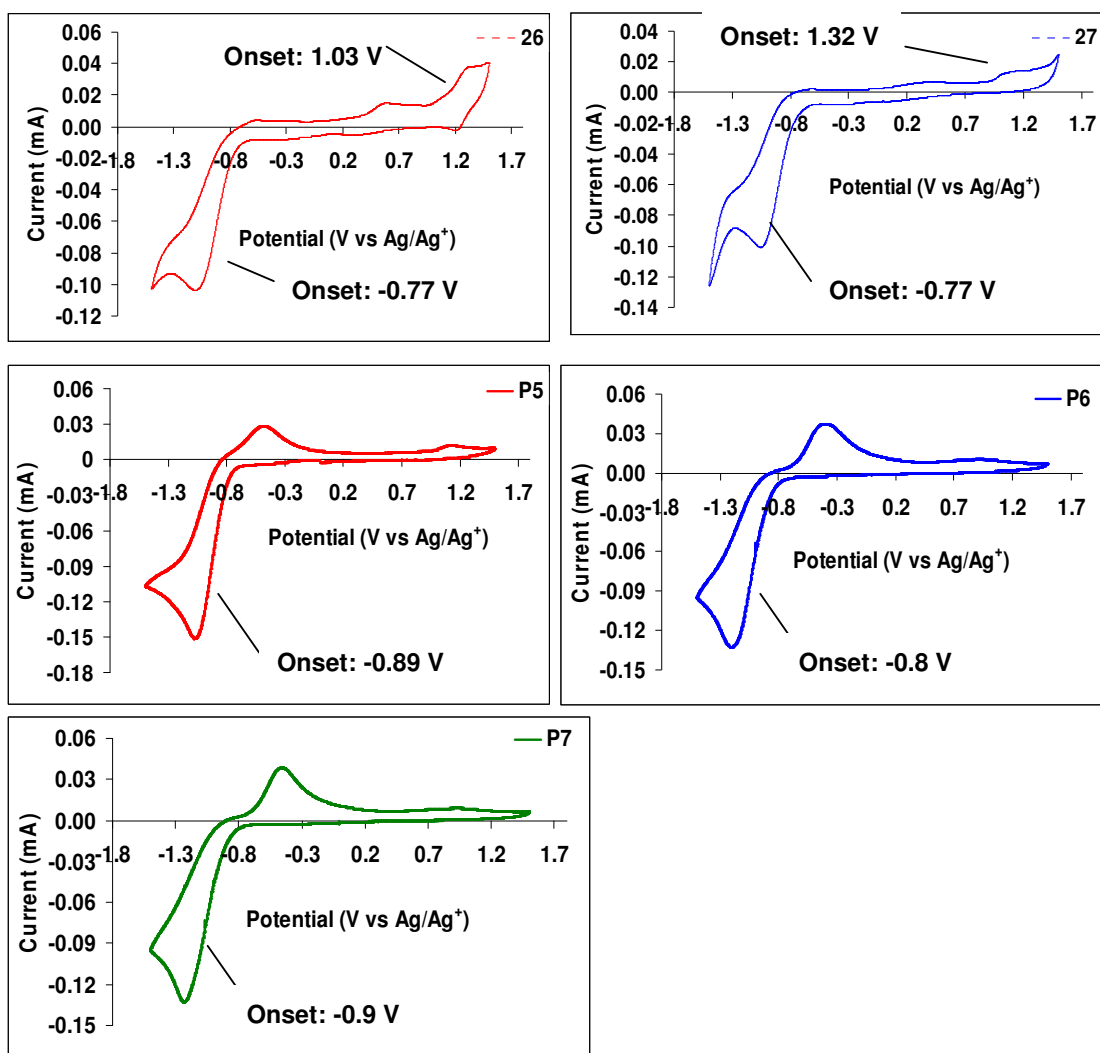
Figure A61   Cyclic voltammograms of **26–27** on a platinum electrode (wire) in 0.1 M Bu4NPF6, DCM

solution with a sweep rate of 100 mV/s and **P5–7** on a platinum electrode (wire) in 0.1 M Bu4NPF6,

acetonitrile solution with a sweep rate of 100 mV/s

Zn(II)-self-assembled network of 1 (S1). Zinc(II) acetate dihydrate (6.6 mg, 0.03 mmol)

in NMP (2 ml) was added dropwise into a solution of **1** (50 mg, 0.015 mmol) in NMP (10

ml). The reaction mixture was then stirred at 105 °C under N_2 for 24 h. An excess of

NH_4PF_6 was then added into the hot reaction mixture and it was continued stirring for 30

min. The reaction mixture was then poured into MeOH. The precipitate was then filtered

off and washed with MeOH. Precipitate was redissolved with NMP followed by reprecipitation of the solid by adding ether. The precipitate was dried at 50 °C under vacuum for 24 h to give **S1** as a yellow solid (55 mg, 92%).

Zn(II)-self-assembled network of 2 (S2). Zinc(II) acetate dihydrate (6.2 mg, 0.028 mmol) in NMP (2 ml) was added dropwise into a solution of **2** (50 mg, 0.014 mmol) in NMP (10 ml). The reaction mixture was stirred at 105 °C under N_2 for 24 h. An excess of NH_4PF_6 was then added into the hot reaction mixture and it was continued stirring for 30 min. The reaction mixture was then poured into MeOH. The precipitate was then filtered off and washed with MeOH. Precipitate was redissolved with NMP followed by reprecipitation of the solid by adding ether. The precipitate was dried at 50 °C under vacuum for 24 h to give **S2** as a light yellow solid (35 mg, 58%).

Zn(II)-self-assembled network of 1 with 26 (S3). S1 (55 mg, 0.014 mmol) in NMP (10 ml) was heated to 105 °C. Zinc(II) acetate dihydrate (6.2 mg, 0.028 mmol) in NMP (2 ml) was added dropwise into the reaction mixture. The reaction mixture was stirred at 105 °C under N_2 for 1 h. **26** (26.6 mg, 0.028 mmol) in NMP (10 ml) was then added dropwise and the resulting reaction mixture was stirred at 105 °C under N_2 for 24 h. An excess of NH_4PF_6 was then added into the hot reaction mixture and it was continued stirring for 30 min. The reaction mixture was then poured into MeOH. The precipitate was then filtered off and washed with MeOH. Precipitate was redissolved with NMP followed by reprecipitation of the solid by adding ether. The precipitate was dried at 50 °C under vacuum for 24 h to give **S3** as a yellow solid (84 mg, 90%).

Zn(II)-self-assembled network of 1 with 27 (S4). S1 (55 mg, 0.014 mmol) in NMP (10 ml) was heated to 105 °C. Zinc(II) acetate dihydrate (6.2 mg, 0.028 mmol) in NMP (2 ml) was added dropwise into the reaction mixture. The reaction mixture was stirred at 105 °C under N_2 for 1 h. **27** (36 mg, 0.028 mmol) in NMP (10 ml) was then added dropwise and the resulting reaction mixture was stirred at 105 °C under N_2 for 24 h. An excess of NH_4PF_6 was then added into the hot reaction mixture and it was continued stirring for 30 min. The reaction mixture was then poured into MeOH. The precipitate was then filtered off and washed with MeOH. Precipitate was redissolved with NMP followed by reprecipitation of the solid by adding ether. The precipitate was dried at 50 °C under vacuum for 24 h to give **S4** as a red solid (64 mg, 63%).

Zn(II)-self-assembled network of 2 with 26 (S5). S2 (45 mg, 0.0105 mmol) in NMP (10 ml) was heated to 105 °C. Zinc(II) acetate dihydrate (4.61 mg, 0.021 mmol) in NMP (2 ml) was added dropwise into the reaction mixture. The reaction mixture was stirred at 105 °C under N_2 for 1 h. **26** (20 mg, 0.021 mmol) in NMP (10 ml) was then added dropwise and the resulting reaction mixture was stirred at 105 °C under N_2 for 24 h. An excess of NH_4PF_6 was then added into the hot reaction mixture and it was continued stirring for 30 min. The reaction mixture was then poured into MeOH. The precipitate was then filtered off and washed with MeOH. Precipitate was redissolved with NMP followed by reprecipitation of the solid by adding ether. The precipitate was dried at 50 °C under vacuum for 24 h to give **S5** as a yellow solid (50 mg, 70%).

Zn(II)-self-assembled network of 2 with 27 (S6). S2 (45 mg, 0.0105 mmol) in NMP (10 ml) was heated to 105 °C. Zinc(II) acetate dihydrate (4.61 mg, 0.021 mmol) in NMP (2 ml) was added dropwise into the reaction mixture. The reaction mixture was stirred at 105 °C under N_2 for 1 h. **27** (27 mg, 0.021 mmol) in NMP (10 ml) was then added dropwise and the resulting reaction mixture was stirred at 105 °C under N_2 for 24 h. An excess of NH_4PF_6 was then added into the hot reaction mixture and it was continued stirring for 30 min. The reaction mixture was then poured into MeOH. The precipitate was then filtered off and washed with MeOH. Precipitate was redissolved with NMP followed by reprecipitation of the solid by adding ether. The precipitate was dried at 50 °C under vacuum for 24 h to give **S6** as a red solid (50 mg, 63%).
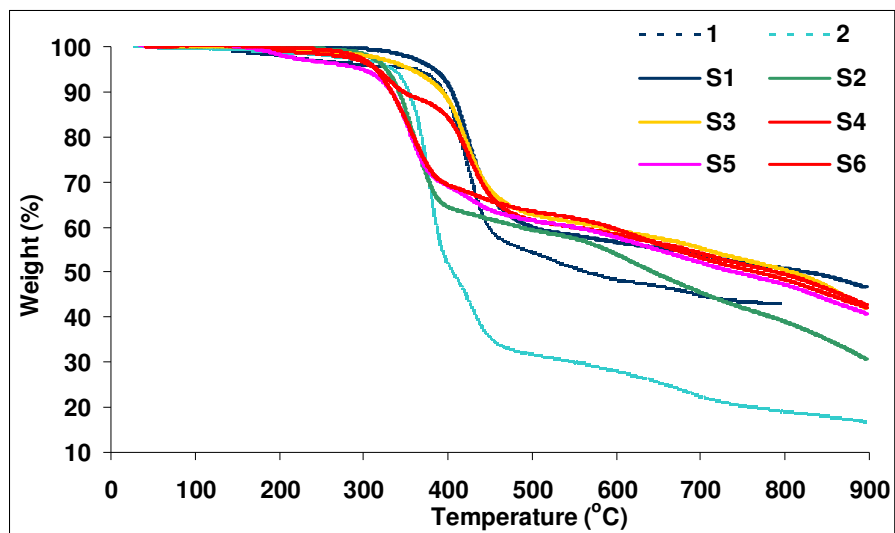

Figure A62   TGA scans of 3D metal-coordinated self-assembled supramolecular networks **S1–6**
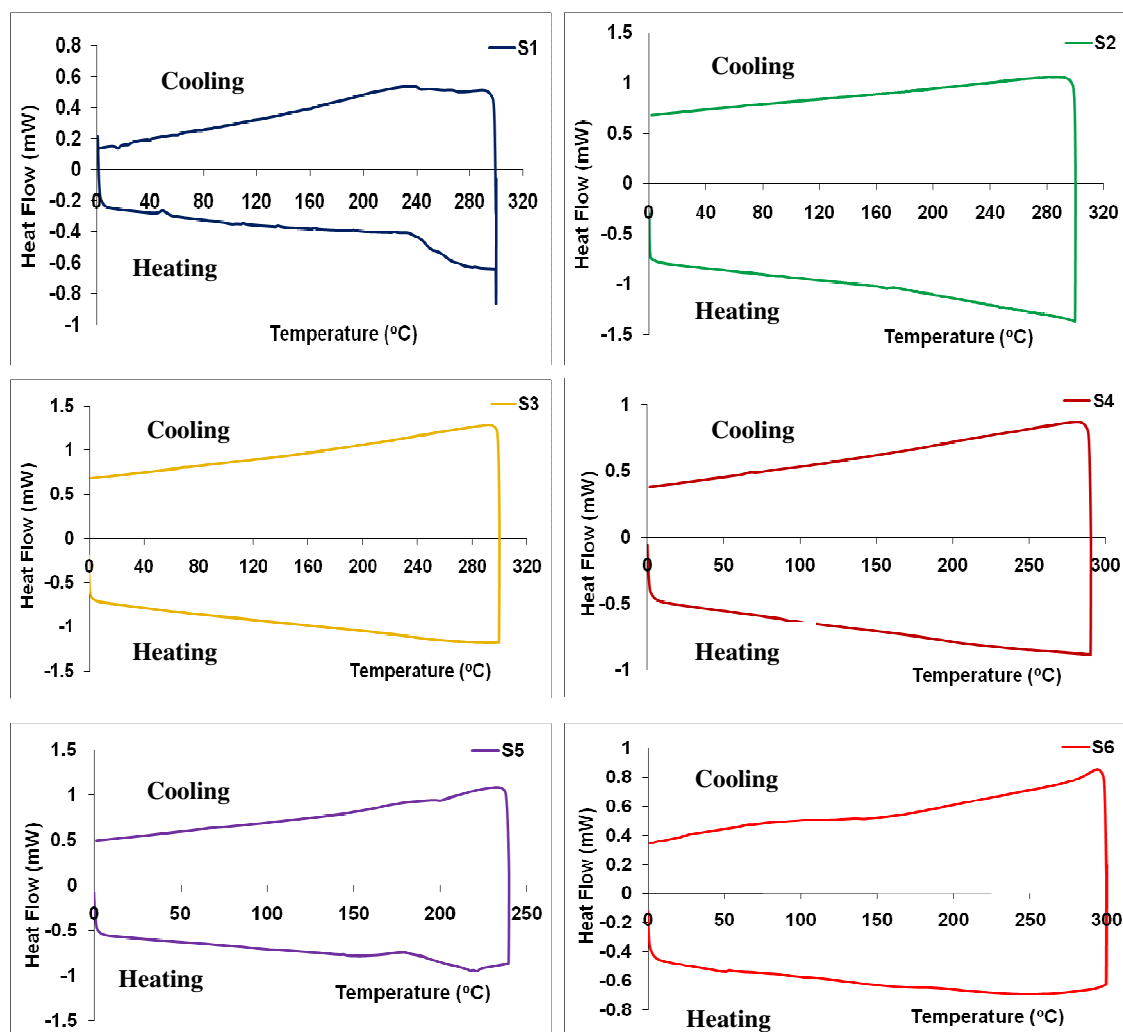
Figure A63   DSC scans (2nd cycle) of 3D metal-coordinated self-assembled supramolecular networks

S1–6

Nanocomposite (S3 (with CdSe)). S1 (27 mg, 0.007 mmol) in NMP (5 ml) was heated to 105 °C. Zinc(II) acetate dihydrate (3.1 mg, 0.014 mmol) in NMP (1 ml) was added dropwise into the reaction mixture. The reaction mixture was stirred at 105 °C under N$_2$ for 1 h. CdSe in excess (50 mg) was added into the reaction mixture followed by injection of NMP (5 ml). **26** (13.3 mg, 0.014 mmol) in NMP (5 ml) was then added dropwise and the resulting reaction mixture was stirred at 105 °C under N$_2$ for 24 h. An excess of

NH_4PF_6 was then added into the hot reaction mixture and it was continued stirring for 30 min. The reaction mixture was then poured into MeOH. The precipitate was then filtered off and washed with MeOH. Precipitate was redissolved with NMP followed by reprecipitation of the solid by adding ether. The precipitate was dried at 50 °C under vacuum for 24 h to give **S3 (with CdSe)** as a dark orange solid (48 mg).

Nanocomposite (S4 (with CdSe)). **S1** (27 mg, 0.007 mmol) in NMP (5 ml) was heated to 105 °C. Zinc(II) acetate dihydrate (3.1 mg, 0.014 mmol) in NMP (1 ml) was added dropwise into the reaction mixture. The reaction mixture was stirred at 105 °C under N_2 for 1 h. CdSe in excess (50 mg) was added into the reaction mixture followed by injection of NMP (5 ml). **27** (18 mg, 0.014 mmol) in NMP (5 ml) was then added dropwise and the resulting reaction mixture was stirred at 105 °C under N_2 for 24 h. An excess of NH_4PF_6 was then added into the hot reaction mixture and it was continued stirring for 30 min. The reaction mixture was then poured into MeOH. The precipitate was then filtered off and washed with MeOH. Precipitate was redissolved with NMP followed by reprecipitation of the solid by adding ether. The precipitate was dried at 50 °C under vacuum for 24 h to give **S4 (with CdSe)** as a red solid (38 mg).

Nanocomposite (S3 (with Au) (1)). **S3** (20 mg, 0.003 mmol) and tetrachloroauric acid ($HAuCl_4 \cdot 3H_2O$) (1.2 mg, 0.003 mmol) were dispersed in toluene (4 ml). The reaction mixture was stirred at RT for 24 h. The reaction mixture was treated with hydrazine monohydrate (0.15 ml, 0.003 mmol). The reaction mixture was then stirred at RT overnight, filtered and washed with toluene.

Nanocomposite (S4 (with Au) (1)). **S4** (22 mg, 0.003 mmol) and tetrachloroauric acid (HAuCl$_4$•3H$_2$O) (1.2 mg, 0.003 mmol) were dispersed in toluene (4 ml). The reaction mixture was stirred at RT for 24 h. The reaction mixture was treated with hydrazine monohydrate (0.15 ml, 0.003 mmol). The reaction mixture was then stirred at RT overnight, filtered and washed with toluene.
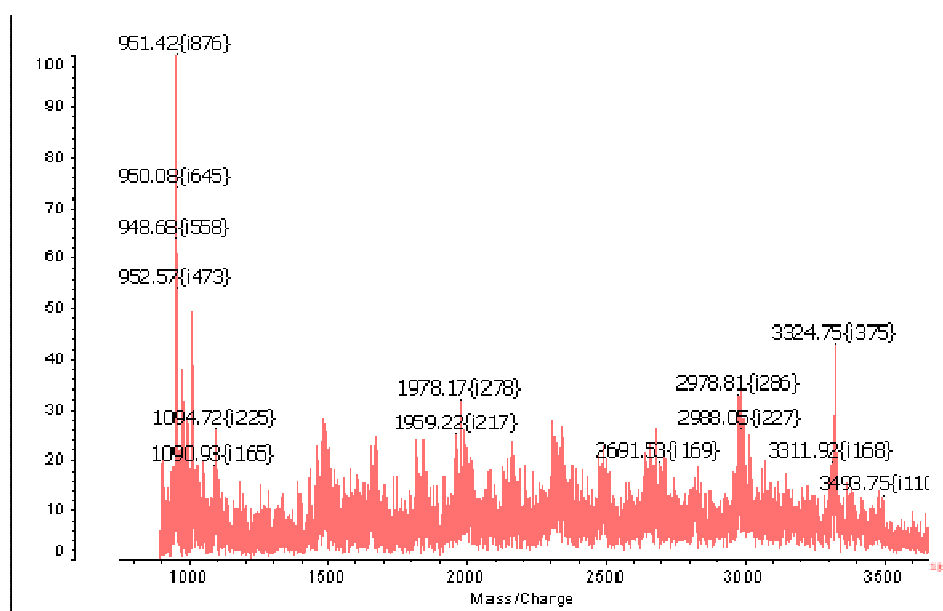
Figure A64   MALDI MS of filtrate of **S3 (with Au) (1)**
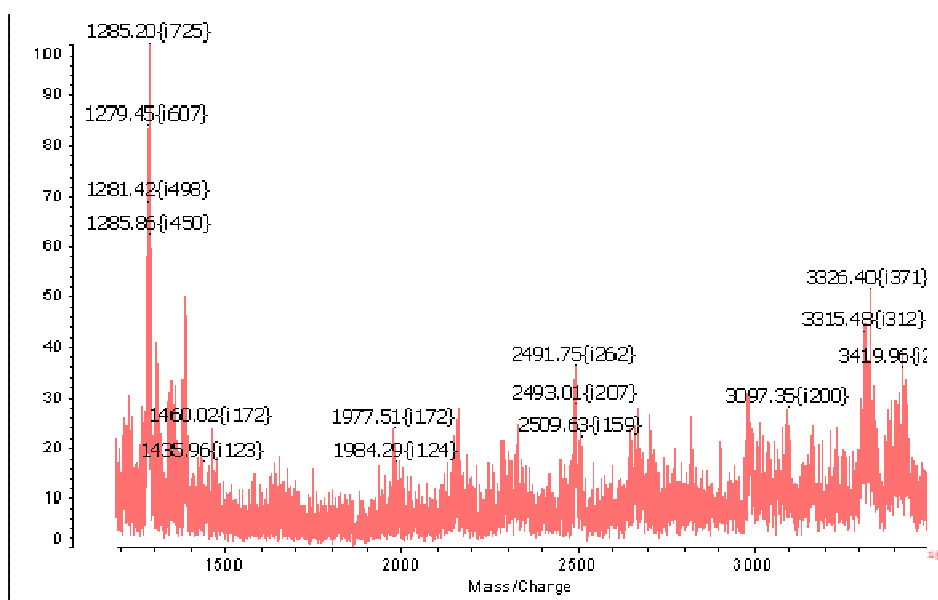
Figure A65   MALDI MS of filtrate of **S4 (with Au) (1)**

Nanocomposite (S3 (with Au) (2)). S3 (20 mg, 0.003 mmol) and tetrachloroauric acid (HAuCl$_4$•3H$_2$O) (1.2 mg, 0.003 mmol) were dispersed in NMP (10 ml). The reaction mixture was heated to 105 °C. The reaction mixture was then added dropwise with sodium citrate dihyrate (7 mg, 0.003 mmol) in water (1 ml). The reaction mixture was then stirred at 105 °C for 45 min. The reaction mixture was cooled to RT, poured into water to precipitate. The precipitate was filtered and washed with water.

Nanocomposite (S4 (with Au) (2)). S4 (22 mg, 0.003 mmol) and tetrachloroauric acid (HAuCl$_4$•3H$_2$O) (1.2 mg, 0.003 mmol) were dispersed in NMP (10 ml). The reaction mixture was heated to 105 °C. The reaction mixture was then added dropwise with sodium citrate dihyrate (7 mg, 0.003 mmol) in water (1 ml). The reaction mixture was then stirred at 105 °C for 45 min. The reaction mixture was cooled to RT, poured into water to precipitate. The precipitate was filtered and washed with water.
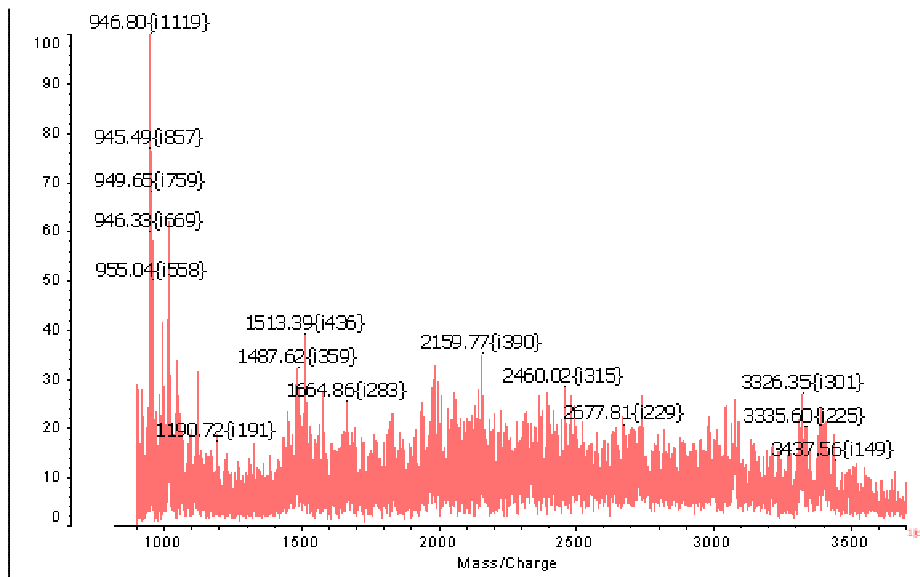
Figure A66 MALDI MS of filtrate of **S3 (with Au) (2)**
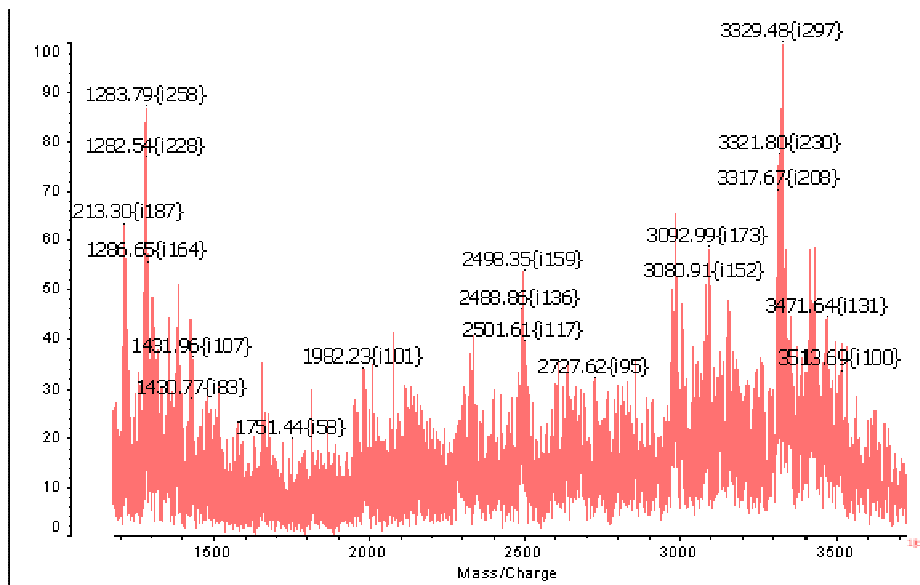
Figure A67 MALDI MS of filtrate of **S4 (with Au) (2)**

Tris(4-iodophenyl)methane (29). Triphenylmethane (1 g, 4.1 mmol), bis[(trifluoroacetoxy)iodo]benzene (3 g, 7 mmol) and I_2 (1.68 g, 6.6 mmol) were dissolved in $CHCl_3$ (20 ml) in a RBF. The reaction mixture was then heated at 55 °C until

191

the colour of I$_2$ disappeared. The CHCl$_3$ was then removed using a rotary evaporator to give crude **29** which was contaminated with tris(4-iodophenyl)methanol. Formic acid (20 ml) was then added to the crude reaction residue and the reaction mixture was refluxed at 110 °C for 22 h (in order to convert tris(4-iodophenyl)methanol to **29**). After cooling down to RT, the reaction mixture was then extracted with DCM and water and neutralized with NaHCO$_3$. The DCM layer was dried over MgSO$_4$, concentrated by a rotary evaporator. The crude reaction mixture was then subjected to column chromatography on silica gel eluting with a solvent mixture of 5% DCM in hexane to give impure **29** (minor contamination with tris(4-iodophenyl)methanol) as a light yellow solid (0.8 g, 30%). **^{1}H NMR (CDCl$_3$):** δ 7.613 and 6.824 (AA'XX', 2 x apparent d, *J* = 8.4 Hz, 12 H), 5.355 (s, 1 H). **^{13}C NMR (CDCl$_3$):** δ 142.33, 137.63, 131.22, 92.30, 55.38. **MALDI TOF MS**: m/z 622.72 (M).
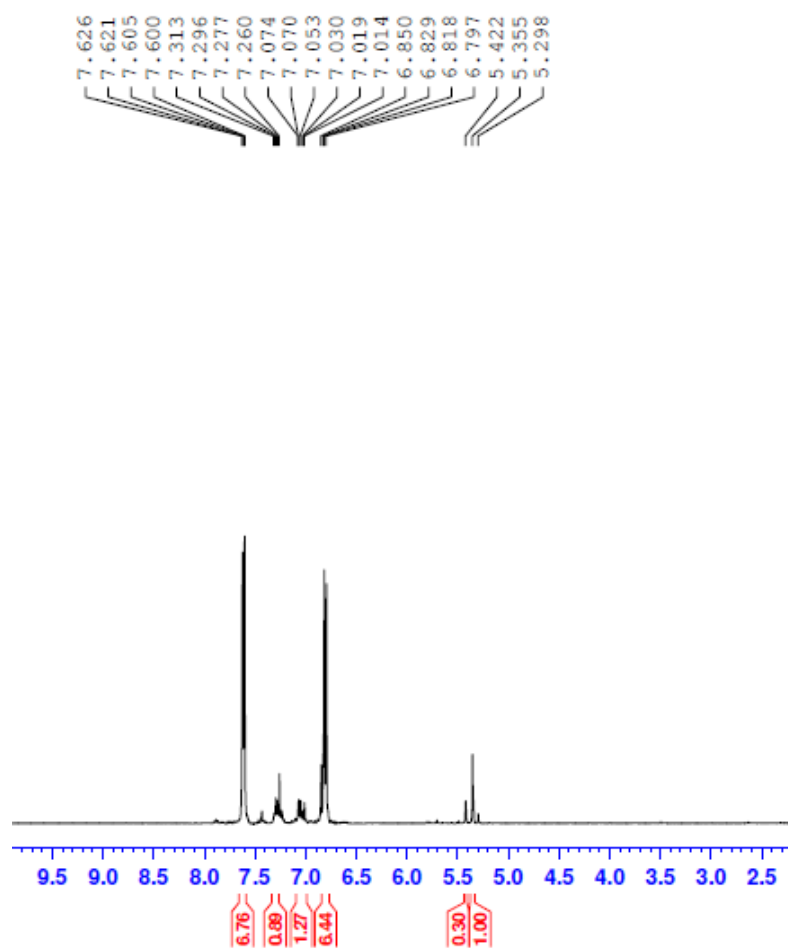
Figure A68 ^{1}H NMR spectrum of tris(4-iodophenyl)methane **(29)**
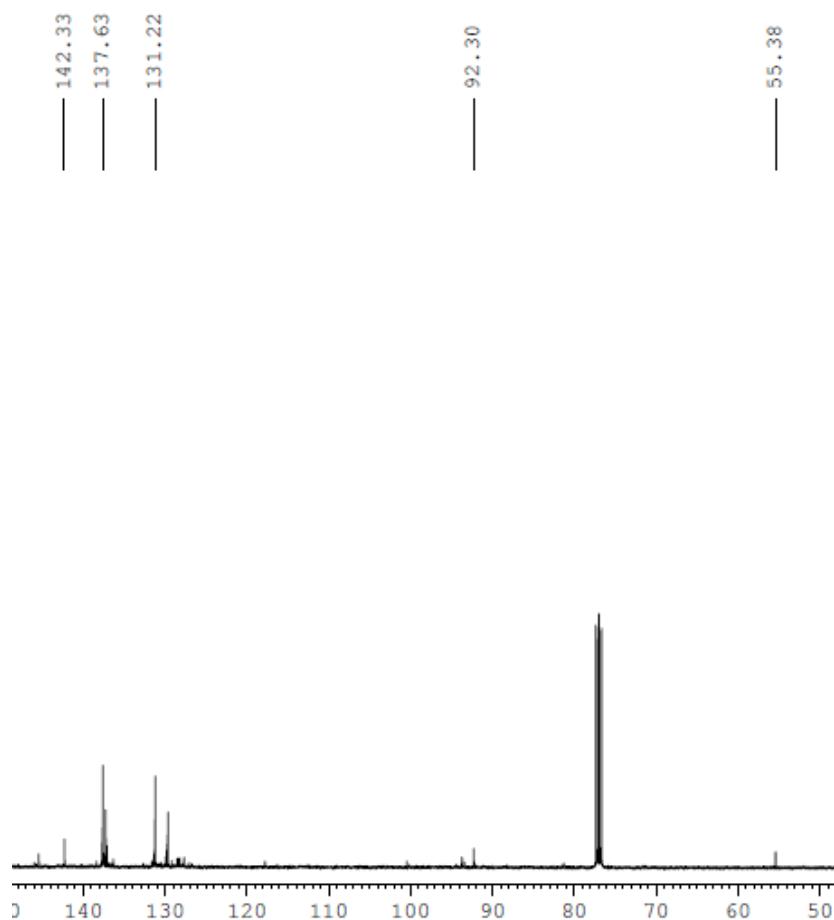
Figure A69 ^{13}C NMR spectrum of tris(4-iodophenyl)methane **(29)**
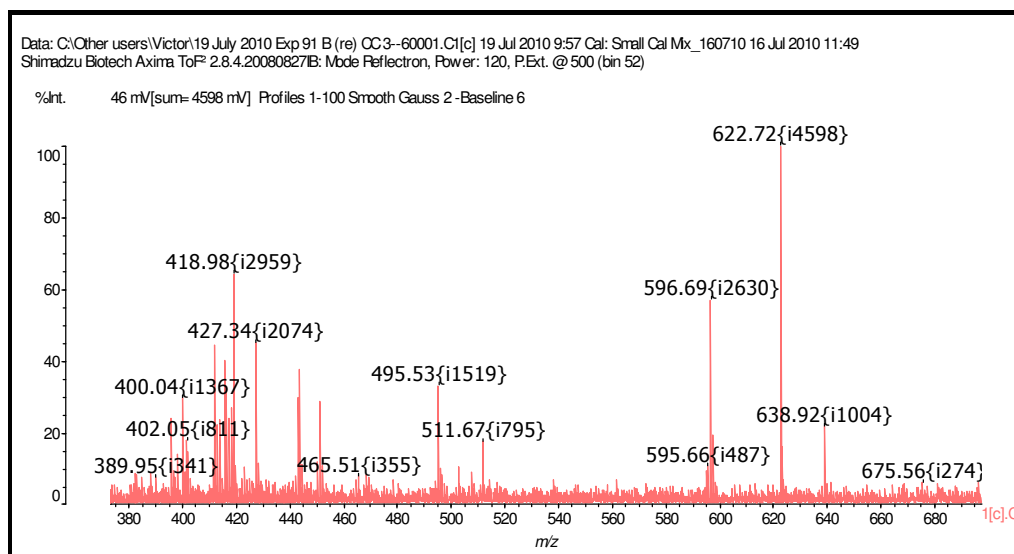
Figure A70   MALDI MS of tris(4-iodophenyl)methane **(29)**

Tris(4-(4,4,5,5-tetramethyl-1,3,2-dioxaborolan-2-yl)phenyl)methane (30). **29** (0.32 g, 0.51 mmol), bis(pinacolato)diborane (0.65 g, 2.56 mmol), potassium acetate (0.6 g, 6.14 mmol) and PdCl$_2$(dppf) (52 mg, 0.064 mmol) were dissolved in anhydrous DMSO (10 ml) in a RBF and the reaction mixture was degassed using N$_2$. The reaction mixture was stirred at 80 °C for 12 h. After cooling down to RT, the reaction mixture was extracted with CHCl$_3$ and water. The CHCl$_3$ layer was dried over MgSO$_4$ and concentrated using a rotary evaporator. The residual mixture was then recrystallized from MeOH–THF to give **30** as an off-white solid (0.13 g, 40%). **^{1}H NMR (CDCl$_3$):** δ 7.711 and 7.101 (AA'XX', 2 x apparent d, *J* = 8 Hz, 12 H), 5.563 (s, 1H), 1.327 (s, 36 H). **^{13}C NMR (CDCl$_3$):** δ 146.65, 134.84, 128.94, 83.73, 57.34, 24.86. **MALDI TOF MS**: m/z 623.76 (M+1H). **Anal. Calcd.** for C$_{37}$H$_{49}$B$_3$O$_6$: C, 71.42; H, 7.94; B, 5.21; O, 15.43. Found: C, 71.48; H, 10.54. **HR ES$^+$-TOF MS**: calculated m/z: 623.3887 (M$^+$), found: m/z 623.3890 (M$^+$).
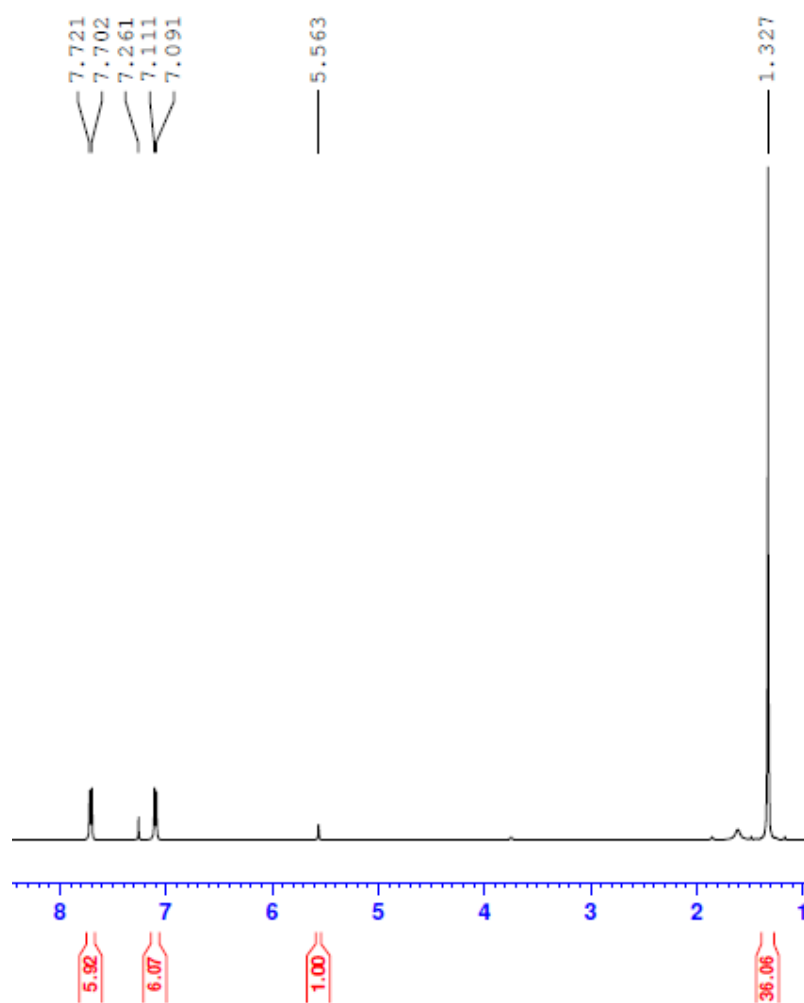
Figure A71   ¹H NMR of tris(4-(4,4,5,5-tetramethyl-1,3,2-dioxaborolan-2-yl)phenyl)methane **(30)**
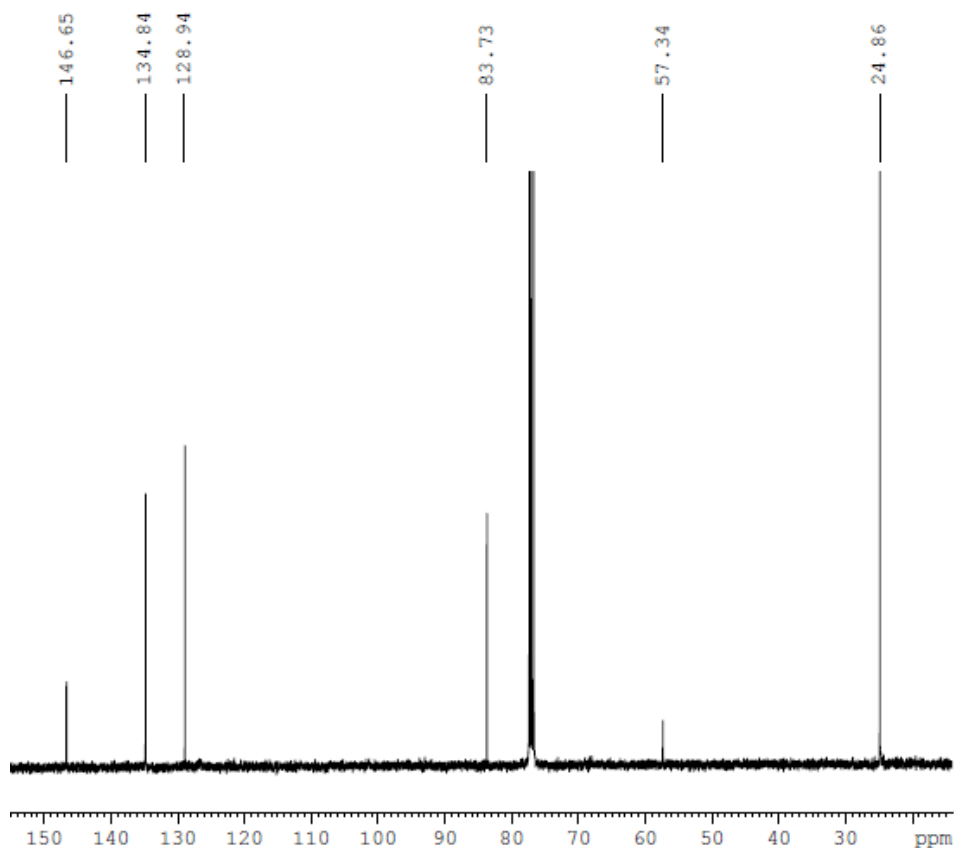
Figure A72 ^{13}C NMR of tris(4-(4,4,5,5-tetramethyl-1,3,2-dioxaborolan-2-yl)phenyl)methane **(30)**
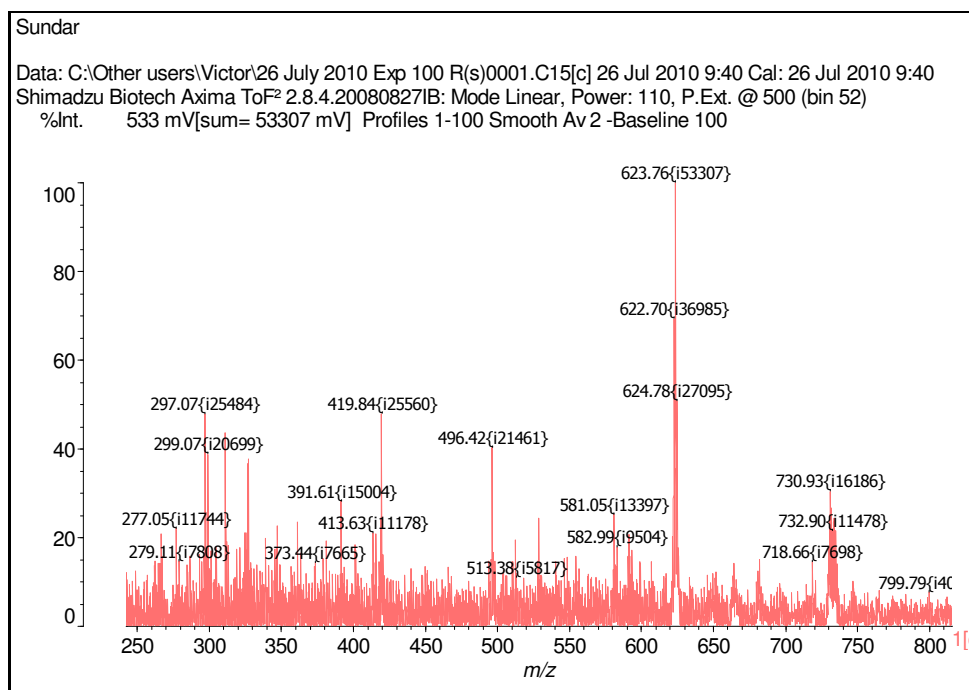
Figure A73   MALDI MS of tris(4-(4,4,5,5-tetramethyl-1,3,2-dioxaborolan-2-yl)phenyl)methane **(30)**

Bis(4-iodophenyl)methane (31). Diphenylmethane (1 ml, 6 mmol), bis[(trifluoroacetoxy)iodo]benzene (3.1 g, 7.2 mmol) and I_2 (1.68 g, 6.6 mmol) were dissolved in $CHCl_3$ (20 ml) in a RBF. The reaction mixture was then heated at 55 °C until the colour of I_2 disappeared. The $CHCl_3$ was then removed using a rotary evaporator and the residue mixture was subjected to column chromatography on silica gel eluting with a solvent mixture of 10% DCM in hexane, to give **31** as a colourless solid (1 g, 40%) after recrystallization from hexane–DCM. **^{1}H NMR (CDCl$_3$):** δ 7.617 and 6.917 (AA'XX', 2 x apparent d, J = 8 Hz, 8 H), 3.861 (s, 2 H). **^{13}C NMR (CDCl$_3$):** δ 140.09, 137.67, 131.00, 97.12, 40.94. **MALDI TOF MS**: m/z 420.48 (M).
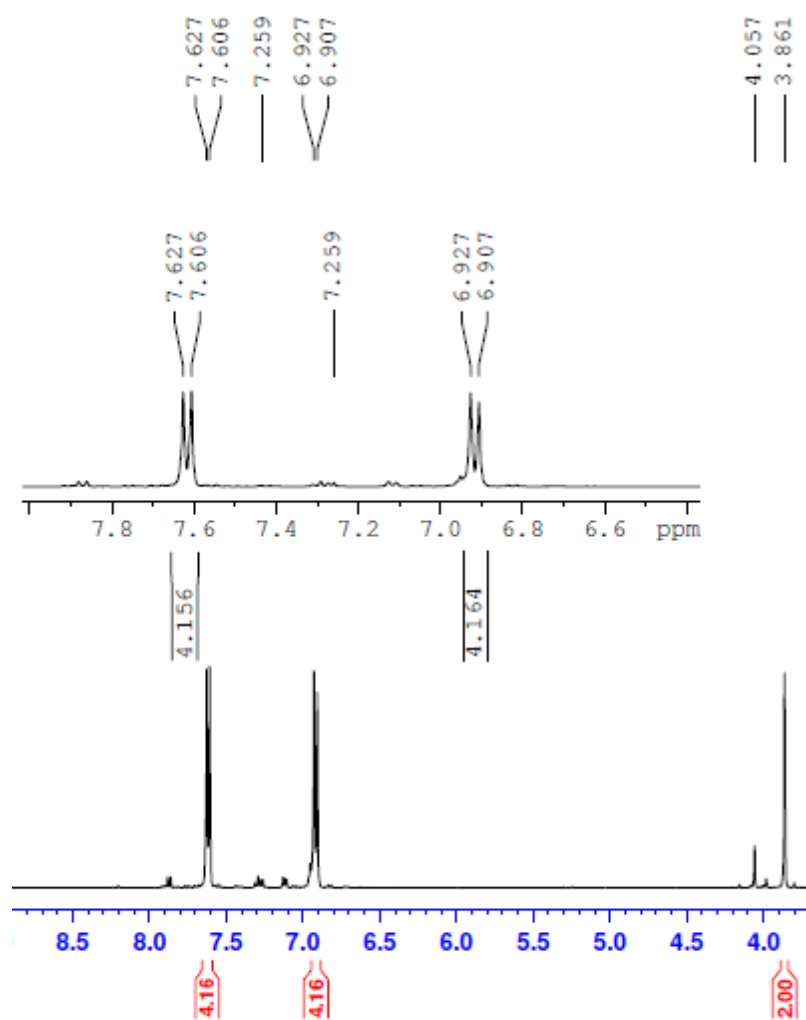
Figure A74 ^{1}H NMR spectrum of bis(4-iodophenyl)methane **(31)**
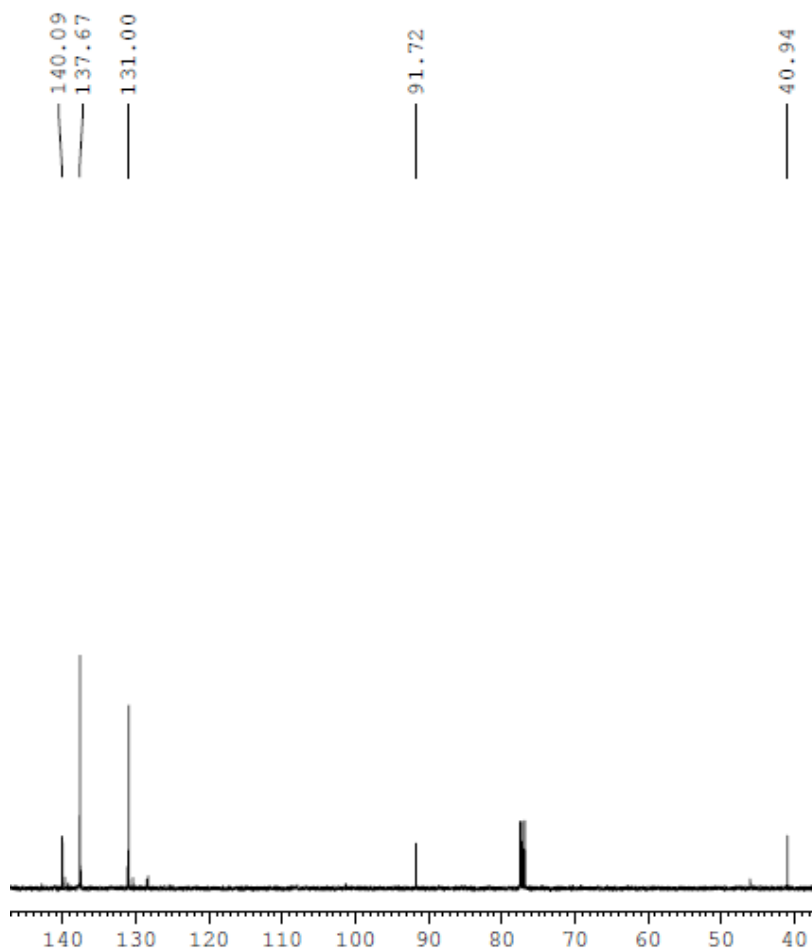
Figure A75 ^{13}C NMR spectrum of bis(4-iodophenyl)methane **(31)**
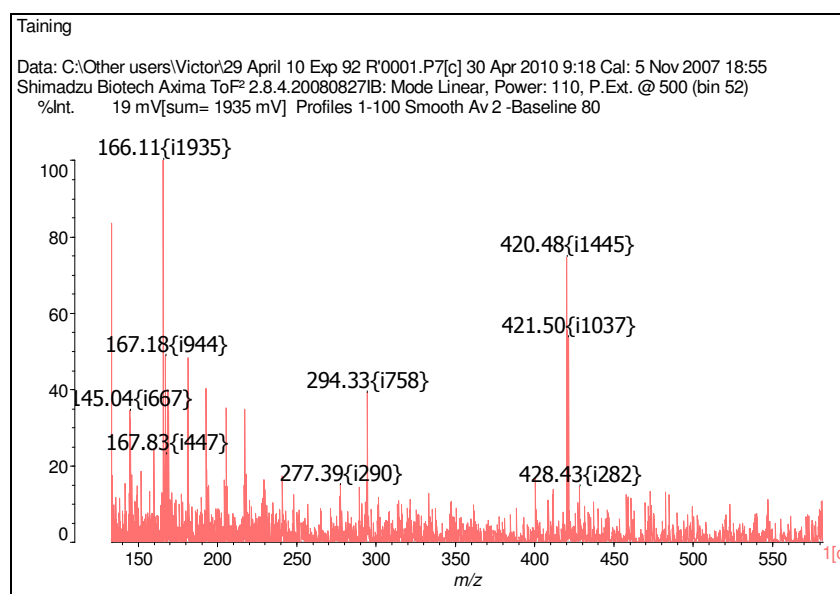
Figure A76   MALDI MS of bis(4-iodophenyl)methane **(31)**

Bis(4-(4,4,5,5-tetramethyl-1,3,2-dioxaborolan-2-yl)phenyl)methane (32). 31 (0.6 g, 1.43 mmol), bis(pinacolato)diborane (1.44 g, 5.7 mmol), potassium acetate (1.26 g, 12.83 mmol) and PdCl$_2$(dppf) (140 mg, 0.171 mmol) were dissolved in anhydrous DMSO (10 ml) in a RBF and the reaction mixture was degassed using N$_2$. The reaction mixture was stirred at 80 °C for 12 h. After cooling down to RT, the reaction mixture was extracted with CHCl$_3$ and water. The CHCl$_3$ layer was dried over MgSO$_4$ and concentrated using a rotary evaporator. The residual mixture was then recrystallized from MeOH–THF to give **30** as an off-white solid (0.6 g, 52%). **^{1}H NMR (CDCl$_3$):** δ 7.722 and 7.182 (AA'XX', 2 x apparent d, J = 8 Hz, 8 H), 4.005 (s, 2 H), 1.329 (s, 24 H). **^{13}C NMR (CDCl$_3$):** δ 144.12, 135.01, 131.66, 128.44, 83.68, 42.30, 24.85. **Anal. Calcd.** for C$_{25}$H$_{34}$B$_2$O$_4$: C, 71.47; H, 8.16; B, 5.15; O, 15.23. Found: C, 71.32; H, 12.00. **HR ES$^+$-TOF MS**: calculated m/z: 421.2721 (M$^+$), found: m/z 421.2718 (M$^+$).
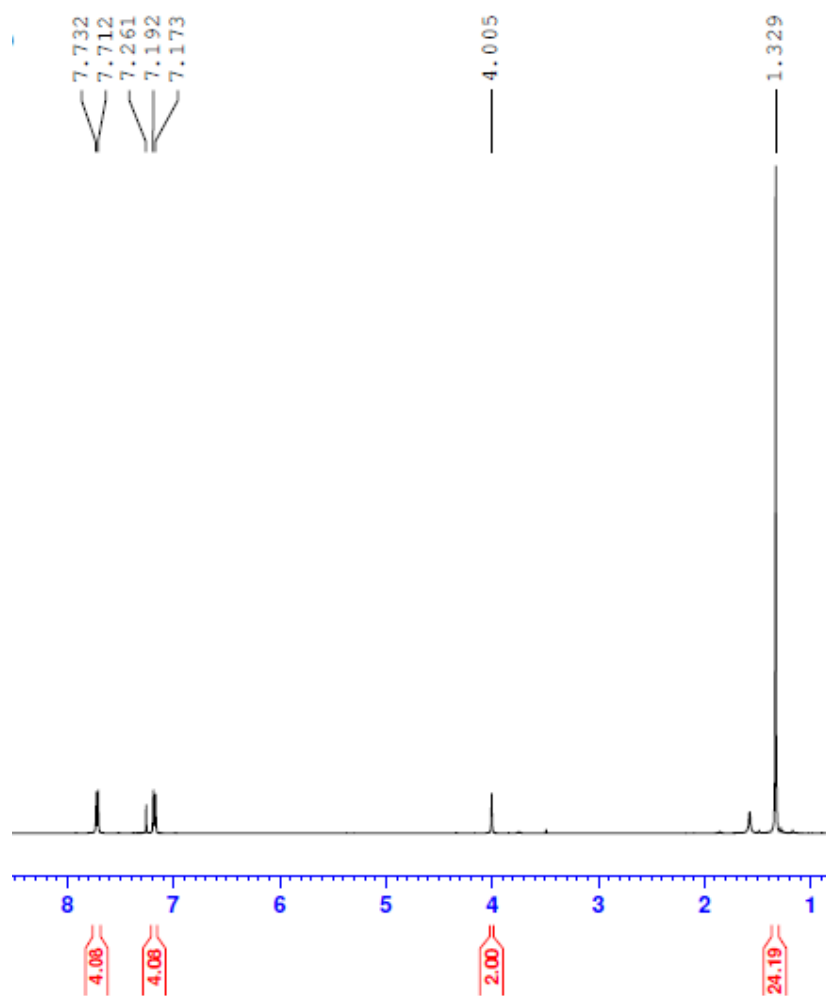
Figure A77 ^{1}H NMR of bis(4-(4,4,5,5-tetramethyl-1,3,2-dioxaborolan-2-yl)phenyl)methane **(32)**
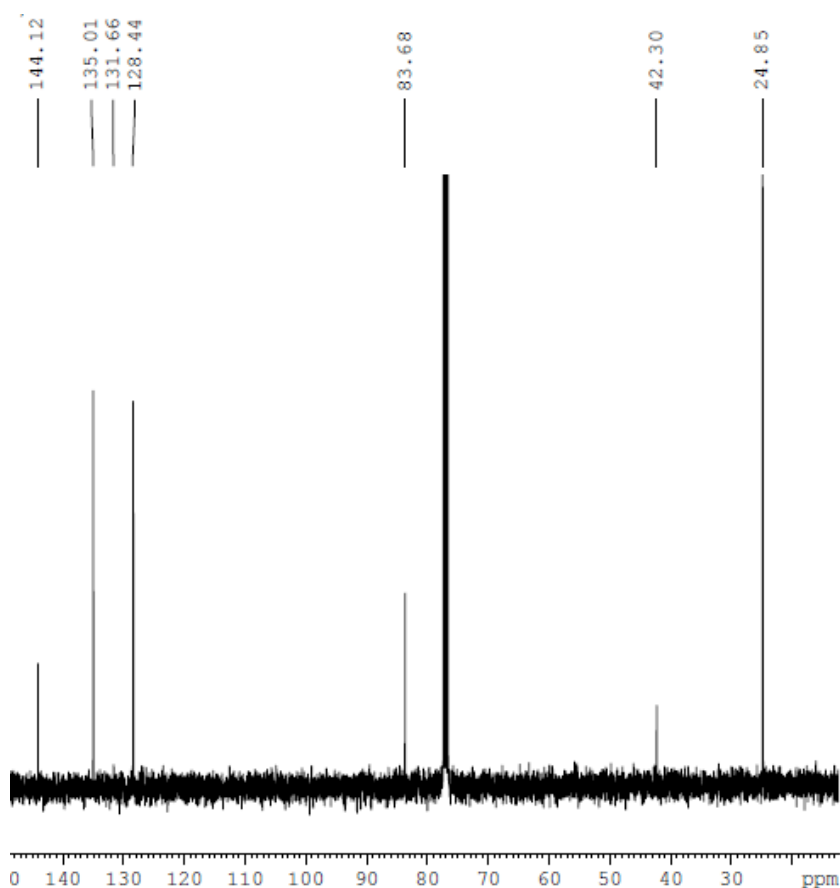
**Figure A78**   ^{13}C NMR of bis(4-(4,4,5,5-tetramethyl-1,3,2-dioxaborolan-2-yl)phenyl)methane **(32)**

4'-[4-(trimethylsilylethynyl)phenyl]-2,2':6',2"-terpyridine (37). Triphenylphosphine (0.473 g, 1.803 mmol), **5** (7 g, 18.03 mmol), palladium (II) acetate (0.28 g, 1.26 mmol), Et$_3$N (12.6 ml) and CuI (0.34 g, 1.803 mmol) were put inside RBF with N$_2$ flushing. The reaction mixture was injected with toluene (100 ml) in closed environment and the reaction mixture was stirred at 70 °C. Trimethylsilylacetylene (TMSA) (7.5 ml, 54.09 mmol) was then added separately into the RBF during the 2 days reaction. Solvent was then concentrated using a rotary evaporator followed by column chromatography on silica gel eluting with a solvent mixture of 20% EA in hexane, which gave **37** as a brown solid (4.37 g, 60%). **^{1}H NMR (CDCl$_3$):** δ 8.768 (s, 2 H), 8.754 (d, *J* = 4.8 Hz , 2 H), 8.706 (d, *J* = 8 Hz, 2 H), 7.927 (td, *J* = 7.6 Hz , 2 H), 7.890 and 7.610 (AB q, *J* = 8.4 Hz, 4 H), 7.400

(td, *J* = 4.8 Hz, 2 H). **^{13}C NMR (CDCl$_3$):** δ 155.58, 155.47, 149.56, 148.65, 138.05, 137.57, 132.58, 127.18, 124.10, 124.04, 121.73, 119.05, 104.66, 95.94, -0.03. **MALDI TOF MS**: m/z 406 (M + H).
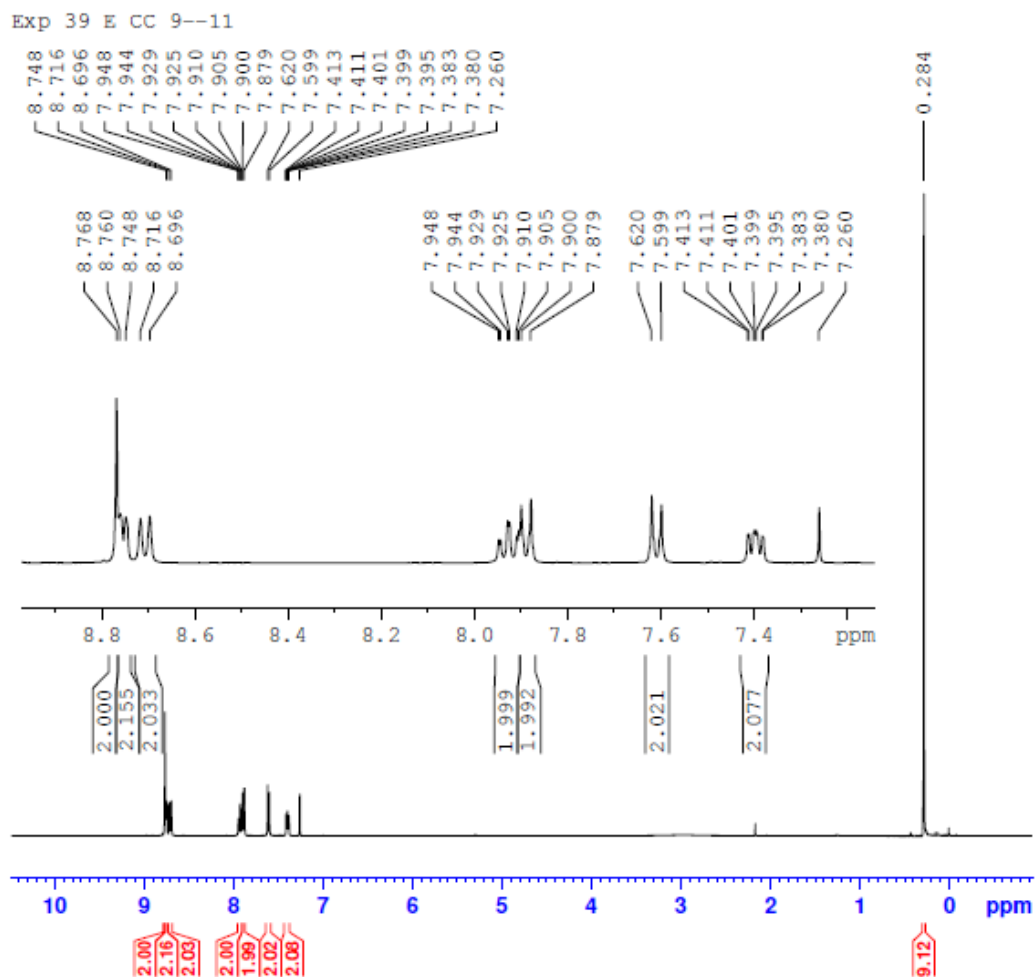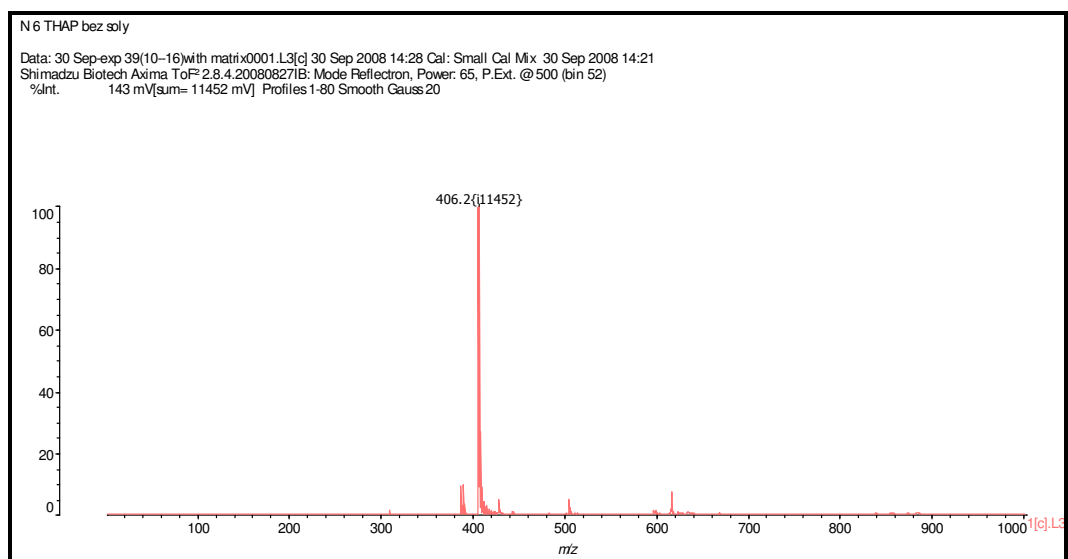

**Figure A79** ^{1}H NMR of 4'-[4-(trimethylsilylethynyl)phenyl]-2,2':6',2''-terpyridine **(37)**
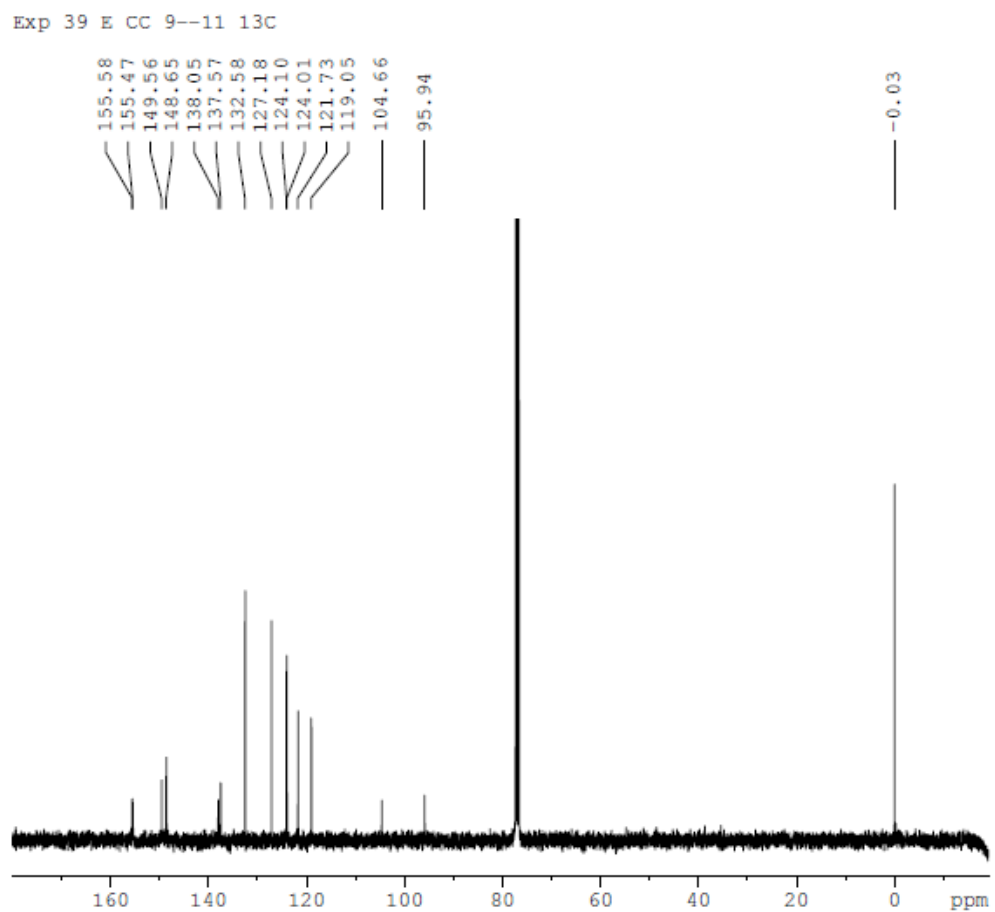
**Figure A80** ^{13}C NMR of 4'-[4-(trimethylsilylethynyl)phenyl]-2,2':6',2''-terpyridine **(37)**

Figure A81   MALDI-TOF mass spectra of 4'-[4-(trimethylsilylethynyl)phenyl]-2,2':6',2''-terpyridine

(37)

4'-(4 -Ethynylphenyl) -2,2':6',2''-terpyridine (38). 37 (0.83 g, 2.05 mmol) and K_2CO_3

(6 g, 43.4 mmol) were dissolved in MeOH (40 ml) and THF (40 ml). The reaction

mixture was stirred for 24 h at RT. Reaction mixture was then extracted using DCM and

water. Organic layer was dried over $MgSO_4$ and concentrated using a rotary evaporator.

38 was then obtained as a white solid (0.64 g, 94%) after recrystallization using EtOH. **[1]H**

NMR (CDCl3): δ 8.757–8.738 (br, 4 H), 8.688 (d, J = 8 Hz, 2 H), 7.906 (m, 4 H), 7.639

(d, J = 8.4 Hz, 2 H), 7.385 (t, J = 4.8 Hz, 2 H), 3.188 (s, 1 H). **^{13}C NMR (CDCl3):** δ

155.69, 149.44, 148.80, 138.61, 137.37, 132.74, 127.29, 124.07, 122.92, 121.61, 119.00,

82.30, 78.60. **MALDI TOF MS**: m/z 334.16 (M + H) & m/z 666.32 (dimer).
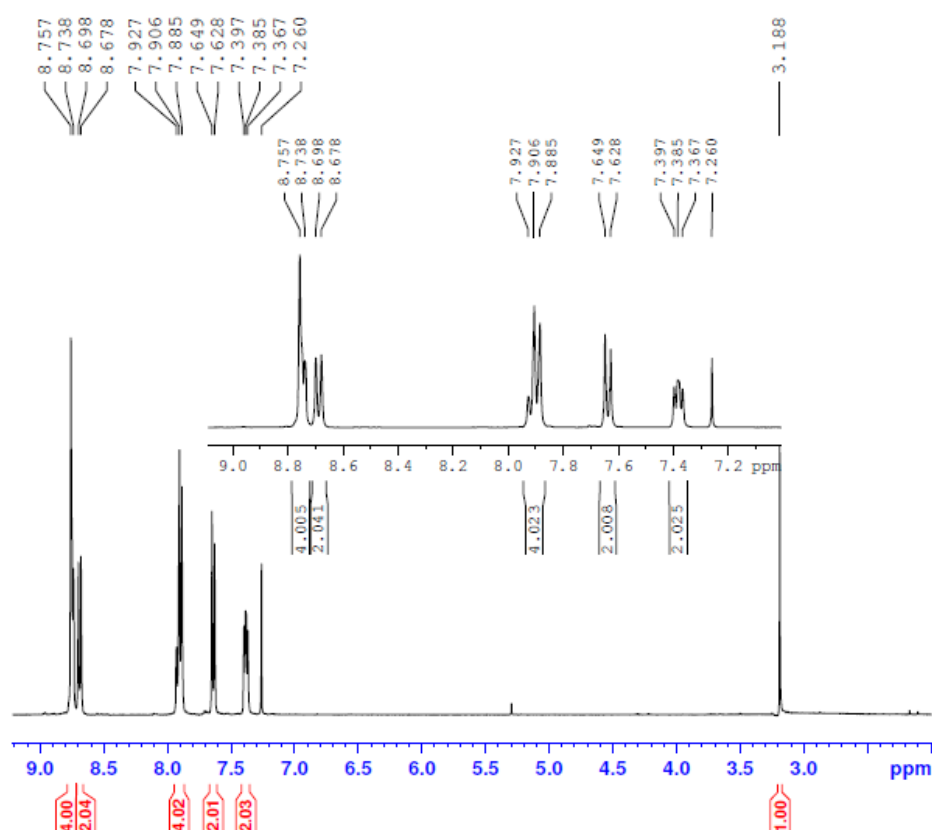
Figure A82   ^{1}H NMR of 4'-(4 -Ethynylphenyl) -2,2':6',2''-terpyridine **(38)**
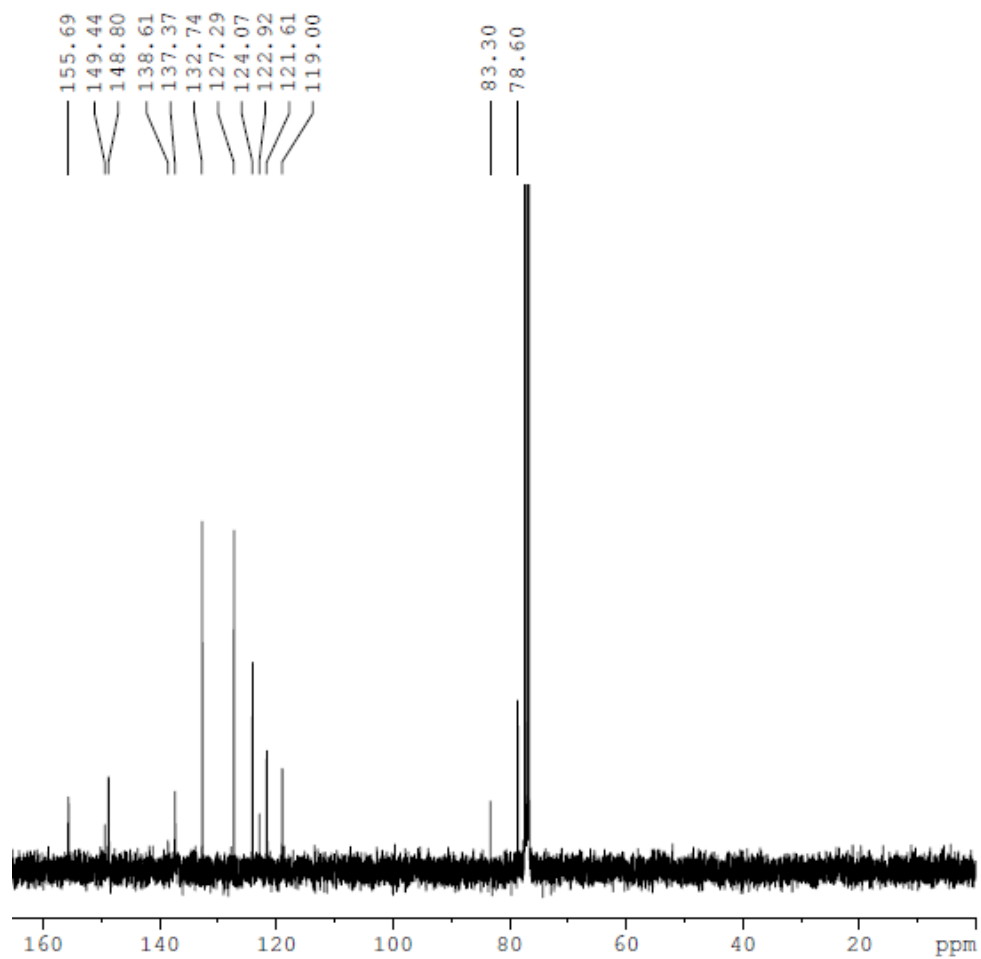
Figure A83 ^{13}C NMR of 4'-(4 -Ethynylphenyl) -2,2':6',2''-terpyridine **(38)**
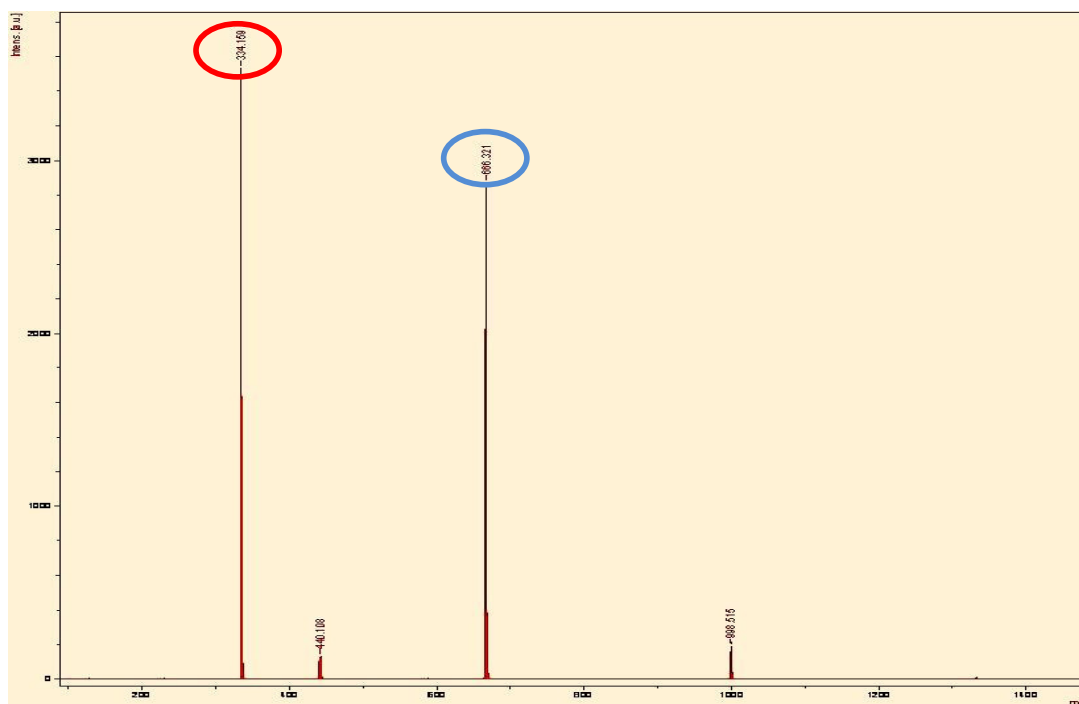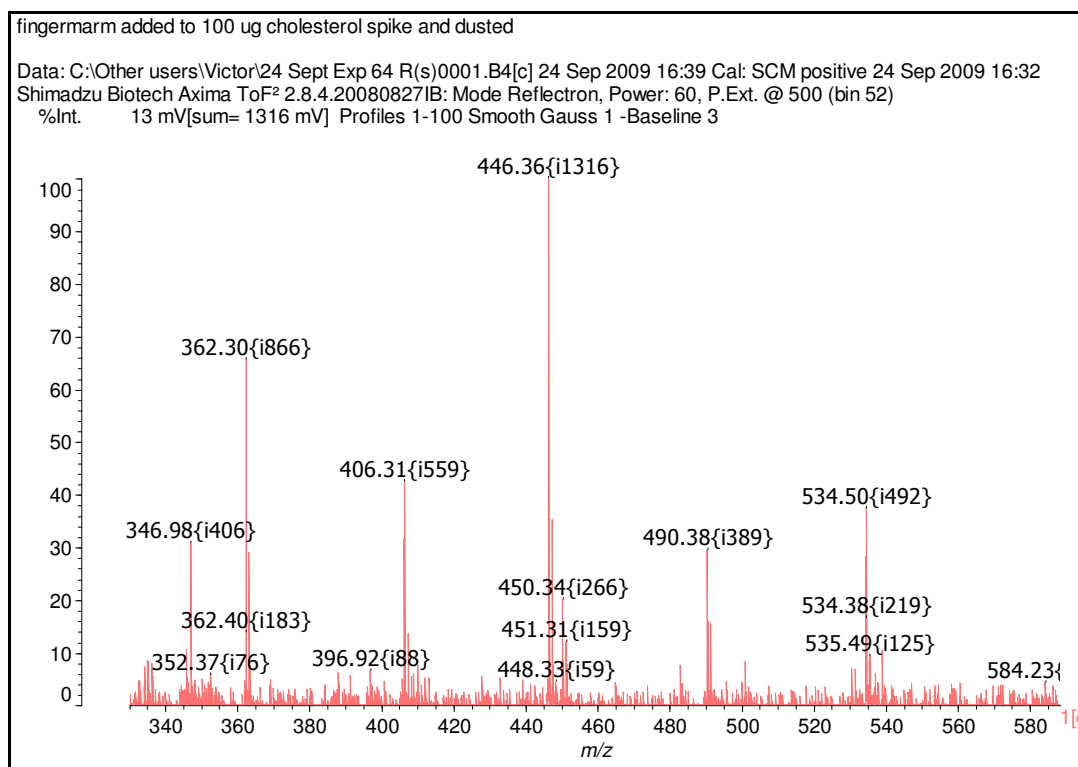
Figure A84   MALDI-TOF mass spectra of 4'-(4 -Ethynylphenyl) -2,2':6',2''-terpyridine **(38)**

1,4-bis(dodecyloxy)benzene (39). Hydroquinone (20 g, 181.64 mmol) was dissolved in absolute EtOH (500 ml) containing NaOH (10.9 g, 272.6 mmol) at RT under N_2. The reaction mixture was heated at 80 °C, followed by the dropwise addition of dodecylbromide (87 ml, 363.28 mmol). After 24 h of stirring under N_2, the reaction mixture was cooled and filtered, and the precipitate was washed with water. After recrystallized using MeOH, **39** was obtained as an off-white solid (34.065 g, 42%). **^{1}H NMR (CDCl$_3$):** δ 6.815 (s, 4 H), 3.894 (t, *J* = 6.4 Hz, 4 H), 1.746 (m, 4 H), 1.473 (m, 4 H), 1.263—1.326 (br, 32 H), 0.88 (t, *J* = 6.8 Hz, 6 H). **^{13}C NMR (CDCl$_3$):** 153.1, 115.3, 68.6, 31.9, 29.6, 26.1, 22.7, 14.1[1]. **MALDI TOF MS**: m/z 446.36 (M), m/z 362.30 (M-C$_6$H$_{12}$).
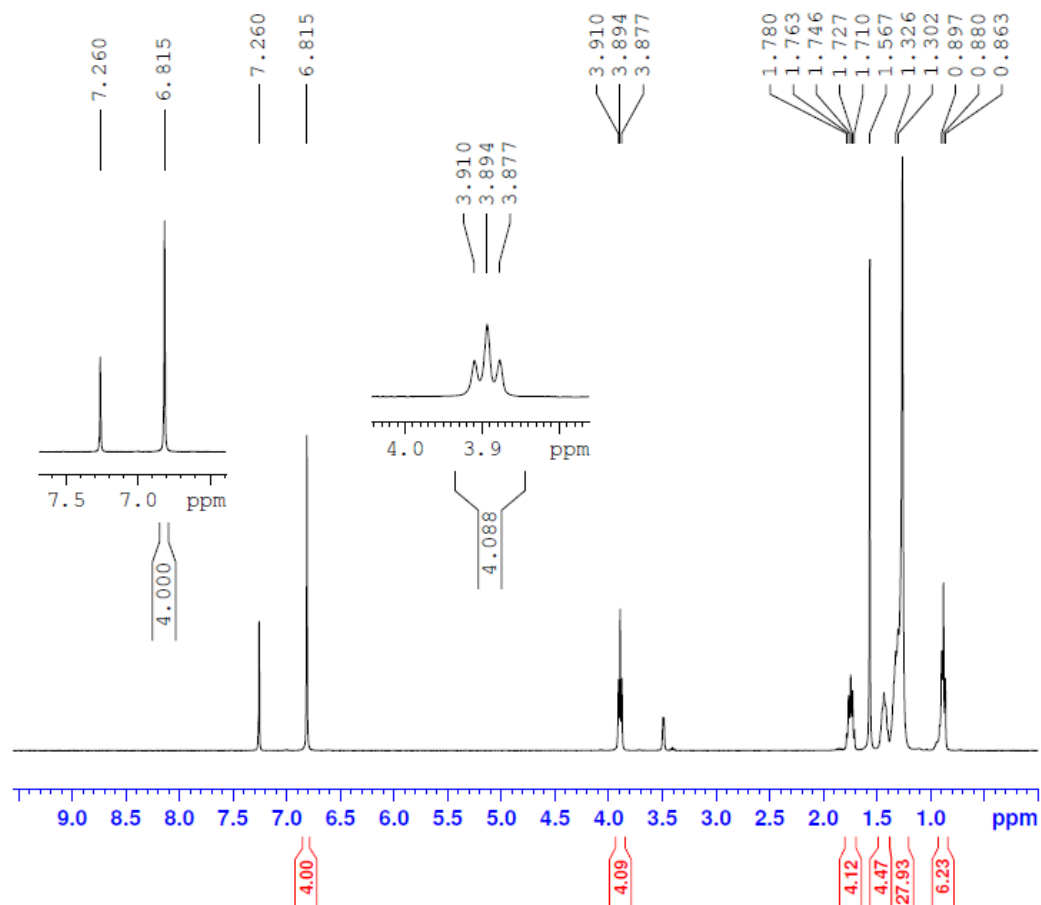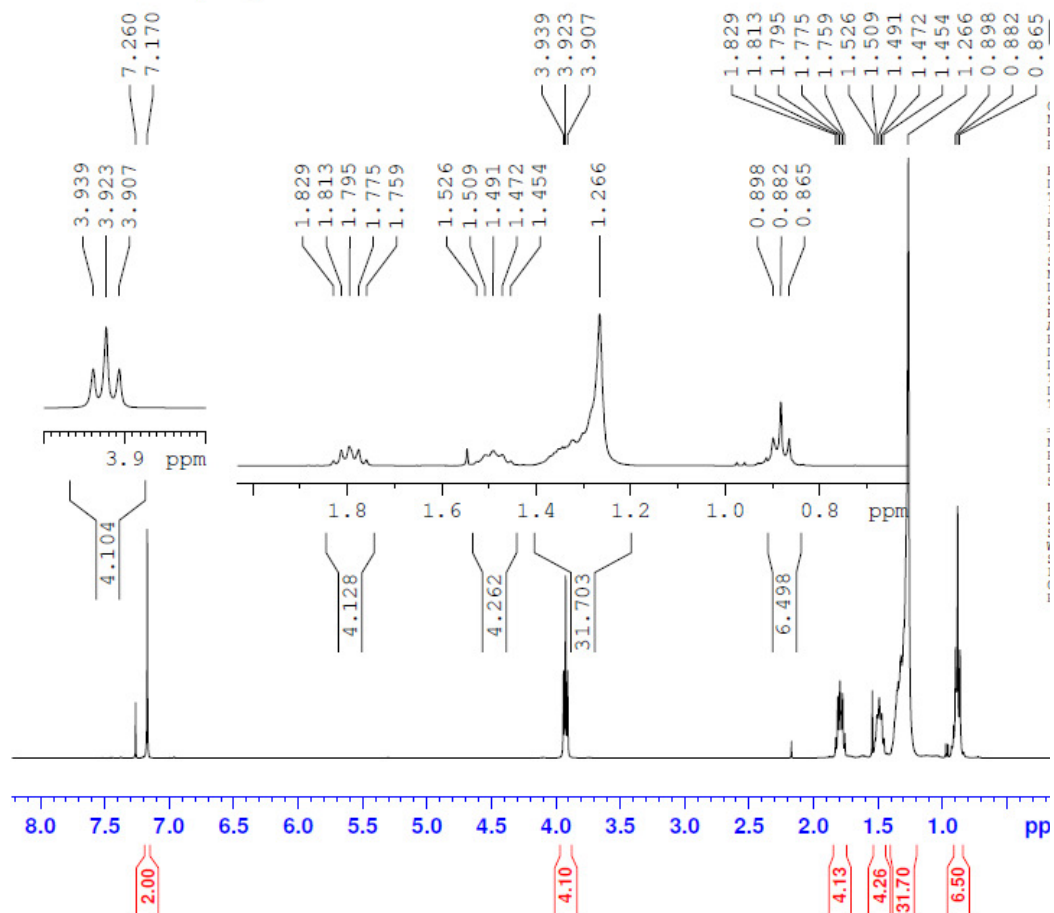
Figure A85 ^{1}H NMR of 1,4-bis(dodecyloxy)benzene **(39)**

Figure A86   MALDI-TOF mass spectra of 1,4-bis(dodecyloxy)benzene **(39)**
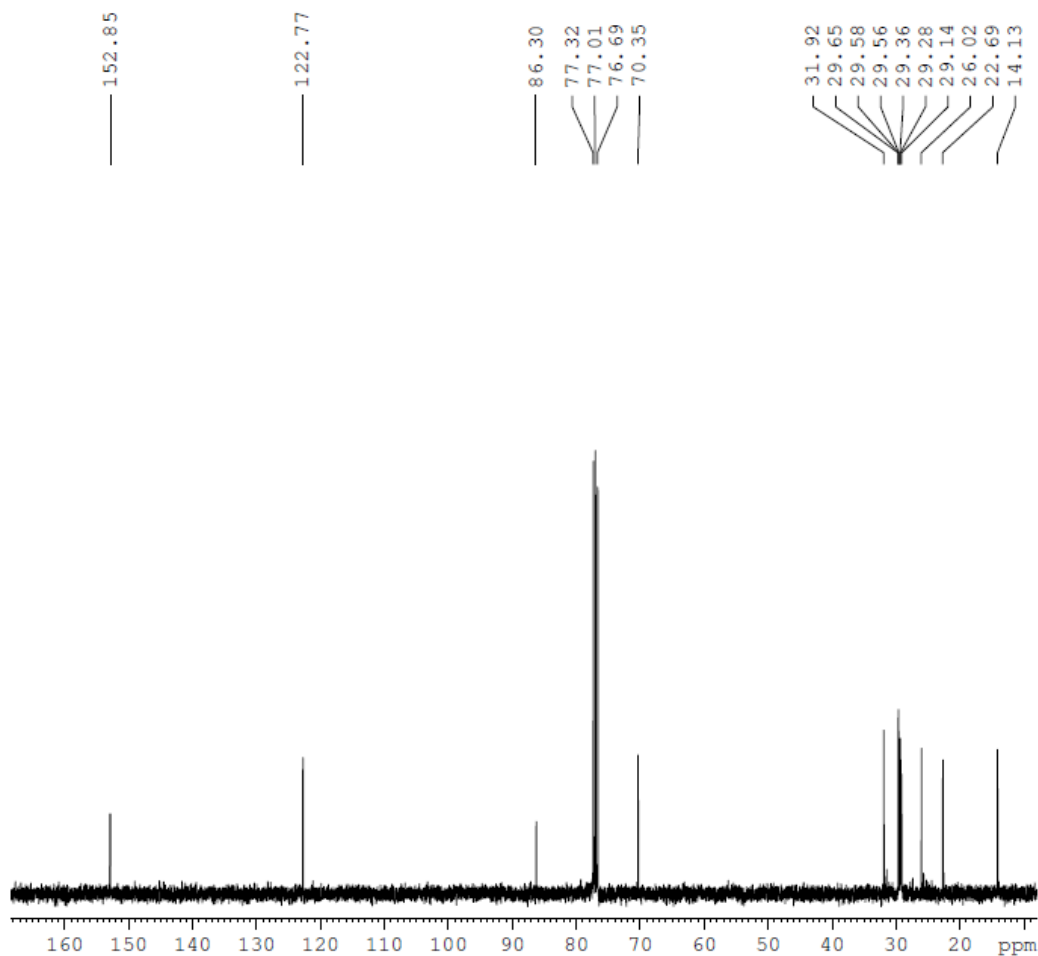
1,4-bis(dodecyloxy)-2,5-diiodobenzene (40). 39 (10 g, 22.38 mmol), KIO_3 (1.92 g, 9 mmol) and I_2 (11.37 g, 44.76 mmol) were added to a stirred solution of acetic acid (135 ml), H_2SO_4 (2.4 ml) and H_2O (10 ml). The reaction mixture was refluxed for 6 h and then cooled to RT. Aqueous Na_2SO_3 was added until the brown colour of iodine disappeared, and the reaction mixture was poured into ice water (250 ml). The precipitate in the ice water was then filtered and extracted with hexane and water. Hexane layer was dried over $MgSO_4$ and concentrated using a rotary evaporator, followed by column chromatography on silica gel eluting with pure hexane which gave **40** as a white solid (10 g, 64%). **^{1}H NMR (CDCl₃):** δ 7.170 (s, 2 H), 3.923 (t, *J* = 6.4 Hz, 4 H), 1.795 (m, 4 H), 1.491 (m, 4 H), 1.266 (br, 32 H), 0.882 (t, *J* = 6.4 Hz, 6 H). **^{13}C NMR (CDCl₃):** δ 152.85, 122.77, 86.3, 70.35, 31.92, 29.14–29.56, 26.02, 22.69, 14.13.

Diiodo-didodecyloxybenzene

**Figure A87**   ¹H NMR of 1,4-bis(dodecyloxy)-2,5-diiodobenzene **(40)**

Figure A88 ^{13}C NMR of 1,4-bis(dodecyloxy)-2,5-diiodobenzene **(40)**

Monoadduct of 4'-(4-Ethynylphenyl)-2,2':6',2''-terpyridine with 1,4-bis(dodecyloxy)-2,5-diiodobenzene (41). In a sealed system containing **38** (0.35 g, 1.05 mmol), **40** (0.73 g, 1.05 mmol), (Ph$_3$P)$_2$PdCl$_2$ (0.15 g, 0.21 mmol) and CuI (0.04 g, 0.21 mmol), dry THF (25 ml) was injected into the reaction mixture, followed by injecting of dry triethylamine (1 ml, 5.25 mmol). After stirring overnight at RT, the reaction mixture was concentrated using a rotary evaporator. The reaction mixture was then purified by column chromatography on silica gel eluting with 10% EA in hexane which gave **41** as a light yellow solid (0.33 g, 35%). **^{1}H NMR (CDCl$_3$):** δ 8.757 (s, 2 H),

7.326 (s, 1H), 6.943 (s, 1H), 8.737 (d, J = 4.8 Hz, 2 H), 8.682 (d, J = 8 Hz, 2 H), 7.888 (m, 4 H), 7.666 (d, J = 8.4 Hz, 2 H), 7.363 (t, J = 5.2 Hz, 2 H), 4.001 (2 overlap triplets, J = 6.4 Hz, 4 H), 1.835 (m, 4 H), 1.55 (m, 4 H), 1.372 (m, 4 H), 1.271 (br, 28 H), 0.882 (t, J = 6.4 Hz, 3 H), 0.82 (t, J = 6.4 Hz, 3 H). **^{13}C NMR (CDCl$_3$):** δ 156.13, 156.04, 154.41, 151.87, 149.38, 149.13, 138.13, 136.88, 132.06, 127.23, 124.17, 123.88, 121.35, 118.62, 115.93, 113.49, 109.91, 93.92, 87.79, 87.10, 70.04, 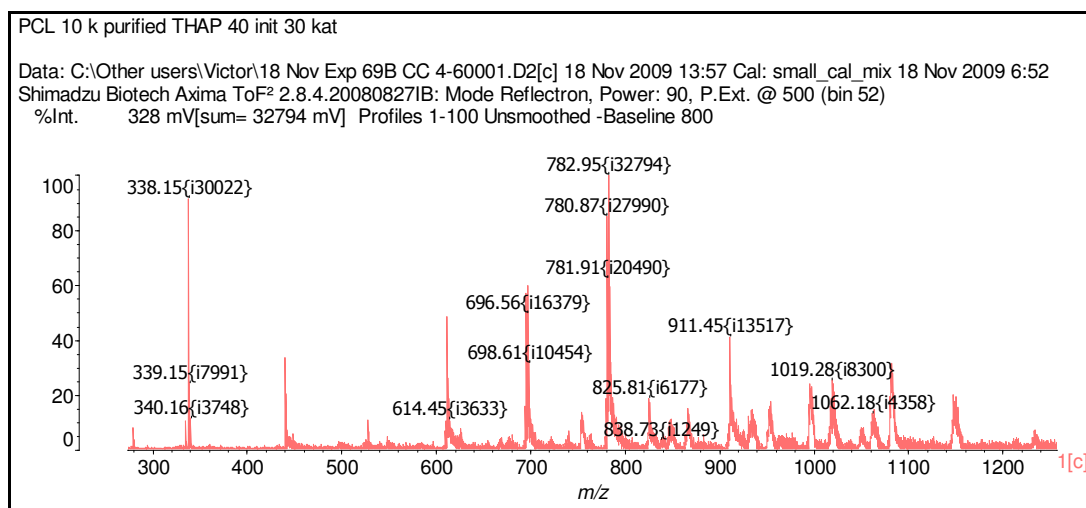31.92, 29.48, 26.07, 22.68, 14.09. **MALDI TOF MS**: m/z 782.95 (M-(I+CH$_3$)), 696.56 (M-(I+C$_7$H$_{14}$)) and others. **HR ES$^+$-TOF MS**: calculated m/z: 904.4278 (M$^+$), found: m/z 904.4272 (M$^+$).
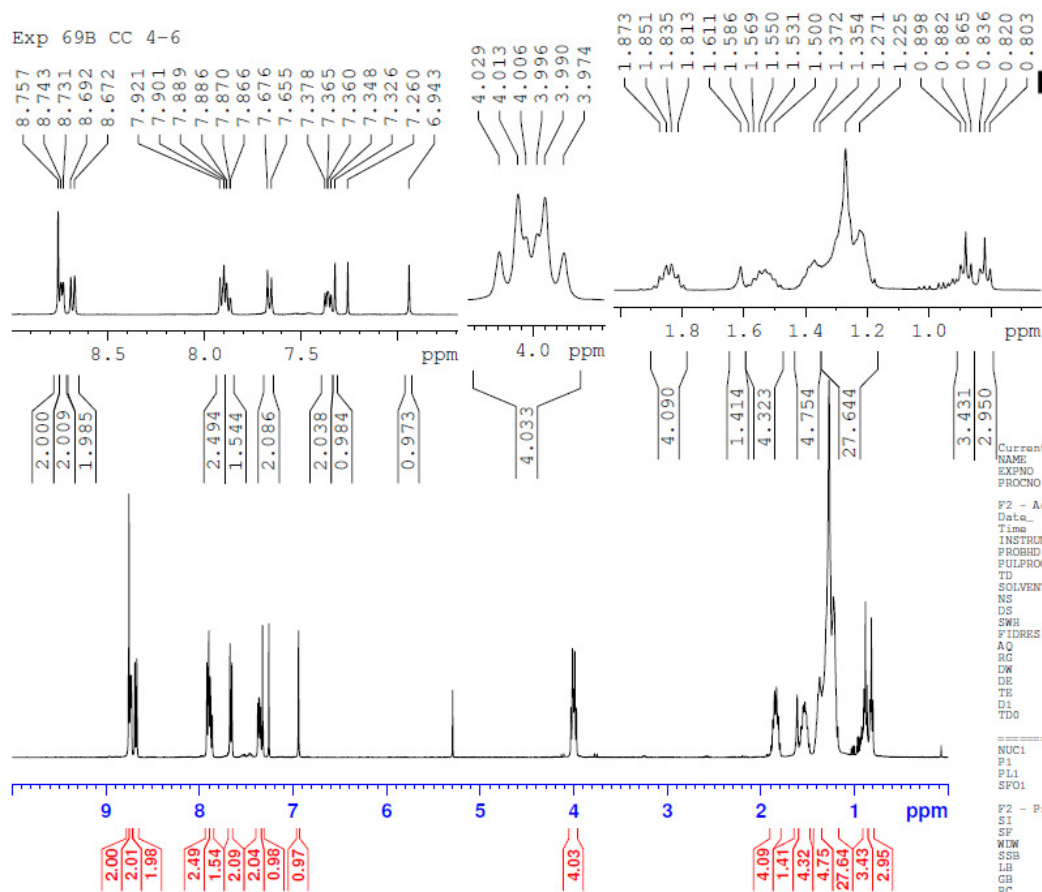
Figure A89 ^{1}H NMR of **41**
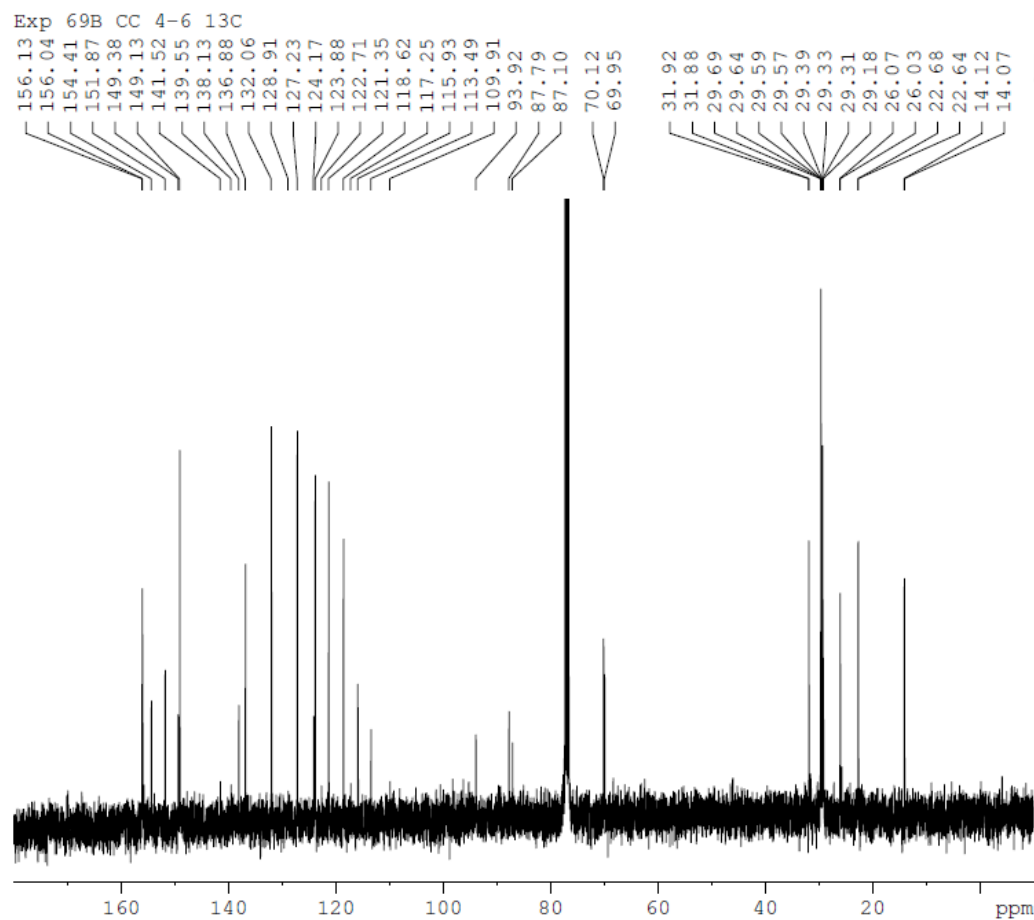
Figure A90 ^{13}C NMR of **41**

Figure A91 MALDI-TOF MS of **41**

Coupling of 41 with trimethylsilylacetylene (42). In a sealed system containing **41** (0.5 g, 0.55 mmol), $(Ph_3P)_2PdCl_2$ (0.04 g, 0.055 mmol) and CuI (0.02 g, 0.11 mmol), dry THF (20 ml) was injected into the reaction mixture, followed by injecting dry triethylamine (0.38 ml, 2.75 mmol). After 10 min of stirring at RT, trimethylsilylacetylene (0.23 ml, 1.65 mmol) was injected and the reaction mixture was stirred at RT for 24 h. The reaction mixture was then concentrated using a rotary evaporator and purified by column chromatography on silica gel eluting with 10% EA in hexane, which gave **42** as a white solid (0.23 g, 48%). **^{1}H NMR (CDCl$_3$):** δ 8.755 (s, 2 H), 6.997 (s, 1H), 6.964 (s, 1H), 8.735 (d, J = 4.8 Hz, 2 H), 8.680 (d, J = 8 Hz, 2 H), 7.895 (m, 4 H), 7.663 (d, J = 8.4 Hz, 2 H), 7.363 (t, J = 6 Hz, 2 H), 4.009 (q, J = 6.8 Hz, 4 H), 1.838 (m, 4 H), 1.537 (m, 4 H), 1.267 (br, 32 H), 0.881 (t, J = 6.4 Hz, 3 H), 0.819 (t, J = 6.8 Hz, 3 H), 0.272 (s, 9H); **^{13}C NMR (CDCl$_3$):** δ 156.16, 156.06, 154.21, 153.57, 149.16, 138.15, 136.90, 132.17, 127.25, 124.21, 123.90, 121.37, 118.65, 117.29, 116.84, 114.07, 113.88, 101.15, 100.21, 94.60, 87.45, 69.57, 31.92, 29.46, 26.08, 22.67, 14.12, 0; **MALDI TOF MS**: m/z 875.37 (M), 696.56 {M-(C_4H_7Si)} and 539 (M-$2C_{12}H_{25}$). **HR ES$^+$-TOF MS**: calculated m/z: 874.5707 (M$^+$), found: m/z 874.5711 (M$^+$).
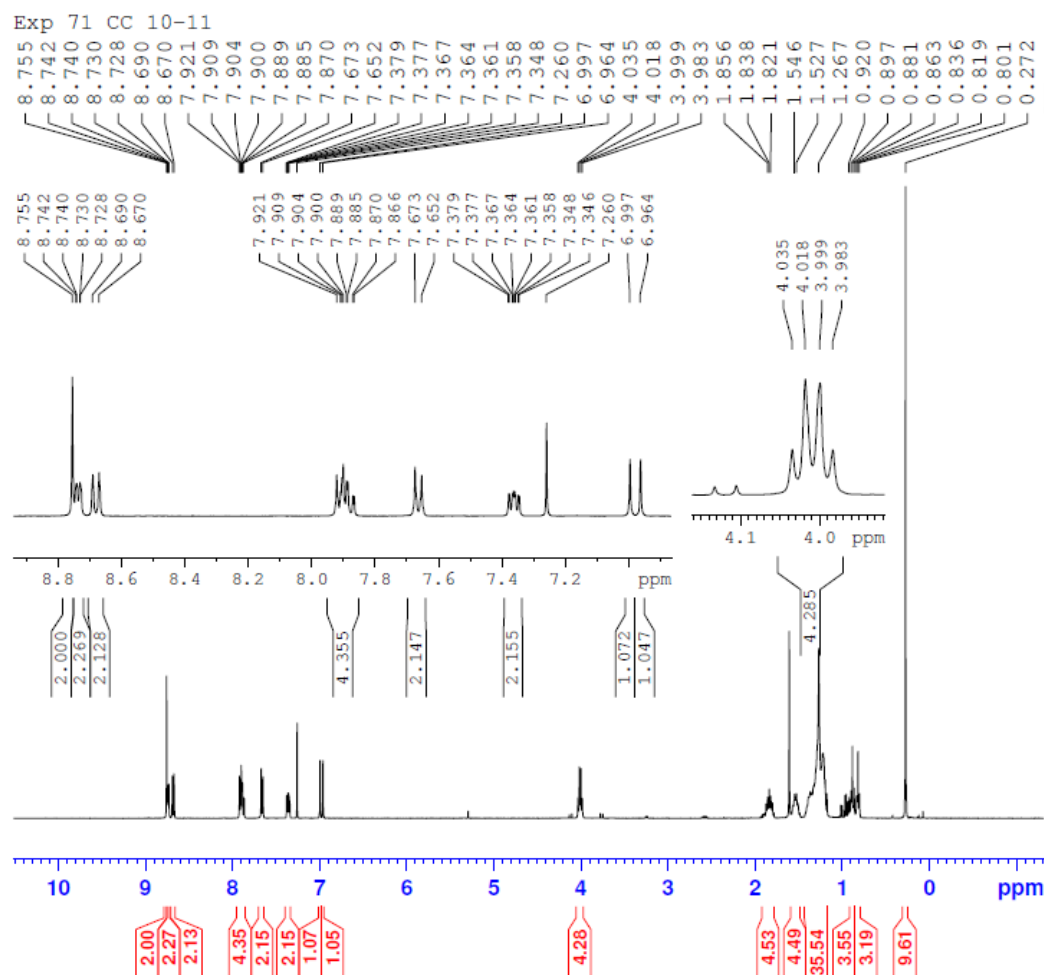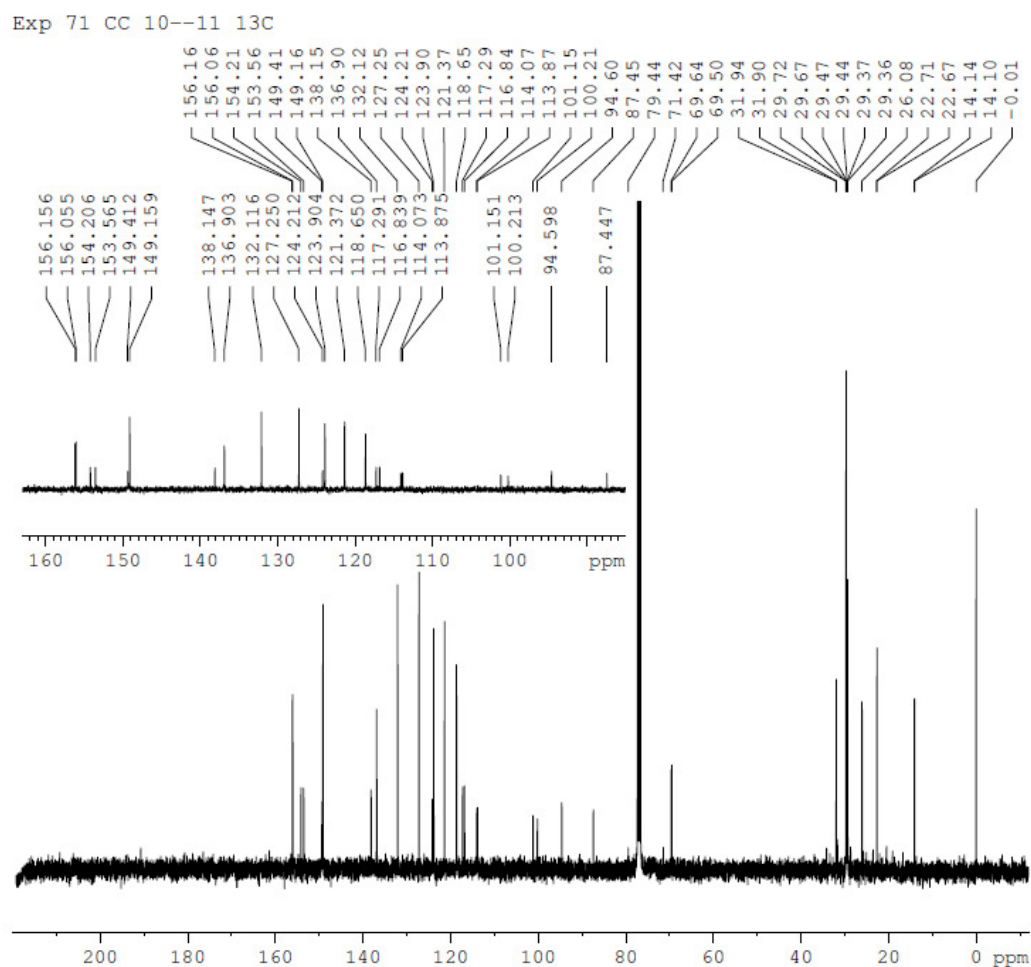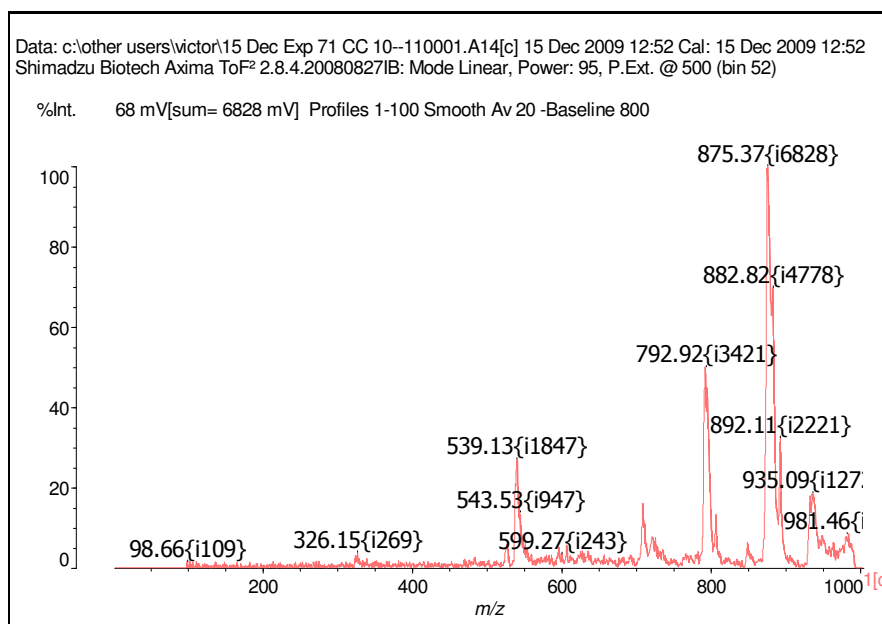
Figure A92 ^{1}H NMR of **42**

Exp 71 CC 10--11 13C

Figure A93 ^{13}C NMR of **42**

Data: c:\other users\victor\15 Dec Exp 71 CC 10--110001.A14[c] 15 Dec 2009 12:52 Cal: 15 Dec 2009 12:52
Shimadzu Biotech Axima ToF² 2.8.4.20080827IB: Mode Linear, Power: 95, P.Ext. @ 500 (bin 52)

%Int.   68 mV[sum= 6828 mV] Profiles 1-100 Smooth Av 20 -Baseline 800

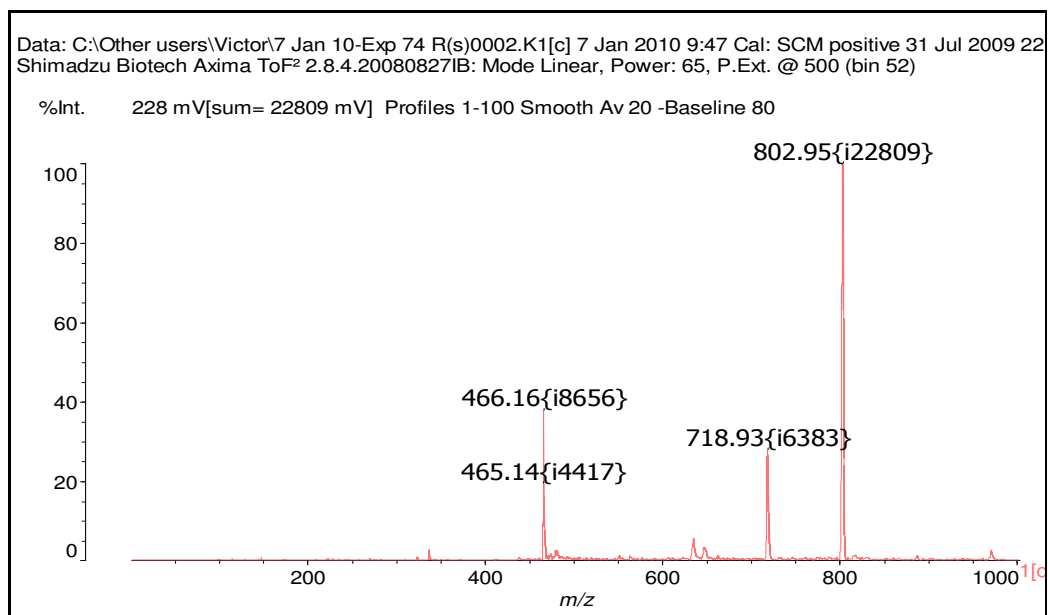**Figure A94**   MALDI-TOF mass spectra of **42**

Deprotection of 42 (43). **42** (0.12 g, 0.14 mmol), K_2CO_3 (0.4 g, 2.9 mmol) were added with a solution mixture of MeOH (3 ml) and THF (3 ml). The reaction mixture was then stirred at RT for 24 h. The reaction mixture was then concentrated using a rotary evaporator. The crude solid was then extracted with DCM and water. DCM layer was then dried over $MgSO_4$ and concentrated using a rotary evaporator. The crude solid was then recrystallized in EtOH–THF to give **43** as a white solid (0.09 g, 81%). **^{1}H NMR (CDCl$_3$):** δ 8.758 (s, 2 H), 7.027 (s, 1H), 6.995 (s, 1H), 8.737 (d, $J = 4$ Hz, 2 H), 8.682 (d, $J = 8$ Hz, 2 H), 7.888 (m, 4 H), 7.674 (d, $J = 8.4$ Hz, 2 H), 7.363 (t, $J = 6.4$ Hz, 2 H), 4.020 (m, 4 H), 3.536 (s, 1H), 1.846 (m, 4 H), 1.552 (m, 2H), 1.461 (m, 2H), 1.369 (m, 4 H), 1.267 (br, 28 H), 0.880 (t, $J = 6.8$ Hz, 3 H), 0.819 (t, $J = 6.8$ Hz, 3 H); **^{13}C NMR (CDCl$_3$):** δ 156.15, 156.06, 154.18, 153.54, 149.16, 138.22, 136.91, 132.14, 127.26, 124.14, 123.91, 121.37, 118.65, 117.82, 116.84, 114.50, 112.74, 94.65, 87.25, 82.38, 80.03, 69.68, 31.94, 29.52, 26.08, 22.69, 14.10; **MALDI TOF MS**: m/z 802.95 (M), m/z 718.93 (M-C_6H_{11}), m/z 465.50 (M-$C_{24}H_{48}$). **HR ES$^+$-TOF MS**: calculated m/z: 802.5312 (M$^+$), found: m/z 802.5314 (M$^+$).
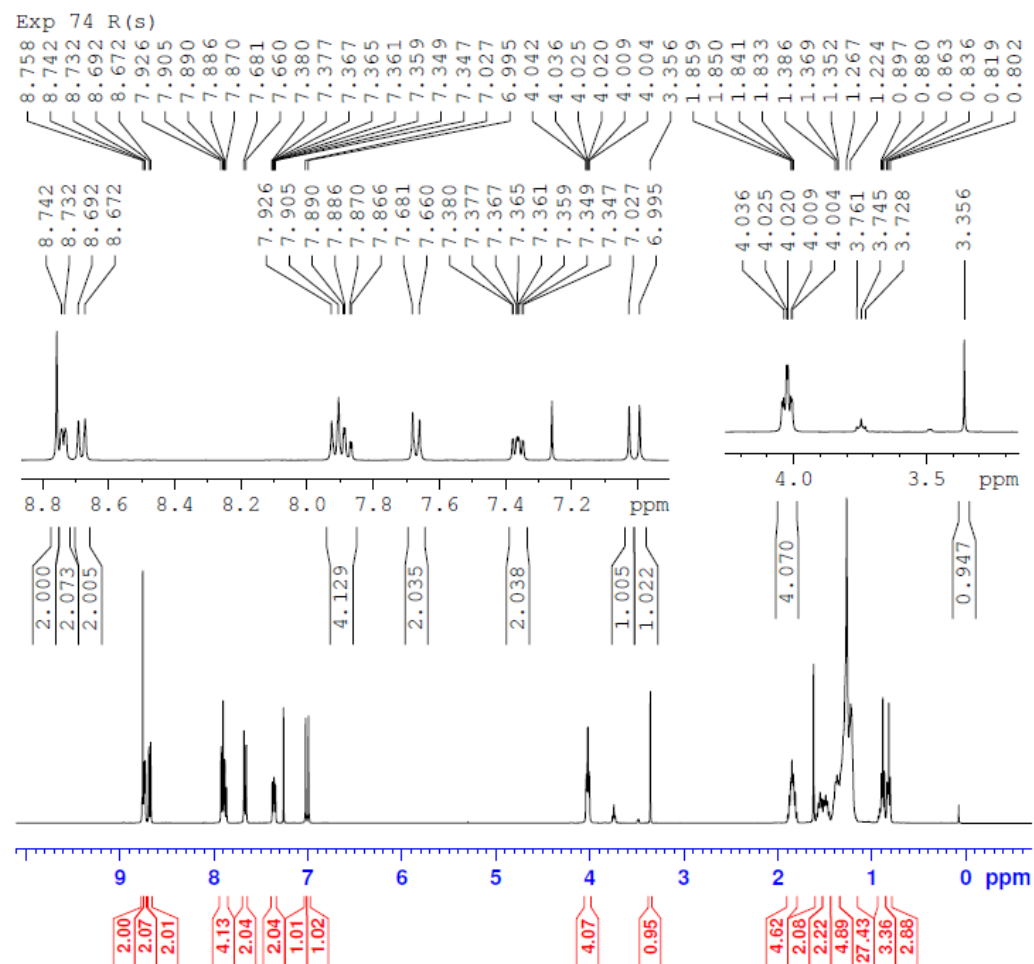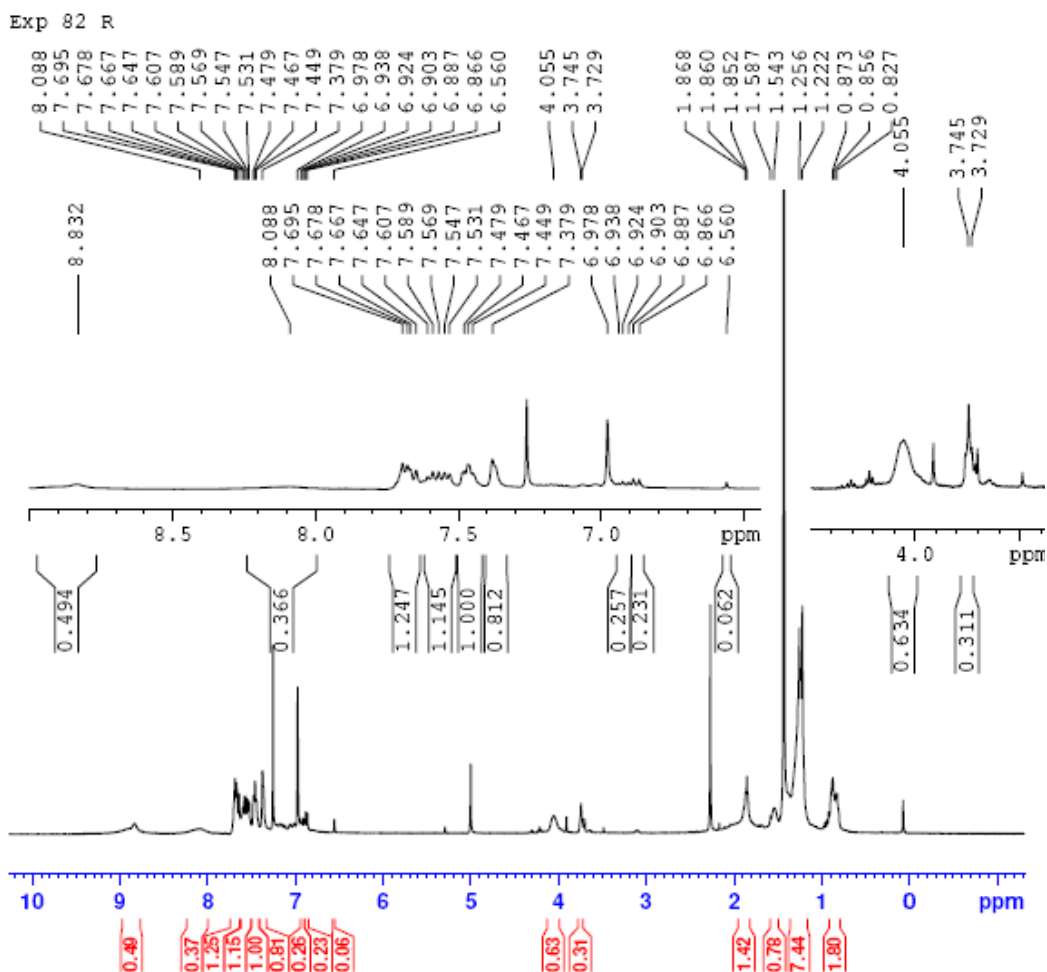
Figure A95 ¹H NMR of **43**
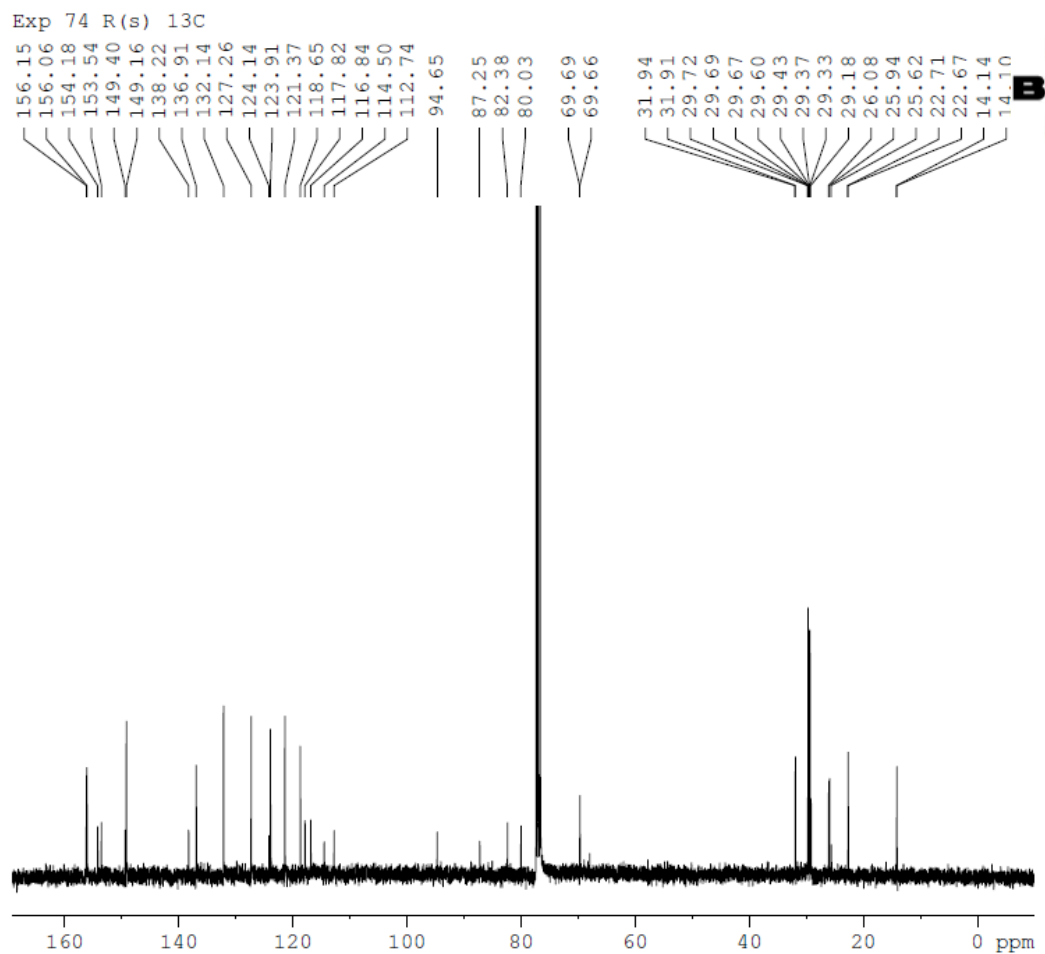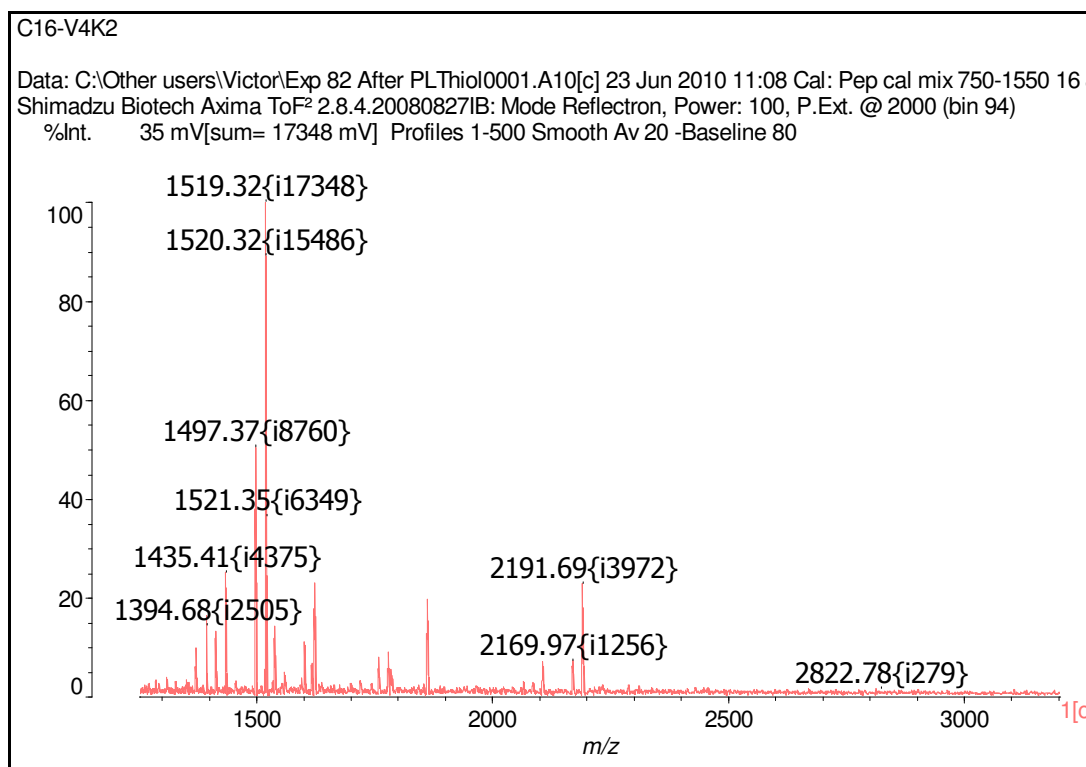
Figure A96 ^{13}C NMR of **43**

Figure A97 MALDI-TOF mass spectra of **43**

Tetraadduct of 43 with tetrakis(4-iodophenyl)methane (44). Toluene (15 ml) was added into a reaction mixture of **3** (0.05 g, 0.06 mmol), **43** (0.1 g, 0.12 mmol), $(Ph_3P)_2PdCl_2$ (0.025 g, 0.036 mmol) and CuI (7 mg, 0.036 mmol). The reaction mixture was then injected with triethylamine (0.13 ml, 0.9 mmol). The reaction mixture was then stirred at RT overnight. During 2nd day, more **43** (0.1 g, 0.12 mmol), $(Ph_3P)_2PdCl_2$ (0.025 g, 0.036 mmol) and CuI (7 mg, 0.036 mmol) were added into the reaction mixture and the reaction mixture was stirred at RT overnight. Toluene and triethylamine of the reaction mixture were then removed using a rotary evaporator to give a residue (0.44 g) as brown solid.

Figure A98 ^{1}H NMR of reaction mixture of **44**

C16-V4K2

Data: C:\Other users\Victor\Exp 82 After PLThiol0001.A10[c] 23 Jun 2010 11:08 Cal: Pep cal mix 750-1550 16
Shimadzu Biotech Axima ToF² 2.8.4.20080827IB: Mode Reflectron, Power: 100, P.Ext. @ 2000 (bin 94)
%Int.   35 mV[sum= 17348 mV] Profiles 1-500 Smooth Av 20 -Baseline 80

1519.32{i17348}
1520.32{i15486}
1497.37{i8760}
1521.35{i6349}
1435.41{i4375}
1394.68{i2505}
2191.69{i3972}
2169.97{i1256}
2822.78{i279}

m/z

Figure A99   MALDI-TOF mass spectra of reaction mixture of **44**

Reference:

(1) Andersen, C. S.; Gothelf, K. V. *Organic & Biomolecular Chemistry* **2009**, *7*, 58-60.